Two Windows on the Quantum World

By

Rose Evann Baunach
Dissertation

Submitted in partial satisfaction of the requirements for the degree of

Doctor of Philosophy

in

Physics

in the

Office of Graduate Studies

of the

University of California

Davis

Approved:

Andreas Albrecht, Chair

Lloyd Knox

Rajiv Singh

Committee in Charge

2023

For everyone near and far who has supported me during my Ph.D.

Thank you!

Contents

List of Figures

List of Tables

Abstract

Two Windows on the Quantum World

In this dissertation, I describe my work investigating quantum entanglement in a variety of contexts, with the aim of making concrete technical progress towards answering deep physical questions about the quantum nature of the world around us. Part One discusses work that broadly falls under quantum information science—with some motivations from cosmology—while the work in Part Two is mainly cosmological.

The research presented in Part One of this dissertation involves developing and utilizing the adapted Caldeira-Leggett (ACL) model, a toy model that describes a harmonic oscillator coupled to an idealized environment. The model has allowed my collaborators and me to explore novel quantum entanglement phenomena. In Part One I introduce the model and demonstrate its robustness (as done in [1]). I then present a derivation and investigation of behavior that occurs in the early stages of entanglement between a system initially in a quantum superposition and its environment (as done in [2]). Part One concludes with an investigation of entanglement phenomena in equilibrium, to see if the emergence of classicality requires an arrow of time, and what that might imply for deep questions about our Universe (as done in [3]).

Part Two considers entanglement in another cosmological context. In a series of papers [4, 5, 6] my collaborators and I investigated the influence entanglement may have on the period of inflation in the very early universe. Specifically, we calculated how entanglement can be generated between the quantum perturbations in the inflaton field—which drives inflation—and those in another spectator field. In Part Two I begin by deriving and demonstrating how entanglement is naturally and inevitably generated during inflation (as done in [4]). I then present results from a full parameter estimation using Monte Carlo techniques to determine what amount of entanglement is allowed by current cosmological data, and what that might imply for our Universe's quantum origins (as done in [5]). Finally, I present results that explore whether signatures of entanglement during inflation can be used to answer other questions about the history of the early universe—via dis-

tinguishing features of phase transitions and/or the inflationary energy scale that may be imprinted on cosmological observables due to entanglement (as explored in [6]).

Acknowledgments

First, I would like to thank my advisor Prof. Andreas Albrecht for his mentorship, guidance, and encouragement during graduate school. Andy, you have been a joy to collaborate with, and I look forward to discussing physics with you for many years to come.

Second, I would like to thank all my outstanding research collaborators: Arsalan Adil, Andrew Arrasmith, Nadia Bolis, Rich Holman, Stacie Moltner, Raquel Ribeiro, and Ben Richard. Without your insights and hard work this dissertation would not be possible.

Lastly, I thank all my mentors, colleagues, loved ones, and friends who have supported me during graduate school—I appreciate you all immensely.

Introduction

Chapter 1

Background and Overview

1.1 Entanglement

The world around us is fundamentally quantum, yet we have only begun to discover what a fully quantum description might imply. Any complete description of a quantum world, however, would have to include entanglement.

Entanglement is when a pair or group of objects, such as particles or fields, exist in such a way that the quantum state of each object cannot be described independently—even when the objects are separated by large distances. Any attempts to measure entangled objects individually will result in correlated outcomes when the measurements are compared.

For example, if systems A and B are entangled, a measurement of the state of A will determine the result of a subsequent measurement of the state of B, and vice versa. Moreover, A and B don't have to be in the same location to influence the outcome of each other's measurements. In fact we need not talk about measurement at all. If the states of A and B are entangled, that will be reflected in their evolution. If we discuss how the state of A evolves in time, the result will depend on the state of B as well.

However one might interpret these points, quantum entanglement is now routinely created and measured in laboratory experiments. Thus, a more thorough understanding of quantum entanglement and its effects is important not only for increasing our knowledge of the world, but also for many practical applications that seek to utilize quantum

entanglement, such as quantum computing.

In this dissertation, I describe my work investigating quantum entanglement in a variety of contexts, with the aim of making concrete technical progress towards answering deep physical questions about the quantum nature of the world around us. Part One discusses work that broadly falls under quantum information science—with some motivations from cosmology—while the work in Part Two is mainly cosmological.

1.2 Introduction for Part One

1.2.1 Open quantum systems, decoherence, and einselection

In reality, all quantum systems are open—the only truly closed (isolated) system is the entire universe. For many systems the effects of the surrounding environment are small, so one may model them as approximately closed. However, there are many cases where such approximations do not hold, and one is forced to consider environmental effects on the system of interest [7, 8, 9]. In an era of quantum computing that demands precise control over quantum systems, even small environmental effects can have observable consequences [7, 9].

Consider a "world" Hilbert space, comprised of a system and environment: $w = s \otimes e$. If we start the system and environment in a product state, interactions between the system and environment will cause entanglement between the two so that the total state is no longer separable, or:

$$|\psi_w\rangle = |\psi_s\rangle\,|\psi_e\rangle \quad \Longrightarrow \quad \sum_{i,j} b_{ij}\,|i\rangle_s\,|j\rangle_e \ . \tag{1.1}$$

Before interactions, the system and environment can be described by separate pure states, $|\psi\rangle$, but afterwards they are generally each in mixed states described by density matrices $\rho = \sum_{i,j} a_{ij}\,|i\rangle\,\langle j|$.

If our system is a single qubit[1] in the pure state $|\psi\rangle_s = a\,|\uparrow\rangle + b\,|\downarrow\rangle$ before it begins interacting with the environment, what influence does the environment have on its subsequent time evolution as the two become entangled? The onset of entanglement between

[1] Qubit: a two state quantum system.

the system and environment is the onset of decoherence—a term that describes the loss of coherence of the system as pure states are transformed into mixed states described by density matrices, i.e.:

$$|\psi_s\rangle = a\,|\uparrow\rangle + b\,|\downarrow\rangle \quad \overrightarrow{decoherence} \quad \rho_s = \sum_{i,k} p_{ik}\,|i\rangle_s\,\langle k|_s = Tr_e(|\psi_w\rangle\,\langle\psi_w|)\;. \tag{1.2}$$

A special case of decoherence, called einselection [10, 11], occurs when environmental interactions induce the system's density matrix to become diagonal in some preferred basis as the system decoheres, i.e.:

$$\rho_s = \sum_{i,k} p_{ik}\,|i\rangle_s\,\langle k|_s \quad \overrightarrow{einselection} \quad \sum_i p_i\,|i\rangle_s\,\langle i|_s\;. \tag{1.3}$$

A standard narrative would say that a single qubit system $|\psi\rangle_s = a\,|\uparrow\rangle + b\,|\downarrow\rangle$ will eventually evolve into $\rho_s = |a|^2\,|\uparrow\rangle\,\langle\uparrow| + |b|^2\,|\downarrow\rangle\,\langle\downarrow|$ under the influence of decoherence and einselection, if the qubit basis $\{|\uparrow\rangle, |\downarrow\rangle\}$ is the einselection basis set by various factors [10, 11]. This type of decoherence is measurable in the lab. However, exactly what happens to the system between these two times is still not fully explored—though the work in Chapter 3 of this dissertation adds more to the story.

1.2.2 A case for the ACL model

Throughout Part One of this dissertation I will make use of the adapted Caldeira Leggett (ACL) model, which was developed by my collaborators and me [1]. The ACL model is a tool to simulate system-environment interactions and their effects. It is a finite-dimensional, fully unitary, and numerically tractable adaption of the Caldeira-Leggett toy model describing a harmonic oscillator coupled to an idealized environment. The original Caldeira Leggett (CL) model [8, 12] utilizes a Hamiltonian of the form:

$$\begin{aligned} H_{world} &= H_{system} + H_{interaction} + H_{environment} \\ &= H^s_{SHO} \otimes 1^e + q_{SHO} \otimes H^e_{int} + H^e \otimes 1^s\;. \end{aligned} \tag{1.4}$$

In the CL model the system is a simple harmonic oscillator (SHO) moving in the standard harmonic potential, and the environment is represented by an infinite set of SHOs. As noted above, the ACL model accomplishes this in a finite dimensional Hilbert space.

Moreover, the fact that the ACL model can be evolved in a fully reversible unitary manner allows one to avoid the limitations of standard approximation schemes often used with the CL model.[2]

The ACL model is well suited to studying decoherence and einselection. The model allowed our collaboration to explore novel quantum entanglement phenomena and demonstrate results in a series of papers [1, 2, 3] with implications for condensed matter, cosmology, and other questions in quantum information science. In [1] we introduced the model and demonstrated its robustness for reproducing standard results in the existing literature, as discussed in Chapter 2 of this dissertation. The second paper in the series [2] presented a derivation and investigation of a novel behavior we found—the copycat process—that occurs in the early stages of decoherence between a system initially in a quantum superposition and its environment. I discuss these results in Chapter 3 of this dissertation. The technical analytic results from [2] are a useful tool for precisely studying the first stages of decoherence in open quantum systems. Also, the results presented for the early time evolution of Pauli spin observables occur in a time domain which may be measured in NMR and quantum computing experiments.

Lastly, the third paper in this series [3] has strong cosmological motivations. In [3] our collaboration investigated the possibility of einselection—decoherence into a preferred system basis—in equilibrium with the ACL model, to see if the emergence of classicality requires an arrow of time and what that might imply about initial conditions for our Universe. Let me unpack this statement a bit further. Our observed Universe has a very strong arrow of time, which is rooted in its low entropy starting point. It also evolves largely 'classically' on cosmological scales despite its quantum origins. The process of einselection plays an essential role in the emergence of classical from quantum and had previously only been studied in scenarios with an explicit arrow of time. This led us to the question, does the emergence of classicality require an arrow of time? An answer to the

[2]In practice the CL model is often treated in the "Markovian limit" where the particle evolution can be described by an irreversible master equation [7, 8]. Working in this limit provides tractable mathematics, but only allows one to explore situations which naturally have an arrow of time. As discussed subsequently, one of our motivations with the ACL model was to study the connection between einselection and the arrow of time, which necessitates utilizing a model outside the Markovian limit.

affirmative would have strong implications for the origins of our Universe. To concretely test this, we started with an equilibrium system—which has no global arrow of time by definition—and investigated through concrete calculations in the ACL model whether such a system can exhibit einselection. We performed our calculations in a formalism which ensured no external observer was assumed—a necessary choice in order to generalize our results to cosmology. The results of our investigations in [3], described in Chapter 4 of this dissertation, have stimulated interesting conversations in the physics community, and we are still processing their cosmological implications ourselves. However, a couple of results stand out. First, we found individual histories that exhibit an arrow of time within the overall equilibrium state of the system—demonstrating that a global arrow of time is not required for the emergence of classical behavior, at least at the level of our toy model. Second, our results imply that we may be much more disconnected from cosmic initial conditions than previously thought.

1.3 Introduction for Part Two

1.3.1 Inflation and the expanding universe

A central task of cosmology is to describe how the universe evolved into its present form. There is still much to be discovered, but a general consensus in the field is that building our observable Universe requires a period of inflation [13]. Inflation is a period of accelerated expansion in the very early universe, potentially only 10^{-34} seconds after the start [14]. It conventionally solves many cosmological "puzzles"—such as the observed uniformity in the cosmic microwave background (CMB)[3]—and it provides a mechanism for the origins of perturbations that source CMB fluctuations and the growth of large scale structure, such as galaxies [14, 15, 16, 17].

Let us expand more on the second point. The universe is always expanding, but the rate at which it stretches is different at different epochs in the past. Our Universe is approximately flat, homogeneous, and isotropic on large scales, which allows us to describe

[3]The CMB is electromagnetic radiation streaming towards us from approximately 400,000 years after the start of the universe. Its observed spectrum is nearly uniform, with small fluctuations [15].

distances by a Friedmann Robertson Walker (FRW) metric of the form:

$$\mathrm{ds}^2 = -\mathrm{dt}^2 + a^2(t)[\mathrm{dr}^2 + r^2(\mathrm{d}\theta^2 + \sin^2(\theta)\mathrm{d}\phi^2)] \tag{1.5}$$

where $a(t)$ is called the "scale factor". The scale factor parameterizes the stretching of space. If we visualize the universe as a grid, this would mean objects are located at fixed (r, θ, ϕ) while the space between them continues to expand,

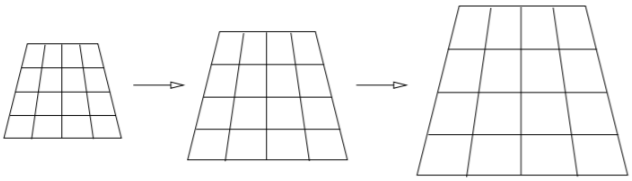

such that:

$$d_{\text{physical}}(t) = a(t) d_{\text{coordinate}} \ . \tag{1.6}$$

A useful quantity in cosmology is the Hubble parameter:

$$H(t) = \frac{1}{a(t)} \frac{da(t)}{dt} \ . \tag{1.7}$$

The Hubble parameter has units of inverse time, so $R_H = \frac{1}{H(t)}$ gives a length scale (in $c = 1$ units) which roughly describes the size of the observable universe at different times in its evolution. Using the Einstein Equations for a flat FRW universe, one can derive:

$$\left(\frac{\dot{a}}{a}\right)^2 = H^2 = \frac{\rho}{3} \qquad \frac{d\rho}{dt} + 3H(\rho + p) = 0 \ , \tag{1.8}$$

after setting $8\pi G = 1$. These are a form of the Friedmann Equations [14], where ρ is energy density and p is pressure. Given an equation of state parameter $w = \frac{p}{\rho}$, one can determine a variety of approximate scaling relations for different eras in our Universe's history:

Era	w	$\rho(a)$	$a(t)$	$R_H \propto \rho(a)^{-1/2}$
Matter Dominated	0	a^{-3}	$t^{2/3}$	$a^{3/2}$
Radiation Dominated	$\frac{1}{3}$	a^{-4}	$t^{1/2}$	a^2
Λ (Dark Energy) Dominated	-1	a^0	e^{Ht}	a^0

(We are approximately in a Λ dominated era today.)

Fig. 1.1 shows R_H vs $a(t)$. The red diagonal lines represent the physical wavelength of perturbations, $\lambda_{phys}(t) = a(t)\lambda$, created during inflation.

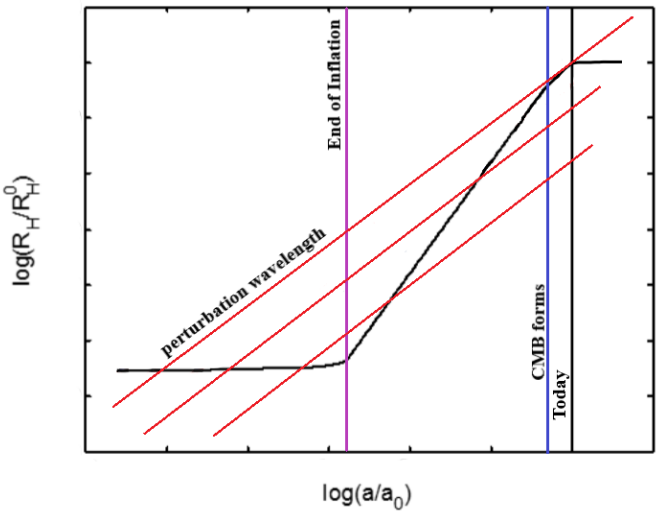

Figure 1.1: Log-log plot of $R_H = \frac{1}{H(t)}$ vs $a(t)$. Diagonal red lines show how the wavelengths of perturbations evolve in an expanding universe.

As one can see from the figure, a period of inflation with $\rho_I \approx a^0$ allows initial perturbations from inflation to be "mapped" later in time. Given standard inflationary theory, an approximate narrative is that these perturbations don't evolve when $\lambda_{physical} > R_H$ [18, 14, 15, 16, 17]. Thus, a period of inflation will take perturbations from the inflationary era and map them to later times—such as the era of the CMB—without change during the time $\lambda_{physical} > R_H$. This gives us a tool to refine our theory of inflation. For example, one can theoretically calculate the spectrum of inflationary perturbations when $\lambda_{physical} = R_H(\text{inflation})$, and then compare the results with what we observe from the CMB.

Inflation is a semi-classical theory of quantum fluctuations around a classical background. The inflaton field, Φ, models both qualities: $\Phi(t, \mathbf{x}) = \phi(t) + \delta\phi(t, \mathbf{x})$. The evolution of the classical background, $\phi(t)$, is modeled by the following equation of motion:

$$\ddot{\phi} + 3H\dot{\phi} + \frac{dV(\phi)}{d\phi} = 0 \tag{1.9}$$

along with the Friedmann equation:

$$H^2 = \frac{1}{3}\rho_{inflation} = \frac{1}{3}(\frac{1}{2}\dot{\phi}^2 + V(\phi)) \ . \tag{1.10}$$

Using the "slow-roll" conditions [14]—which state that $\ddot{\phi}$ can be ignored and $V(\phi) \gg \dot{\phi}^2$ in the above equations—one can verify that we obtain a period of accelerated expansion with approximately constant H. This is consistent with the narrative surrounding Fig. 1.1.

To model the quantum fluctuations in the inflaton field, a key concept is that short wavelength modes must be in their ground state. The standard choice for this ground state is to pick the Bunch-Davies (BD) vacuum state [19]—which is the particle physics ground state adapted for an expanding universe.

Given inflationary quantum perturbations $\widehat{\delta\phi}_{\mathbf{k}} = v_k(\tau)\widehat{a}_{\mathbf{k}} + v_k^*(\tau)\widehat{a}_{\mathbf{k}}^\dagger$ in Heisenberg picture [14], the mode functions v_k satisfy:

$$v_k'' + \omega_k^2(\tau)v_k = 0 \tag{1.11}$$

which is the equation of motion of a harmonic oscillator with time-dependent frequency. Bunch-Davies corresponds to a specific choice for $v_k(\tau)$.

The variance

$$\langle\widehat{\delta\phi}_{\mathbf{k}}\widehat{\delta\phi}_{\mathbf{k}}^\dagger\rangle = |v_k(\tau)|^2 \ , \tag{1.12}$$

characterizes the size of inflationary perturbations for each k mode—this can eventually be compared with the CMB (see Chapters 5, 6, and 7 of this dissertation, or e.g. [14, 15, 16, 17] for further technical details).

1.3.2 Motivation for entanglement during inflation

As discussed in the previous section, inflation is a period of accelerated expansion in the very early universe whose quantum fluctuations are postulated to source all the structure in our Universe. The set of inflationary models that best fit our current data are all driven by a single slowly rolling scalar field, called the inflaton. A key assumption in these models is that the quantum fluctuations in the inflaton field are generated by a particular vacuum state, the Bunch-Davies (BD) vacuum [19]. The BD state has a number of attractive theoretical features, including the fact that it approaches the Minkowski

flat space vacuum in the infinite past. Observationally, it produces a primordial power spectrum—describing the amplitude of quantum fluctuations in the inflaton field at the end of inflation, as a function of wavenumber—that is nearly scale invariant, in excellent agreement with the Λ-Cold Dark Matter (ΛCDM) concordance model of cosmology [20].

The standard picture of inflation, including its choice of vacuum state, is incredibly simple. However, in our current era of abundant observational data it's both possible and worthwhile to explore how strongly our data prefers the standard scenario. In particular, it would be fascinating to know to a precise degree that the vacuum state of the inflaton *is* the BD state. Such a result would be a rigorous statement about our cosmic origins, confirm standard assumptions in the field, and would no doubt stimulate theoretical research to explain what mechanisms protect the standard inflationary scenario from additional quantum corrections, among other questions.

With these motivations in mind, my collaborators and I looked at entangled states—specifically states where the quantum fluctuations in the inflaton field are entangled, due to gravity, with those of another subdominant spectator scalar field. Such entangled states are some of the simplest perturbative modifications to the BD vacuum, and many early universe models include spectator scalars. In Chapter 5 of this dissertation I present how our collaboration discovered that even when both fields start in the BD vacuum state at the onset of inflation, entanglement is both naturally and inevitably dynamically generated during inflation [4]. Observationally, this entanglement generates small oscillations in the primordial power spectrum on top of the standard BD result. (The exact features of these oscillations depend on the details of the spectator scalar field's potential.) These oscillations in the primordial power spectrum then imprint features in cosmic microwave background (CMB) observables, which can be constrained using data from experiments like Planck [21].

In [4] our collaboration showed that entangled states were not only natural, but also potentially consistent with Planck data. Next, we performed a full Monte Carlo parameter estimation [5] to see whether cosmological data truly prefers the BD vacuum over an entangled state. This analysis enabled us to set the first precise limits on the amount of

entanglement in the vacuum state of the inflaton allowed by current data, and our results found parameter values that fit the data as well as ΛCDM. I present the results from this study in Chapter 6 of this dissertation. This study also substantially extended and refined the technical framework for entangled states in Schrödinger picture quantum field theory that we developed in [4].

Finally, in another project [6] I explored whether our entangled states framework could be used to answer other questions about early universe history. Using a Higgs-like potential as the spectator field, I investigated whether distinguishing features of phase transitions and/or the inflationary energy scale could be imprinted on cosmological observables due to entanglement. The results of this study are presented in Chapter 7 of this dissertation.

Part One

Chapter 2

Adapted Caldeira-Leggett Model

The material in this chapter previously appeared in ***Adapted Caldeira-Leggett Model*** *by Andreas Albrecht, Rose Baunach, and Andrew Arrasmith [1].*

ABSTRACT: We preset a variant of the Caldeira-Leggett (CL) model of a harmonic oscillator coupled to an environment. The CL model is a standard tool for studying the physics of decoherence. Our "adapted Caldeira-Leggett" (ACL) model is built in a finite Hilbert space which makes it suitable for numerical studies. Taking a numerical approach allows us to avoid the limitations of standard approximation schemes used with the CL model. We are able to evolve the ACL model in a fully reversible unitary manner, without the built-in time asymmetry and other assumptions that come with the master equation methods typically used. We have used the ACL model to study new topics in the field of decoherence and einselection where the full unitary evolution is essential to our work. Those results (reported in companion papers) include an examination of the relationship between einselection and the arrow of time, and studies of the very earliest stages of einselection. This paper provides details about the ACL model and our numerical methods. Our numerical approach makes it straightforward to explore and plot any property of the physical system. Thus we believe the examples and illustrations we present here may provide a helpful resource for those wishing to improve their familiarity with standard decoherence results, as well as those looking to probe the underpinnings of our companion papers. We expect the ACL model will be a useful tool for exploring

additional phenomena that cannot be studied using traditional approximation schemes.

2.1 Introduction

The Caldeira-Leggett (CL) model is a toy model describing a particle which moves in its own potential and is also coupled to an environment [22, 12, 23]. The environment is usually treated as an infinite set of harmonic oscillators, and the particle is often taken to move in a harmonic potential as well. The particle plus environment describe a closed system which can in principle be treated quantum mechanically as a system undergoing reversible unitary evolution. In practice the CL model is often treated in the "Markovian limit" where the particle evolution can be described by an irreversible master equation. Working in this limit provides tractable mathematics which can be used to study particle-environment interactions in situations which naturally have an arrow of time. For example the CL model has been used in pioneering explorations of decoherence [24] and einselection [25].

This paper introduces an "adapted Caldeira-Leggett" (ACL) model. The adaptations are chosen to reproduce the essential features of the CL model as fully as possible within a finite Hilbert space. The goal is to be able to evolve the ACL model easily on a desktop computer in its full unitary form, thus enabling the convenient exploration of a more complete range of physical situations including those outside the Markovian limit.

Aside from describing various technicalities of how we construct the ACL model, we present here results from "putting it through its paces" which demonstrate that the ACL model does a good job of reproducing physics phenomena that are an established part of the decoherence literature. These cross-checks give us a solid foundation on which to explore the new directions, which we report in companion papers [3, 2]. For the most part, we do not expect the phenomena presented in this paper to be new to an expert on decoherence. On the other hand, someone learning this topic might find our graphical presentation centered on a specific physical system a useful compliment to a more thorough

review such as [26] and may even provide a helpful starting point.

The physics of einselection plays an important role in many physical phenomena (see for example [26, 27, 28]). The development of the ACL model was originally motivated by our interest in exploring the physics of einselection under equilibrium conditions[1]. The Markovian limit, with its definite arrow of time, clearly cannot describe the full fluctuations of an equilibrium system. We also expect the ACL model will be useful in exploring other physics outside of the Markovian regime, and we have already found one such example (which we've named the "copycat process") that we mention briefly in Sect. 2.3.5 and develop further in a companion paper [2]. We have also found the ACL model useful for exploring notions of thermalization in finite systems [30].

While there are a variety of other methods that can also go beyond the limitations of Markovian evolution (see e.g. this review [31] and references therein), our goal was to specifically model einselection in a clear and transparent manner with as few computational resources as possible. We found that a simplistic model of the environment (as a general scrambler following [32, 33]) helped realize these priorities (versus basing the environment on a detailed physical system [2]). Also, since the CL model is one of the pioneering models of einselection, it made sense to develop the ACL model, to better compare with the existing decoherence literature.

We organize this paper as follows. Section 2.2 defines the ACL model and demonstrates the robustness of our numerical calculations. Section 2.3 explores a variety of standard results from the literature using the ACL model. For example we show how an initial Schrödinger cat state of superposed wavepackets is einselected to a classical mixture of single packets. We also introduce the "copycat process," a new phenomenon which we explore extensively in [2]. Section 2.4 explores the way the ACL model both approaches and then remains solidly situated in a fluctuating equilibrium state when evolved long enough. The presence of a fully fluctuating equilibrium state is a behavior not accessible

[1]These motivations originate in cosmology where connections between the emergence of classicality (related to einselection) and the arrow of time (which originates with cosmology, as discussed for example in [29]) might lead to useful insights.

[2]Still, we note some connections between the ACL model and NMR systems in Sects. 2.5 and 2.6.3 and also in [2].

through master equation techniques, but one which is very naturally achieved with our methods. This equilibrium behavior forms a foundation for our exploration of the relationship between einselection and the arrow of time in [3]. In Sect. 2.5 we introduce the "reduced Caldeira-Leggett" (RCL) model which replaces the SHO with a single qubit. We demonstrate how the RCL model can access a different set of phenomena. The results from this paper are placed in the context of the existing literature in Sect. 2.6. Among other things, we relate some of our results to Nuclear Magnetic Resonance (NMR) physics and "Loschmidt echos" (a concept developed in discussions of the arrow of time). Section 2.7 presents our conclusions.

A series of appendices present additional technical information. Appendix 2.A explores einselection in the "quantum limit" of the ACL model. Appendix 2.B presents details of the eigenstates of the truncated SHO, which reveal differences between the truncated and the continuum cases. We give a detailed picture of the spectra of the different Hamiltonians (SHO, environment and combined) in Appendix 2.C. Appendix 2.D presents our numerical techniques and tolerances.

2.2 The ACL model

We consider a "world" Hilbert space $w = s \otimes e$ which is a tensor product of a "system" Hilbert space s and the environment space e. We consider a Hamiltonian of the form

$$H_w = H_s \otimes \mathbf{1}^e + q_s \otimes H_e^I + \mathbf{1}^s \otimes H_e. \tag{2.1}$$

Equation 2.1 describes the form of both the CL and ACL models. The differences arise in the specifics of the different ingredients. These are the system Hamiltonian H_s, the self-Hamiltonian for the environment H_e, and the piece of the interaction Hamiltonian in the e subspace, H_e^I. We focus on the case where s is a simple harmonic oscillator (SHO). The position operator of the system, $q_s = q_{SHO}$, is defined in the usual way for the CL model. However for the ACL model s is a "truncated SHO" (in order to allow a numerical treatment) and the definition of q_{SHO} for that case is nontrivial. Hamiltonians of this form have features that enable the system to become entangled with the environment in ways that reflect certain realistic physical situations. The interaction term changes the state

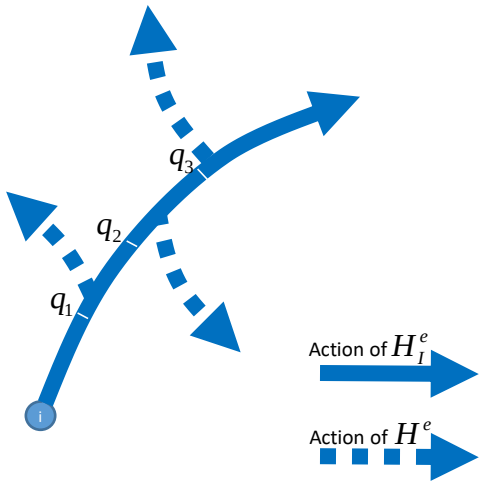

Figure 2.1: The interaction term $q \otimes H_e^I$ moves the initial environment state along a specific path in the e Hilbert space determined by H_e^I, illustrated by the solid curve. The rate of movement along this path is proportional to the value of q, and that allows different q states to become entangled with different environment states. In the case where $\left[H_e^I, H_e\right] \neq 0$, the action of H_e can push the evolution off the original path in a variety of different directions depending on the starting point ($\propto$ the value of q). These various paths are illustrated by the dashed curves. The non-commuting property can make the process of entanglement much more efficient (especially for the large N_e case, not shown in this sketch).

of the environment with a strength proportional to the value of q_s, so different positions become entangled with different environment states. When H_e and H_e^I don't commute (the case for both CL and ACL models) the entangling process is much more effective, as illustrated heuristically in Fig. 2.1.

2.2.1 The SHO

For a normal (un-truncated) SHO the matrix elements of the lowering operator $\mathbf{a}$ in the basis given by number (or energy) eigenstates is given by

$$\langle i| \mathbf{a} |j\rangle = \sqrt{j}\delta_{i,j-1} \tag{2.2}$$

with $j \geq 1$. For our truncated SHO the same formula is valid for $\hat{\mathbf{a}}$ (where the hat denotes the truncated version) but it only applies for $\{i, j \in 1 : N_s\}$ where N_s is the size of the truncated SHO Hilbert space. The operator $\hat{\mathbf{a}}^\dagger$ is formed by conjugating $\hat{\mathbf{a}}$, and $\hat{\mathbf{q}}$, $\hat{\mathbf{p}}$ and

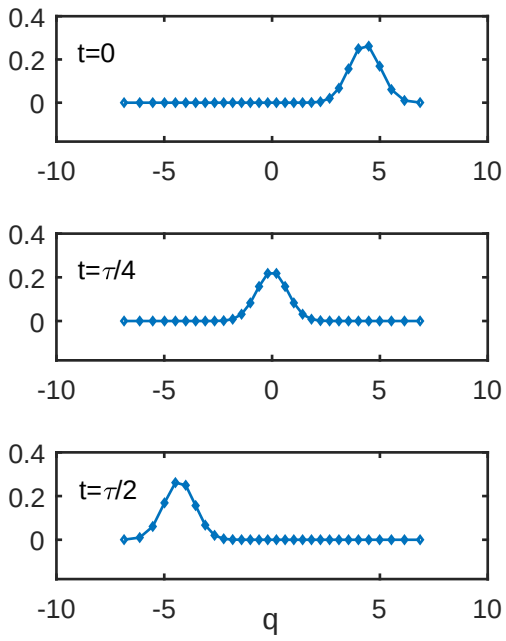

Figure 2.2: A coherent state wavefunction (squared) for the truncated SHO shown at different points in its period τ. Despite certain differences from the continuum case noted in the text, the shape and robustness under evolution of this state corresponds to the properties of continuum coherent states.

$\hat{\mathbf{H}}_{\mathbf{SHO}}$ are all constructed from $\hat{\mathbf{a}}$ and $\hat{\mathbf{a}}^\dagger$ using the usual formulas from the un-truncated case. These operators in the truncated space don't have all the usual properties due to the truncation. For example

$$\left[\hat{\mathbf{a}}, \hat{\mathbf{a}}^\dagger\right] = \mathbf{1} + \Delta \tag{2.3}$$

where $\Delta(i,j) = -N_s \delta_{i,N_s} \delta_{j,N_s}$. We chose these definitions for the truncated operators because they have some practical advantages over other choices. The main advantage is illustrated in Figs. 2.2 and 2.3. Figure 2.2 shows a coherent state constructed thus:

$$\psi_\alpha(q) = \langle q \mid \alpha \rangle = \langle q | \exp\left(\alpha \hat{\mathbf{a}}^\dagger - \alpha^* \hat{\mathbf{a}}\right) |0\rangle \tag{2.4}$$

where $|0\rangle$ is the ground state of $\hat{\mathbf{H}}_{\mathbf{SHO}}$ and $\langle q|$ is the q eigenstate of $\hat{\mathbf{q}}$. The x axis gives the eigenvalue of $\hat{\mathbf{q}}$, which is really a discrete quantity ($\hat{\mathbf{q}}$ has only N_s eigenvalues, which run

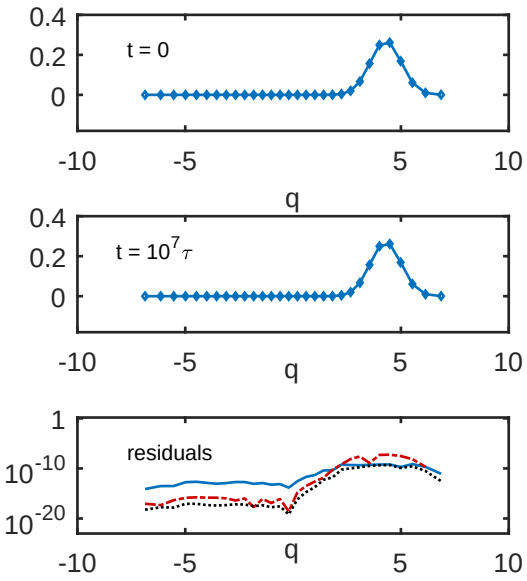

Figure 2.3: A coherent state at $t = 0$ and $t = 10^7\tau$. The third panel shows the residuals for the probabilities (solid) and for the real (dotted) and imaginary (dot-dashed) part of the amplitude. These curves illustrate that the numerically evolved truncated model reproduces the periodic properties expected of the continuum case to an excellent degree of accuracy.

from -2π to 2π). The discrete sets of points plotted (shown by markers) are connected only to reference the continuum of the un-truncated SHO which this system is intended to approximate[3]. We call the SHO period τ and in our units $\tau = 2\pi$. We've taken $N_s = 30$ here, and in all the examples shown in this paper.

The top two panels of Fig. 2.3 show the same coherent state at $t = 0$ and $t = 10^7\tau$. The third panel shows the residuals. The very small sizes of the residuals further demonstrate the robust nature of the truncated SHO. The specifics of our numerical approach (including several additional checks) are discussed in Appendix 2.D.

[3]The truncated form does lead to some novel features in the eigenstates of H_s as discussed in Appendix 2.B.

2.2.2 The interaction and environment self-Hamiltonian

The interaction Hamiltonian has the form $q_s \otimes H_e^I$. For the ACL model we use $q_s = \hat{\mathbf{q}}$. The environment piece, H_e^I, has the form

$$H_e^I = E_I R_I^e + E_I^0. \tag{2.5}$$

The matrix R_I^e is a random matrix constructed by drawing each of the real and imaginary parts of each independent matrix element of a $N_e \times N_e$ Hermitian matrix uniformly from the interval $[-0.5, 0.5]$ using the computer's random number generator.

The environment self-Hamiltonian is given by

$$H_e = E_e R^e + E_e^0 \tag{2.6}$$

where R^e is constructed in the same manner as R_I^e, but as a separate realization. In Eqns. 2.5 and 2.6, E_I and E_e are c-numbers which parameterize the overall energy scales. Both R_I^e and R^e are fixed initially and are not changed during the time evolution. The full Hamiltonian of the ACL model is time independent. All the results in this paper use $E_I^0 = E_e^0 = 0$, but we have found nonzero values for these offset parameters to be helpful for other calculations we report elsewhere.

The job of H_e^I and H_e is to move states around in the environment efficiently, so that entanglement between the SHO and the environment can emerge as fully as possible despite working within the confines of a finite system[4]. We find the random form of these operators does this job well, and since $\left[H_e^I, H_e\right]$ is just another random matrix the non-commutivity discussed with Fig. 2.1 is easily achieved. The work presented here uses $N_e = 600$. This choice, along with $N_s = 30$, was made via an informal optimization process to maximize the utility of the ACL model within the constrained resources of our desktop computer.

There is also a simple way to modify our ACL model to create H_e's with different spectra. The crucial aspect achieved by the random matrices in H_w is the non-commutivity of H_e^I and H_e. This aspect is enabled by the eigen*vectors* of independently generated

[4]The approach to H_e^I and H_e used here is similar to that pioneered in [32], although in that work the "system" was a single qubit.

random matrices in large spaces having very little overlap. One could alternatively create H_e^I and H_e by starting in diagonal form (with a spectrum of eigenvalues of your choosing) and then changing basis using a random unitary to produce a "random matrix" with the specified eigenvalue spectrum. We experimented a bit with this approach to generating H_e^I and H_e, but did not find that the extra complexity sufficiently changed the quality of the explorations we were doing to be worthwhile for our purposes.

The next few sections contain some illustrative examples to showcase how standard decoherence phenomena are realized in the ACL model. We also lay groundwork for new results discussed in more detail in [2, 3]. The technical minded reader may also wish to refer to Appendices 2.B and 2.D, as these appendices provide more details on the numerical realization of the ACL model (Appendix 2.D), and its sensitivity to the finite dimensional Hilbert space quantities introduced in Sect. 2.2 (Appendix 2.B).

2.3 Some illustrative examples

2.3.1 Decoupled "Schrödinger cat"

Here we consider the "Schrödinger cat" state formed as a coherent superposition of two coherent states:

$$|\psi\rangle = a_1 |\alpha_1\rangle + a_2 |\alpha_2\rangle \tag{2.7}$$

where each $|\alpha\rangle$ is given by Eqn. 2.4.

Figures 2.4 and 2.5 are of the same form as figs. 2.2 and 2.3 but showing a state given by Eqn. 2.7 with $a_1 = 1/\sqrt{3}$, $\alpha_1 = 3$, $a_2 = \sqrt{2/3}$ and $\alpha_2 = -2.1$. Again, these are evolved with system-environment interactions turned off. These figures show that the evolution of coherent superpositions is also robust for the ACL model, even though the discrete nature of the truncated SHO shows up in the jagged features of the wavefunction when the two packets collide.

2.3.2 Generating entanglement

Now we consider the case where system-environment interactions are turned on. The interactions will cause an initial product state given by

$$|\psi\rangle_w = |\psi\rangle_s |\psi\rangle_e \tag{2.8}$$

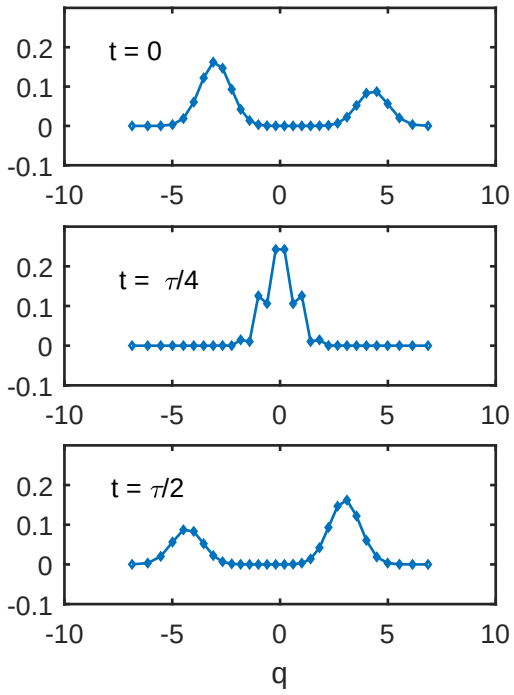

Figure 2.4: Evolution of a "Schrödinger Cat" superposition of coherent states (specifics similar to Fig. 2.2).

to evolve into an entangled state, where the states of the system and environment are described by the density matrices

$$\rho_s \equiv Tr_e \left(|\psi\rangle_{ww} \langle\psi| \right) \tag{2.9}$$

and

$$\rho_e \equiv Tr_s \left(|\psi\rangle_{ww} \langle\psi| \right). \tag{2.10}$$

The Von Neumann entropy,

$$S \equiv tr \left(\rho_s \ln \rho_s \right) = tr \left(\rho_e \ln \rho_e \right), \tag{2.11}$$

takes larger values when the degree of entanglement is greater. The maximum possible value for the entropy is given by

$$S_{\max} = \ln \left(N_{\min} \right) \tag{2.12}$$

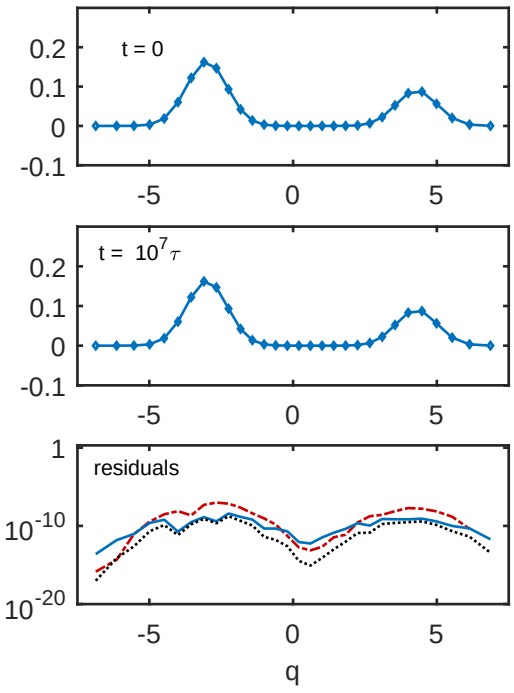

Figure 2.5: Evolution of a "Schrödinger Cat" superposition of coherent states (specifics similar to Fig. 2.3).

where $N_{\min}$ is the smaller of N_s and N_e. Figure 2.6 shows the evolution of the entropy for two values of E_I. Throughout this work we use units where $\hbar = \omega_{SHO} = 1$. We also take $E_e = 0.75$ throughout. For Fig. 2.6 the initial state has the product form (Eqn. 2.8) with $|\psi\rangle_s$ given by the Schrödinger cat state discussed above and $|\psi\rangle_e$ given by the 500^{th} eigenstate of H_e (indexed from lowest to highest eigenvalues). The choice of $|\psi\rangle_e$ will be discussed further Sect. 2.4. We consider a "weak coupling" ($E_I = 0.03$) case and a "strong coupling" ($E_I = 0.25$) case.

2.3.3 Einselection

A generic state for w will be an entangled state with non-trivial density matrices, ρ, for system and environment. Thus, it is not surprising that in the interacting case that starts in a product state the entanglement entropy will increase from zero. This process is generally called decoherence, and it would take place with just about any Hamiltonian for

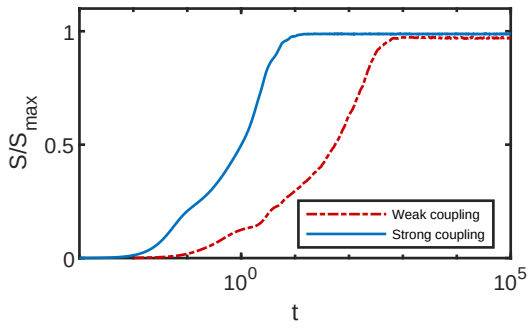

Figure 2.6: The evolution of the von Neumann entropy for $E_I = 0.03$ ("weak coupling," dashed) and $E_I = 0.25$ ("strong coupling," solid). Increasing the interaction strength causes the entanglement to increase more rapidly, and also allows the system to come a bit closer to $S_{\max}$.

w[5]. For a randomly chosen H_w, one would expect the entanglement entropy to become large and the eigenstates of ρ_s and ρ_e to evolve randomly over time without displaying any regular behavior.

There is a special case of decoherence called "einselection" where the initial state and interactions can be set up to favor a special set of eigenstates for ρ_s called "pointer states." The CL model has been used in many of the pioneering studies of decoherence and einselection. Here we revisit some of these results using the ACL model.

The Schrödinger cat state depicted in the top panel of Fig. 2.5 is a superposition of two coherent states which can be thought of as "classical wavepackets." Fig. 2.7 shows what this initial state evolves into by time $t = 2.5\tau$ for the weakly interacting case. The state of s for $t > 0$ is a density matrix, and Fig. 2.7 shows the two eigenstates of ρ_s with the largest eigenvalues. One can see that these look like single classical wavepackets. Figure 2.8 depicts similar information about the state but evolved further in time, to $t = 4\tau$. These eigenstates also look like classical wavepackets, just caught at a different phase of their oscillation.

There are a variety of technical tools that are useful in studying einselection. One can anticipate the pointer states and study the decrease in the off diagonal element of ρ_s

[5]See [33] for some general reflections quantum coherence and the emergence of entanglement.

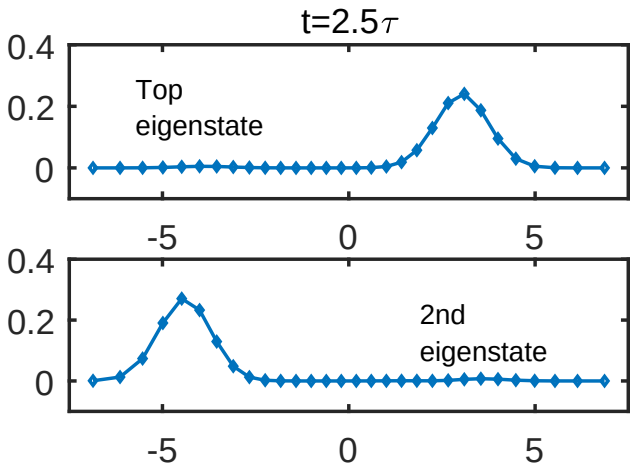

Figure 2.7: The two most probable eigenstates of ρ_s after einselection has completed. The initial states was the Schrödinger cat state depicted in Fig. 2.3.

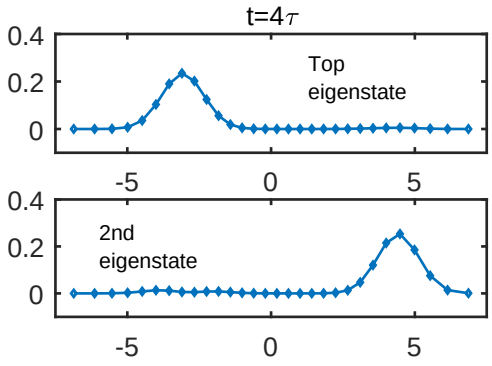

Figure 2.8: The top post-einselection eigenstates of ρ_s shown in Fig. 2.7, but here shown at a different phase in their periodic motion.

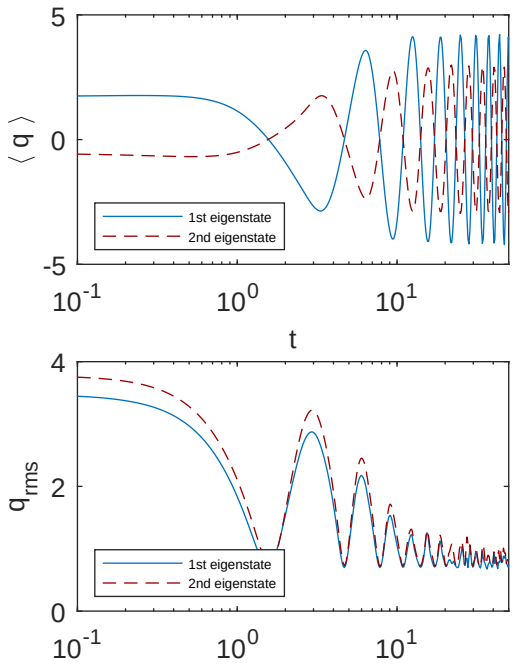

Figure 2.9: The evolution $\langle q \rangle$ and q_{rms} as a function of time for the top two eigenstates of ρ_s shown in Figs. 2.7 and 2.8. (The most probable eigenstate is shown with the solid curve, the next most probable is dashed.) One can see these attributes evolve from those of the Schrödinger cat initial state (oscillating q_{rms} and small oscillating values of $\langle q \rangle$) to those of individual wavepackets (essentially constant q_{rms} with larger oscillations in $\langle q \rangle$).

in that basis (as per [10]). The consistent histories framework can also be useful. The approach we use here, focusing on the eigenstates of ρ_s, parallels that developed in [32] (where a comparison with the consistent histories approach is also presented). We also use the consistent histories method extensively with the ACL model in [3].

One can look at this phenomenon a bit more systematically by studying how various moments of the eigenstates evolve over time. Figure 2.9 shows the time evolution of $\langle q \rangle$ and q_{rms}. One can see how these quantities first exhibit the "Schrödinger cat" properties, but over time develop the properties of einselected pointer states. We conclude that the ACL model nicely reproduces the well-known phenomenon of "einselection," as it should if it is to reflect key properties of the CL model.

2.3.4 Evolution of the eigenvalues of ρ

Figure 2.10 shows the eigenvalues p_i of ρ_s (for pure states in w, the nonzero ones are always identical to the nonzero eigenvalues of ρ_e). The evolution of the p_i's includes the information reflected in the von Neumann entropy (Fig. 2.6), and clearly shows a transient phase during einselection and a subsequent equilibrium phase where the p_i values are closer together and hold reasonably steady. One can infer from Fig. 2.9 that the time to full einselection is $O(20)$. The dissipation processes that lead to equilibration operate on a time scale roughly 20 times longer. One can see that by the time einselection is complete there are somewhat more than two nonzero p_i's. This is related to the relative closeness of the decoherence and dissipation times[6], which in turn is connected with the competition between the interaction Hamiltonian (which tries to localize the SHO in space) and the SHO Hamiltonian (which causes localized states to spread).

Figure 2.11 shows a case with more widely separated decoherence and dissipation times. The calculation shown in Fig. 2.11 uses $\tau_{SHO} = 2\pi \times 10^3$ and the initial state is a superposition of eigenstates of $\mathbf{q}_{SHO}$ (in the same proportions and locations as the coherent states used in Fig. 2.10). These differences mean the interaction term ($\propto \mathbf{q}_{SHO}$) is not trying to "chop up" the initial wavepackets, in contrast to the coherent state initial conditions, which spread across several eigenstates of $\mathbf{q}_{SHO}$.

Note that for a while p_1 and p_2 in Fig. 2.11 correspond to the probabilities assigned to the wavepackets in the initial superposed state. This feature means that the environment can be thought of as "making a good measuremnt" of the SHO, in the sense that interactions with the environment have put the SHO in a classical mixture of wavepackets with the right probabilities. Later, this good measurement comes unraveled as dissipation sets in.

2.3.5 The copycat process

Our ACL model allows us to scrutinize the very first steps of the einselection process. In doing so we've become intrigued by certain aspects of these early stages. Figure 2.12 shows

[6]This is in contrast to more macroscopic systems, where the decoherence and dissipation timescales are typically widely separated (see e.g. [24, 34, 26]).

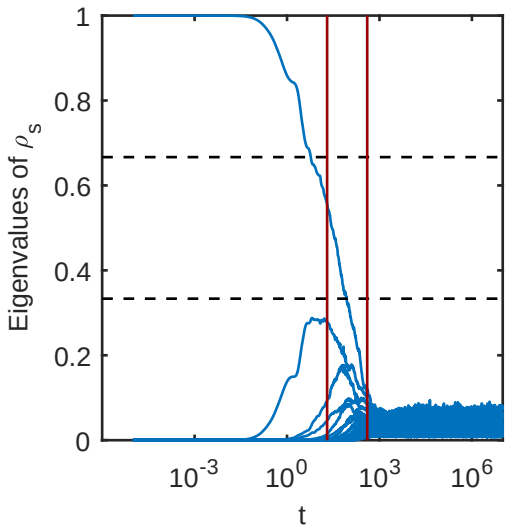

Figure 2.10: The eigenvalues of ρ_s. The purity of the initial state is reflected in the fact that only one eigenvalue is nonzero initially. The "einselection time" (marked by the left vertical line) corresponds to the "collapse" of the Schrödinger cat pure state into a mixture of wavepackets. The dissipation time (right vertical line) is about 20 times longer. The dashed horizontal lines show the probabilities assigned to the two wavepackets in the initial Schrödinger cat state.

the early evolution of the 2nd eigenvalue and eigenstate of ρ_s, in the case where the system starts in a pure Schrödinger cat state which becomes entangled with the environment. The eigenstate takes an intriguing form that appears to be a "mirror image" of the initial state, and remains in this form in a transiently stable way over several decades of time evolution (and growth of p_2). We call these mirror image states "copycat" states. In [2] we systematically investigate this curious behavior and argue that it is quite generic for early time evolution of Schrödinger cat states. We also discuss how this phenomenon generalizes in the case of larger numbers of "cats."

2.4 Approach to Equilibrium

Figure 2.13 shows the evolution of entropy and energies over time for a variety of initial states of the environment for the weakly coupled case ($E_I = 0.03$). The strong coupling case is shown in Fig. 2.14. We start the environment in an eigenstate of H_e, with values

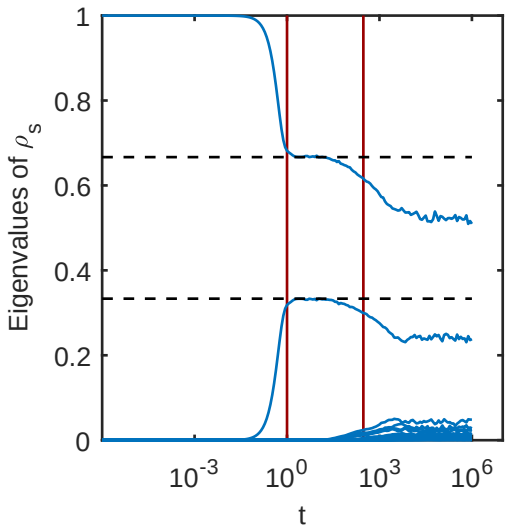

Figure 2.11: Similar to Fig. 2.10 but with the initial state and Hamiltonian parameters modified as discussed in the text. This example shows more strongly separated decoherence times and dissipation times. Note in particular that the two top eigenvalues spend an extended period of time at the probability values (dashed lines) assigned to the initial (superposed) wavepackets, indicating that the environment has made a "good measurement" of the SHO.

of the index i_e chosen from $\{1, 100, 200, 300, 400, 500, 600\}$ (ordered so the i_e runs from lowest to highest eigenvalues). Each case shows characteristics of equilibration. Each curve corresponds to a single realization of the random Hamiltonians used in H_e^I and H_e. We have found that the noteworthy features of the curves remain unchanged as different realizations are chosen, except for the cases at the ends of the spectrum where the density of the eigenstates of H_e is low and the noise from the randomness shows up more strongly. Also note that the timescale for the first significant evolution of the entropy up from zero is similar for all values of i_e except the extremal ones, which rise more slowly. This also chimes with what one might expect from the low density of states case.

The finite sizes of the systems makes standard definitions of temperature difficult to utilize. Still, in [30] we have found some generalized notions of equilibration and even thermalization apply, without reference to temperature. These ideas allow us to understand the behavior of the ACL model as "equilibration", as suggested strongly by

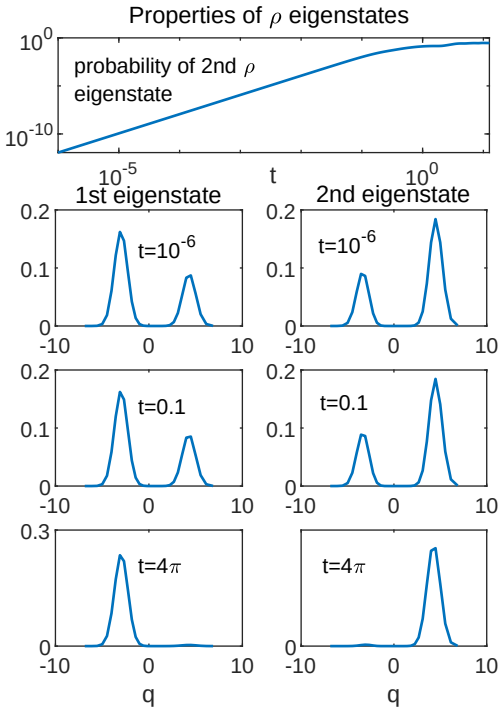

Figure 2.12: Copycats in the early stages of entanglement: The system is initially taken to be in a Schrödinger cat state (2nd row, left panel) which becomes entangled with the environment as it evolves. The 2nd eigenvalue and $|\psi(q)|^2$ for the first two eigenstates of ρ_s are shown from early stages of the evolution. The 2nd eigenstate generically takes the mirror image "copycat" form over several decades of evolution before finally einselecting to a coherent state form.

Figs. 2.13 and 2.14.

2.5 The reduced Caldeira-Leggett model

The ACL can be reduced by replacing the SHO with a single qubit, and turning off the self-Hamiltonians of both the system and the environment. The resulting "reduced Caldeira-Legget" (RCL) model has this Hamiltonian[7]:

$$H_{RCL} = \lambda S_z \otimes H_e^I \tag{2.13}$$

[7]The RCL is the same model discussed in [32] with $H_1^{\uparrow} = -H_1^{\downarrow}$ and $E_1 = 0$.

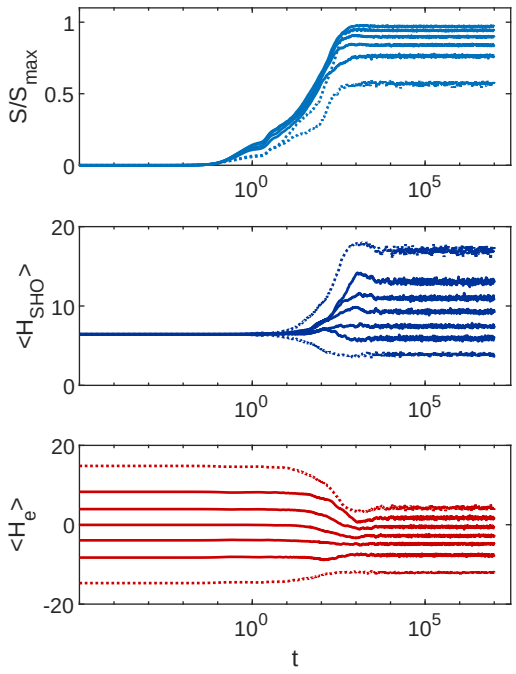

Figure 2.13: The evolution of entropy and subsystem energies over time, choosing the environment initial state from among the eigenstates of H_e. The dotted curves correspond to the very lowest and very highest eigenvalues, and the other curves run from lowest to highest index (from the set given in the text) corresponding to the low or high positions on plots. Each entropy curve stabilizes over time around its highest value, and the corresponding energy curves stabilize as well (implying no net energy flow after the initial transient). These are characteristics of equilibration.

where $S_z \equiv |\uparrow\rangle\langle\uparrow| - |\downarrow\rangle\langle\downarrow|$. We consider an initial Schrödinger cat state of the form

$$|\psi\rangle_s = a_1 |\uparrow\rangle + a_2 |\downarrow\rangle \tag{2.14}$$

and present results using $a_1 = 1/\sqrt{3}$ and $a_2 = \sqrt{2/3}$ (as with the SHO Schrödinger cat state discussed above).

Figure 2.15 shows the evolution of the eigenvalues of ρ_s. The simplified form of the RCL model means there is no self Hamiltonian for the system competing with the interaction term, and the pointer states are simply the spin states $\{|\uparrow\rangle, |\downarrow\rangle\}$ determined by the form of the interaction Hamiltonian. Thus the "good measurement" behavior (with the p_i's stabilizing at the values $|a_1|^2$ and $|a_2|^2$ given by the dotted lines) is realized more robustly

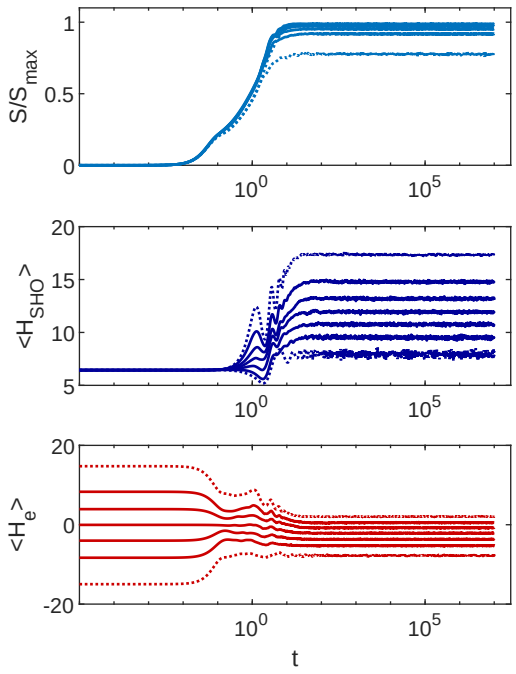

Figure 2.14: This figure is constructed the same way as Fig. 2.13 except here strong coupling ($E_I = 0.25$) is shown. The behavior is broadly similar in terms of equilibration (with the overall entropies tending to be larger, as mentioned with Fig. 2.6). In the strong coupling case the backreaction tends to significantly impact the effective potential in which the oscillator moves, and can even shift around the location of the minimum. The additional broad oscillations on the approach to equilibrium vs Fig. 2.13 appear to be related to this effect.

than in the case depicted in Fig. 2.11.

Figure 2.16 shows the (real parts of the) off-diagonal elements of ρ_s in the pointer state basis (a.k.a. $\langle S_x \rangle$). From this perspective, the approach of $\langle S_x \rangle$ toward zero reflects the process of einselection. The uneven fluctuations in the approach toward zero reflect inefficiency in the decoherence process. The RCL model has no self-Hamiltonian for e and thus the decoherence boosting effects depicted in Fig. 2.1 are not available (Figure 2.17 shows results comparable to Fig. 2.16 but with a self-Hamiltonian added, and one can see that the oscillations have essentially disappeared). In Sec. 2.6.3 we discuss how such curves relate to phenomena seen in NMR experiments, and connect these features with a

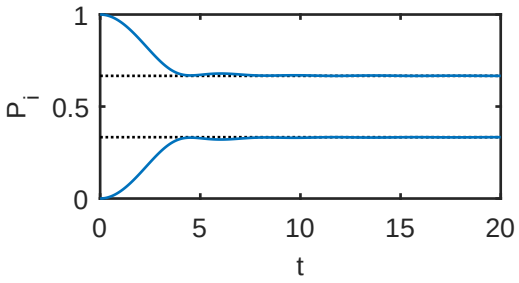

Figure 2.15: Eigenvalues of ρ_s (P_i) as a function of time for the RCL model. The simplified form of the RCL (vs the ACL) model allows the P_i's to settle at the values set by the initial Schrödinger cat state, producing a stable "quantum measurement."

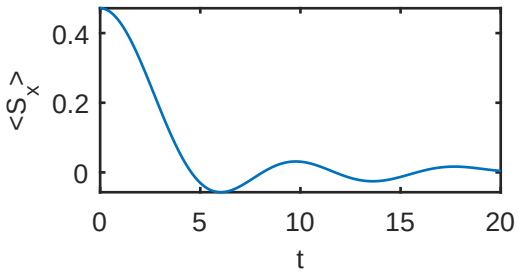

Figure 2.16: The quantity $\langle S_x \rangle$, giving the off diagonal elements of ρ_s in the spin basis for the RCL model. While the the spin basis is nominally the pointer basis, the inefficiencies of einselection in the RCL model allow significant deviations from zero at late times.

phenomenon known as "Loschmidt echos." And in [2] we explore more systematically the variety of behaviors possible for the full complex values of the off-diagonal elements of ρ_s.

2.6 Comparison with other work

2.6.1 Limits of einselection

As reviewed in [26], Zurek and collaborators have (in the context of CL models) considered various interesting limits which cause different pointer states to be selected by the decoherence processes. We have reproduced each of these limits in this paper.

The "quantum measurement limit" occurs when the interaction term dominates. In that limit the pointer states are eigenstates of the interaction Hamiltonian. The case we

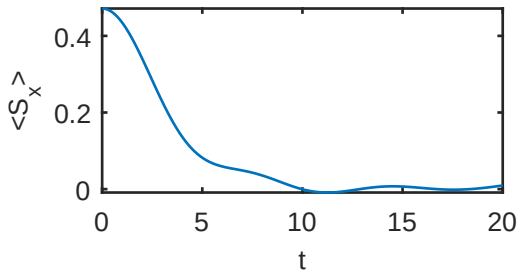

Figure 2.17: Off diagonal elements of ρ_s in the spin basis for the RCL model amended to include a self-Hamiltonian for the environment. As discussed in the text, this modification suppresses the late time oscillations observed in Fig. 2.16. (The added term in H_w has the form of the last term in Eqn. 2.1, with H_e defined by Eqn 2.6 with $E_e = 0.025$ and $E_e^0 = 0$.)

illustrate in Fig. 2.11 is approaching the quantum measurement limit. Another extreme is the "quantum limit," where the self-Hamiltonian of the system dominates. The pointer states in this case are the energy eigenstates of the system. We explore this limit for the ACL model in Appendix 2.A.

When the effects of the interaction term and self-Hamiltonian are similar (the "intermediary regime"), the pointer states tend to be the coherent states. Much of our discussion in Sect. 2.3 covers this regime[8].

2.6.2 Other treatments of the CL Model and the Markovian limit

Physicists studying decoherence and einselection often encounter the CL model in the context of master equations. These master equations describe the evolution of the system density matrix, without the need to specify the full dynamics of the surrounding environment [26]. However, to derive such master equations, approximations such as the "Born approximation" and "Markov approximation" are typically made. Both are reviewed in [26, 8], but we draw attention to the Markov approximation here.

In the Markov approximation, the environment is assumed to be 'memoryless.' This assumes any quantum correlations between parts of the environment that were created

[8]For the way we have parameterized H_e^I, the environment size N_e impacts the strength of the interaction term. When that effect is taken into account, the effective strengths of H_e^I and H_s are similar for the "weakly interacting" parameters chosen in the first parts of Sect. 2.3.

due to system-environment interactions are quickly 'forgotten.' 'Quickly forgotten' is often quantified by the statement $\tau_{corr} \ll \tau_s$—where τ_{corr} is the timescale for destroying such dynamically generated environmental self-correlations and τ_s is the timescale over which the system density matrix changes noticeably [26]. The Markov approximation is often appropriate for cases where the system and environment are weakly coupled, for example. However, there are many situations of physical interest where this inequality does not hold and the influence of environmental correlations on the system cannot be neglected [26, 8]. Nevertheless, the Markov approximation is standard in many master equation approaches to studying decoherence, including the CL master equation—though there are exceptions, e.g. [35].

Other assumptions that typically enter into deriving the CL master equation are a high temperature environment—such that the thermal energy of the environment is much larger than the energy scale set by the system's natural frequency—and an environment which is described by an 'ohmic' spectral density with a suitable UV cutoff scale.

One consequence of these assumptions, along with the Markov approximation, is that the CL master equation typically predicts exponential decay for the off-diagonal elements of the system density matrix—an exponential rate of decoherence. This exponential result is also found in other parts of the literature on decoherence, such as scattering induced decoherence [34, 26] and particular limits of spin-boson models [36, 26]. While even within master equation approaches it is known that exponential decay is not always valid [37, 8, 26], there remains strong focus in the literature on exponential decay.

In contrast to the CL master equation approach, our results from the ACL and RCL models show a more varied range of time dependence in the decay of off-diagonal system density matrix elements. Examining Figs. 2.16 and 2.17, for example, the decay is not exponential at all (except perhaps in a narrow time range). In our work we have not made any assumptions of Markovian evolution, we have simply solved the Schrödinger equation directly for system and environment in its fully unitary form as discussed in Sec. 2.2. Therefore, deviations from Markovian behavior and exponential decay should be unsurprising. As Zurek and collaborators [10, 38, 39] explicitly note in the context of the

formalisms they develop—which have some parallels to our work—exponential behavior is a very special case.

Furthermore, our main motivation for developing the ACL model is to study equilibrium systems. The detailed balance exhibited by such systems would imply that the "forgetting" of correlations and "(re-)emergence" of correlations should contribute equally to the physics. Markovian treatments are by construction unable to include such features.

2.6.3 Loschmidt echos and NMR

In [38, 39] Cucchietti, Paz, and Zurek (CPZ) consider a model very similar to our RCL model. They observe oscillations similar to those that appear at later times in our Figs. 2.16 and 2.17. CPZ point out that these oscillations can be thought of as "Loschmidt echos," and also notes that such features appear in NMR experiments (e.g. [40]). The notion of Loschmidt echo originates in discussions of fluctuations in the arrow of time (the direction of entropy increase) in equilibrium systems [41]. The Loschmidt echo refers to the possibility of *partial* time reversal occurring. CPZ note that in expressions like our Eqn. 2.13, H_e^I multiplies $|\uparrow\rangle\langle\uparrow|$ and $|\downarrow\rangle\langle\downarrow|$ with an opposite sign, something that can be thought of as effectively generating two evolutions in the e subspace, each the time reverse of the other. In this way they make the connection with Loschmidt echos.

In this paper we have interpreted the oscillations as inefficiencies (or more specifically, non-monotonicity) in the establishment of entanglement between system and environment. These inefficiencies reflect the finite environment size and various properties of H_w, as discussed in Sect. 2.5. This narrative also seems to work well for the NMR results, where it appears that in the cases where the oscillations occur the environment is effectively finite (comprised predominantly of nearby spins). While the different narratives ("inefficient decoherence" and "partial time reversal") may superficially sound quite different, in this case they are describing the same phenomenon.

2.7 Conclusions

We have presented a modified version of the classic Caldeira-Leggett (CL) model which can be studied using full unitary evolution in the combined system-environment space.

This adapted Caldeira-Leggett (ACL) model enables explorations beyond the various approximation schemes which are usually used with the CL model. Examples of such new explorations are presented in companion papers devoted to studying whether the notion of einselection makes sense under conditions which do not exhibit an arrow of time [3], and examining the very earliest stages of the einselection process [2]. This paper provides background information, including details of how the ACL model is constructed and of our highly accurate numerical techniques.

We have also reproduced a number of well-known results from the literature on decoherence and einselection. These build our confidence that the ACL model is well suited for our intended studies, and also help us know its limitations. Our full numerical treatment enables detailed scrutiny of all aspects of the process of einselection, and our extensive graphical representations of that phenomenon may provide a useful resource for those wishing to learn more about einselection.

In addition, Sec. 2.3.5 briefly introduces new results which anticipate the work presented in [2]. Also, experts versed in the notion of the "quantum limit" of the einselection process might enjoy our exploration of that limit in Appendix 2.A. While such experts would not find those results altogether surprising, we appreciate the way the ACL model allows us to explore interesting intermediate behaviors on the way to the full quantum limit.

We conclude that the ACL model provides a reliable tool with which to explore decoherence and einselection under conditions which cannot be treated using the standard approximation schemes.

2.8 Acknowledgments

We thank Wojciech Zurek for numerous inspiring conversations (over many years in the case of one of us, AA) which created the foundation for this work. We also thank Fabio Anza, Nick Curro and Zhipang Wang for discussions of NMR phenomena. This work was supported in part by the U.S. Department of Energy, Office of Science, Office of High Energy Physics QuantISED program under Contract No. KA2401032.

2.A The Quantum Limit

In [42] Paz and Zurek consider the case where H_s dominates over the other terms in H_w. They call this case the "quantum limit." We consider the quantum limit in the context of the ACL model here. While our results are broadly consistent with the existing literature, we also noticed several interesting behaviors which have so far not been reported.

The pointer states in the quantum limit have been shown to be the eigenstates of H_s [42]. To explore this limit with the ACL model we use the "predictability sieve" ideas [43, 44, 25, 45, 46, 47, 48, 26], which are grounded in the notion that the pointer states should be the states which are most stable against entanglement with the environment[9]. Here we consider the case where $E_I = 3 \times 10^{-3}$ and $E_e = 0.015$, well below the values considered elsewhere in this paper, while keeping H_s the same. We considered initial states of product form (Eqn. 2.8) where $|\psi\rangle_s$ is either an eigenstate of H_s, the Schrödinger cat (SC) state shown in Fig. 2.5, or a single ($\alpha = 3$) coherent state (CS), and compare the evolution in these cases.

Figures 2.18 and 2.19 show the evolution of the von Neumann entropy for these choices of initial state. Identifying robustness against entanglement with small values of the entropy at late times, once can conclude that the cat state is least robust, the lower n energy eigenstates are most robust, and the coherent state comes in about the same as $n = 11$. (We found the larger n values reach larger late-time entropies but, as discussed in Appendix 2.B, we also expect significant finite size effects to come in for the higher eigenstates of H_s.) Interestingly, the cat and the CS states exhibit much lower entropies for several decades of earlier time evolution which suggests a different (and transient) hierarchy of robustness. Furthermore, if one uses the timescale for the early time onset of entanglement as the measure of robustness, the coherent state is significantly more robust than the other cases considered. The original work on the quantum limit [42] only showed the stability of eigenstates of H_s at late times, and did not actually compare the rate of onset of entanglement. It appears that during the early and intermediate periods

[9]While we're not doing a thorough sifting of the entire Hilbert space in our analysis here, we find utilizing "predictability sieve" arguments to make comparisons between specific states sufficient for our purposes.

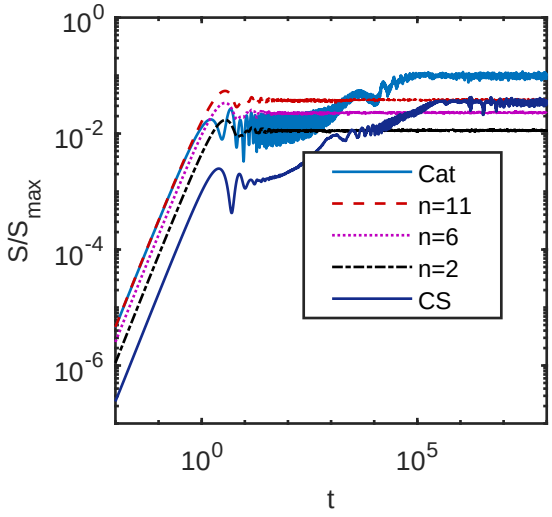

Figure 2.18: von Neumann Entropy evolution in a case where H_s dominates. The initial state is a product state with $|\psi\rangle_s$ given by a cat state (solid, upper), energy eigenstates with index 11 (dashed), 6 (dotted), 2 (dot dashed) or a single coherent state (CS, solid, lower). In the idealized "quantum limit" where H_s fully dominates, the energy eigenstates are the pointer states which are expected to be the "most robust" against the onset of entanglement. In this example we see that there is an early and intermediate period where the coherent state is favored, and it is only later that the full einselection of the energy eigenstates sets in.

the coherent states exhibit the strongest resistance to entanglement (reflecting the sort of behavior demonstrated in Sect. 2.3.5), and only later does the long time behavior set in ultimately favoring the energy eigenstates.

Figure 2.20 shows the evolving properties of the top two eigenstates of ρ_s (aka "Schmidt states"). For the coherent initial state (CS), these Schmidt states exhibit the properties of coherent states (steadily oscillating $\langle q \rangle$ and constant q_{rms}) for an extended period before degrading into more noisy, unstable behavior. This fits with the narrative we surmised from the entropy curves. For the energy eigenstate initial state the top Schmidt is perfectly stable, maintaining the energy eigenstate features, as expected for a pointer state. The second Schmidts (panels 2 and 4) emerge due to the process of decoherence (they are ill defined at $t = 0$, where ρ_s has only one nonzero eigenvalue) and reflect

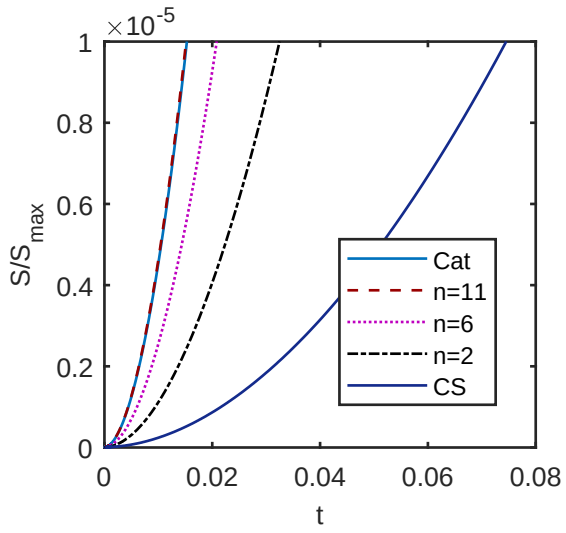

Figure 2.19: Zooming in on Fig. 2.18 and showing linear axes. The different initial rates of the onset of entanglement are clearly exhibited here. In this initial period the coherent state (CS) is the most robust against entanglement.

interesting properties of the decoherence process (also discussed in Sect. 2.3.5). For the energy eigenstate initial state, the 2nd Schmidt (4th panel) first reflects some oscillating behavior before becoming highly stable as well. The curves for CS initial state case exhibit a transient period of stable behavior around $t = 10^6$ but the stability does not extend to other moments of the Schmidts. Those Schmidts are not actual eigenstates of H_s.

Figure 2.21 shows the full wavefunctions of the Schmidt states for the case where the initial state is an energy eigenstate (the top two of these have moments shown in Fig. 2.20). These "snapshots" are taken for $t >= 10^4$, where the corresponding curves in in Fig. 2.20 are very stable. One can see that these Schmidts are highly stable in this time period and are very close to true eigenstates of H_s[10].

Finally, in Fig 2.22 we show the evolution several of the top eigenvalues of ρ_s. Not surprising for a case with very weak interactions, the top eigenvalue does not deviate too far from unity. We also note the interesting "crossover" behavior, where alternate

[10]It is interesting that despite their high degree of stability, the 2nd and 3rd Schmidts do not match perfectly to eigenstates of H_s. We conjecture that this is due to a small "effective potential" for the SHO due to the interactions with the environment.

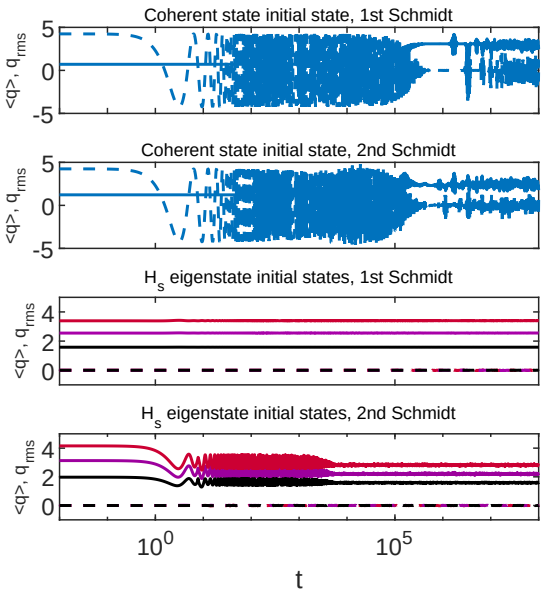

Figure 2.20: Evolution of $\langle q \rangle$ (dashed) and q_{rms} (solid) for the first and 2nd most probable eigenstates of ρ_s starting with different initial states. The coherent state initial state in the top panel initially exhibits the usual oscillatory behavior, but then degrades into noise. The energy eigenstate initial state in the third panel is highly stable as expected in the quantum limit. The 2nd Schmidt states (second and fourth panels) are ill defined at $t = 0$, but they emerge due to the interactions with the environment. Each roughly reflects the behaviors of their corresponding 1st Schmidt, although the energy eigenstate initial state case takes a while to get there. The energy eigenstate initial states, in order descending from the top curve are $n = 11$, $n = 6$, and $n = 2$.

eigenvalues rise faster and experience an initial noisy period in equilibrium before settling down. We speculate that this behavior is related to the eventual emergence of the other eigenstates of H_s as eigenstates of ρ_s and suspect that the two types of behavior are related to the parity of the energy eigenstates that emerge.

All the results reported in this Appendix appear to be consistent with statements in the literature about the quantum limit case, although we've not done a sufficiently thorough investigation to explicitly demonstrate that eigenstates of H_s are the *most robust* against interactions with the environment out of all possible choices. The behavior of the other eigenstates of ρ_s noted here is intriguing. While it appears broadly consistent with established ideas about the quantum limit, we've not found any report of these particular

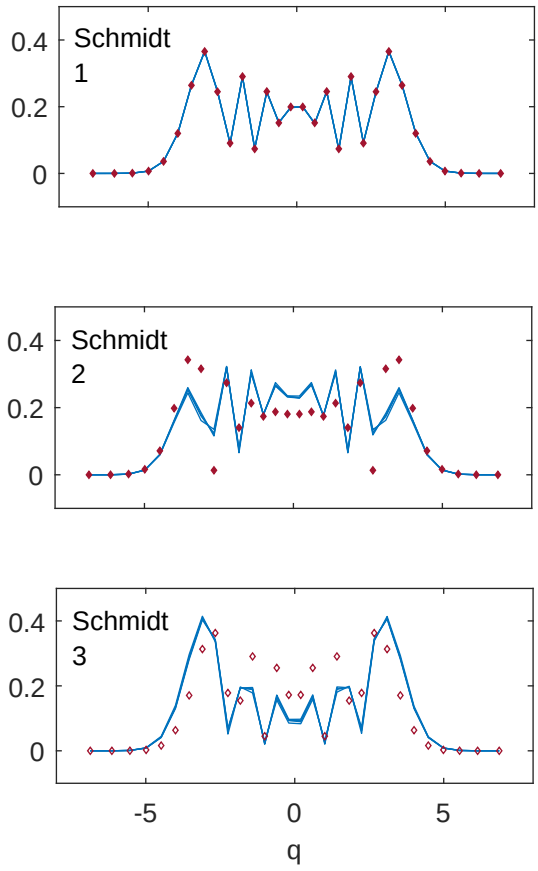

Figure 2.21: Energy eigenstates as pointer states: Snapshots of the $|\psi(q)|$ for the three most probable eigenstates of ρ_s (solid curves). Each panel shows the state at $t = 10^4$, $t = 10^5$, $t = 10^6$ and $t = 10^7$. These correspond to the period of time where all the curves in the 4th panel of Fig. 2.20 are very stable. The wavefunctions at these different times are mostly indistinguishable to the eye, indicating that the stability goes well beyond the two moments plotted in Fig. 2.20. Also plotted on each panel are (top to bottom) the $n = 6$, $n = 7$ and $n = 5$ eigenstates of H_s (markers). As discussed in the text, the behaviors depicted here strongly reflect the fact, developed in earlier literature, that the energy eigenstates of H_s are the pointer states in the quantum limit. We are especially intrigued by the 2nd and 3rd panels which illustrate that Schmidt states similar to these pointer states are distilled out of the messy physics of decoherence by the einselection process. (The eigenvalues are 0.98, 0.015 and 0.004.)

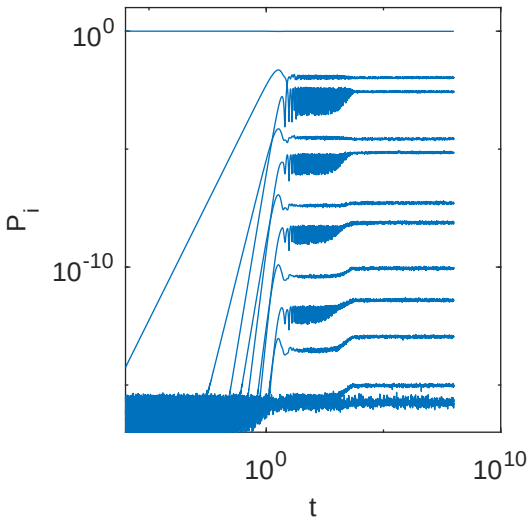

Figure 2.22: The evolution of the top 12 eigenvalues of ρ_2 for the case where the system starts in its $n = 6$ energy eigenstate. The interesting crossing behavior and alternating "noise bulges" are discussed in the text.

effects in the literature.

2.B Eigenstates of H_s

Our form of H_s does a nice job of describing the evolution we associate with the continuum SHO using a finite Hilbert space, as discussed in the body of this paper. Here we provide some further information, focusing especially on the eigenstates of H_s.

Figure 2.23 and 2.24 depict selected eigenstates of H_s shown along with their continuum counterparts, given in the q basis. In these figures the states of the truncated SHO are shown only as markers (with no connecting lines) to emphasize the fact that these states exists in a finite space. (In these figures the normalization is adjusted for easy cross-comparison.) One can see that the lower energy eigenstates (Fig. 2.23) follow the behavior of the continuum states quite nicely. As one approaches higher energies (Fig. 2.24) the eigenstates reach the edge of the finite q range and start showing nonzero values at the q edges. This leads to behaviors at high energies that deviate significantly from the details of the continuum case, although some broad features remain. Because of this behavior, we

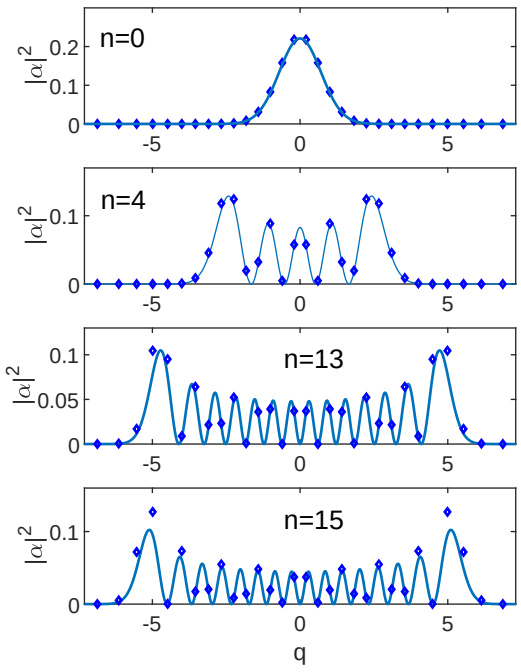

Figure 2.23: Energy eigenstates of the truncated SHO (markers) along with the corresponding continuum SHO eigenstates (curves). The two track one another nicely, although the tracking comes under a bit of strain for the $n = 15$ state where the continuum state starts pressing up against the finite bounds on q which exist in the truncated case.

have avoided studying cases that put the SHO in higher energy excitations in this paper as well as in other work using the ACL model, since our intention is to represent a realistic SHO as well as possible. We found for example that coherent states with considerably higher amplitudes than those shown here executed interesting combinations of reflection and periodic transmission at the q boundaries, hardly surprising given the forms of the higher energy eigenstates.

We also note an exotic feature that appears as an artifact of our finite construction. Figure 2.25 shows the same ground state wavefunction shown in the top panel of Fig. 2.23, but here we show $\psi(q)$ both with and without the norm. The un-normed values show a jaggedly varying sign. In continuum terms such jaggedness would result in an energy much higher than the ground state energy, but our H_s has correspondingly complicated

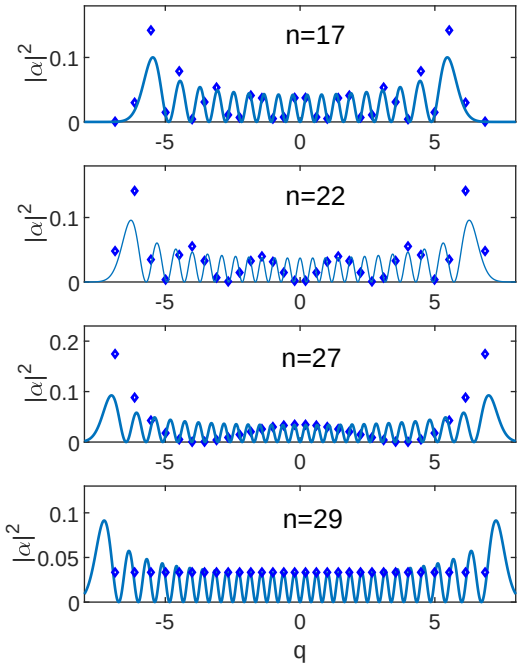

Figure 2.24: Energy eigenstates of the truncated SHO (markers) along with the corresponding continuum SHO eigenstates (curves) shown for larger n values. The tracking behavior noted in Fig. 2.23 is present here as well, although the edge effects are more pronounced. For these n values, taken alone the markers appear to trace very different curves, but this is only because the discrete grid on which they lie beats in an interesting way off of the frequencies exhibited by the continuum states.

off diagonal elements coupling certain neighboring points which make the $\psi(q)$ shown truly the lowest energy state. We've also checked that these considerations do not disrupt our use of continuum intuition with other eigenstates of H_s, at least for $n \lesssim N_s/2$. The robust behavior of the isolated oscillator reported in Figs. 2.3 and 2.5 also supports our confidence that our truncated SHO is overall a good approximation to the continuum case.

2.C Energy spectra

Here we take a look at the eigenvalue spectrum of H_w, and see how it relates to the spectra of H_s and H_e. Figure 2.26 shows histograms of the eigenvalues of each of these

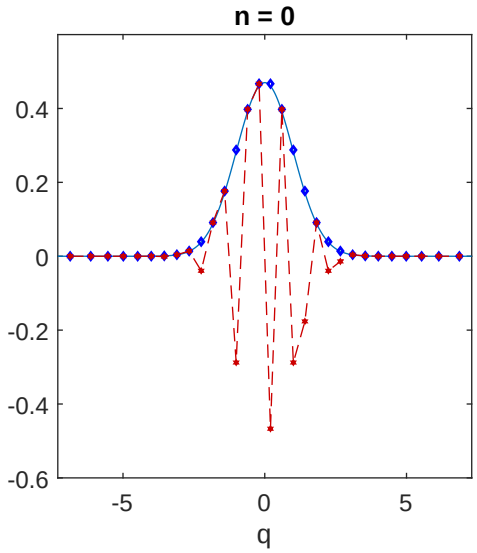

Figure 2.25: The ground state of H_s. Blue: $|\psi(q)|$, Red: $Re(\psi(q))$. The state is defined in an N_s dimensional Hilbert space, and the discrete nature of that space is expressed by the markers on the plot. The markers are connected by lines in order to reference the continuum SHO case. In the case of $|\psi(q)|$ this correspondence appears to be simple, but $Re(\psi(q))$ has jagged features not found in the continuum SHO ground state. We discuss the nature of these features in the text and note that while appearing to be exotic, they do not interfere with an intuitive understanding of our truncated SHO, which overall exhibits behaviors very similar to the continuum case.

H's using $E_I^e = 0.01$, $E_e = 0.05$, $E_I^0 = E_I^e$ and $E_e^0 = E^e$. (These are different from the values used in this paper but match those used in [3], where the spectrum of H_w will be relevant for a discussion of our "eigenstate einselection hypothesis.") The spectrum of a true SHO is flat, and so is the spectrum for our SHO shown in the top panel of Fig. 2.26, although this spectrum is truncated at $E = 29$ reflecting the finite Hilbert space inhabited by our truncated SHO. The spectrum of H_e (middle panel) reflects the well-known "Wigner semicircle" property of random matrices. The eigenvalues of H_w are essentially sums of eigenvalues of H_s and H_e (with a small additional contribution from the interaction term). So it is not surprising that the full spectrum of H_w (lower panel) appears to be a combination of the spectra shown in the upper and middle panels. For these parameters the energy of the SHO dominates, and the spectrum of H_w roughly

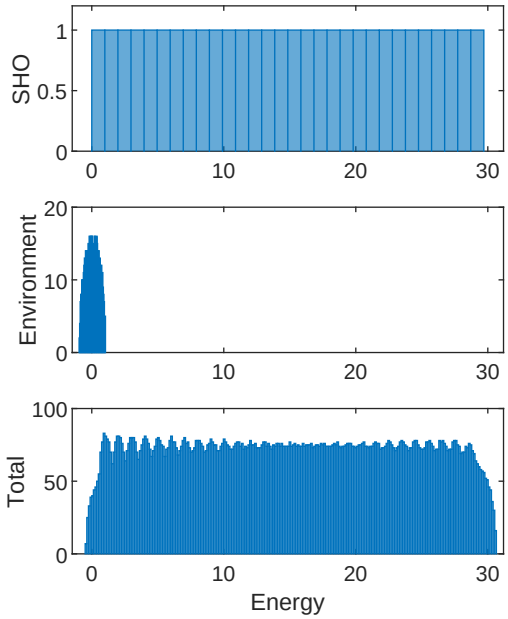

Figure 2.26: The eigenvalues spectra of H_w (lower panel) and its two main components, the SHO (upper) and H_e (middle). We discuss in the text how these spectra relate to one another and reflect the way the different H's are defined.

takes the form of the SHO spectrum (modulated by little semicircles). For cases where H_e dominates the spectrum of H_w looks more like a single semicircle, with "wings" giving a broadening induced by the SHO spectrum.

2.D Numerical techniques and tolerances

The total Hamiltonian (H_w) was constructed as described in the text and then diagonalized numerically. The initial states were constructed in the appropriate subsystem bases and then expanded in the basis of eigenstates of H_w. Time evolution was performed by rotating the phases of the coefficients of the eigenstates of H_w according to the Schrödinger equation. Density matrices for subsystems s and e at a given time were generated by rotating into an $s \times e$ product basis and tracing over e and s respectively. These density matrices were then used to extract information about the two subsystems. (Note, the state of w expressed in the eigenbasis of H_w was always saved so there was never a need to "rotate back" and thus no associated noise introduced in the evolution.) Algorithm 1

shows a schematic of the procedure to generate $\rho_s(t)$ and $\rho_e(t)$ in the ACL model.

Regarding numerical accuracy, the critical aspect was the ability of our code to accurately evaluate exponentials with potentially large imaginary arguments (to rotate the phases). The residuals shown in Figs. 2.3 and 2.5 give some sense of the capabilities of our code. Note that while those figures refer to the case where $E_I = 0$ and focus on the behavior of the SHO, the results were generated with $E^e = 0.03$ and $N_e = 600$ (and thus $N_w = 18,000$) so the residuals reflect a stronger test than one might initially expect. Figure 2.27 shows several quantities discussed in this paper evolved to later times than previously shown. One can see evidence of the breakdown of numerical accuracy around $t = 10^{14}$, when the exponential expressions for the (extremely large) phases start failing to compute properly. For example energy conservation (the constancy of the solid curve in the lower panel) is lost, and the requirement that $S \leq S_{max} = \ln(N_s)$ (Eqn. 2.12) is violated. These, and many other tests of the numerics proved robust up to times just below the $t \approx 10^{14}$ breakdown point. The availability of accurate numerical computations over such a wide time range provides excellent latitude for exploring the physics of the ACL model. (For context, recall that the period of the oscillator is $\tau = 2\pi$.)[11]

Our calculations were performed using Matlab on a 64 bit Windows computer with a 3.6GHz Intel i7-4790 processor and 32GB RAM. Each time step, which included calculating a wide variety of information from ρ_s and ρ_e (including the sort reported here), took 20-30 seconds. (We noticed a roughly 25% speedup after simultaneously upgrading from Windows 8.1 to 10 and from Matlab R17a to R18b.) The initial construction of all relevant matrices (of which the diagonalization of H_w is the most time consuming) takes around 1.5 hours for the case with $N_s = 30$ and $N_e = 600$. We rarely wanted more than 2000 time steps to produce long times views such as shown in Figs. 2.13 and 2.14, and for many purposes (such as Fig. 2.9 and various rough explorations) a lot fewer were sufficient. Much of our code development and testing could be done with smaller environment sizes, for which the time steps were more or less instantaneous. With these sorts of turnaround times we found it possible to work with the ACL model in a reasonably

[11]For the senior member of this collaboration whose last experience with this kind of calculation was in the 1990's [32] the comparison of capabilities between then and now is truly remarkable.

Algorithm 1 Steps to generate $\rho_s(t)$ and $\rho_e(t)$ in the ACL model

Inputs: Choices for E_I and E_e (overall energy scales of the interaction and environmental Hamiltonian), $|\psi(t=0)\rangle_s$, $|\psi(t=0)\rangle_e$, N_s and N_e (system and environment dimensions, set to $N_s = 30$ and $N_e = 600$ in the text).

Outputs: $\rho_s(t_f)$, $\rho_e(t_f)$.

Runtime: $O(2)$ hrs for all steps, given $N_s = 30$, $N_e = 600$, and the computing setup discussed in this appendix.

Procedure:

1. Construct H_w

$$H_w = H_s \otimes \mathbf{1}^e + q_s \otimes H_e^I + \mathbf{1}^s \otimes H_e$$
$$H_s = \hat{\mathbf{a}}^\dagger \hat{\mathbf{a}} + \frac{1}{2}$$
$$\langle n-1| \hat{\mathbf{a}} |n\rangle = \sqrt{n}, \quad n \in \{1, N_s\}, \quad \hat{\mathbf{a}}^\dagger = (\hat{\mathbf{a}})^\dagger$$
$$q_s = \hat{\mathbf{q}} = \frac{1}{\sqrt{2}}\left(\hat{\mathbf{a}} + \hat{\mathbf{a}}^\dagger\right)$$
$$H_e^I = E_I R_I^e, \quad H_e = E_e R^e$$

   where R_I^e and R^e are separately constructed random $N_e \times N_e$ Hermitian matrices (see Sect. 2.2.2)

2. Diagonalize H_w

   Find eigenstates and eigenvalues of H_w

3. Construct $|\psi(t=0)\rangle_w = |\psi(t=0)\rangle_s \otimes |\psi(t=0)\rangle_e$

4. Expand $|\psi(t=0)\rangle_w$ in eigenstates of H_w

$$|\psi(t=0)\rangle_w = \beta_i |E_i\rangle_w$$

5. Evolve $|\psi\rangle_w$ to desired t_f

$$\beta_i(t_f) = e^{-iE_i t_f} \beta_i(t=0)$$

6. Calculate $\rho_s(t_f)$, $\rho_e(t_f)$

$$\rho_s(t_f) \equiv Tr_e\left(|\psi(t_f)\rangle_{ww} \langle\psi(t_f)|\right)$$
$$\rho_e(t_f) \equiv Tr_s\left(|\psi(t_f)\rangle_{ww} \langle\psi(t_f)|\right)$$

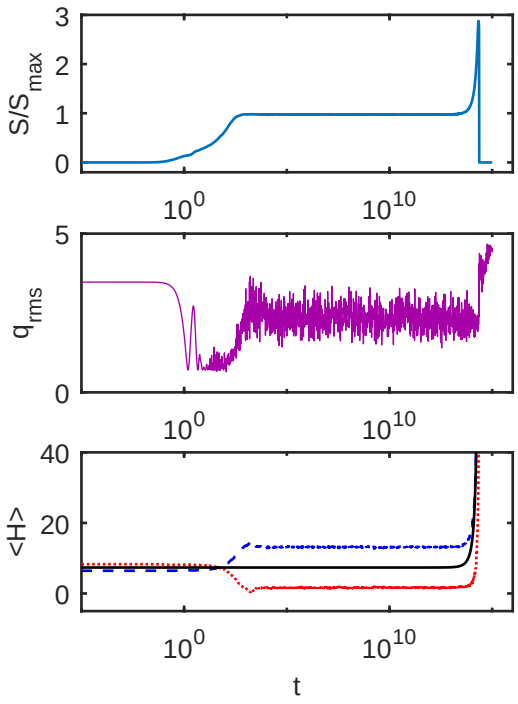

Figure 2.27: Various quantities are shown evolved over a huge time range to illustrate the point where our numerical computations fail. Top panel: Entropy. Middle panel: q_{rms} of the most probable eigenstate of ρ_s (discussed in Fig. 2.9). Bottom Panel: $< H^s_{SHO} >$ (dashed), $< H_e >$ (dotted) and $< H_w > \equiv < H_s > + < H_e > + < H^I >$ (solid). All the quantities show the expected physical behavior until $t \approx 10^{14}$ where the breakdown of the numerical computation of the phases sets in. This figure illustrates the very large dynamic range of our numerical computations. (Recall that the SHO period is 2π.)

interactive manner.

Chapter 3

Copycat Process in the Early Stages of Einselection

The material in this chapter previously appeared in ***Copycat process in the early stages of einselection*** *by Rose Baunach, Andreas Albrecht, and Andrew Arrasmith [2].*

ABSTRACT: We identify and describe unique early time behavior of a quantum system initially in a superposition, interacting with its environment. This behavior—the copycat process—occurs after the system begins to decohere, but before complete einselection. To illustrate this behavior analytic solutions for the system density matrix, its eigenvalues, and eigenstates a short time after system-environment interactions begin are provided. Features of the solutions and their connection to observables are discussed, including predictions for the continued evolution of the eigenstates towards einselection, time dependence of spin expectation values, and an estimate of the system's decoherence time. In particular we explore which aspects of the early stages of decoherence exhibit quadratic evolution to leading order, and which aspects exhibit more rapid linear behavior. Many features of our early time perturbative solutions are agnostic of the spectrum of the environment. We also extend our work beyond short time perturbation theory to compare with numerical work from a companion paper.

3.1 Introduction

There are many reasons why one would want to study the effects of decoherence and einselection on a quantum system interacting with its environment—from interest in theoretical interpretations of quantum mechanics to applications in quantum computing [49, 11, 34, 9, 36, 38, 8, 7]. In [1] we introduced the "adapted Caldeira Leggett" (ACL) model, a tool designed to explore these phenomena using fully unitary calculations in the combined system-environment space. This tool enables us to examine behaviors outside of the standard approximation schemes common in the field.

Our original aim was a study of the relationship between einselection and the arrow of time. We present the outcome of that work in [3]. On the path of exploring decoherence and einselection with the ACL model numerically, we witnessed a curious phenomenon—the copycat process—which we investigate in this paper. Figure 3.1 (Fig. 12 in [1]) gives a general picture of this process.

The ACL model describes a simple harmonic oscillator (SHO) coupled to an environment. For Fig. 3.1 the SHO was set up in a "Schrödinger cat" superposition of coherent state classical wavepackets. Over time, decoherence with the environment brings the SHO into a classical mixture of wavepackets described by a density matrix (ρ) with the wavepackets as eigenstates. In this manner the classical wavepackets are specially selected by the specifics of the decoherence physics, a process called "einselection."

The evolution shown in Fig. 3.1 starts with the system and environment in a product state. At that moment the SHO density matrix, ρ, has only one nonzero eigenvalue. An instant later a second nonzero (but infinitesimal) eigenvalue emerges. As soon as this second eigenvalue becomes resolved in our calculations, the corresponding eigenstate takes on the intriguing "mirror image" (copycat) form shown in Fig. 3.1. The first and second eigenstates keep these forms as the second eigenvalue evolves over many decades in magnitude. Eventually on a timescale given by the decoherence time, einselection takes place. [1] [2]

[1] The SHO has a period of 2π. Thus, choosing $t = 4\pi$ for the final time shown in Fig. 3.1 simplifies our presentation. More details about the behavior of the ACL model can be found in [1].

[2] In Fig. 3.1, q labels the discrete set of eigenvalues of the (dimensionless) position operator of the ACL

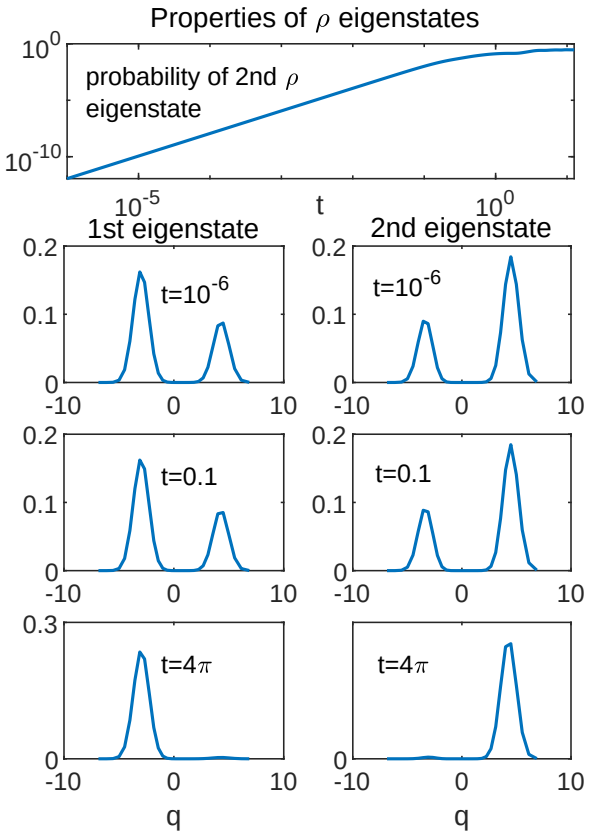

Figure 3.1: Copycats in the early stages of entanglement: A system that is initially in a pure superposition of two coherent states becomes entangled with the environment as it evolves. We plot the second eigenvalue and eigenstates of the system density matrix ρ for early times. The 2nd eigenstate takes the mirror image "copycat" form over several decades of evolution. The bottom row shows these two states after einselection is complete, and the initial superposition has become a mixture of classical wave packets. The eigenstate plots show $|\psi(q)|^2$ for the first two eigenstates, where q is a generalized position. Time is shown in units where the oscillator period is 2π. (The absence of phase information means the orthogonality of the eigenstates does not appear manifest in these plots.)

While initially the copycat phenomenon seemed striking and unusual to us, and we were a bit concerned about the possible role of numerical artifacts in our results, we have come to understand this process in relatively simple physical terms. The "transient stability" we observe relates to the slow quadratic start to the early time evolution of the eigenstates. Furthermore, the mirror image copycat form seems quite natural if one thinks

model [1], and $\psi(q)$ used here corresponds to $\psi_\alpha(q)$ (from Eqn. 4 in [1]), the discrete set of coefficients from expanding the state in eigenstates of position. In the panels giving eigenstates the discrete set of points $|\psi(q)|^2$ are connected to guide the eye, but there is no actual continuum and $|\psi(q)|^2$ is dimensionless.

of the two wavepackets as spanning a two dimensional reduced Hilbert space (effectively a single qubit). From that point of view, the form shown is the only option for the 2nd eigenstate of ρ until the first eigenstate has time to evolve appreciably. In fact, the copycat picture we describe here is implicit in standard results from Nuclear Magnetic Resonance (NMR) physics, although they have not been previously presented from that point of view.

This work originally came about through our need to fully understand the behaviors of the ACL model before applying it to the new problems explored in [3]. Having satisfied ourselves that the copycat process was indeed physical, and having extended it in a number of directions, we've decided those explorations are worth reporting in this paper. We feel they may be of interest to those studying the early stages of decoherence, perhaps in the context of quantum technologies. In particular we offer explorations of the extent to which the early stages of decoherence are quadratic to leading order, and which aspects evolve with a more rapid linear behavior.

The rest of this paper is devoted to describing and analytically deriving the copycat process. In Sect. 3.2 we briefly review the ACL and reduced Caldeira-Leggett (RCL) models as presented in [1]. Then in Sect. 3.3 we present perturbative analysis of the copycat process by calculating the system density matrix, associated eigenvalues, and eigenstates of a two-state system entangled with its environment a short time after system-environment interactions begin. In our derivations we chose to model the superposition of coherent states in Eqn. 3.3 as a two state system, both for simplicity and because such coherent superpositions were observed to behave as essentially a two-state system in our numerical work [1]. Section 3.4 is a discussion of some specific features and applications of our derived solutions for the two state system, including predictions for the continued evolution of the system eigenstates, early time behavior of spin observables, and an estimate of the system's decoherence time. In Sect. 3.5 we extend our solutions beyond short time perturbation theory to compare with our numerical work in [1]. We also comment on the duration of the perturbative copycat regime in Sect. 3.5.2 and graphically demonstrate that the perturbative solutions can model the full numerical evolution for a sizable span

of time. Our further discussion and conclusions are provided in Sect. 3.6, which include discussion of how the copycat process generalizes for initial states with larger numbers of 'cats' and comparisons of our work with existing literature.

Appendix 3.A extends our technical results from a qubit model to the qutrit case, providing additional perspective on the possibility of linear behaviors (which we summarize is Sect. 3.6). These investigations offer further nuance to the technical aspects of the copycat process discussed in the main text, as we discover the possibility of linear time evolution in the orthogonal eigenstates for some cases, even though the evolution of the eigenvalues and initial state remains quadratic, as in the qubit case. We also illustrate how results from our qutrit analysis are reflected in the behaviors of more complicated ACL-like models with three wavepacket Schrödinger cat initial states.

3.2 Formalism

3.2.1 Basics

We consider a "world" Hilbert space, comprised of a system and an environment: $w = s \otimes e$. We take $|\psi_w\rangle$ initially to be a product state and study the entanglement caused by system-environment interactions:

$$|\psi_w\rangle = |\psi_s\rangle\,|\psi_e\rangle \quad \overrightarrow{entanglement} \quad \sum_{i,j} b_{ij}\,|i\rangle_s\,|j\rangle_e\,. \tag{3.1}$$

The onset of system-environment entanglement is called decoherence. Once entanglement has taken place, the system is described by the density matrix

$$\rho_s = Tr_e(|\psi_w\rangle\,\langle\psi_w|). \tag{3.2}$$

Einselection is the special case of decoherence where environmental interactions induce the system density matrix to become diagonal in a preferred basis. These preferred basis states are called pointer states in the literature [10, 11].

Under certain conditions (which apply in Fig. 3.1) coherent states will be einselected as the pointer states [50, 49, 1]. Under those conditions, a system that starts in a superposition of coherent states

$$|\psi_s\rangle = a_1\,|\alpha_1\rangle + a_2\,|\alpha_2\rangle \tag{3.3}$$

would evolve into the density matrix

$$\rho_s = |a_1|^2 |\alpha_1\rangle \langle\alpha_1| + |a_2|^2 |\alpha_2\rangle \langle\alpha_2| . \tag{3.4}$$

Here we have labeled coherent states with the parameter α, a standard convention articulated in detail for the ACL model in [1]. Indeed Eqn. 3.4 roughly describes what we see in Fig. 3.1. (Inspection of the full analysis presented in [1] reveals that in this particular case, the finite form of the ACL model leads to a number of small deviations from the idealized picture described by Eqn. 3.4.) It is in the early stages of the evolution toward the Eqn. 3.4 form that we notice the copycat behavior.

As illustrated in Fig. 3.1, at early times there is an eigenstate of the system density matrix that resembles the initial state and one that has the "copycat" form. The initial evolution of these eigenstates are quadratic in time—as we will prove subsequently—or "slow," hence the appearance of "transient stability." We call the appearance of a copycat state and its subsequent behavior the "copycat process". To the best of our knowledge the copycat process and its implications have not been directly explored in the literature, although we will discuss how earlier work has come very close to this topic in an indirect way.

3.2.2 The ACL Model

As discussed in [1], the original Caldeira Leggett (CL) model is a toy model describing a system interacting with its environment with a Hamiltonian of the form [12, 49, 8]:

$$H_w = H^s_{SHO} \otimes 1^e + q_{SHO} \otimes H^e_I + H^e \otimes 1^s. \tag{3.5}$$

In the CL model the system is a simple harmonic oscillator (SHO) moving in the standard SHO potential, and the environment is an infinite set of SHOs. The system and environment together describe a closed system undergoing unitary evolution, but generally the system and environment individually do not have to evolve unitarily.

The adapted Caldeira Leggett (ACL) model was introduced as an adaptation of the CL model which operates in a finite dimensional Hilbert space—so its evolution can be investigated numerically in its full unitary form [1]. In the ACL model, the Hamiltonian

is also given by Eqn. 3.5, but the components are modified since the Hilbert space is finite—for example, the system is given by a truncated SHO. Full technical details are given in [1].

3.3 Modelling the Copycat Process

3.3.1 Setting up and the RCL model

We start our technical explorations of the copycat process with the following observation: The ACL model used to produce Fig. 3.1 had parameters adjusted to make the coherent states especially stable, making them the pointer states. We also note that while the coherent state wavefunctions are nowhere truly zero, the overlap between the two coherent states shown in Fig. 3.1 is exponentially suppressed making the two coherent states essentially orthogonal. The SHO dynamics will ultimately move the two packets into positions of greater overlap, but the copycat process takes place on time scales short compared to the SHO evolution. We use both the stability of the coherent states and their lack of overlap to argue heuristically that they span a two dimensional subspace, which is effectively decoupled from the rest of the SHO Hilbert space at early times. Based on these considerations, we model the superposition of coherent states in Eqn. 3.3 (used to generate Fig. 3.1) with a single qubit coupled to an environment and undertake analytical calculations of early time behavior using perturbation theory in the small time parameter.

As with the full SHO case, we start with a pure product state at $t = 0$ with no initial entanglement. At $t = 0$ the system (now just a qubit) is a two-state superposition and the environment is in some pure state which we call $|\phi_e\rangle$:

$$\begin{aligned} |\psi_w(0)\rangle &= |\psi_s(0)\rangle\,|\phi_e\rangle \\ &= \big(a\,|\uparrow\rangle + b\,|\downarrow\rangle\,\big)\,|\phi_e\rangle\,. \end{aligned} \tag{3.6}$$

Here a and b can be complex, and $|a|^2 + |b|^2 = 1$. We consider a Hamiltonian given by:

$$H_w \equiv H = \lambda\big(\,|\uparrow\rangle\,\langle\uparrow|\,H_e^{\uparrow} + |\downarrow\rangle\,\langle\downarrow|\,H_e^{\downarrow}\big) \tag{3.7}$$

where λ is a real parameter to adjust the strength of the interaction, and $H_e^{\uparrow}$ and $H_e^{\downarrow}$ only operate in the subspace of the environment. We will refer to H_w as H for brevity in what

follows.

We take $H_e^{\uparrow}$, $H_e^{\downarrow}$, and H to all be time independent, and we generally allow $H_e^{\uparrow}H_e^{\downarrow} \neq H_e^{\downarrow}H_e^{\uparrow}$. For most of what follows, no additional assumptions are made about the eigenvalue spectra of the H_e's or the dimensionality of the environment. We note that H in Eqn. 3.7 is very similar to what we call the "reduced Caldeira-Leggett" (RCL) model Hamiltonian in [1], although there we considered the special case where $H_e^{\uparrow} = -H_e^{\downarrow}$. We call the model we use here an RCL model as well, and note that as discussed in [1] this model will einselect the pointer states $|\uparrow\rangle$ and $|\downarrow\rangle$.

Working in the Schrodinger picture with:

$$\imath\hbar\frac{\partial}{\partial t}|\psi\rangle = H|\psi\rangle \qquad\qquad U(t) = e^{\frac{-\imath Ht}{\hbar}} \tag{3.8}$$

we can perturbatively compute the state of the system and environment at a short time $t = \Delta$, using the series expansion of the time evolution operator

$$\begin{aligned} |\psi_w(\Delta)\rangle &= U(\Delta)|\psi_w(0)\rangle \\ &= \Big(1 - \frac{\imath H\Delta}{\hbar} - \frac{1}{2}\frac{(H\Delta)^2}{\hbar^2} + O(\Delta^3)\Big)|\psi_w(0)\rangle\,. \end{aligned} \tag{3.9}$$

The result is:

$$\begin{aligned} |\psi_w(\Delta)\rangle = &\big(a|\uparrow\rangle + b|\downarrow\rangle\big)|\phi_e\rangle \\ &- \frac{\imath\Delta\lambda}{\hbar}\big(a|\uparrow\rangle H_e^{\uparrow}|\phi_e\rangle + b|\downarrow\rangle H_e^{\downarrow}|\phi_e\rangle\big) \\ &- \frac{\Delta^2\lambda^2}{2\hbar^2}\big(a|\uparrow\rangle H_e^{\uparrow}H_e^{\uparrow}|\phi_e\rangle + b|\downarrow\rangle H_e^{\downarrow}H_e^{\downarrow}|\phi_e\rangle\big). \end{aligned} \tag{3.10}$$

We have found the important leading order behavior occurs at second order, so we keep terms up to $O(\Delta^2)$ in what follows.

3.3.2 System Reduced Density Matrix

We compute the reduced density matrix of the system after a short time $t = \Delta$:

$$\rho_s(t=\Delta) = \mathbf{Tr_e}\big(|\psi_w(\Delta)\rangle\langle\psi_w(\Delta)|\big). \tag{3.11}$$

The result expressed in the $|\uparrow\rangle, |\downarrow\rangle$ basis is:

$$\rho_s(\Delta) = \begin{bmatrix} aa^* & ab^*\Big(1 + \imath\beta\Delta - \eta\Delta^2\Big) \\ ba^*\Big(1 - \imath\beta\Delta - \eta^*\Delta^2\Big) & bb^* \end{bmatrix} \tag{3.12}$$

where the coefficients β and η are given by:

$$\beta = \frac{\lambda}{\hbar}\big(\langle\phi_e| H_e^{\downarrow} |\phi_e\rangle - \langle\phi_e| H_e^{\uparrow} |\phi_e\rangle \big) \tag{3.13}$$

$$\eta = \frac{\lambda^2}{\hbar^2}\Big(\frac{\langle\phi_e| H_e^{\uparrow}H_e^{\uparrow} |\phi_e\rangle + \langle\phi_e| H_e^{\downarrow}H_e^{\downarrow} |\phi_e\rangle}{2} - \langle\phi_e| H_e^{\downarrow}H_e^{\uparrow} |\phi_e\rangle \Big). \tag{3.14}$$

To obtain the above it is necessary to recognize that $\langle\phi_e| H_e^{\downarrow} |\phi_e\rangle$ and $\langle\phi_e| H_e^{\uparrow} |\phi_e\rangle$ are real numbers, but that $\langle\phi_e| H_e^{\uparrow}H_e^{\downarrow} |\phi_e\rangle$ can be complex (since $H_e^{\uparrow}H_e^{\downarrow} \neq H_e^{\downarrow}H_e^{\uparrow}$). This requires β to be purely real, but allows η to be complex. It follows that the system density matrix in Eqn. 3.12 is Hermitian and properly normalized since $\rho^{\dagger} = \rho$, and $Tr[\rho] = |a|^2 + |b|^2 = 1$.

3.3.3 Eigenvalues and eigenvectors of ρ_s

We use the general analytic form for the eigenvalues and eigenstates of a 2 x 2 Hermitian matrix. After obtaining the exact solutions from Eqn. 3.12, we then compute the series expansions in Δ—keeping terms to $O(\Delta^2)$—to obtain the following perturbative expressions:

$$|\psi_1\rangle = \Big(\frac{b^*}{|b|}\Big)\left[a\left(1 + \imath\beta\Delta + \Delta^2\big[\epsilon\big(\frac{2|a|^2|b|^2 + |a|^2}{2}\big) - \eta\big]\right)|\uparrow\rangle + b\left(1 + \Delta^2\epsilon\Big(\frac{2|a|^2|b|^2 - |a|^2}{2}\Big)\right)|\downarrow\rangle\right] \tag{3.15}$$

$$|\psi_2\rangle = \Big(\frac{-a}{|a|}\Big)\left[b^*\left(1 + \imath\beta\Delta + \Delta^2\big[\epsilon\big(\frac{2|a|^2|b|^2 + |b|^2}{2}\big) - \eta\big]\right)|\uparrow\rangle - a^*\left(1 + \Delta^2\epsilon\Big(\frac{2|a|^2|b|^2 - |b|^2}{2}\Big)\right)|\downarrow\rangle\right] \tag{3.16}$$

with associated eigenvalues:

$$p_1 = 1 - |a|^2|b|^2\epsilon\Delta^2 \tag{3.17}$$

$$p_2 = |a|^2|b|^2\epsilon\Delta^2 \tag{3.18}$$

where the parameter ϵ is defined by:

$$\epsilon \equiv \eta + \eta^* - \beta^2. \tag{3.19}$$

We note that ϵ can also be written as

$$\epsilon = \frac{\lambda^2}{\hbar^2}\Big[\langle\phi_e| (H_e^{\downarrow} - H_e^{\uparrow})^2 |\phi_e\rangle - \big(\langle\phi_e| (H_e^{\downarrow} - H_e^{\uparrow}) |\phi_e\rangle \big)^2\Big] \tag{3.20}$$

(using Eqns. 3.13 and 3.14). Equation 3.20 shows that ϵ is just the variance of $\frac{\lambda}{\hbar}(H_e^{\downarrow} - H_e^{\uparrow})$, so $\epsilon \geq 0$ by definition. Furthermore, $\epsilon = 0$ is a degenerate case where einselection does not occur—you can see, for example, that when $\epsilon = 0$ the second eigenvalue in Eqn. 3.18 exactly disappears and the only state remaining with any probability is the initial state. Thus, for cases of interest here $\epsilon > 0$. Also note that $\langle\psi_1|\psi_2\rangle = \langle\psi_2|\psi_1\rangle = 0 + O(\Delta^3)$ and $\langle\psi_1|\psi_1\rangle = \langle\psi_2|\psi_2\rangle = 1 + O(\Delta^3)$, as you would expect from an $O(\Delta^2)$ calculation.

Inspecting Eqns. 3.15 and 3.16, the zeroth order terms identify $|\psi_1\rangle$ with the original state of the system ($|\psi_s(0)\rangle$ from Eqn. 3.6 apart from an irrelevant overall phase) and $|\psi_2\rangle$ as the orthogonal state. In a two dimensional Hilbert space, there is (up to an overall phase) only one orthogonal state to $|\psi_1\rangle$. From the way a and b alternate locations in the expressions for $|\psi_1\rangle$ vs $|\psi_2\rangle$, one can see that the two states have the "mirror image" feature which led us to call the second eigenstate a"copycat" state in Fig. 3.1. Thus, we see that at very early times the copycat profile is achieved automatically in this simple illustration.

We noted in the introduction that the initial time evolution of the copycat state appeared to be "slow" in our numerical simulations. This is also apparent in our analytic solutions—they show the time dependence of the eigenstates and their associated probabilities to be quadratic to leading order modulo a linear complex phase (which we have by convention placed in the coefficients of $|\uparrow\rangle$). The quadratic early time dependence of the eigen*values* has been anticipated before by calculations in [51, 34]—where their "rate of deseparation" is analogous to the quantity $|a|^2|b|^2\epsilon$—but the eigenstate solutions and their copycat nature is a new feature of our analysis.

3.4 Further perturbative analysis

3.4.1 Continued evolution of eigenstates

To investigate what happens to the system density matrix eigenstates after the copycat state appears, let us again consider Eqns. 3.15 and 3.16. At the onset of the copycat process, for small $t = \Delta$, the system has already begun to decohere, but einselection has hardly started. While the system and environment are clearly entangled, the system

density matrix eigenstates are not yet described by the pointer states $|\uparrow\rangle$ and $|\downarrow\rangle$ of the Hamiltonian in Eqn. 3.7.

We now explore the perturbative behavior as Δ increases. Here we focus on $|\psi|^2$ of each eigenstate, given by

$$\begin{aligned}\langle\psi_1|\psi_1\rangle = |a|^2\Big[1+\epsilon\Delta^2(2|a|^2|b|^2-|b|^2)\Big]\,\langle\uparrow\,|\,\uparrow\rangle \\ +|b|^2\Big[1+\epsilon\Delta^2(2|a|^2|b|^2-|a|^2)\Big]\,\langle\downarrow\,|\,\downarrow\rangle \qquad (3.21)\\ \langle\psi_2|\psi_2\rangle = |b|^2\Big[1+\epsilon\Delta^2(2|a|^2|b|^2-|a|^2)\Big]\,\langle\uparrow\,|\,\uparrow\rangle \\ +|a|^2\Big[1+\epsilon\Delta^2(2|a|^2|b|^2-|b|^2)\Big]\,\langle\downarrow\,|\,\downarrow\rangle \qquad (3.22)\end{aligned}$$

where we have made use of Eqn. 3.19.

For $\epsilon > 0$—which is true in all cases where our analysis holds (see the discussion below Eqns. 3.19 and 3.20)—we can re-write Eqns. 3.21 and 3.22 as:

$$\langle\psi_1|\psi_1\rangle = |a|^2\Big[1+C_1^{\uparrow}(\Delta)\Big]\,\langle\uparrow\,|\,\uparrow\rangle + |b|^2\Big[1+C_1^{\downarrow}(\Delta)\Big]\,\langle\downarrow\,|\,\downarrow\rangle \qquad (3.23)$$

$$\langle\psi_2|\psi_2\rangle = |b|^2\Big[1+C_2^{\uparrow}(\Delta)\Big]\,\langle\uparrow\,|\,\uparrow\rangle + |a|^2\Big[1+C_2^{\downarrow}(\Delta)\Big]\,\langle\downarrow\,|\,\downarrow\rangle \qquad (3.24)$$

and construct the following chart for the sign of the time dependent coefficients as time increases:

Original State	$C_1^{\uparrow}(\Delta)$	$C_1^{\downarrow}(\Delta)$	$C_2^{\uparrow}(\Delta)$	$C_2^{\downarrow}(\Delta)$
$\lvert a\rvert^2 > \lvert b\rvert^2$	+	-	-	+
$\lvert a\rvert^2 < \lvert b\rvert^2$	-	+	+	-
$\lvert a\rvert^2 = \lvert b\rvert^2$	0	0	0	0

Comparing Eqns. 3.21 and 3.22 with Eqns. 3.23, 3.24, and the chart illustrates that the subsequent evolution of the system eigenstates towards einselection is determined by the hierarchy of $|a|^2$ and $|b|^2$, the initial system probabilities—and that interactions with the environment control how fast this evolution occurs through the parameter ϵ.

For example, suppose the initial state of the system is such that $|a|^2 > |b|^2$ at $t = 0$. As $t = \Delta$ grows we see that the probability to observe $|\psi_1\rangle$ in the $|\uparrow\rangle$ state increases, since $C_1^{\uparrow}(\Delta)$ is increasing over time, and that the probability of observing $|\psi_1\rangle$ in the

$|\downarrow\rangle$ state is decreasing by the same token. The exact opposite trends occur in $|\psi_2\rangle$, the orthogonal state. So long as $\langle\psi_1|\psi_1\rangle = \langle\psi_2|\psi_2\rangle = 1 + O(\Delta^3)$ is preserved (namely that the perturbation expansion remains valid), the full system will exhibit these trends. The system approaches complete einselection once $1 + C_1^{\downarrow}(\Delta) \approx 1 + C_2^{\uparrow}(\Delta) \approx 0$. An exactly analogous explanation occurs for the case of $|a|^2 < |b|^2$.

For the case of $|a|^2 = |b|^2$, all time dependent coefficients vanish for a properly normalized state to leading order $O(\Delta^2)$. One could interpret this as evidence for a static system—that after the onset of the copycat process no further evolution of the eigenstates occurs. However, in the exactly degenerate limit $|a|^2 = |b|^2$ all states are equally "good" eigenstates of the system density matrix, so einselection into a specific basis of pointer states has no meaning in this limit.[3]

3.4.2 Decoherence Time

Full einselection will take place on the timescale set by the decoherence processes. A system that has fully einselected will have the off-diagonal elements of its density matrix close to zero when ρ_s is expressed in the pointer state basis [11]. Although this stage is only reached outside of the range of our perturbative calculations, we can still estimate the decoherence time by solving for the value of Δ where the off-diagonal elements are zero for our perturbative calculations. Applying this to Eqn. 3.12 gives:

$$\begin{aligned} \rho_{|\uparrow\rangle\langle\downarrow|} &= ab^*\Big(1 + \imath\beta\Delta - \eta\Delta^2\Big) = 0 \\ \rho_{|\downarrow\rangle\langle\uparrow|} &= ba^*\Big(1 - \imath\beta\Delta - \eta^*\Delta^2\Big) = 0 \end{aligned} \tag{3.25}$$

which can be rewritten as

$$ab^* + ba^* + \imath\beta\Delta(ab^* - ba^*) - \Delta^2(ab^*\eta + ba^*\eta^*) = 0 \tag{3.26}$$

$$ab^* - ba^* + \imath\beta\Delta(ab^* + ba^*) - \Delta^2(ab^*\eta - ba^*\eta^*) = 0. \tag{3.27}$$

[3] In cases with very small deviations away from complete degeneracy, small irregularities (due, for example, to the finite size of the environment) can disrupt any tendency toward einselection. We have seen this phenomenon in our numerical work, where for sufficiently degenerate cases finite size effects introduced large random fluctuations which dominated over the einselection process.

Solving Eqns. 3.26 and 3.27 together and simplifying yields the following perturbative estimate for the decoherence time:

$$\Delta_d = \sqrt{\frac{2}{\eta + \eta^*}} \tag{3.28}$$

where η is given by Eqn. 3.14. Note that this result is independent of a and b (the initial state of the system). We have compared this expression with our numerical work and found it gives reasonable estimates of the decoherence time.

3.4.3 Spin Observables

Here we consider the behavior of the Pauli spin operators in our RCL solutions. This will allow contact to be made with various experimental contexts such as NMR and quantum computing [38, 39, 49].

Our basis states for our system density matrix, $\{|\uparrow\rangle, |\downarrow\rangle\}$, can be identified with the S_z eigenbasis for spin-$\frac{1}{2}$, so we can compute the expectation values for the spin operators S_x, S_y and S_z by

$$\langle S_i \rangle = Tr(\rho_s S_i) = \frac{\hbar}{2} Tr(\rho_s \sigma_i) \tag{3.29}$$

where the σ_i are the usual Pauli matrices

$$\sigma_x = \begin{bmatrix} 0 & 1 \\ 1 & 0 \end{bmatrix} \quad \sigma_y = \begin{bmatrix} 0 & -\imath \\ \imath & 0 \end{bmatrix} \quad \sigma_z = \begin{bmatrix} 1 & 0 \\ 0 & -1 \end{bmatrix}. \tag{3.30}$$

This gives

$$\langle S_z \rangle = \frac{\hbar}{2}(|a|^2 - |b|^2) \tag{3.31}$$

$$\langle S_x \rangle = \frac{\hbar}{2}\Big(2Re[ab^*] - 2\beta\Delta Im[ab^*] - 2\Delta^2 Re[ab^*\eta]\Big) \tag{3.32}$$

$$\langle S_y \rangle = \frac{\hbar}{2}\Big(- 2Im[ab^*] - 2\beta\Delta Re[ab^*] + 2\Delta^2 Im[ab^*\eta]\Big). \tag{3.33}$$

Note that the system will have fully decohered/completed einselection when $\langle S_x \rangle = \langle S_y \rangle = 0$. For our perturbative expressions, this condition is the same as that imposed by Eqns. 3.26 and 3.27.

3.5 Beyond Perturbation Theory

An intriguing part of the copycat process is that its general features are agnostic about the spectrum of the environment. The Hamiltonian in Eqn. 3.7 used to derive our results thus far makes no assumptions about the pieces that operate on the state of the environment, $H_e^{\uparrow}$ and $H_e^{\downarrow}$, except that they are time independent. This gives our results a flavor of generality often missing from canonical toy models in the literature—reviewed in [49, 8] and others—which typically make specific assumptions of "ohmic" environments and the like in order to arrive at concrete mathematical expressions.

However, if we do further specify $H_e^{\uparrow}$ and $H_e^{\downarrow}$ we can compute a non-perturbative version of the density matrix in Eqn. 3.12, closely following an approach by Zurek for a similar model [10]. This has two benefits. First, it is possible to re-derive a form of the copycat results as leading order terms in the time series expansion of the non-perturbative solutions—as should be the case. Second, a non-perturbative approach allows us to interpret the full time range of our numerical results discussed in [1] from an analytic perspective.

3.5.1 An Alternate Derivation

To derive a non-perturbative version of Eqn. 3.12, we begin by specifying the following:

$$H_e^{\uparrow} = \sum_i^N \hbar\omega_i \left|\omega_i\right\rangle \left\langle\omega_i\right| \tag{3.34}$$

$$H_e^{\downarrow} = \sum_i^N \hbar f^{\uparrow\downarrow}\omega_i \left|\omega_i\right\rangle \left\langle\omega_i\right| \tag{3.35}$$

so that

$$\omega_i^{\downarrow} = f^{\uparrow\downarrow}\omega_i^{\uparrow} \tag{3.36}$$

i.e. $H_e^{\uparrow}$ and $H_e^{\downarrow}$ are almost identical, except for a tuneable real dimensionless constant $f^{\uparrow\downarrow}$. (The RCL model discussed in [1] has this form with $f^{\uparrow\downarrow} = -1$.) This simplifying assumption about the relationship between $H_e^{\uparrow}$ and $H_e^{\downarrow}$ enables the analysis which follows.

We can express the state of the environment in the energy eigenbasis of $H_e^{\uparrow}$ and $H_e^{\downarrow}$,

so that

$$|\phi_e\rangle = \sum_i^N \alpha_i |\omega_i\rangle \tag{3.37}$$

with the normalization condition:

$$\sum_i^N |\alpha_i^{\uparrow}|^2 = 1. \tag{3.38}$$

Both the ACL and RCL models operate within a finite dimensional Hilbert space, so we have made that explicit in our forms for $H_e^{\uparrow}$ and $H_e^{\downarrow}$. The exact frequency spectrum of the ω_i's is still arbitrary. However, when comparisons with our numerical work are made in the next section, we will take their distribution to be random and centered around zero—to coincide with the random nature of $H_e^{\uparrow}$ and $H_e^{\downarrow}$ in the ACL model [1].

Given the definitions in Eqns. 3.34 - 3.38, we can re-express the original state of the system and environment as:

$$|\psi_w(0)\rangle = (a|\uparrow\rangle + b|\downarrow\rangle) \otimes \sum_i^N \alpha_i |\omega_i\rangle \tag{3.39}$$

and the RCL Hamiltonian originally given in Eqn. 3.7 becomes:

$$\begin{aligned} H_w =& (\lambda |\uparrow\rangle\langle\uparrow| \otimes \sum_i^N \hbar\omega_i |\omega_i\rangle\langle\omega_i|) \\ &+ (\lambda |\downarrow\rangle\langle\downarrow| \otimes \sum_i^N \hbar\omega_i f^{\uparrow\downarrow} |\omega_i\rangle\langle\omega_i|) \end{aligned} \tag{3.40}$$

Since we have made the eigenvalues of our Hamiltonian explicit from the start, we may write down the full time evolved state as:

$$\begin{aligned} |\psi_w(t)\rangle =& (a \sum_i^N \alpha_i e^{-\imath\lambda\omega_i t} |\uparrow\rangle \otimes |\omega_i\rangle) \\ &+ (b \sum_i^N \alpha_i e^{-\imath\lambda f^{\uparrow\downarrow}\omega_i t} |\downarrow\rangle \otimes |\omega_i\rangle) \end{aligned} \tag{3.41}$$

Tracing over the environment then gives the following system density matrix:

$$\begin{aligned} \rho_s(t) =& |a|^2 |\uparrow\rangle\langle\uparrow| + ab^* z(t) |\uparrow\rangle\langle\downarrow| \\ &+ ba^* z^*(t) |\downarrow\rangle\langle\uparrow| + |b|^2 |\downarrow\rangle\langle\downarrow| \end{aligned} \tag{3.42}$$

where the quantity $z(t)$ has been called the correlation amplitude or decoherence factor [10, 11, 38, 39] for similar toy models and is given in our notation by:

$$z(t) = \sum_{i}^{N} |\alpha_i|^2 e^{-\imath t \lambda \omega_i (1 - f^{\uparrow\downarrow})} \tag{3.43}$$

Note that $z(t)$ is a sum of complex exponentials that directly depends on the difference in eigenvalues of our two environmental Hamiltonians. As Zurek originally discussed in [10], the quantity $|\alpha_i|^2$ describes the probability of finding the environment in the different eigenstates of the interaction Hamiltonian, and it is possible to show that the average value of $z(t)$ will approach zero for sufficiently long times, effectively damping out the off-diagonal system density matrix elements.

Together Eqns. 3.42 and 3.43 are the non-perturbative version of the system density matrix in Eqn. 3.12, for the specific realization of environment parameters given by Eqns. 3.34 - 3.38. To show how these results connect with the copycat process solutions, first write $z(t)$ in terms of trigonometric functions.

$$z(t) = \sum_{i}^{N} |\alpha_i|^2 \big[\cos(\lambda \omega_i (1 - f^{\uparrow\downarrow}) t) - \imath \sin(\lambda \omega_i (1 - f^{\uparrow\downarrow}) t) \big] \tag{3.44}$$

Then we take the limit $t \to \Delta$ by keeping only the first non-trivial term in each trigonometric function's series expansion. We still keep the sum over the states of the environment, all we are doing is an early time expansion. This yields:

$$\begin{aligned} z(\Delta) =& 1 + \imath \sum_{i}^{N} |\alpha_i|^2 \lambda \omega_i (f^{\uparrow\downarrow} - 1) \Delta \\ & - \sum_{i}^{N} |\alpha_i|^2 \omega_i^2 \frac{\lambda^2 (f^{\uparrow\downarrow} - 1)^2}{2} \Delta^2 \\ =& 1 + \imath \beta \Delta - \eta \Delta^2 \end{aligned} \tag{3.45}$$

which is exactly the time dependent off-diagonal element in Eqn. 3.12, given the definitions in Eqns. 3.34 - 3.38. One can verify the equivalence between the two lines of Eqn. 3.45 by starting with the definitions of β and η given by Eqns. 3.13 and 3.14, and then substituting in the specific forms of $H_e^{\uparrow}$, $H_e^{\downarrow}$, and $|\phi_e\rangle$ given in this section—the result will be the same

as Eqn. 3.45. An analogous expression for $z^*(\Delta)$ holds, which enables us to re-express Eqn. 3.12 as

$$\begin{aligned}\rho_s(\Delta) =& |a|^2 \left|\uparrow\right\rangle \left\langle\uparrow\right| + ab^* z(\Delta) \left|\uparrow\right\rangle \left\langle\downarrow\right| \\ &+ ba^* z^*(\Delta) \left|\downarrow\right\rangle \left\langle\uparrow\right| + |b|^2 \left|\downarrow\right\rangle \left\langle\downarrow\right| \end{aligned} \tag{3.46}$$

From Eqns. 3.45 and 3.46, one can then go on to determine the eigenvalues, eigenvectors and decoherence time of the system density matrix. The results will match the more general calculations in Sections III and IV, for the specific versions of η and β given in Eqn. 3.45.

To summarize, in this section we have derived a specific realization of the copycat results as leading order terms in the time series expansion of Eqns. 3.42 and 3.43. Note that if the relationship between $H_e^{\uparrow}$ and $H_e^{\downarrow}$ in Eqns. 3.34 and 3.35 was more complicated—if they did not share the same energy eigenbasis or if the relationship between eigenvalues was non-linear, for example—then a derivation of the early time density matrix from a non-perturbative approach might not proceed as smoothly as we just described. However, the early time results of Sect. 3.3 will have a more general range of validity.

3.5.2 Comparison with numerical results

In this section we consider two quantities that depend strongly on the off-diagonal elements of the system density matrix—the linear entropy and $\langle S_x \rangle$—and compare numerical non-perturbative results to semi-analytic early-time expressions.

The linear entropy for a density matrix is defined as:

$$S_l(\rho) = 1 - Tr[\rho^2] \tag{3.47}$$

which is bounded according to $0 \leq S_l \leq 1$ [8]. For the system density matrix given in our perturbative analysis (Eqn. 3.12), this yields:

$$S_{l,P} = 2|a|^2|b|^2\epsilon\Delta^2 + O(\Delta^3) \tag{3.48}$$

with ϵ given by:

$$\epsilon = \lambda^2(f^{\uparrow\downarrow} - 1)^2 \left[\sum_i^N \omega_i^2 |\alpha_i|^2 - \left(\sum_i^N \omega_i |\alpha_i|^2 \right)^2 \right] \tag{3.49}$$

assuming Eqns. 3.34 - 3.38 from the previous section.

For the non-perturbative case, given Eqns. 3.42 and 3.43, one obtains:

$$S_{l,NP} = 1 - |a|^4 - |b|^4 - 2|a|^2|b|^2|z(t)|^2 \tag{3.50}$$

with

$$|z(t)|^2 = \sum_{i,j}^{N} |\alpha_i|^2|\alpha_j|^2 e^{-\imath\lambda(1-f^{\uparrow\downarrow})(\omega_i-\omega_j)t} \tag{3.51}$$

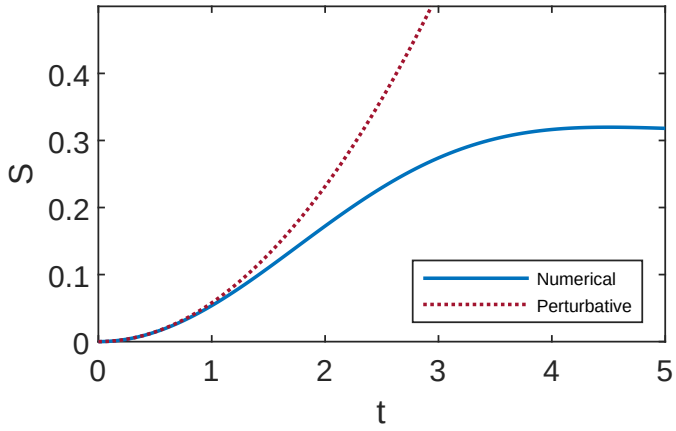

Figure 3.2: Linear entropy curves. Solid: Non-perturbative (corresponding to numerically evaluating Eqns. 3.50 and 3.51). Dotted: Perturbative expression from Eqn. 3.48, using ϵ (given by Eqn. 3.49) drawn from the same numerical calculation shown.

Figure 3.2 shows the perturbative and non-perturbative linear entropies as functions of time. To numerically generate the non-perturbative solid curve, our simulations effectively evaluate the summation in Eqn. 3.51 followed by Eqn. 3.50 at each time-step and plot the result. For the dotted curve corresponding to Eqn. 3.48, the summation in Eqn. 3.49 is evaluated once numerically and then the expression in Eqn. 3.48 is plotted for the same time-steps as those used for Eqn. 3.50. For both curves: $a = 1/\sqrt{5}$, $b = 2/\sqrt{5}$, $f^{\uparrow\downarrow} = -1$, and the distribution of environmental frequencies, ω_i, is taken to be random and centered around zero—to coincide with the random nature of $H_e^{\uparrow}$ and $H_e^{\downarrow}$ in the ACL model [1].

Next, consider $\langle S_x \rangle$. For the early-time regime we simply have Eqn. 3.32, reprinted

here:

$$\langle S_x \rangle_P = \frac{\hbar}{2}\Big(2Re[ab^*] - 2\beta\Delta Im[ab^*] - 2\Delta^2 Re[ab^*\eta]\Big) \tag{3.52}$$

with the quantities η and β as defined in Eqn. 3.45. For the non-perturbative case we obtain:

$$\langle S_x \rangle_{NP} = \frac{\hbar}{2}(2Re[ab^* z(t)]) \tag{3.53}$$

with $z(t)$ given by Eqn. 3.43.

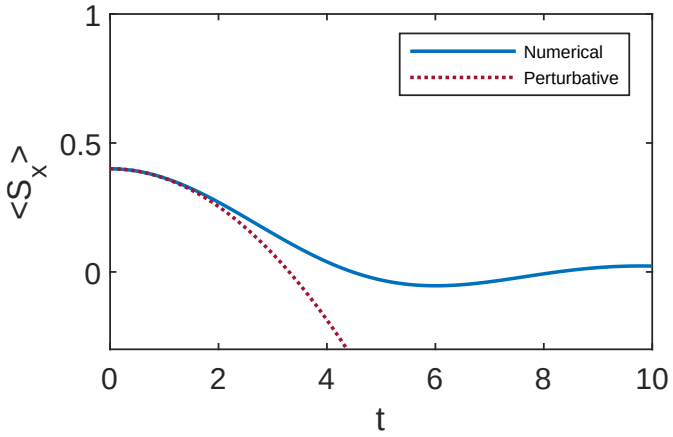

Figure 3.3: $\langle S_x \rangle$, giving the real part of the off-diagonal element of ρ_s. The solid curve is non-perturbative, corresponding to numerically evaluating Eqn 3.53. The dotted curve corresponds to the early time analytic expression in Eqn. 3.52, with the the quantities defined in Eqn 3.45 drawn from the numerical calculation. We take $\hbar = 1$.

Figure 3.3 shows the perturbative and non-perturbative results for $\langle S_x \rangle$ as a function of time. As with the linear entropy, the non-perturbative curve was generated numerically in our simulations essentially by evaluating Eqn. 3.53 for each time step, while the early-time result is the analytical function in Eqn. 3.52 with the summations for η and β in Eqn. 3.45 evaluated numerically. The values for a, b, $f^{\uparrow\downarrow}$, and ω_i are the same as in Fig. 3.2, and we take $\hbar = 1$.

We note here that the RCL model is not highly efficient at completing the process of einselection, as evidenced by the small oscillation around zero of the numerical curve in Fig. 3.3. We further discuss the interpretation of these oscillations in [1] and link them to

phenomena seen in NMR experiments. We also identify a modification to the RCL model which reduces these oscillations, thereby further illuminating their physical origins.

Both Figs. 3.2 and 3.3 demonstrate that the perturbative regime—characterized by the copycat density matrix in Eqn. 3.12—can be a sizable portion of the full time evolution of the system's linear entropy and $\langle S_x \rangle$. The duration may vary somewhat for different system-environment coupling strengths or environmental frequency spectra, but the overall presence of a significant period of quadratic time behavior is clear.

3.6 Discussion and Conclusions

In this paper we have identified and described unique early time behavior of a quantum system interacting with its environment—the copycat process. The copycat process is a new and potentially important addition to the narrative of decoherence and einselection. By considering the evolution of the system density matrix from an eigenstate perspective, we were able to recognize the early-time emergence of a distinct transiently stable "copycat" state, as illustrated in Fig. 3.1. We have derived the same effect analytically in Sect. 3.3, and then utilize the solutions and their implications to obtain new insights into how small quantum systems einselect in Sects. 3.4 and 3.5. Furthermore, the comparison with our numerical work in section V.B demonstrates that one might expect key features of the copycat process to dominate for a significant portion of the full time to full einselection.

The generality of our results in Sects. 3.3 and 3.4 is also noteworthy. As we briefly commented in Sect. 3.5, an intriguing part of the copycat process is that it is agnostic about the spectrum of the environment. The Hamiltonian in Eqn. 3.7 used to derive the copycat results makes no assumption of any of the standard environmental spectra—such as "ohmic" environments—typically employed in the literature to make analytical progress [49, 8], and it also does not assume the random environment that we utilize for our numerical work in section V.B and [1]. This suggests that the onset of einselection could begin with the copycat process in a wide variety of cases.

While we acknowledge our analytical modelling of system-environment interactions

is fairly simplified in the RCL model, our numerical work with the ACL model in [1] demonstrates that the copycat process persists even in the presence of strong self Hamiltonians of the system and environment. Furthermore, we expect the copycat process to be present in some form for larger and more complicated systems. The orthogonal nature of the copycat eigenstates might be unsurprising for the two-state system results—the small Hilbert space greatly limits the possibilities—but we have also seen that the same copycat behavior holds for superpositions of two coherent states of an SHO.

When the evolution of the global (w) system is unitary, the evolution of a subsystem density matrix is always deterministic. Thus (except for the case of degenerate eigenvalues) the evolution the density matrix eigenstates is also deterministic. The copycat process is an example of a form of this deterministic evolution which generically appears in two state systems, as well as some larger systems that are started in "two cat" states.

To explore further, in Appendix 3.A we extend our analytical perturbative analysis to the case where the system is a qu*trit*. There we see that many of the same copycat features appear, although the pattern of early quadratic behavior is partially broken by the possibility of linear evolution in the (2d) system subspace orthogonal to the original system state.

Exploring further still, Fig. 3.4 shows the evolution of a particular example with a higher dimensional system, set up in a form that might be thought of as "eight Schrödinger cats." In that case we did observe overall quadratic behavior to leading order, resulting in the same transient stability. One would be hard pressed to describe the states that appear in the right column as "copycat states," but these are the states which emerge from the deterministic Schrödinger evolution in the w space for the particular chosen initial state. These results give some sense how the equivalent process can look in a more complex situation.

There are several connections between the results we present here and the existing literature. Early-time quadratic decay of the off-diagonal elements of the system density matrix for decohering systems has been mentioned to varying degrees in several places [49, 8, 36, 52, 10, 38, 39, 34, 51, 53, 54]. However, these references typically do not look

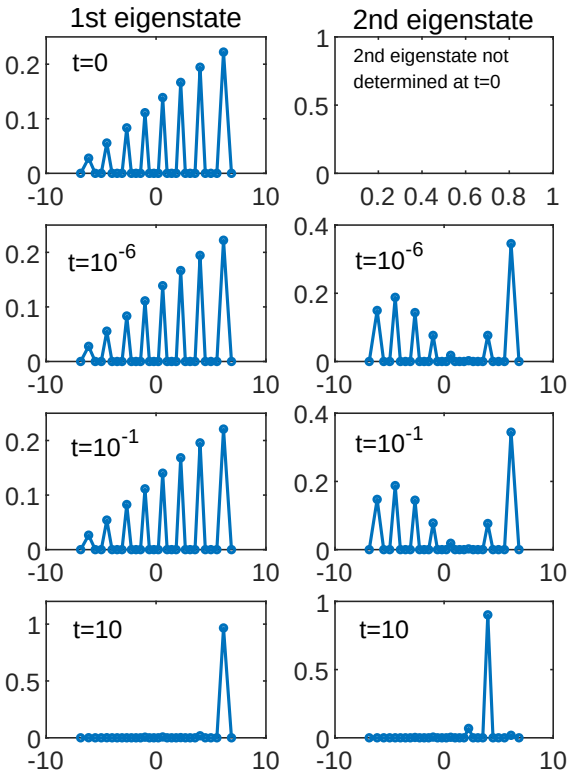

Figure 3.4: The evolution of an initial eight-cat state, showing the top two eigenstates of ρ_s. The term "copycat" might not be a great description of the second eigenstate, but we have found that the quadratic transient stability is still present. The process of einselection is essentially complete at the final time shown. We use the RCL model, with a $d = 30$ qudit system. The markers show the amplitude squared for each basis vector, and the lines are added for illustrative purposes.

explicitly at the eigenstates of ρ_s. Other explorations of the early-time behavior of open quantum systems appear in discussions of the "quantum Zeno paradox" [8, 55, 56], where the behavior of the system density matrix eigenstates is also typically not considered.

Generally, we have found that features of the evolution that might be associated with "decay," or the onset of entanglement, are quadratic to leading order. Such features are controlled by the eigen*values* of ρ_s, which are always quadratic (to leading order) in our results and in the literature we cite here. We have also quite generally found aspects of

the evolution which are *linear* at lowest order in time. These aspects describe evolution of the system in ways not associated with the onset of entanglement. For example, the linear piece $\propto \beta$ in Eqns. 3.15 and 3.16 describes the evolution of the relative phase between the coefficients of the pointer states, and in Appendix 3.A we saw a real linear part to the evolution of the second and third eigenstates of ρ_s.

We also note that many approaches to studying decoherence and einselection—see reviews in [49, 8], for example—utilize a master equation approach to analyze the time evolution of the system density matrix. As discussed in [1], this master equation approach typically carries with it assumptions of Markovian evolution and the resulting exponential decay of off-diagonal system density matrix elements. Even within the master equation approach it is known that exponential decay is not always valid [57, 8, 49], however the exponential case remains the focus of much of the literature. There are some exceptions to this focus. Zurek and collaborators [10, 38, 39] explicitly note the generally dominant early quadratic behaviors and point out that, in the context of the formalisms they develop, the exponential behavior is a very special case. And Peres [58] offers a general analysis of the diverse range of possible behaviors. Our approach in this paper and in our numerical work [1] is agnostic of Markovian assumptions by simply solving the Schrödinger equation directly. This has led to us observing more complicated non-Markovian time dependence in our system density matrix, including the copycat regime.

Looking forward, we are curious whether our calculations of the copycat process could provide a useful tool for studying decoherence and einselection in open quantum systems. Examining the time dependence of the system density matrix eigenstates and eigenvalues allows one to see the system smoothly transition from an initial quantum superposition to a classical mixture of pointer states, with the copycat process describing the first stages of this transition.

3.7 Acknowledgements

We are grateful to F. Anza, N. Curro, P. Coles, B. Nachtergaele, R. Singh, A. Sornborger, and Z. Wang for valuable conversations. This work was supported in part by the U.S.

Department of Energy, Office of Science, Office of High Energy Physics QuantISED program under Contract No. KA2401032.

3.A The qutrit RCL

Here we extend our perturbative treatment of the RCL model to the case where the single qubit system is replaced with a qu*trit*. This enables us, among other things, to study the evolution of three cat Schrödinger cat initial states.

Our results show that the early time behavior of the eigenvalues is quadratic to leading order, as we have already shown analytically in the qubit case and have also observed numerically in much larger systems. In many respects the behavior of the eigenstates also reflects what we saw for the qubit case. However, we have identified circumstances where the leading behavior of the second and third eigenstates has a real linear contribution, in contrast to the qubit case where the linear piece just showed up in a relative phase.

The derivation is nearly identical to the treatment in Section III, in that we begin with an initial state

$$|\psi_w(0)\rangle = (a\,|1\rangle + b\,|0\rangle + c\,|{-1}\rangle)\,|\phi_e\rangle \tag{3.54}$$

with $|a|^2 + |b|^2 + |c|^2 = 1$ and Hamiltonian of the form[4]

$$H_w = \lambda\big(\,|1\rangle\langle 1|\,H_e^1 + |0\rangle\langle 0|\,H_e^0 + |{-1}\rangle\langle -1|\,H_e^{-1}\big). \tag{3.55}$$

Following the same methods as Section III, we obtained the reduced density matrix

$$\rho_s = \begin{bmatrix} \rho_{|1\rangle\langle 1|} & \rho_{|1\rangle\langle 0|} & \rho_{|1\rangle\langle -1|} \\ \rho_{|0\rangle\langle 1|} & \rho_{|0\rangle\langle 0|} & \rho_{|0\rangle\langle -1|} \\ \rho_{|-1\rangle\langle 1|} & \rho_{|-1\rangle\langle 0|} & \rho_{|-1\rangle\langle -1|} \end{bmatrix} \tag{3.56}$$

[4]Note that the "-1" superscript here is an index, not an inverse operation.

with entries defined as:

$$\begin{aligned}
\rho_{|1\rangle\langle 1|} &= aa^* \\
\rho_{|1\rangle\langle 0|} &= ab^*\big(1 + \imath\Delta\beta_{10} - \Delta^2\eta_{10} + \imath\Delta^3\nu_{10} + \Delta^4\kappa_{10}\big) \\
\rho_{|1\rangle\langle -1|} &= ac^*\big(1 + \imath\Delta\beta_{1-1} - \Delta^2\eta_{1-1} + \imath\Delta^3\nu_{1-1} + \Delta^4\kappa_{1-1}\big) \\
\rho_{|0\rangle\langle 1|} &= ba^*\big(1 - \imath\Delta\beta_{10} - \Delta^2\eta^*_{10} - \imath\Delta^3\nu^*_{10} + \Delta^4\kappa^*_{10}\big) \\
\rho_{|0\rangle\langle 0|} &= bb^* \\
\rho_{|0\rangle\langle -1|} &= bc^*\big(1 + \imath\Delta\beta_{0-1} - \Delta^2\eta_{0-1} + \imath\Delta^3\nu_{0-1} + \Delta^4\kappa_{0-1}\big) \\
\rho_{|-1\rangle\langle 1|} &= ca^*\big(1 - \imath\Delta\beta_{1-1} - \Delta^2\eta^*_{1-1} - \imath\Delta^3\nu^*_{1-1} + \Delta^4\kappa^*_{1-1}\big) \\
\rho_{|-1\rangle\langle 0|} &= cb^*\big(1 - \imath\Delta\beta_{0-1} - \Delta^2\eta^*_{0-1} - \imath\Delta^3\nu^*_{0-1} + \Delta^4\kappa^*_{0-1}\big) \\
\rho_{|-1\rangle\langle -1|} &= cc^*.
\end{aligned} \tag{3.57}$$

It ends up being necessary to calculate the reduced density matrix to $O(\Delta^4)$, in order to not lose information when calculating the eigenvalues and eigenstates to $O(\Delta^2)$. The β and η parameters are defined analogously to Eqns. 3.13 and 3.14, i.e.

$$\beta_{ij} = \frac{\lambda}{\hbar}\big(\langle\phi_e| H_e^j |\phi_e\rangle - \langle\phi_e| H_e^i |\phi_e\rangle\big) \tag{3.58}$$

$$\begin{aligned}
\eta_{ij} = \frac{\lambda^2}{\hbar^2}\Big(&\frac{\langle\phi_e| H_e^i H_e^i |\phi_e\rangle + \langle\phi_e| H_e^j H_e^j |\phi_e\rangle}{2} \\
&- \langle\phi_e| H_e^j H_e^i |\phi_e\rangle\Big)
\end{aligned} \tag{3.59}$$

with

$$\epsilon_{ij} = \eta_{ij} + \eta^*_{ij} - \beta^2_{ij} \tag{3.60}$$

and the additional third and forth order parameters, ν_{ij} and κ_{ij}, are defined according to:

$$\begin{aligned}
\nu_{ij} = \frac{\lambda^3}{\hbar^3}\Big(&\frac{\langle\phi_e| (H_e^i)^3 |\phi_e\rangle - \langle\phi_e| (H_e^j)^3 |\phi_e\rangle}{6} \\
&+ \frac{\langle\phi_e| (H_e^j)^2 H_e^i |\phi_e\rangle - \langle\phi_e| H_e^j (H_e^i)^2 |\phi_e\rangle}{2}\Big)
\end{aligned} \tag{3.61}$$

$$\begin{aligned}
\kappa_{ij} = \frac{\lambda^4}{\hbar^4}\Big(&\frac{\langle\phi_e| (H_e^i)^4 |\phi_e\rangle + \langle\phi_e| (H_e^j)^4 |\phi_e\rangle}{24} \\
&- \frac{\langle\phi_e| (H_e^j)^3 H_e^i |\phi_e\rangle + \langle\phi_e| H_e^j (H_e^i)^3 |\phi_e\rangle}{6} \\
&+ \frac{\langle\phi_e| (H_e^j)^2 (H_e^i)^2 |\phi_e\rangle}{4}\Big).
\end{aligned} \tag{3.62}$$

Because this 3 x 3 system reduced density matrix is Hermitian, general analytical solutions for the eigenvalues and eigenstates exist [59, 60]. Using these exact solutions as a starting point, we then performed another sequence of series expansions for the small parameter $t = \Delta$ to obtain analytic solutions. For the sequence of series expansions we kept terms up to $O(\Delta^4)$, only truncating the results to $O(\Delta^2)$ at the end. As mentioned earlier, this is essential to not lose information when calculating the eigenvalues and eigenstates to $O(\Delta^2)$—for example, one needs to keep up to $O(\Delta^4)$ to navigate the series expansion of the ratio involving a square root in Eqn. 9 of [59] correctly. The eigenvalues to lowest order in time are given by:

$$\begin{aligned} p_1 &= 1 - \Delta^2\Big(|a|^2|b|^2\epsilon_{10} + |a|^2|c|^2\epsilon_{1-1} + |b|^2|c|^2\epsilon_{0-1}\Big) \\ &= 1 - \Delta^2\lambda_1 \qquad (3.63) \\ p_2 &= \frac{\Delta^2}{2}\Big(\lambda_1 + \sqrt{\Lambda}\Big) \\ &= \Delta^2\lambda_2 \qquad (3.64) \\ p_3 &= \frac{\Delta^2}{2}\Big(\lambda_1 - \sqrt{\Lambda}\Big) \\ &= \Delta^2\lambda_3 \qquad (3.65) \end{aligned}$$

with

$$\begin{aligned} \Lambda = \lambda_1^2 + 4|a|^2|b|^2|c|^2\Big(&|\eta_{0-1}|^2 + |\eta_{10}|^2 + |\eta_{1-1}|^2 \\ &+ \beta_{10}\beta_{1-1}\mathrm{Re}[\eta_{0-1}] + \beta_{0-1}\beta_{1-1}\mathrm{Re}[\eta_{10}] \\ &- \beta_{0-1}\beta_{10}\mathrm{Re}[\eta_{1-1}] - \mathrm{Re}[\eta_{0-1}\eta_{10}] \\ &- \mathrm{Re}[\eta_{1-1}\eta_{0-1}^*] - \mathrm{Re}[\eta_{1-1}\eta_{10}^*]\Big). \qquad (3.66) \end{aligned}$$

To obtain the above it is necessary to recognize that

$$(\beta_{0-1} + \beta_{10} - \beta_{1-1}) = 0 \qquad (3.67)$$

generically, simply following from the definition in Eqn. 3.58. This sets the leading order time dependence of the eigenvalues to be quadratic, as with the two-state results earlier in this paper. Note the $\pm\sqrt{\Lambda}$ part of Eqns. 3.64 and 3.65 is what saves p_2 and p_3 from

being degenerate at $O(\Delta^2)$. In the limit that any of the initial state coefficients a, b, or c are sent to zero, we exactly recover the two state eigenvalues given by Eqns. 3.17 and 3.18 from Eqns. 3.63 - 3.66.

The normalized eigenstate results have the general form:

$$|\psi_1\rangle = \chi_1 |1\rangle + \gamma_1 |0\rangle + \zeta_1 |-1\rangle \tag{3.68}$$

$$|\psi_{2,3}\rangle = \chi_{2,3} |1\rangle + \gamma_{2,3} |0\rangle + \zeta_{2,3} |-1\rangle \tag{3.69}$$

where for the top eigenstate χ, γ, and ζ are defined by:

$$\chi_1 = \frac{x_0}{N_0}\Big[1 + \imath\,\frac{x_1}{x_0}\Delta + \big(\frac{x_2}{x_0} - \frac{1}{2}\frac{N_2}{(N_0)^2}\big)\Delta^2\Big] \tag{3.70}$$

$$\gamma_1 = \frac{y_0}{N_0}\Big[1 + \imath\,\frac{y_1}{y_0}\Delta + \big(\frac{y_2}{y_0} - \frac{1}{2}\frac{N_2}{(N_0)^2}\big)\Delta^2\Big] \tag{3.71}$$

$$\zeta_1 = \frac{1}{N_0}\Big[1 - \frac{1}{2}\frac{N_2}{(N_0)^2}\Delta^2\Big] \tag{3.72}$$

given

$$N_0 = \sqrt{1 + |x_0|^2 + |y_0|^2} \tag{3.73}$$

$$N_2 = |x_1|^2 + |y_1|^2 + 2\mathrm{Re}[x_0 x_2^*] + 2\mathrm{Re}[y_0 y_2^*] \tag{3.74}$$

with

$$y_0 = \frac{b}{c} \tag{3.75}$$

$$y_1 = \frac{b}{c}\big(\beta_{1-1} - \beta_{10}\big) \tag{3.76}$$

$$y_2 = \frac{b}{c}\Big[(\beta_{10} - \beta_{1-1})\beta_{1-1} + \eta_{1-1}^* - \eta_{10}^* + |c|^2(\delta_1 - \epsilon_{0-1}) + |b|^2\delta_1\Big] \tag{3.77}$$

and

$$x_0 = \frac{a}{c} \tag{3.78}$$

$$x_1 = \frac{a}{c}\beta_{1-1} \tag{3.79}$$

$$x_2 = \frac{a}{c}\frac{1}{|a|^2}\Big[(1 - |c|^2)(\epsilon_{1-1} - \eta_{1-1}) - \lambda_1 - cb^* y_2 + |b|^2\big[\beta_{0-1}^2 - 2\beta_{0-1}\beta_{1-1} - \epsilon_{1-1} + \eta_{1-1} + \eta_{0-1}^*\big]\Big] \tag{3.80}$$

where λ_1 is defined in Eqn. 3.63, y_2 in Eqn. 3.77, and δ_1 is shorthand for:

$$\delta_1 = \beta_{0-1}\beta_{10} + \eta^*_{0-1} + \eta^*_{10} - \eta^*_{1-1}. \tag{3.81}$$

As with the two-state solutions, it is purely a matter of our chosen convention (chosen for convenience) that the linear complex phase is present in $|1\rangle$ and $|0\rangle$ but not $|-1\rangle$ in Eqns. 3.70 - 3.72.

Additional complexity is present for $|\psi_2\rangle$ and $|\psi_3\rangle$. For these eigenstates, $\chi_{2,3}$, $\gamma_{2,3}$, and $\zeta_{2,3}$ are defined as:

$$\begin{aligned}\chi_{2,3} = \frac{u_0}{M_0}\Big[1 + \imath\,\frac{u_1}{u_0}\Delta + \frac{M_1}{(M_0)^2}\Delta \\ + \big(\frac{u_2}{u_0} + \frac{u_1 M_1}{2u_0(M_0)^2} - \frac{3(M_1)^2}{8(M_0)^4} - \frac{M_2}{2(M_0)^2}\big)\Delta^2\Big]\end{aligned} \tag{3.82}$$

$$\begin{aligned}\gamma_{2,3} = \frac{v_0}{M_0}\Big[1 + \imath\,\frac{v_1}{v_0}\Delta + \frac{M_1}{(M_0)^2}\Delta \\ + \big(\frac{v_2}{v_0} + \frac{v_1 M_1}{2v_0(M_0)^2} - \frac{3(M_1)^2}{8(M_0)^4} - \frac{M_2}{2(M_0)^2}\big)\Delta^2\Big]\end{aligned} \tag{3.83}$$

$$\zeta_{2,3} = \frac{1}{M_0}\Big[1 + \frac{M_1}{(M_0)^2}\Delta - \big(\frac{3(M_1)^2}{8(M_0)^4} + \frac{M_2}{2(M_0)^2}\big)\Delta^2\Big] \tag{3.84}$$

given:

$$M_0 = \sqrt{1 + |u_0|^2 + |v_0|^2} \tag{3.85}$$

$$M_1 = \mathrm{Im}[u_1 u_0^*] + \mathrm{Im}[v_1 v_0^*] \tag{3.86}$$

$$M_2 = |u_1|^2 + |v_1|^2 + 2\mathrm{Re}[u_0 u_2^*] + 2\mathrm{Re}[v_0 v_2^*] \tag{3.87}$$

with

$$v_0 = \Big(\frac{b}{c}\Big)\left[\frac{\lambda_{2,3} + |c|^2(\delta_1 - \epsilon_{0-1})}{\lambda_{2,3} - |b|^2\delta_1}\right] \tag{3.88}$$

$$\begin{aligned} v_1 = \Big(\frac{b}{c}\Big)&\left[\frac{1}{(\lambda_{2,3} - |b|^2\delta_1)^2}\right] \\ &\times \Bigg[\big(\lambda_{2,3} + |c|^2(\delta_1 - \epsilon_{0-1})\big)\big[\lambda_{2,3}\beta_{1-1} - |b|^2\delta_3\big] \\ &\quad + \big(\lambda_{2,3}\beta_{10} - |c|^2\delta_2\big)\big[|b|^2\delta_1 - \lambda_{2,3}\big]\Bigg] \end{aligned} \tag{3.89}$$

$$\begin{aligned} v_2 = \Big(\frac{b}{c}\Big)&\left[\frac{1}{(\lambda_{2,3} - |b|^2\delta_1)^3}\right] \\ &\times \Bigg[(\lambda_{2,3} - |b|^2\delta_1)(\lambda_{2,3}\beta_{1-1} - |b|^2\delta_3)(\lambda_{2,3}\beta_{10} - |c|^2\delta_2) \\ &- (\lambda_{2,3} - |b|^2\delta_1)^2(\lambda_{2,3}\eta^*_{10} - |c|^2\delta_4) \\ &- \Big[(\lambda_{2,3} - |c|^2(\delta_1 - \epsilon_{0-1}))\big[(\lambda_{2,3}\beta_{1-1} - |b|^2\delta_3)^2 \\ &\quad - (\lambda_{2,3} - |b|^2\delta_1)(|b|^2\delta_5 + \lambda_{2,3}\eta^*_{1-1})\big]\Big]\Bigg] \end{aligned} \tag{3.90}$$

and

$$u_0 = \Big(\frac{-1}{ca^*}\Big)\Big[|c|^2 + v_0 cb^*\Big] \tag{3.91}$$

$$u_1 = \Big(\frac{-1}{ca^*}\Big)\Big[|c|^2\beta_{1-1} + cb^*\big(v_1 + v_0(\beta_{1-1} - \beta_{0-1})\big)\Big] \tag{3.92}$$

$$\begin{aligned} u_2 = \Big(\frac{1}{ca^*}\Big)&\Bigg[\lambda_{2,3} + |c|^2(\eta_{1-1} - \epsilon_{1-1}) \\ &\quad - cb^*\big[v_2 + v_1(\beta_{0-1} - \beta_{1-1}) \\ &\qquad + v_0(\beta_{0-1}\beta_{1-1} + \epsilon_{1-1} - \eta_{1-1} - \eta^*_{0-1})\big]\Bigg] \end{aligned} \tag{3.93}$$

with the additional mixing parameters:

$$\delta_2 = \beta_{1-1}\eta_{0-1} - \beta_{0-1}\eta_{1-1} + \nu_{0-1} + \nu^*_{10} - \nu^*_{1-1} \tag{3.94}$$

$$\delta_3 = \beta_{10}\eta^*_{0-1} - \beta_{0-1}\eta^*_{10} - \nu^*_{0-1} - \nu^*_{10} + \nu^*_{1-1} \tag{3.95}$$

$$\delta_4 = \beta_{1-1}\nu_{0-1} - \beta_{0-1}\nu^*_{1-1} + \eta_{0-1}\eta^*_{1-1} + \kappa_{0-1} - \kappa^*_{10} + \kappa^*_{1-1} \tag{3.96}$$

$$\delta_5 = \beta_{10}\nu^*_{0-1} + \beta_{0-1}\nu^*_{10} - \eta^*_{0-1}\eta^*_{10} - \kappa^*_{0-1} - \kappa^*_{10} + \kappa^*_{1-1} \tag{3.97}$$

where for $|\psi_2\rangle$ one chooses λ_2 defined in Eqn. 3.64, with a similar convention for $|\psi_3\rangle$.

These solutions for the eigenstates exhibit the increased complexity present in the three dimensional case. The numerical factors in Eqns. 3.75 - 3.80 and Eqns. 3.88 - 3.93 showcase a complicated interplay between the environmental factors β_{ij}, η_{ij}, ϵ_{ij}, ν_{ij}, and κ_{ij} for the three different states. The time dependence of the top eigenstate, $|\psi_1\rangle$, is reminiscent of the two state solutions in that the leading order real time dependence is quadratic with a linear complex phase. However, note that for general H^1_e, H^0_e, and H^{-1}_e the leading order real time dependence for $|\psi_2\rangle$ and $|\psi_3\rangle$ is actually linear if one considers Eqns. 3.82 - 3.84. However, this linear time dependence will disappear if all the environmental factors β_{ij}, η_{ij}, ϵ_{ij}, and ν_{ij} are purely real, due to the vanishing of Eqn. 3.86 in that limit.

In the case where the linear time dependence is present, one can think of it this way: All aspects of the way in which the initial state is being diminished are occurring at a quadratic rate (to leading order). But in the qutrit case, the probability is flowing from the initial state into a two dimensional subspace orthogonal to the initial state. Under certain conditions it is possible for the description of the system in this orthogonal subspace to move around with a linear time dependence, even as the profile of the evolution of the initial state remains quadratic.

In this paper we took a phenomenon observed in the ACL model and provided a systematic analysis in the simpler case of the single qubit system, and in this Appendix we've extended the analysis to the qutrit. We now circle back to the more complicated

ACL case. Figure 3.5 shows results from calculations similar to the ACL calculations shown in Fig. 3.1, but with an initial state comprised of three wavepackets. The broad features of the copycat process are also present in this more complicated case [5] [6].

In our numerical explorations of different models we always found the second largest eigenvalue of ρ_s evolved as t^2 at early times, and the smaller eigenvalues evolved as an even power of t greater than or equal to two. This faster than linear evolution of the eigenvalues, in comparison with the slower evolution of the eigenstates, is an essential part of the copycat process. To achieve the t^2 behavior for the third eigenvalue shown by dashed curve in Fig. 3.5 (which matches our qutrit analysis) we used the ACL model with the interaction term modified to give

$$\begin{aligned} H_w = H^s_{SHO} \otimes 1^e \\ + \left(\sum_{i=1}^{10} |q_i\rangle \, q_i \, \langle q_i| \right) \otimes H^e_A \\ + \left(\sum_{i=11}^{20} |q_i\rangle \, q_i \, \langle q_i| \right) \otimes H^e_B \\ + \left(\sum_{i=21}^{30} |q_i\rangle \, q_i \, \langle q_i| \right) \otimes H^e_C + H^e \otimes 1^s, \end{aligned} \tag{3.98}$$

where H^e_A, H^e_B and H^e_C are each independently generated random hermitian matrices and the three sums divide the eigenstates of q (defined in the 30-dimensional system subspace) into three equal ranges. Note that Eqn. 3.98 is a more direct generalization of Eqn. 3.55 (used for the qutrit) than the original ACL Hamiltonian (Eqn. 3.5).

[5] Figure 3.5 shows a more narrow time range than Fig 3.1 because we had to wait until $t \approx 10^{-3}$ for the third eigenvalue to resolve numerically, and the limited overall size of the system Hilbert space forced us to place the three packets too close together to einselect cleanly. The latter restriction is irrelevant to the points we make here which are about early time behavior.

[6] In principle one could compare the forms of the eigenstates in Fig. 3.5 with the analytical results for the qutrit—as well as derive the qutrit versions of other quantities discussed in Secs. 3.4 and 3.5—but we did not feel such an involved analysis would add much of interest to this paper.

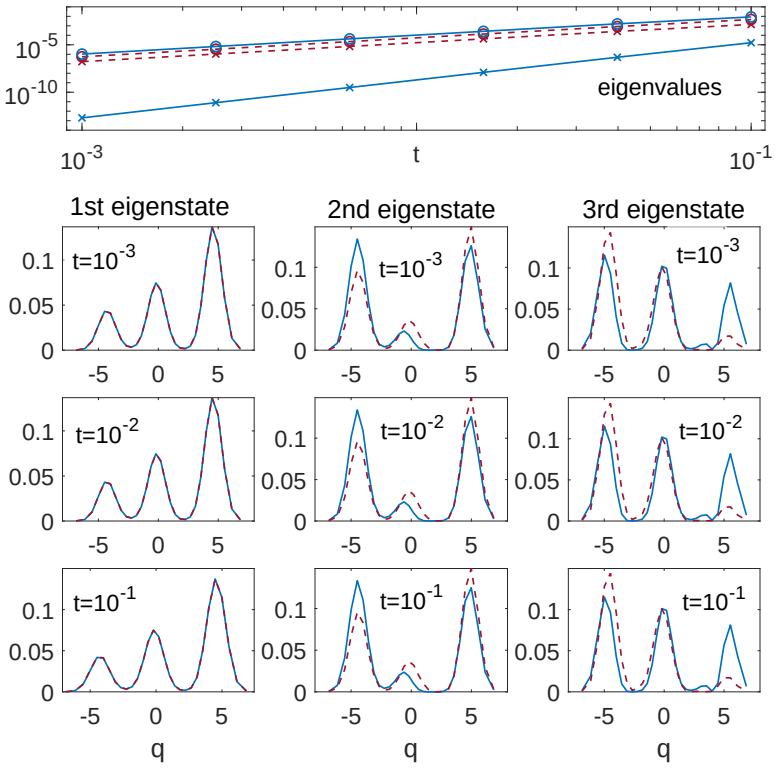

Figure 3.5: The evolution of an initial Schrödinger cat state formed from three wavepackets. Eigenstates and the 2nd (circle markers) and 3rd ("x" markers) eigenvalues of ρ_s are shown in a similar manner to Fig. 3.1. The Hamiltonians used are given by the original ACL model (Eqn. 3.5, solid curves) and a modified ACL model (Eqn. 3.98, dashed curves). These results allow us to link the qutrit results from this Appendix to the behaviors of more complex systems. The quadratic (or faster) time dependence of the eigenvalues and transient stability of the eigenstates express the main features of the copycat process, even for these generalized cases. Note that the solid and dashed curves for the first eigenstate overlap completely.

Chapter 4

Einselection, Equilibrium, and Cosmology

The material in this chapter previously appeared in ***Einselection, Equilibrium, and Cosmology*** *by Andreas Albrecht, Rose Baunach, and Andrew Arrasmith [3].*

ABSTRACT: Our observed Universe has a very strong arrow of time rooted in its low entropy starting point. This low entropy start can be related to various "tuning puzzles" about the early state of the Universe. Here we explore the relationship between the arrow of time and the emergence of classical from quantum in the hopes of ultimately gaining insights into cosmological initial conditions. Our focus is on einselection, the process whereby interactions with an environment select preferred states for a quantum system. This process plays an essential role in the emergence of classical from quantum. Studies of einselection have so far been limited to cases that exhibit an arrow of time. Here we study the ability of equilibrium systems to exhibit einselection—and investigate whether detailed balance prevents this—motivated by the question of whether classicality requires an arrow of time. We present calculations in the adapted Caldeira-Leggett model which demonstrate that einselection can indeed take place in equilibrium systems, and show how this phenomenon is tied to histories which express an arrow of time, despite the global equilibrium. We discuss some interesting implications of our results for cosmology and cosmological initial conditions. We are intrigued and a bit surprised by the role the

consistent histories formalism has ended up playing in our analysis.

4.1 Introduction

A quantum system coupled to an environment will generically exhibit entanglement between the system and environment. The onset of such entanglement is called decoherence. The process of decoherence will cause un-entangled initial states (products in the system-environment partition) to evolve into entangled states, where the system and environment are each described by density matrices (even in the case where the global evolution is unitary and the total state remains pure). Under certain conditions, which are very common in nature, the density matrix that emerges for the system has eigenstates drawn from a preferred stable set called "pointer states". The process whereby special pointer states are dynamically selected by decoherence is called "einselection." This process plays an essential role in the emergence of classical behavior in quantum systems, for example by rapidly turning "Schrödinger cat" superpositions into classical mixtures.

So far einselection has only been studied in the literature (or for that matter in nature) under conditions which exhibit an arrow of time (expressed by the increase of entanglement entropy between the system and environment, for example). This invites the question whether an arrow of time is required for classical behavior to emerge.

To examine this question further, consider a quantum system in equilibrium, which does not exhibit a global arrow of time by definition. If one considers the detailed balance exhibited by equilibrium systems, it would seem that both entangling and the time reverse (disentangling) would be happening simultaneously, preventing a clear path to einselection from emerging. If such a result was confirmed, it might imply the necessity of an arrow of time to obtain classical behavior. That implication would have interesting consequences for cosmology and various "tuning puzzles," since the arrow of time we experience originates from the low entropy initial conditions of the Universe. (Linking the low entropy of the early Universe to special properties of the metric was pioneered by Penrose in the context of his Weyl curvature hypothesis [61].)

In this work we have indeed found a link between the emergence of classicality and

the arrow of time, although it is not the simple one we anticipated. Our studies uphold the connection between the arrow of time and einselection, but rather than eliminating the possibility of classical behavior under equilibrium conditions, our explorations of einselection have helped us identify consistent histories which exhibit an arrow of time within the overall equilibrium state.

Note that it is often routine for physicists to think of equilibrium systems as part of a larger picture (a laboratory for example) in which there is a robust arrow of time. In such situations one can consider processes such as measurements of the system, decoherence etc. which all rely on this arrow of time to operate. In our Universe the origin of this "laboratory" arrow of time is cosmological, and it is ultimately the cosmological arrow of time we wish to study here, without any a priori assumption about an external environment with an arrow of time. This motivates our use of the consistent histories formalism, as we discuss below.

Our primary tool in this work is the adapted Caldeira-Leggett (ACL) model, which we developed in [1] specifically to allow calculations which do not assume an arrow of time from the outset. This is an important difference from the standard master equation treatments associated with studies of einselection. As with the original Caldeira-Leggett model, the ACL model describes a simple harmonic oscillator (SHO) coupled to an environment. We evolve the complete SHO-environment "world" fully unitarily, using the highly accurate numerical methods reported in [1]. Our techniques allow us to probe all aspects of the behavior of this model. Reference [1] can also serve as an introduction to the ideas of einselection in the context of the ACL model. A more general review can be found in [26]. Both of these resources provide extensive references to the original literature.

We note that the notion of equilibrium plays something of a dual role in our discussions. Its main role is as a good example of a physical state which does not exhibit an arrow of time. In this role it is something of a "straw man" which allows us to explore the nature of einselection under conditions not previously studied, and examine the role of time's arrow. Certainly an equilibrium state is not the only state that can play such a role, and

we explicitly expand our discussion to other cases in Appendix 4.B. Separately, one can be curious about the possibility that the universe is globally in a state of equilibrium, and our observed Universe is some sort of fluctuation. An equilibrium state is certainly expected to be the long-term condition for any finite system (no matter how large), and perhaps other systems as well. So studies of equilibrium in our toy model might be relevant for assessing such cosmological scenarios. We will explore these angles later in the paper (where we also acknowledge the range of challenges faced by equilibrium cosmological models).

Quantum physics is a topic which can generate fraught discussions about interpretation. Most actual calculations are disconnected from those discussions, following standard conventions that produce uncontroversial mathematical results which in most cases are straightforward to connect with data. Consideration of cosmological questions, in which there is no external observer, can sometimes require a more concrete stand on interpretation. In this paper we ultimately work with the consistent histories formalism, which allows analysis of quantum systems without reference to an external observer (see [62] for some recent reflections on these issues).

The consistent histories (CH) formalism has the well-known feature that there are generally many alternate sets of histories available for interpreting the same quantum system. While the formalism is able to assign relative probabilities to histories *within* a given set, it is agnostic about how one is to make choices among the different sets. This feature has spawned diverse responses. Some are content to accept this ambiguity as part of the nature of quantum physics, while others seek to add requirements beyond the CH formalism to pare down the possibilities. Still others feel this feature is grounds for skepticism about the entire CH formalism. We are intrigued by how this intrinsic ambiguity in the CH formalism enables an understanding of the way an equilibrium system can exhibit both detailed balance *and* einselection (along with the associated arrow of time).

This paper reports substantial technical work using the ACL model. The reader who is mainly interested in the conclusions we draw for cosmology may wish to start by reading

Sect. 4.7. The full structure of this paper is as follows: In the next two sections we give a fairly conventional treatment, which will work as a precursor to using the CH formalism. In Sect. 4.2 we introduce the basics of the ACL model and explain how we construct the equilibrium state we use throughout the rest of the paper. In Sect. 4.3 we explore einselection in our equilibrium system using standard tools based on correlation functions. We conclude Sect. 4.3 by noting how the standard tools implicitly assume an external environment with an arrow of time. That motivates the extension of our results to a full treatment with the CH formalism which we undertake in Sect. 4.4. This expands our understanding of the nature of the einselection and allows us to more fully examine the role of the equilibrium assumption. The CH formalism also allows us to take a closer look at the relationship between einselection and the arrow of time in our calculations. This we do in Sect. 4.5, where we find that the histories we use to study einselection come with a built-in arrow of time. We interpret this arrow in terms of fluctuations of the equilibrium system, and also study its relationship to the well-known feature that the consistent histories formalism usually describes multiple sets of consistent histories which coexist as alternate and disconnected descriptions of the same system. Section 4.5 is where our concrete technical conclusions for the ACL model are presented.

To facilitate the application of our results to initial conditions for cosmology, in Sect. 4.6 we offer some general observations about the role of initial conditions in the CH formalism. Finally, in Sect. 4.7 we relate the insights that have emerged from this work to cosmological questions, especially as they pertain to cosmological initial conditions. We give some additional attention to the de Sitter Equilibrium cosmological models, but most of our reflections are of a more general nature. We have tried to make Sect. 4.7 a self-contained account of our insights and main conceptual points. We outline our main conclusions in Sect. 4.8. Due to disagreements among experts even about what makes a good theory of initial conditions (which we review in Sect. 4.7.1), our discussions of the implications of our work for cosmology are necessarily more open ended than the concrete technical discussions of the ACL results.

Appendix 4.A examines the robustness of our model and our definition of equilibrium.

Appendix 4.B extends our results to the case where we put the global system in an eigenstate of the total Hamiltonian, suggesting an "Eigenstate Einselection Hypothesis" akin to the well-known "Eigenstate Thermalization Hypothesis."

4.2 The ACL model and equilibrium

The ACL model describes a system coupled to an environment. The ACL Hamiltonian is given by

$$H_w = H_s \otimes \mathbf{1}^e + q_s \otimes H_e^I + \mathbf{1}^s \otimes H_e \tag{4.1}$$

where s and e refer to the system and environment. The system is a SHO, truncated in a particular way to enable stable numerical computation. The second term in Eqn. 4.1 is the interaction term, where q_s is the position operator of the SHO and

$$H_e^I = E_I R_I^e + E_I^0. \tag{4.2}$$

The self Hamiltonian of the environment is given by

$$H_e = E_e R^e + E_e^0. \tag{4.3}$$

The matrices R^e and R_I^e are independently constructed random Hermitian matrices which are held constant throughout a given calculation[1]. In [1] we provide full details of the ACL model, demonstrate its ability to reproduce standard results from the decoherence and einselection literature, and also demonstrate the ability of the ACL model to evolve into an equilibrium state.

Figure 4.1 shows the evolution of the von Neumann entropy and system and environment energies for a product initial state. Initially the entropy grows and energy flows between s and e, but later equilibration occurs: After $t \approx 10^3$ there is no net flow of energy and the entropy holds steady, up to small fluctuations. The equilibrium state used throughout this paper is arrived at by tracking this evolution and taking a snapshot of

[1]Each independent matrix element is drawn uniformly from the interval $[-0.5, 0.5]$. We have checked that (basically due to the central limit theorem) this is equivalent to drawing the random numbers from a normal distribution for the values of N_e we consider.

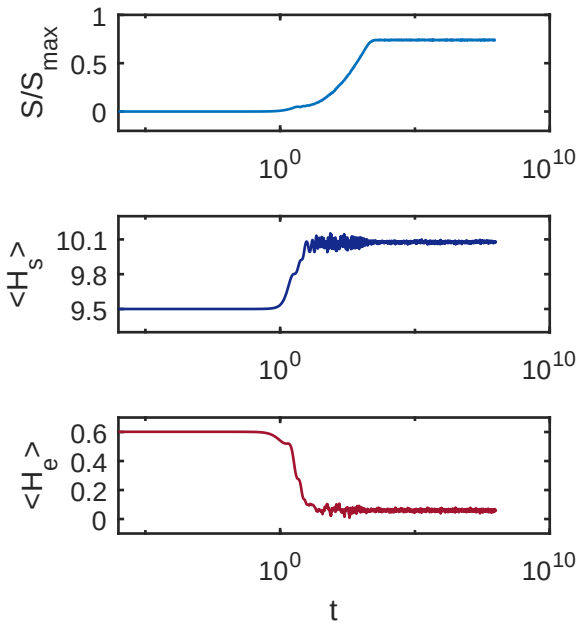

Figure 4.1: Entropy (top panel), SHO energy (middle) and environment energy (bottom). By $t = 3 \times 10^6$ these curves have stabilized, supporting the case that the global state at this time represents an equilibrium state. We use this state in our subsequent calculations.

the state of the entire system at $t = 3 \times 10^6$, well into the equilibrium phase. We write this equilibrium state (in the full $w = s \otimes e$ space) as $|\mathcal{E}\rangle$.[2]

For Fig. 4.1 we use $E_I^e = 0.01$, $E_e = 0.05$, $E_I^0 = E_I^e$ and $E_e^0 = E^e$. The initial state is a product of the $\alpha = 3$ coherent state for s, and the $i = 500$ eigenstate of H_e for e. The subsystem dimensions are $n_s = 30$ and $n_e = 600$. Information about how we approximate an SHO in a finite space, the accuracy of our numerical computations and details of how these states are constructed can be found in [1]. Also, in Appendix 4.A we further scrutinize the notion of equilibrium we use here.

[2]The energy curves in Fig. 4.1 show a noisy period as equilibrium fully sets in which gives the appearance, if closely scrutinized, that energy might not be completely conserved. This is an artifact of the energy in the interaction term of H_w not being shown. Our techniques ensure that the full energy of w is conserved to machine precision [1].

4.3 Einselection

Einselection is related to the robustness of the system states under interaction with the environment. Several standard approaches were used in [1] to study einselection. Here we utilize a scheme related to the "predictability sieve" approach (a scheme developed by Zurek and collaborators [43, 25] and applied in [1], where we give more extensive reference). We pose the conditional probability question, "if the SHO is found in state $|\psi(t_0)\rangle_s$ at t_0, what is the probability of finding the system in $|\psi(t_1)\rangle_s$ at t_1?" where

$$|\psi(t_1)\rangle_s = \exp(-i(t_1 - t_0)H_s/\hbar)|\psi(t_0)\rangle_s. \tag{4.4}$$

To address this question we use the projection operators

$$P_0 \equiv |\psi(t_0)\rangle_{ss} \langle\psi(t_0)| \otimes \mathbf{1}_e \tag{4.5}$$

and

$$P_1 \equiv |\psi(t_1)\rangle_{ss} \langle\psi(t_1)| \otimes \mathbf{1}_e \tag{4.6}$$

and construct

$$\left|\widetilde{1,0}\right\rangle \equiv P_1 T(t_1 - t_0) P_0 |\mathcal{E}\rangle \times (\langle\mathcal{E}| P_0 |\mathcal{E}\rangle)^{-1/2} \tag{4.7}$$

where $|\mathcal{E}\rangle$ is the equilibrium state in the full $w = s \otimes e$ space and

$$T(\Delta t) \equiv \exp(-iH_w \Delta t/\hbar). \tag{4.8}$$

With these definitions,

$$p_{10}(\Delta t) \equiv \left\langle \widetilde{1,0} \mid \widetilde{1,0} \right\rangle \tag{4.9}$$

is the quantity which answers the conditional probability question posed. (Note the appearance of a normalization factor in Eqn. 4.7 which produces the standard normalization used when constructing conditional probabilities.)

Figure 4.2 shows p_{10} for $|\psi(t_0)\rangle_s$ chosen to be either a coherent state (with $\alpha = 3$), an eigenstate of q_s (situated at a location similar to the position of the $\alpha = 3$ coherent state) or the $n = 7$ eigenstate of H_s (which has a similar energy to the other states used here). One can see that for a period of time one is certain to find the SHO in the state time

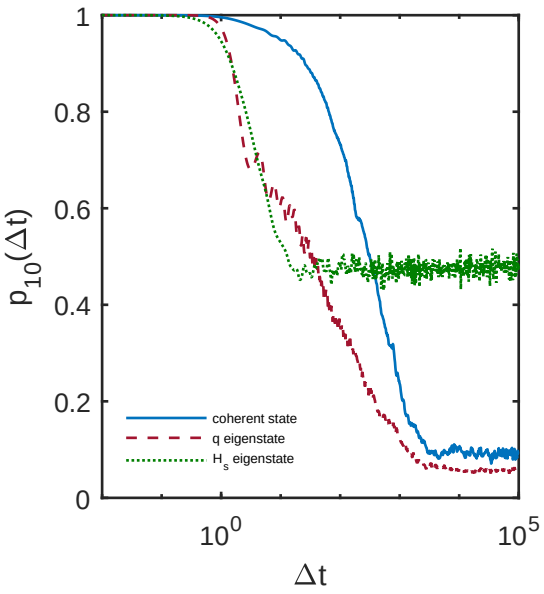

Figure 4.2: These three curves (defined in Eqn. 4.9) indicate the stability of specific SHO states against interaction with the environment. The coherent state (solid curve) remains stable longer than the position eigenstate (dashed) or the energy eigenstate (dotted), indicating that the coherent state is einselected over the others. (The SHO period is 2π in these units.)

evolved from its initial state by H_s. This is the period during which p_{10} stays at unity. Eventually the interactions take their toll, and the state of the SHO has less and less overlap with the state it would have had if it were decoupled from the environment. This phase is manifested by decreasing values of p_{10}. The fact that p_{10} remains close to unity for much longer in the coherent state case shows that the coherent states are more stable against decoherence with the environment[3]. This is a situation often found in nature, which we realize in the ACL model by appropriate choices for the various parameters. (In [1] we show how different parameter choices in the ACL model can lead to different pointer states being einselected, but here we stay in the limit where the coherent states are the pointer states.)

[3]The fact that for the H_s eigenstate case p_{10} levels off at around 0.5 suggests that at late times our system may be approaching the quantum limit, as discussed in Appendix A of [1].

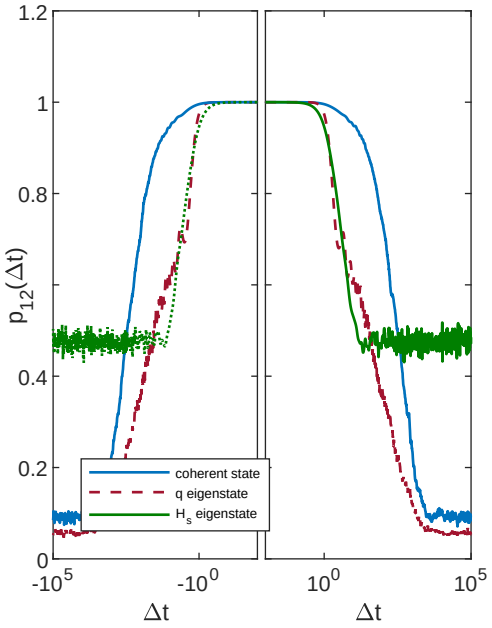

Figure 4.3: Figure 4.2 is shown in the right panel, with the same quantities evaluated for negative values of Δt in the left panel. Taken together, these curves reflect the specific states cohering out of equilibrium, becoming fully cohered at $\Delta t = 0$, and then decohering back as Δt takes increasing positive values. The approximate time symmetry that appears here is expected given that the primary condition is placed at $\Delta t = 0$. These results will contribute to our more thorough discussion of the arrow of time in Sect. 4.5.

One can also evaluate p_{10} for negative values of Δt. This corresponds to probing the SHO state at times prior to t_0, where the P_0 condition is imposed. Figure 4.3 shows p_{10} for both negative and positive values of Δt. The results appear to show the chosen SHO state "cohering" out of equilibrium into the chosen state at $\Delta t = 0$ and then decohering back toward equilibrium[4]. We will come back to this picture when studying the system from the point of view of consistent histories.

Naively, it would appear that we have demonstrated that einselection can indeed happen in equilibrium systems, thus answering in the affirmative a question which motivated

[4]Generally, the phenomena which degrade the correlations include both decoherence and dissipation. In everyday macroscopic systems decoherence operates on a much faster timescale and is the focus of discussions of stability and einselection. We've shown in [1] that both phenomena are present in the ACL model, although the timescales are much closer together (as one might expect in a finite toy model).

this paper. However, the formalism we developed in this section requires more scrutiny. A standard interpretation would say that the projection operators we use here would describe measurements of the SHO by some apparatus external to both s and e. Such a measurement could be expected to throw the whole thing out of equilibrium, so it is not clear if we have really addressed the original question.

Specifically, after operating with P_0, one is left with a product state with zero entanglement entropy between the system and environment. The only aspect that reflects the fact that we started with the equilibrium state $|\mathcal{E}\rangle$ is the specific environment state which multiplies the system state $|\psi(t_0)\rangle_s$ (determined by P_0). The subsequent evolution is that of an initial product state such as shown in Fig. 4.1 and studied extensively in [1]. Motivated by these considerations, we now turn to the consistent histories formalism which allows an analysis which looks less like an external disruption of our equilibrium system. We will see how this formalism introduces some new considerations to our assessment of einselection.

4.4 Consistent Histories

The consistent histories (CH) formalism is a tool for identifying classical behavior in a closed quantum system without reference to an outside observer. It was proposed in 1984 [63], and since then a substantial literature has emerged (see for example [64, 32, 65, 66, 67, 68, 69, 70, 71, 72, 73, 74] and for a recent review see [75]). We use the formalism here in a very similar manner to the way it is used in [32]. The next subsection sets up our techniques in a way that might serve as a very brief introduction to the CH formalism, at least in the form we use here. The subsequent *Results* subsection presents results which address the topics of interest in this paper using the CH formalism. This subsection also offers intuitive interpretations of the CH quantities, which may be all some readers need to know about the CH formalism. Such readers might try skipping straight to Sect. 4.4.2.

4.4.1 Formalism

The CH formalism expresses the full time evolution of a quantum system in terms of histories formed using complete sets of projection operators. We start our discussion by

using P_0 and P_1 from Eqns. 4.5 and 4.6 to define the complementary projectors

$$\begin{aligned} P_{\not 0} &\equiv \mathbf{1} - P_0 \\ P_{\not 1} &\equiv \mathbf{1} - P_1. \end{aligned} \tag{4.10}$$

We consider the time evolution given by

$$|\psi(t_1)\rangle = T(t_1 - t_0)\,|\psi(t_0)\rangle \tag{4.11}$$

$$= \mathbf{1}T(t_1 - t_0)\,\mathbf{1}\,|\psi(t_0)\rangle\,. \tag{4.12}$$

with T defined in Eqn. 4.8. (Here the states and operators are in the full $w = s \otimes e$ space.) Since $P_1 + P_{\not 1} = P_0 + P_{\not 0} = \mathbf{1}$ (thus forming "complete sets"), one can continue by writing

$$\begin{aligned} |\psi(t_1)\rangle &= \left(P_1 + P_{\not 1}\right) T(t_1 - t_0) \\ &\times \left(P_0 + P_{\not 0}\right) |\psi(t_0)\rangle \qquad (4.13) \\ &= P_1 T(t_1 - t_0)\, P_0\, |\psi(t_0)\rangle \\ &+ P_1 T(t_1 - t_0)\, P_{\not 0}\, |\psi(t_0)\rangle \\ &+ P_{\not 1} T(t_1 - t_0)\, P_0\, |\psi(t_0)\rangle \\ &+ P_{\not 1} T(t_1 - t_0)\, P_{\not 0}\, |\psi(t_0)\rangle \qquad (4.14) \\ &\equiv |1,0\rangle + |1,\not 0\rangle + |\not 1, 0\rangle + |\not 1, \not 0\rangle \qquad (4.15) \end{aligned}$$

where the quantities in Eqn. 4.15 are defined by

$$|i,j\rangle \equiv P_i T(t_1 - t_0)\, P_j\, |\psi(t_0)\rangle\,. \tag{4.16}$$

Note that Eqns. 4.7 and 4.16 are related by

$$\left|\widetilde{i,j}\right\rangle = |i,j\rangle \left(\langle\psi(t_0)|\, P_0\, |\psi(t_0)\rangle\right)^{-1/2}, \tag{4.17}$$

meaning that these two quantities just differ by a normalization.

Equation 4.15 amounts to organizing the time evolution in terms of paths or histories, where each term in Eqn. 4.15 represents a different history determined by which projections are chosen at each of the two times[5]. In general the consistent histories formalism

[5]This construction has the look of a derivation of the path integral, but in the consistent histories formalism there is generally no expectation that the usual continuum limits need be taken.

can accommodate any number of times where complete sets of projection operators are inserted, as well as more finely grained sets of projections themselves. Here we stick to using only two projection times (t_0 and t_1), and a very simple choice of projectors (P_1, P_0 and their compliments). These will suffice to explore the physical questions of interest while keeping our formalism and computations as simple as possible.

Next we define the "Decoherence functional"

$$D_{ij,kl} \equiv \langle i, j \mid k, l \rangle \tag{4.18}$$

(with $|i, j\rangle$ defined in Eqn. 4.16)[6]. The CH formalism seeks to use the diagonal elements of D to assign the probability

$$p_{ij}^{CH} = D_{ij,ij} \tag{4.19}$$

to the ij path. The paths are considered consistent if the p_{ij}^{CH} obey the sum rules expected of classical probabilities. For example, one could define a coarse grained history (labeled by $1\circ$) where no projections are inserted at t_1, and classically one would expect

$${}^{c}p_{1\circ}^{CH} = p_{10}^{CH} + p_{1\backslash 0}^{CH}. \tag{4.20}$$

However, in general off diagonal elements of D come in giving

$${}^{q}p_{1\circ}^{CH} = {}^{c}p_{1\circ}^{CH} + D_{10,1\backslash 0} + D_{1\backslash 0,10}. \tag{4.21}$$

We say we have identified good sets of consistent histories when the off diagonal contributions in Eqn. 4.21 (which describe quantum interference effects) are sufficiently small, so that the classical expression (Eqn. 4.20) is obeyed to the desired tolerance[7].

Figure 4.4 illustrates the full set of paths considered here, along with the path labels and corresponding projection operators. In a more general CH formalism, with many projection times and many components to the complete sets of projectors, there are

[6]Technically our D is a *function* of discrete variables, not a function*al*, but we stick to the standard usage to avoid generating arcane nomenclature.

[7]We note that, in addition to its use in the CH formalism, Eqn. 4.20 shows up in other contexts as a metric of classicality. For example, Eqn. 4.20 corresponds to a form of the Kolmogorov consistency condition, and there is a body of work investigating deviations from Eqn. 4.20 in quantum systems and their implications for classicality within a projective measurement framework (e.g. [76, 77, 78]).

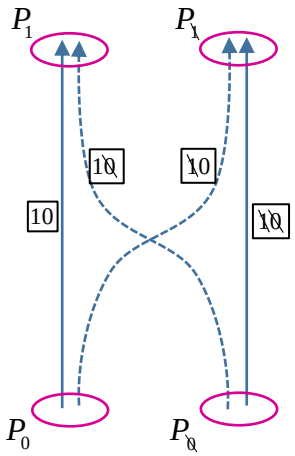

Figure 4.4: A schematic illustrating the four paths constructed in Sect. 4.4.1. The projection operators correspond to circles and the path labels are marked in boxes. In Sect. 4.4.2 we focus mainly on the two paths which end at P_1 (Fig. 4.5). One path (10, solid) arrives from P_0 (giving the simple behavior of a decoupled SHO), the other ($1\bar{0}$, dashed) arrives from $P_{\bar{0}}$. (The $1\bar{0}$ path would be impossible without interactions with the environment.)

a multitude of sum rules that can be checked. For our purposes the relatively simple framework set up here suffices.

The formalism described here is perfectly well formulated for either $t_1 > t_0$ or $t_1 < t_0$. The subscript refers to the order in which the projections appear in Eqn. 4.14, but $T(t_1 - t_0)$ is well defined for both positive and negative arguments. Thus the arrows in Fig. 4.4 really refer to the order of the projections, and one can consider cases where time flows from top to bottom in this diagram. One can think of the projection at t_0 giving initial conditions for the path when $t_1 > t_0$ and as giving final conditions when $t_1 < t_0$[8]. This aspect will be important to the discussion in Sect. 4.5.

4.4.2 Results

Here we revisit the physical question posed in Sect. 4.3—does einselection happen in equilibrium—this time using the CH formalism. We condition on the case where the SHO is found in state $|\psi(t_0)\rangle_s$ at t_0, and compute the probability of finding it in the corresponding evolved state $|\psi(t_1)\rangle_s$ at t_1. While the framework of Sect. 4.3 implies the

[8]Use of final conditions in the CH formalism has been discussed for example in [64, 67].

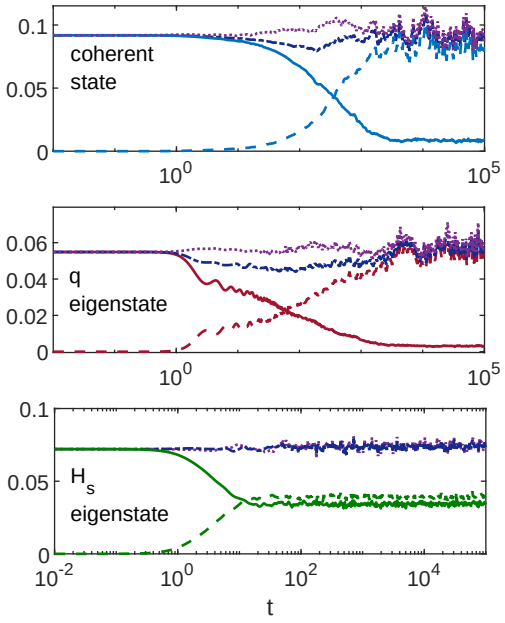

Figure 4.5: A CH treatment of different initial system states as they interact with the environment. The solid curves are $p_{10}^{CH}(t)$ (which are none other than the correlation functions shown in Fig. 4.2). The dashed curves are the same quantity for the alternate $1\bar{0}$ path. The two top curves give ${}^{c}p_{1\circ}^{CH}(t)$ and ${}^{q}p_{1\circ}^{CH}(t)$. The extent to which the top two curves are different from one another signals quantum interference effects between the 10 and $1\bar{0}$ paths which undermine attempts to assign classical probabilities. As discussed in the text, the interference effects do not change our conclusions about einselection for these cases. (A pictorial representation of the paths considered is shown in Fig. 4.4.)

measurement of the SHO by an external apparatus, the CH formalism uses projectors to identify paths. The solid curves in each panel of Fig. 4.5 are called p_{10}^{CH} in the CH formalism, but they are none other than the $p(\Delta t)$ curves shown in Fig. 4.2, rescaled according to Eqn. 4.17. Crucially, the CH formalism requires us to consider additional quantities in order to interpret these curves. The dashed curve in each panel shows the probability that the SHO was *not* in $|\psi(t_0)\rangle_s$ at t_0, but is none the less found in $|\psi(t_1)\rangle_s$ at t_1. This is the quantity called $p_{1\bar{0}}^{CH}$ in Sect. 4.4.1. The presence of this alternate pathway to $|\psi(t_1)\rangle_s$ is part of what makes the CH formalism different from our treatment in Sec. 4.3. Figure 4.4 illustrates the full set of paths considered here, along with the path labels and corresponding projection operators (Fig. 4.5 only shows information about the two paths

which arrive in the upper left of Fig. 4.4).

The dot-dashed curve in each panel of Fig. 4.5 is just the sum of the solid and dashed curves (${}^{c}p^{CH}_{1\circ}$ from Eqn. 4.20 giving the expected total classical probability), and the dotted curve shows ${}^{q}p^{CH}_{1\circ}$ from Eqn. 4.21, which includes quantum interference effects. The degree to which the dot-dashed curves (classical) and the dotted curves (quantum) differ indicates the breakdown of the classical rules for probabilities.

In Sect. 4.3 we examined the (rescaled) solid curves from Fig. 4.5 which we presented in Fig. 4.2. We used the deviation from constant behavior as a signal of instability under interaction with the environment. The fact that the coherent state case stayed constant for longer than the other cases led us to conclude that the coherent states were more stable under interactions with the environment, and thus were einselected by these interactions. Since these same curves appear in the CH discussion, it seems we would draw the identical conclusions using the identical information.

The new feature that is added by the CH formalism is the chance to check for interference effects among different paths, which can undermine the assignment of classical probabilities to the paths. This sort of breakdown is a physically different way the interactions with the environment can erode classical behavior, and this erosion is signalled by deviations between the dotted and dot-dashed curves in Fig. 4.5. Since the deviations between these two curves appear (to the extent that they occur) around the same time as the solid curves start to deviate from constant values, we can argue that the emergence of interference effects does not change our conclusions about einselection for these particular calculations. (In Appendix 4.B we present examples where interference effects do change our conclusions about einselection.)

To make such an argument more carefully, one would need a measure of how large the interference effects need to be to register a breakdown of classicality. If our tolerance was very tight, we might need to zoom in to the early-time parts of the curves in Fig. 4.5 to check for small deviations, and it is possible that these small deviations would not appear in the same time order across the three panels. If that were the case, our argument about einselection could be undermined. On the other hand, a more lax tolerance of interference

effects could regard all the interference effects shown in Fig. 4.5 as inconsequential. Under those conditions our discussion of einselection would revert completely back to the form it took in Sect. 4.3.

As usual in physics, the choice of which tolerances to use should be grounded in practical considerations related to what we intend to do with the SHO. For example, if the SHO is intended to represent the pendulum of a clock, the accuracy of the clock would dictate the degree of classicality needed for the pendulum. Such considerations lie far outside scope of our little toy model. The value we see in our analysis of the ACL model is that it has given us a sufficiently concrete framework for calculations to compel us to carefully organize our ways of thinking about the relationship between einselection and equilibrium. We now turn to a discussion of how what we have reported so far relates to the arrow of time.

4.5 Arrow of Time

4.5.1 Time's arrow and einselection

The results we have presented so far clearly have an arrow of time. By construction, the p_{10}^{CH}'s (solid curves in Fig. 4.5) correspond to paths in which the SHO and the environment are not entangled at $\Delta t = 0$. The eventual deviations of p_{10}^{CH} from constant behavior correspond to a "branching" as the probability for the "10" path declines, and the probability for arriving at $|\psi(t_1)\rangle_s$ from a state different from $|\psi(t_0)\rangle_s$ (given by $p_{1\not 0}^{CH}$) increases.

As we did with the correlation functions discussed in Sect. 4.3, one can consider the $t_1 < t_0$ case, where P_0 and $P_{\not 0}$ impose *final* conditions. In that case, our formalism explores different histories by which the system can arrive at $|\psi(t_0)\rangle_s$ from the past. Figure 4.6 shows the quantities given in the top panel of Fig. 4.5, along with the same quantities evaluated for negative values of Δt. Here the x-axis has a linear scale, allowing both negative and positive values of Δt to be shown together. In linking these two paths (positive and negative values of Δt) together, one is effectively imposing a "middle condition" at t_0 rather than an initial or final one.

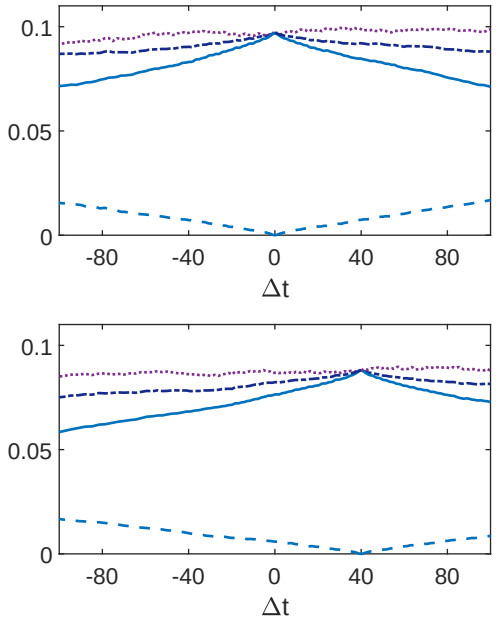

Figure 4.6: Alternate histories: We show the CH quantities from Fig. 4.5 (coherent state case only), but with a linear x-axis and negative values of Δt included. As discussed in the text, each panel shows an alternate CH narrative for the identical quantum state. The different narratives give conflicting accounts of the arrow of time, both of which are equally valid.

The top panel of Fig. 4.6 describes the SHO starting with significant entanglement with the environment at negative Δt values. As Δt approaches zero from below, the entanglement approaches zero, and the 10 and 1$\bar{0}$ paths join together (as $p^{CH}_{1\bar{0}} \to 0$). After reaching zero at $\Delta t = 0$, the entanglement increases again and the two paths branch out[9]. The top panel corresponds to the top panel of Fig. 4.5. For the bottom panel we've used $t_0^{'} = t_0 + 40$ in constructing the projection operators (but still show Δt on the x-axis rather than $\Delta t'$, to make our narrative simpler). What we have done in this case is evolve the equilibrium state to

$$|\mathcal{E}\rangle^{'} = T(40)\,|\mathcal{E}\rangle \tag{4.22}$$

and used $|\mathcal{E}\rangle^{'}$ in the expressions for the CH quantities shown in the lower panel. Thus,

[9]Technically the CH formalism is able to consider branching that is not connected to entanglement with an environment, but such a connection *is* present in the cases we consider here.

the two panels represent different CH narratives for the identical quantum state. In one case the SHO is in a pure state at $\Delta t = 0$, and becomes more entangled as Δt deviates from zero in either direction. In this case, the SHO has become significantly entangled with the environment by $\Delta t = 40$. In the 2nd case, at $\Delta t = 0$ the SHO is in the process of becoming disentangled from the environment, a process which completes at $\Delta t = 40$ and then starts reversing. Each panel represents a double headed arrow of time, but the time at which the arrow changes direction is different in the two cases.

Here we have encountered a well-known feature of the CH formalism, namely that there are typically many different sets of histories that coexist as alternate accounts of classical behavior for a given quantum system [65, 32, 66, 79, 68]. The CH formalism on its own is unable assign a preference to one of these sets over another (or assign relative probabilities between the *sets*, even as it does assign relative probabilities to histories drawn from the same set). As illustrated in Fig. 4.6, this ambiguity shows up in the lack of preference for the point in time when the entropy is at a minimum (and its arrow switches directions).

Figure 4.6 also allows us to revisit the question of detailed balance we raised in the introduction. There we asked whether the detailed balance properties of equilibrium systems mean that entangling and disentangling processes are happening simultaneously, which would suggest there is no clear route to einselection. We see that the CH formalism allows us to interpret an equilibrium state with paths which have separate periods dominated by either entangling or disentangling. On such paths these two processes are *not* happening simultaneously (at least not on an equal basis). Looking at $\Delta t = 20$ in Fig. 4.6, indeed both entanglement and disentanglement are happening "simultaneously" in the sense that both processes are represented. But they are represented on different paths, each of which has a clear direction, and is interpreted as a separate classical description of the behavior of the system. Such paths single out a special time which marks the transition between these two periods, and one might wonder how an equilibrium system can "choose" what time that would be. The answer is that the system does not choose that time, but rather multiple interpretations coexist where the transition between entangling

and disentangling occurs at different times. The multiplicity of the sets of paths (along with the double-headed nature of the arrows) captures the notion of detailed balance, even as the individual paths appear to disregard that notion.

4.5.2 Related considerations

It is standard practice to quantify properties of equilibrium using correlation functions, often time averaged. Indeed this is how we presented earlier versions of this work, for example in [80]. However, the time averaging and other specifics of those analyses seemed to obscure the relationship between our calculations and traditional ideas about einselection. We feel the approach we use here offers greater clarity. For one, we see that equilibrium systems can admit descriptions which *do* exhibit an arrow of time. We find it intriguing that rather than equilibrium conditions preventing the system from exhibiting einselection (as we initially suspected might be the case), exploring the physics of einselection led us to histories which exhibit an arrow of time, even under equilibrium conditions. While our picture might be described as "capturing a transient downward, and then upward, fluctuation of the entropy" in an equilibrium system (certainly a notion commonly associated with a double headed arrow of time), the CH formalism gives a technical account of what such a statement might mean. In particular, it does *not* mean waiting for a recurrence which would bring the full entanglement entropy to a small value. Rather, it means choosing histories which reflect such a fluctuation. Such histories which place the fluctuation at any chosen moment in time are equally available. There is no need to *wait* for any fluctuation, let alone a recurrence.

In fact, it is straightforward to extend the formalism we've developed here so that the entire set of projectors has the form of Eqn. 4.5. To do that, one would replace the projectors $P_{\tilde{i}}$ (defined in Eqn. 4.10) with sets of $N_s - 1$ projectors of the form of Eqn. 4.5 using a set of $|\psi_j(t_0)\rangle_s$, where j labels a set of states which, along with the original $|\psi(t_0)\rangle_s$, form an orthonormal basis for s. Creating histories from such projectors would ensure that *every* path had zero entanglement entropy at t_0, and that the zero entropy time could be chosen arbitrarily using the ideas discussed in Sect. 4.5.1. The overall (large) entanglement between system and environment would be expressed by nonzero

probabilities assigned to many paths, but the entropy on each would be zero at that moment. Generally, the equilibrium nature of the whole system would also show up in the branching behavior we've demonstrated here, which makes the zero entropy feature only a transient property of the paths which emerge and then decohere according to a double-headed arrow of time.

While we are on the topic of alternate sets of histories, we should note that the process of einselection itself has long been regarded as a useful tool for selecting a preferred set among the many possible sets of consistent histories [32, 65, 66]. If the CH projections are made on the pointer states, their robustness leads to greater stability and thus a longer period of classicality. This is a more formal way of stating the importance of einselection, which we sketched in a more heuristic way in the introduction. "Quantum Darwinism" [81, 82, 83, 84] is another idea for selecting preferred sets of histories. While our toy model is far too simple to illustrate this idea directly, we do not expect that quantum Darwinism could select a preferred set among the histories showing fluctuations at different moments in time, such as those shown in Fig. 4.6.

To further complete our discussion, we present Fig. 4.7, which shows the CH quantities for all four paths shown in Fig. 4.4. The additional paths (both of which start with $P_{\bar{1}}$) shown in the lower panel exhibit broadly the same features discussed so far for the paths with start with P_1, and reflect the same phenomena. The main difference is that the probability remains high for the $\bar{1}0$ path, which is not surprising since each of the $P_{\bar{i}}$ projectors cover most of the s Hilbert space, and the whole system is in equilibrium (and thus quite spread out in the Hilbert space). Figure 4.8 provides a zoomed in picture of part of the lower panel of Fig 4.7. This allows us to see that the breakdown of the classical sum rules is happening on similar overall scales for both pairs of paths.

Thus far we have presented a variety of results from our toy model related to einselection and the arrow of time in equilibrium systems. We want to explore the implications of these results for cosmological theories, especially theories of cosmic initial conditions. That is the fundamental motivation for this project. Our first step in this direction is to look more generally at the role of initial conditions in the CH formalism.

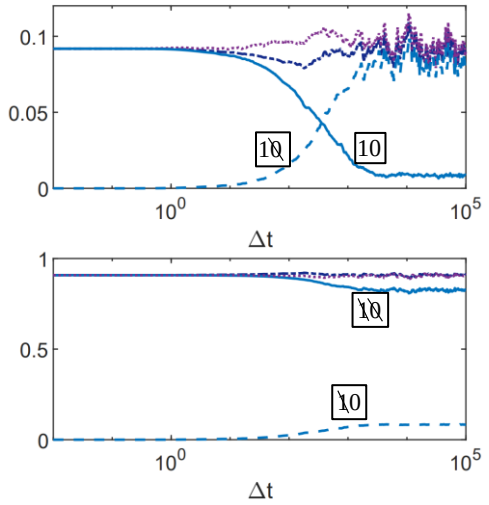

Figure 4.7: The complete set of histories: The top panel is the same as the top panel of Fig. 4.5, and the bottom panel gives the same information for the remaining histories from Fig. 4.4 (labeled as in Fig.4.4).

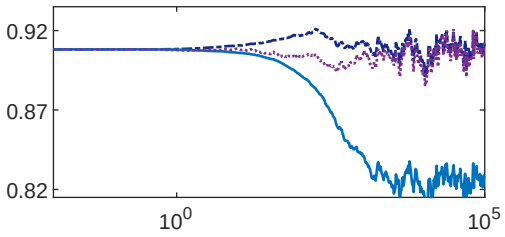

Figure 4.8: Zooming in on the top curves from the lower panel of Fig. 4.7. Here y-axis is on the same scale as the upper panel of Fig 4.7, for easier comparison. One can see that the breakdown of the classical sum rules (indicated by the deviation of the dot-dashed and dotted curves) is of a similar size in both cases.

4.6 The role of initial conditions in the CH formalism

We first approached einselection intuitively using a correlation function approach. We then expanded that discussion using the CH formalism to avoid inadvertently evoking an external observer. We want to apply the insights we have gained about the presence of einselection in equilibrium, and what that implies for a link between an arrow of time and classical behavior, to the question of cosmological initial conditions. To facilitate that focus, we first step back and take a broader look at the role of initial conditions in the CH formalism.

4.6.1 Microstate Histories

We start by looking at a very special case which we call "Microstate Histories" (MH). It is well known that it is always easy to create consistent histories by choosing projection operators which, unlike those we defined above, project onto microstates of the entire Hilbert space w. We write these as

$$P_i^{MH}(t_0) \equiv |\psi_i(t_0)\rangle_{ww}\langle\psi_i(t_0)|. \tag{4.23}$$

Furthermore, in the MH scheme projectors at later times, $P_i^{MH}(t_j)$, are constructed by using

$$|\psi_i(t_j)\rangle_w \equiv T(t_j - t_0)\,|\psi_i(t_o)\rangle_w \tag{4.24}$$

in Eqn. 4.23. One can construct a flawlessly consistent set of histories by letting i run across a complete basis for w. Because T is unitary, the orthonormality of the $|\psi_i(t_0)\rangle_w$ states guarantees that all the off-diagonal elements of the decoherence functional will remain exactly zero in this scheme. For this scheme to work, we needed to select $|\psi_i(t_0)\rangle_w$ as a microstate in the full Hilbert space of w so that the unitarity of T can be exploited. If one uses the MH scheme with initial state $|\mathcal{I}\rangle_w$, the only role for $|\mathcal{I}\rangle_w$ is to assign the probability

$$p_i^{MH} \equiv |{}_w\langle\psi_i(t_0)\,|\mathcal{I}\rangle_w|^2 \tag{4.25}$$

to the history constructed with projectors P_i^{MH}. In the MH scheme there is no guarantee that there would be anything particularly classical about the paths, other than that they

(in a trivial way) could be assigned definite probabilities which obey all the classical sum rules. All the MH scheme does is exploit the fact that $|\mathcal{I}\rangle_w$ can be expanded in a complete basis, and that if one evolves that basis with T, the expansion coefficients will not change over time.

If the w space had an internal structure complex enough to describe observers and observables (certainly more complicated than our simple toy model), observers on the i^{th} MH path would naturally regard $|\psi_i(t_0)\rangle_w$ as their initial state, not $|\mathcal{I}\rangle_w$[10]. If any of these observers were cosmologists, they might debate the relative merits of the global state $|\mathcal{I}\rangle_w$, or perhaps a competing theory $|\mathcal{I}'\rangle_w$, and the different values of p_i^{MH} they provide. But aside from certain cosmological considerations, the state $|\psi_i(t_0)\rangle_w$ is all an observer would need to account for the physics they experience on their particular history.

We have presented the highly idealized MH case to illustrate how in the CH formalism the notion of a global initial state can be quite disconnected from the experiences of observers on a particular history. We will now turn to a less idealized case and note that even there a similar disconnect is possible.

4.6.2 General case

Typically the projectors used in the CH formalism are not formed from microstates of the entire Hilbert space, but focus on subspaces (as we've done with our toy model), or perhaps use other forms of "coarse graining." This allows one to focus on observables or other quantities of interest while ignoring unobservable microscopic degrees of freedom. Generally, such a focus has a key role in identifying classical behavior. As we've illustrated with the calculations in this paper (and unlike the idealized MH case), for such histories quantum interference among the paths becomes a real issue which must be quantified. Only histories with sufficiently low interference effects may be assigned classical probabilities. Still, when the conditions are such that the interference effects are low, then each classical history has a "life of its own," and would naturally identify its initial state with the first projector of that history.

[10]Note that in order to account for the existence of observers and observables one would need to drill down to more fine-grained sets of histories describing these aspects.

Careful scrutiny would reveal that in this more general case the disconnect from the global initial state $|\mathcal{I}\rangle_w$ is not as trivial as in the MH case, but in the end it could appear to take a similar form. As we've discussed in our toy model, a projector of the form given in Eqn. 4.5, which projects only on a system state, creates a product state between system and environment when operating on $|\mathcal{I}\rangle_w$. The environment state which is correlated in this way is determined by $|\mathcal{I}\rangle_w$. Since the state of the environment can contribute to decoherence and other effects on the system (which can impact both the evolution of an individual history as well as interference effects between histories), $|\mathcal{I}\rangle_w$ plays a more detailed role in the behavior of the histories than in the MH scheme. Still, once consistent histories are found it would seem natural for observers on a particular history to identify the state at the start of *their* history as the "state of the Universe," rather than $|\mathcal{I}\rangle_w$.

Bringing this perspective to our ACL model calculations, one can say that the correlation functions calculated in Sect. 4.3 could just as well have been calculated starting with the product "initial" states which result from operating with P_0 on $|\mathcal{E}\rangle_w$. Aside from its role in determining which environment state appears in the product, one could simply forget about the role of $|\mathcal{E}\rangle_w$. Turning to the CH calculations which followed, looking closely one can see that $|\mathcal{E}\rangle_w$ plays a role in determining the level of quantum interference among the paths. But if one sticks to the time period where the interference is acceptably low, again the behavior of the path can be described just fine by the product initial state, without direct reference to $|\mathcal{E}\rangle_w$. This disconnect from $|\mathcal{E}\rangle_w$ offers a helpful context for the fact that we were able to identify plenty of phenomena associated with an arrow of time, despite the equilibrium nature of $|\mathcal{E}\rangle_w$[11]. This perspective will also prove interesting in our cosmological discussion.

4.7 Cosmological Discussion

4.7.1 Background

The goal of this work is to illuminate discussions of cosmological initial conditions. Since the arrow of time figures prominently in such discussions, a result requiring an arrow of

[11] We note that our emphasis on this disconnect is a major difference between this paper and [74] (which also discusses the arrow of time, initial conditions and cosmology).

time to realize classical behavior would seem to offer important insights. Our calculations have led us to claims that are not quite so simplistic, but as they are we find them all the more intriguing.

The topic of cosmological initial conditions is a complicated one. There is no universal consensus about what one is trying to accomplish with a theory of cosmic initial conditions, and what features one should require of a successful theory. Some physicists are struck by the apparent tuning that is present in the initial conditions for our observed Universe (which in fact corresponds to the low entropy required to have an arrow of time [61]). Among those concerned about tuning, some are tempted by the attractor behavior of cosmic inflation [85, 86, 87, 88, 89, 90] (or of alternative theories [91]) as a tool for dynamically favoring certain initial conditions[12]. Others have argued, based on various phase space considerations, that a dynamical explanation of the early low entropy is impossible [92, 93, 94, 95, 96] (see [97] for a review of this issue in the context of starting cosmic inflation). And there have been a number of attempts to navigate a more nuanced path among these different points of view [98, 99, 100, 101, 102, 103, 104, 29, 105] (see also discussions at this workshop [106]). Yet another school of thought regards the elegance with which one can state the initial conditions more highly than whatever can be accomplished dynamically, for example in certain "wavefunction of the Universe" formulations such as [107, 108, 97, 109, 110, 111]. From that standpoint, the low entropy can look like a virtue, rather than a tuning problem. One could also just take the practical viewpoint that the initial conditions should simply be declared, without fanfare or extensive scrutiny. This approach might best match how physics is done in fields other than cosmology [13].

This work is motivated by the hopeful view that more thought and technical progress could bring greater clarity and consensus on the topic of cosmic initial conditions. To

[12]Indeed, students typically emerge from contemporary courses on cosmology with the impression that inflation dynamically resolves all cosmological tuning problems.

[13]Quantum gravity, which surely is ultimately the tool we need to address these questions, has a well known "problem of time" which has potentially radical consequences [112]. As is done in much of the literature on cosmic initial conditions, in this paper we implicitly assume a suitable time variable has been identified (for example along the lines of [113, 114]) and pursue an investigation which uses that variable as effectively an external time parameter. We acknowledge that until time in quantum gravity is fully understood it will remain unclear whether our (rather conventional) approach is missing important elements relevant to cosmic initial conditions.

connect our ACL calculations with cosmology, we start with some basic comments about the standard big bang cosmology and the arrow of time. By "big bang" we mean a Friedmann-Robertson-Walker (FRW) model adjusted to describe our observed Universe as well as possible. At early times such a model will have small perturbations which form the seeds of galaxies and other cosmic structure that emerges over time due to gravitational collapse around these seeds. It is currently standard practice to assume such a model emerges after a period of cosmic inflation (or sometimes an alternative dynamical scheme) which accounts for the details of the perturbation spectrum, and perhaps some other aspects, but one could also consider a more "old school" picture where the FRW Universe emerges from an initial singularity in the radiation dominated phase with the perturbations simply imprinted from the start.

In big bang cosmology, the low entropy of the early Universe originates in the FRW form of the metric [61]. The emergence of cosmic structure (and thus deviations from FRW) via gravitational collapse is the origin of the arrow of time in the Universe. As reviewed for example in [99], our local instance of cosmic structure (the hot sun radiating into cold space) is the primary origin of the arrow of time we experience here on earth. Heuristically, it is this instability which prompts concerns about "fine-tuning." Much as one might be surprised to walk into one's office and find a pencil stably balanced on its point, the instabilities of the early Universe reflect an initial balancing act that is at least as striking and mysterious in the eyes of many cosmologists. While certain classic treatments such as [115] focus on the instability associated with curvature within the FRW metric, the more general tuning issue relates to the vast array of other possible metrics that the early Universe apparently "turned down" in favor of FRW [61].

We should note that it is the instability of the early universe to gravitational collapse rather than the FRW metric per se that creates an arrow of time. de Sitter space is also described by an FRW metric, but it is classically stable. In fact, once notions of horizon entropy are factored in, de Sitter space can be considered the highest entropy state accessible to a universe with a positive cosmological constant [116]. In that sense it is a kind of equilibrium state which, as expected for equilibrium conditions, does not

exhibit an arrow of time. The presence of thermal Gibbons-Hawking radiation in de Sitter space [116] further encourages an equilibrium interpretation.

4.7.2 Connecting our ACL results to cosmology

Let us now make some links to our ACL results. A physics laboratory is an out-of-equilibrium system (ultimately thanks to the arrow of time of the cosmos as a whole). An experimentalist could simply displace a pendulum with their hand and create a situation similar to the one depicted in Fig. 4.1, arrow of time and all. More sophisticated experiments could measure the correlation functions depicted in Fig. 4.2. Our experimentalist might also construct a "Schrödinger cat" superposition of oscillator states and allow interactions with the environment to reflect einselection, as modeled for example in [1]. All of these experiments exploit the cosmic arrow of time, which is available to us in abundance, and illuminate its relationship to the emergence of classical from quantum. This paper is motivated by our curiosity about whether the arrow of time is *essential* for the emergence of classical from quantum, particularly with regards to the process of einselection. Given the extent to which we depend on classical physics in the world around us, it would seem that an answer in the affirmative might provides useful insights about the initial state of the Universe, from which time's arrow originates.

We should acknowledge here that we have not mapped out a detailed linkage between the arrow of time needed to einselect our SHO and the specific initial state of our observed Universe. There are many other conceivable initial states which also have an arrow of time to some degree (certainly enough to decohere a single oscillator) but which do not seem as finely tuned. This point is related to the "Boltzmann Brain" problem, which we will return to shortly. We regard this project merely as a small step in an interesting direction, inspired by these larger questions.

The direction this step has taken us is something of a surprise. Rather than disrupting the process of einselection, we have found that using equilibrium states simply drew our attention to the disconnect between the properties of the global initial state and the individual histories experienced by observers. This disconnect allowed us to consider histories with a clear arrow of time, even though the global state did not exhibit one.

In turn, these out-of-equilibrium histories easily manifested einselection. The individual histories were far enough removed from the "detailed balance" associated with equilibrium that the process of einselection could proceed in the same manner in which it has already been observed in situations which have an arrow of time. The notion of detailed balance was expressed in the *variety* of histories one could use to interpret the same quantum state, even as many individual histories had a definite time direction.

We bring several important basic messages from our ACL studies into cosmology. First of all, our work draws attention to the fact that the CH formalism requires one to check for quantum interference effects among histories within a given set, to see which ones can even be assigned classical probabilities. This point was made long ago [64, 67], but it has not been widely implemented. Given the very classical nature of realistic cosmologies, it is unclear to us if this lack of implementation is a serious shortcoming (as argued for example in [73]).

Secondly, while quantum physics is able to assign relative probabilities to histories *within* a specific decohering set, it is unable to give a systematic preference to one set over another. In this sense the different sets of consistent histories represent sets of truly "alternate facts," which describe the same quantum state. This feature plays an important role in the work presented here, and we reflect further on it in Sect. 4.7.3 and in our conclusions.

Next, while the global state does have a role in determining the degree of interference among histories, once sufficiently classical histories have been identified the remaining role of the global state is to assign relative probabilities to the different members of the set. These probabilities have limited meaning to observers who share the same classical history, but they can provide a framework for cosmological discussions of the likelihood of their particular universe[14].

Finally, we note that our results contradict ideas that "nothing happens" in equilibrium states (or even single energy eigenstates as we discussed in Appendix 4.B). Thus we disagree with the application of such ideas to cosmology, as implemented for example

[14]These features are at least somewhat reminiscent of other work that carefully distinguishes between global and observer perspectives, such as [117, 118, 119, 120].

in [121, 105]. On this point our arguments seem similar to those which appear in [122].

4.7.3 Further reflections

We have explored the relationship between a global initial state and the perceived initial state experienced by observers on a particular classical history. Under conditions where interference effects are low, and the history really does look classical, the remaining role of the global state is simply to assign a probability to that history. One could imagine that cosmologists who come up with a global state which assigns unit probability to the classical path they are on might consider their work finished. This would correspond to the "practical approach" mentioned in Sect. 4.7.1. But many other considerations influence people's thinking about a global "wavefunction of the universe." There are cases where cosmologists find these other considerations (essentially "priors") compelling enough to favor global states which assign highly suppressed probabilities to the classical paths we are on. Others are uncomfortable with doing so. This situation reflects the diversity of views about cosmic initial states that we discussed earlier. To some, willingness to accept a theory in which one's own classical trajectory is assigned a small probability is equivalent to accepting a finely tuned theory[15].

To elaborate further, we offer two examples where cosmologists have taken positions in favor of global states where paths exhibiting realistic properties of our observed Universe are exponentially suppressed. The first is the Hartle-Hawking "no boundary" (NB) wavefunction [107]. It is well known that in theories with an inflaton the NB wavefunction exponentially disfavors cosmologies which experience cosmic inflation in favor of states where the inflaton starts at the bottom of its potential. Nonetheless, proponents of the NB wavefunction find its intrinsic merits[16] sufficient to impose additional conditions which favor inflation to allow more realistic cosmologies to be considered (for example [123]).

Another example is de Sitter equilibrium cosmology (dSE) [101, 124, 125, 29]. This is

[15]It's worth noting here that while we've pointed out in Sect. 4.5.2 that the condition of zero bipartite entanglement entropy can be trivially realized on every one of a complete set of paths, at a specific time which can be arbitrarily chosen by suitably choosing the paths, this condition is far from sufficient to provide an arrow of time corresponding to what we see in our observed Universe. Demanding a more realistic condition is likely to highly suppress the associated probability.

[16]For example, it has been argued that the NB state dominates the quantum gravity path integral [100].

a cosmological picture motivated by the idea that the observed cosmic acceleration could be due to a fundamentally stable cosmological constant that defines an equilibrium state for the Universe (along the lines of our discussions of de Sitter space in Sect.4.7.1). In that picture, the equilibrium state would be the global quantum state and our observed Universe would be regarded as fluctuation, destined to equilibrate back to de Sitter as we evolve closer to a state dominated by the cosmological constant (conceptually similar to the behavior of the histories we explored with the ACL model).

Simple arguments suggest that dSE models should suffer from a "Boltzmann Brain" problem [98, 92, 93, 126, 101, 127]. This term refers to the apparent discrepancy between the fact that in equilibrium small fluctuations are much more likely than large ones, yet our Universe appears to be a large fluctuation. Novel quantum gravity effects could provide a way out of the Boltzmann Brain problem for dSE models [29], but even so fluctuations that resemble our Universe would be Boltzmann suppressed. An enthusiast of dSE cosmologies might still find a global state dictated by the laws of physics (via equilibration processes) more compelling than one constructed in a more ad hoc manner, and therefore accept the price of Boltzmann suppression. As discussed in [29], fluctuations like our Universe could be the most likely fluctuations which actually exhibit an arrow of time. On the other hand, should the exotic phenomena such as proposed in [29] not be realized, colleagues who are not willing to favor low probability histories by using theoretical priors may well regard the free availability of out-of-equilibrium histories demonstrated in this work to further enhance the Boltzmann Brain problem. Such a perspective could extend more broadly to many cosmological scenarios, not just dSE.

We add one more general thought about dSE models: While in most of this paper we used the notion of equilibrium as a "straw man" to represent the absence of an arrow of time, for dSE models equilibrium is a fundamental part of the physical picture. If we had concluded that equilibrium conditions prevent the emergence of classicality due to the absence of einselection (as we thought might be the case at the start of this project), that would have created major problems for the dSE picture. Instead, our results are consistent with identifying histories describing an arrow of time despite the

overall equilibrium conditions, as have already been explored heuristically in the dSE literature.

Another feature of our work that has some connections with cosmology is the presence of a double headed arrow of time. Such ideas come up occasionally in cosmological scenarios (some are discussed in [100, 29, 128, 105]). Here we note some differences between that work and the current discussion. In our toy model calculations, examples of double headed arrows of time came about by patching together two histories, one defined by an initial condition and the other by a final condition (thus creating a "middle condition"). In the context of our CH analysis this patching together makes particular sense in cases where the two paths we are connecting are both behaving very classically at the point of connection, thus extending the classical narrative.

As emphasized in [100], the cosmological examples tend not to behave classically at the point where the arrow switches directions. Instead, the patching tends to occur in a highly quantum regime—often a tunneling event. While there may be reasons to consider wavefunctions that offer a double-headed picture, we note that such a picture is intrinsically different from the cases we have showcased with the ACL model, where the patching occurs at a time of highly classical behavior. The discussion in Sect. 5.2 of [124] makes the point (which appears to be uncontroversial) that when the "middle condition" is intrinsically quantum a discussion of classical phenomena naturally draws the focus to histories with a single arrow, even if technically there is another history with the opposite arrow "on the other side of" the quantum domain.

We conclude these reflections with some general comments about the CH formalism. We have made extensive use of the feature of this formalism whereby alternate sets of histories (with potentially conflicting narratives) are available simultaneously, providing coexisting alternate interpretations of the same quantum state. This feature has historically been a source of discomfort and even outright skepticism directed at the CH framework. One of us (AA) recalls voicing some of that skepticism himself in early discussions of the CH formalism [32, 65]. In contrast, this paper has fully embraced that feature and it has played a central role in our analysis. This shift on the part of AA seems

partly rooted in a growing appreciation for the limited capacity of quantum physics to answer all questions one might wish to ask (as explored for example in [119]). But we also found that our efforts to carefully address the questions posed at the start of this project (particularly as related to detailed balance) drove us to accept and exploit that feature.

Stepping back a bit, we recognize that the fraught conversations among physicists about the interpretation of quantum mechanics are not about to end. The fact that the nature of the results and motivating questions in this paper nudged one of us into greater acceptance of the CH formalism does not mean others will respond in the same way. It is certainly reasonable to expect that our results will cause others to become *less* comfortable with that formalism. We have demonstrated histories which seem to give conflicting accounts of the arrow of time (manifesting the well-known capacity for the CH formalism to sustain seemingly conflicting narratives of all sorts). While in this paper we have embraced that feature as a realization of detailed balance, others might regard that feature as evidence that all the histories we consider for equilibrium and stationary systems should be removed from consideration by some enhancement (or outright rejection) of the CH formalism. The concrete thing we offer is sound technical results which reveal interesting features of the CH formalism and which address topics that are relevant to important questions in cosmology. We look forward to rich conversations with colleagues who take different viewpoints about the full implications.

4.8 Conclusions

We have used a simple toy model to explore the relationship between einselection, the arrow of time and equilibrium. Einselection, the systematic preference of decoherence processes for special pointer states, is a key element of how classical behavior can emerge in quantum systems. The process of decoherence, or the onset of system-environment entanglement, involves a clear arrow of time in the direction of increased entanglement. Our work was motivated by the idea that the detailed balance features of an equilibrium state should allow both entanglement increasing and decreasing processes to operate on an equal basis, potentially preventing equilibrium systems from exhibiting einselection.

We sought to confirm or deny this idea by investigating whether einselection could exist in an equilibrium system, with the goal of interpreting the implications of such results for the arrow of time in cosmology and cosmological initial conditions.

Furthermore, because the goal of our work was to apply our findings in a cosmological context, we were required to take extra care to not evoke an external observer in our calculations. Standard correlation function techniques appear to represent measurements by an outside observer, which among other things could reflect a disruption to the assumed equilibrium conditions. To remedy these concerns we used the consistent histories formalism. This formalism interprets the evolution of a quantum state in terms of sets of paths, and assigns classical probabilities to paths when quantum interference among the paths is sufficiently low.

Our calculations reveal interesting relationships among these various ingredients. We found the consistent histories formalism easily identified paths within the equilibrium system which exhibited an arrow of time, corresponding to a direction of increased entanglement. Such paths allowed us to explore standard ideas about einselection and show how the physics of entanglement expresses a preference for special pointer states, even within a system that is globally in an equilibrium state. In contrast to our initial suspicions, detailed balance did not prevent einselection within the equilibrium system in our calculations. Rather, the notion of detailed balance was realized in the diversity of decohering paths with which one could interpret the system—manifesting as disconnected but equally valid sets of paths one could use to describe the identical quantum state. An individual path might express the arrow of time in a particular direction at a given time, but if all the sets of paths were taken together, one would find entangling and disentangling equally represented. We also found sets of paths with double headed arrows of time, and we showed that paths could be found where the point in time at which the arrow switched directions was located at any moment, without preference. These results led us to carefully scrutinize how limited the influence of global initial conditions is on the physics of individual paths described within the global state, and what this might imply for cosmological initial conditions.

The cosmological context for our work starts with the deep relationship between the arrow of time we experience in the world around us and cosmological initial conditions. We have reviewed this relationship and also the general challenges faced by attempts to develop a comprehensive theory of cosmological initial conditions. Placing our results in this cosmological context has yielded a number of interesting insights which we have explored in the previous section. Specifically, we conclude that one cannot reject cosmological models built on an equilibrium picture based solely on the expectation that classicality is unable to emerge in such theories. We have explicitly demonstrated counterexamples to such arguments, at least at the level of our toy model. Our results suggest there is no simple way to leverage our practical need for einselection in the world around us to arrive at insights about the global state of the Universe. The properties of the global state and our experiences on a particular classical history are too disconnected from one another for a simple connection to be made. We've extended our analysis to systems placed in a single global energy eigenstate, and drawn similar conclusions.

Our work does draw attention to the importance of evaluating the degree of interference among different paths, which if large enough could prevent them from behaving classically. But our results suggest that the physical features which intrinsically support classical behaviors (such as the weak coupling between the SHO and the environment) also suppress this interference, whether or not the global state has an arrow of time.

It appears that a broadly agreed upon theory of cosmological initial conditions remains a difficult challenge for the field. We had hoped our explorations would help this endeavor by exploiting our need for emergent classicality to place limits on how the problem might be approached. Instead, our results draw attention to how disconnected the experiences on one classical history are from the properties of the global quantum state. While our results do not move things in the direction we expected, being forced to face these implications feels like a certain kind of progress.

4.9 Acknowledgements

We thank Patrick Coles and Jonathan Halliwell for helpful conversations. This work was supported in part by the U.S. Department of Energy, Office of Science, Office of High Energy Physics QuantISED program under Contract No. KA2401032.

4.A Randomized phases and matrix elements

The equilibrium state $|\mathcal{E}\rangle$ used in our calculations was arrived at (as discussed in Sec. 4.2) by evolving an out-of-equilibrium initial state to a time which appears to be deep in an equilibrium regime. One diagnostic one can try is to take the same state, expand it in eigenstates of the total Hamiltonian (H_w) and completely randomize the phases of the coefficients in this expansion. If replacing $|\mathcal{E}\rangle$ with such a randomized version were to lead to different results, that would signal that artifacts of the out-of-equilibrium initial state could be present in our calculations. Another check involves the random numbers generated in the construction of H_e and H_e^I. We should check that our results do not depend on the seed used for the random number generator.

Figure 4.9 contains six variations on the three curves shown in Fig. 4.2. Three variations reflect the randomized phase diagnostic, and three used different random number seeds. Each set of six curves differs from one another (and from the curves in Fig. 4.2) only in the small-scale noisy features. The broad features on which we based our physical analysis are identical, leading us to conclude that there are no artifacts of the choice of initial state or random number seed in our results. For simplicity Fig. 4.9 only shows some of the quantities examined in this paper, but we have found the other quantities to be similarly well-behaved.

The equilibration behaviors of the ACL model prompt interesting questions about the relationship between these behaviors and notions of thermalization, the Gibbs distribution, etc. These questions are addressed in [30] where it is argued that the qualities exhibited by the equilibration behaviors of the ACL model are sufficient to address the questions posed in this paper (for example by exhibiting detailed balance in equilibrium) even though the toy model nature of the ACL model makes these other notions less gen-

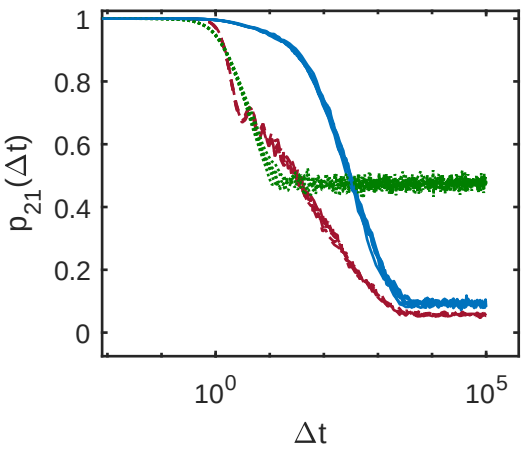

Figure 4.9: The quantities shown in Fig. 4.2 are recalculated, each with six variations to the technical details of the calculation. The similarity of each set of six curves with one another (as well as to the curves in Fig. 4.2) illustrate the robustness of our definition of equilibrium and a lack of dependence on our random number seed.

erally applicable.

4.B Eigenstate Einselection Hypothesis

The random phase diagnostic discussed above suggests our results reflect quite general properties of the eigenstates of H_w, more than specific details of the particular state we chose. We now follow this path further to see if we can get similar results if we start with a single eigenstate of H_w, rather than $|\mathcal{E}\rangle$. This exploration is an extension of the eigenstate thermalization hypothesis (ETH) ideas [129, 130] to the topic of einselection. While the focus of the ETH tends to be multi-particle systems described by field theories, we move ahead here with an exploration in the context of our simple toy model. The idea that the einselection behavior of a system can be reflected in a single energy eigenstate might be called an "eigenstate einselection hypothesis" (EEH). Regardless of nomenclature, this exploration allows us to challenge claims (such as those in [121]) that a system in an eigenstate of its total Hamiltonian cannot exhibit interesting dynamics.

As with the ETH, our results depend on which eigenstate of H_w we choose. To help us navigate among these eigenstates, we start by looking at the spectrum of H_w. The lower

panel of Fig. 4.10 gives a histogram of the eigenstates of H_w, and the upper panel shows p_E, the probability assigned to each histogram bin in the state $|\mathcal{E}\rangle$. Detailed properties

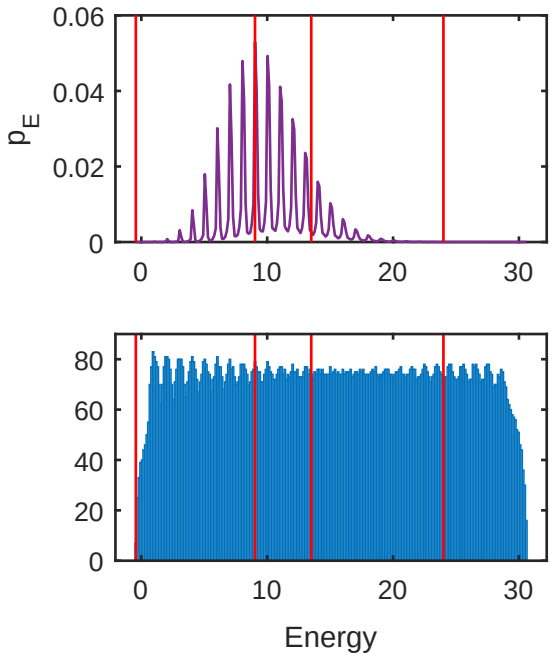

Figure 4.10: The lower panel gives a histogram of the eigenvalues of H_w. The upper panel gives p_E, the probabilities assigned to eigenstates in each bin for the equilibrium state $|\mathcal{E}\rangle$. The vertical lines mark the energies of the particular eigenstates of H_w used for Figures 4.11,4.12, 4.13 and 4.14.

of the spectrum of H_w are discussed in Appendix C of [1]. The oscillatory behavior of p_E reflects the fact that the initial state which equilibrates to generate $|\mathcal{E}\rangle$ is a product state with the environment in a single eigenstates of H_e.

Figures 4.11,4.12,4.13 and 4.14 plot the same quantities shown in Fig. 4.5, except with $|\mathcal{E}\rangle$ replaced with an eigenstate of H_w. The corresponding eigenvalue is indicated at the top of each plot, and the locations of these four energy values are marked with vertical lines in Fig. 4.10. Our broad conclusion based on the four samples shown here as well as additional systematic explorations, is that as long as one chooses an H_w eigenstate which contributes significantly to equilibrium state $|\mathcal{E}\rangle$, the general features of the CH quantities are unchanged. In particular, our conclusions about einselection are sustained. In addi-

tion, choosing states with eigenvalues from troughs in p_E does not generate significant differences. This meshes with our explorations of the ACL model, which indicate that starting the environment in a wide range of eigenstates of H_e does not change the overall einselection behavior significantly. The figure captions mention a few additional details.

Furthermore, we note that Figs. 4.11 and 4.14 both use eigenstates of H_w which have very little overlap with $|\mathcal{E}\rangle$. This shows up in the small corresponding values of p_E in Fig. 4.10, as well as the small overall values of the CH quantities (note the small y-axis scales that appear in these two plots). The curves in the lower panel of Fig. 4.14 have especially anomalous behavior. The dot-dashed curve overlaps the dashed curve and is not shown in order to make the figure clearer. But its location, orders of magnitude away from the dotted curve, signals overwhelming interference effects. We note, as discussed in Appendices B and C of [1], that eigenstates of H_w with large eigenvalues correspond to the larger energy eigenstates of the SHO, which have strange properties due to the truncated nature of the SHO in the ACL model. But the simplest explanation of the variation in the interference effects across the different cases stems from the different probabilities assigned to the paths. If the probability assigned to the 10 path is very small, it does not take much "leakage" in from the $1\not{0}$ path to create significant interference effects. Furthermore, when the probabilities assigned after projecting with $P_{\not{0}}$ are larger, there is more overall capacity for such leakage to occur.

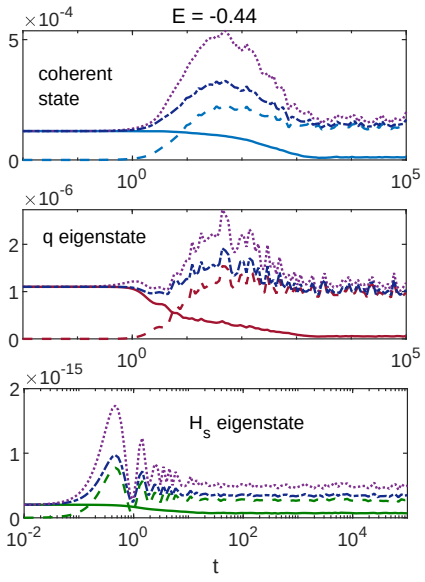

Figure 4.11: CH quantities as per Fig. 4.5, but with the equilibrium state replaced with the ground state of H_w. While the solid curve is still most stable in the top panel, giving one signal that coherent states are being einselected, interference among paths (given by the deviation of the dotted and dot-dashed curves) grows sharply at the same time the other panels destabilize. This suggests that when interference effects are accounted for there is not a strong argument for einselection favoring coherent states in this case.

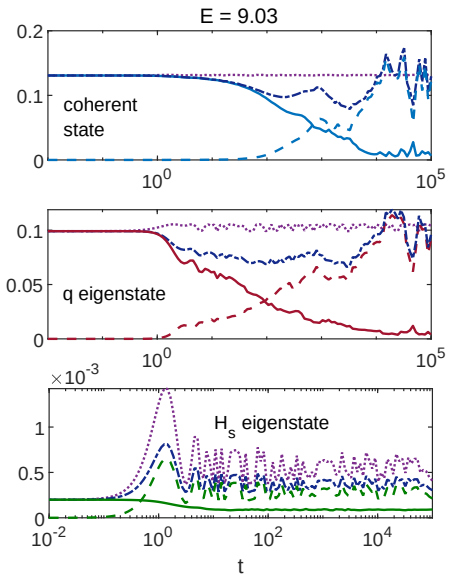

Figure 4.12: CH quantities as per Fig. 4.5, but with the equilibrium state replaced with the eigenstate of H_w corresponding to the peak of p_E in Fig. 4.10. This is the eigenstate that has the strongest overlap with the equilibrium state. The quantities in the upper panel are the most stable, indicating einselection of coherent states is exhibited for this case.

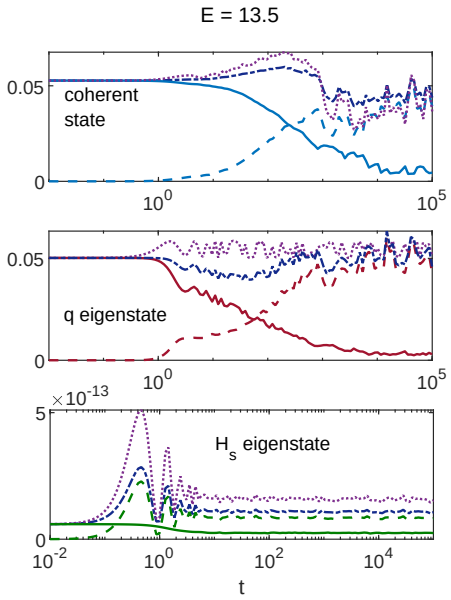

Figure 4.13: CH quantities as per Fig. 4.5, but with the equilibrium state replaced with the $E = 13.5$ eigenstate of H_w. This corresponds to a trough of p_E in Fig. 4.10, but well within the range where p_E is nonzero. The quantities in the upper panel are the most stable, indicating einselection of coherent states is exhibited for this case.

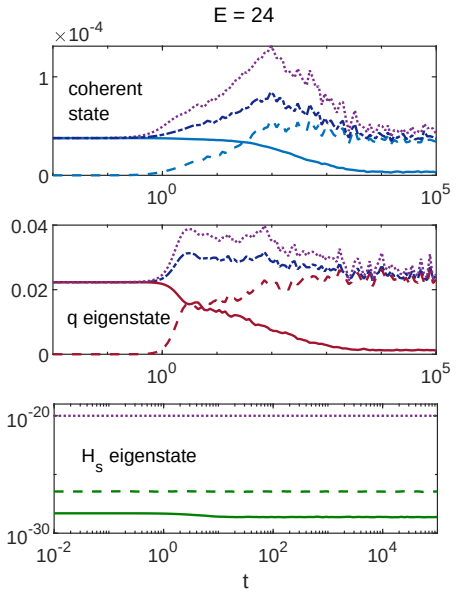

Figure 4.14: CH quantities as per Fig. 4.5, but with the equilibrium state replaced with an eigenstate of H_w with $E_w = 24$. This is another state with very little overlap with the equilibrium state. The picture is similar to that in Fig. 4.11, with some signs of einselection of coherent states shown in the solid curves, but not in the interference effects (given by the deviation of the dotted and dot-dashed curves). A comment about the anomalous appearance of the lower panel appears in the text.

Part Two

Chapter 5

Does Planck actually "see" the Bunch-Davies state?

The material in this chapter previously appeared in ***Does Planck actually "see" the Bunch-Davies state?*** *by Rose Baunach, Nadia Bolis, R. Holman, Stacie Moltner, and Benoit J. Richard [4].*

ABSTRACT: To what extent can the Planck satellite observations be interpreted as confirmation of the quantum part of the inflationary paradigm? Has it "seen" the Bunch-Davies state? We compare and contrast the Bunch-Davies interpretation with one using a so-called *entangled* state in which the fluctuations of a spectator scalar field are entangled with those of the metric perturbations ζ. We first show how a spectator scalar field Σ, with an expectation value $\sigma(t)$ that evolves in time, will generically generate such a state. We then use this state to compute the power spectrum $P_\zeta(k)$ and thence the temperature anisotropies C_l in the Cosmic Microwave Background (CMB). We find interesting differences from the standard calculations using the Bunch-Davies (BD) state. We argue that existing data may already be used to place interesting bounds on this class of deviations from the BD state and that, for some values of the parameters of the state, the power spectra may be consistent with the Planck satellite data.

5.1 Is Bunch-Davies All There Is?

The inflationary paradigm [115, 131, 132, 133, 134] can be thought of as comprising two parts. The first is concerned with *models* of inflation, that is in finding viable field theoretic realizations of inflation. The second, which is the focus of this work, deals with the quantum mechanics of inflationary perturbations.

One of the signal successes of inflation was the realization that quantum fluctuations during the inflationary phase could be stretched to cosmological length scales and that they would decohere so as to be able to be treated classically and serve as a causally generated source of density fluctuations. These in turn would drive the formation of cosmic structure in the early universe [135, 136, 137]. In order to calculate the power spectrum of these fluctuations and how these might show up in physical observables such as temperature anisotropies in the Cosmic Microwave Background (CMB), we need to know the quantum state of the field representing the metric perturbations.

For a scalar field in a near de Sitter background spacetime, there is a preferred quantum state, the so-called Bunch-Davies (BD) state [19]. Though the notion of a lowest energy state is of dubious value in a dynamical spacetime, the BD state has a number of "ground state" traits. It is a state of maximal symmetry in that it is invariant under the symmetries of de Sitter space and it is an adiabatic state [138], which is the nearest approximation to a state devoid of particles that can be obtained in this context. In fact, it is the state that in the short-distance, short-time limit approaches the Minkowski space vacuum state for a scalar field theory.

From this perspective, the BD state becomes a natural one to use for the computation of inflationary cosmological observables. Given a model of inflation, using this state allows us to make predictions about various aspects of the CMB power spectrum, bi-spectrum, as well as other cosmological observables. It is thus a linchpin of the inflationary paradigm. But is the BD state the true state of the inflaton? How can we tell?

If we *were* to find that the BD state is necessarily the quantum state of the inflaton, this would bring up a number of questions, not least of which is what makes the BD state so stable with respect to all the potentially non-adiabatic physical effects that would

surely be taking place before or at the onset of inflation? On the other hand, if we find other states that could conceivably fit the bill as consistent inflationary quantum states, the structure of these states might provide hints to pre-inflationary physics.

These questions drive us to explore the issue of how to delineate the space of allowable inflationary states. In general, this task is a difficult one, made more so by the paucity of cosmological probes that can be directly brought to bear on it. However, there are some requirements that an inflationary quantum state must satisfy. First and foremost, *it must allow inflation to occur!* This is to be interpreted as the requirement that the expectation value of the stress tensor of the inflaton should not give rise to an energy density that exceeds that coming from the inflaton potential. Second, it should give rise to values of cosmological observables consistent with those measured by probes of the CMB as well as those of large scale structure (LSS). While these two conditions are the *sine qua non* of any potential inflaton quantum state, we will add another restriction so as to make the problem tractable; we will assume that the state is Gaussian in the field fluctuations. While this appears to just lead to the standard free field theory quantum state, we will also allow for the existence of *spectator* scalar fields and for the possibility that the state describing spectator field fluctuations is entangled (in the sense of refs. [139, 140, 141]) with the state of the metric perturbations. This opens up the space of states to a larger set than just the free field Gaussian state of metric fluctuations, albeit, in a way that is still amenable to analysis.

Thus, we will assume that an inflationary period is induced by the slow-roll of an inflaton field Φ. We will also suppose that the spectator field does not couple to the inflaton directly so that the potential $V(\Phi, \Sigma) = V_{\rm inf}(\Phi) + V_{\rm spec}(\Sigma)$. We will work in the comoving gauge in which the fluctuations $\delta\phi$ of the inflaton around its rolling expectation value $\phi(t) = \langle \Phi(\vec{x}, t) \rangle$ are gauged away and all their information is encoded in the scalar metric perturbation ζ (which, on superhorizon scales, is proportional to the curvature perturbation $\mathcal{R}$).

In the previous work done with these states, either the initial entanglement was assumed to be non-zero, but otherwise arbitrary, or it was generated [142] by looking at

cubic order terms in the ζ-scalar action [143, 144]. In this work, we will show that, in fact, non-trivial entanglement can be generated even at the quadratic level of the coupled ζ-scalar system, as long as the expectation value of the scalar is initially displaced from the minimum of its potential. Given the appearance of (light) scalar fields in a number of extensions of the standard model as well as the existence of the Higgs, it could be argued that our entangled states might in fact be a generic outcome of early universe evolution.

This then is the aim of our paper: to show that the addition of a spectator field can generate a non-trivial entanglement between the metric perturbations and scalar field fluctuations and then to compute the power spectrum and use it to construct the CMB temperature anisotropies. We will consider both a free massive field as well as a field with an axion-type potential as a spectator field.

What we find is that in both cases, as long as the scalar has an expectation value that is either displaced from its minimum and/or has a non-zero time derivative, a nontrivial entangled state will be generated. The resulting power spectra depend on the initial values of the scalar field and its time derivative, as well as the ratio of the scalar's mass relative to the Hubble parameter of the de Sitter expansion. They exhibit a variety of behaviors, depending on the parameter values. Interestingly, even in the cases where the primordial power spectrum deviates significantly from that of the Bunch-Davies case, when the entanglement happens near when the largest length scales appearing in the CMB leave the inflationary horizon, the C_ls can essentially remain unchanged from the non-entangled case. However, for other parameter values, we will see that large deviations can occur.

Our interest in the quantum state of the system—as opposed to the observables of interest in collider physics such as S-matrix elements, scattering amplitudes and the like—dictates the technique we will use in this work. Schrödinger picture field theory [145, 146] is the natural tool in this setting, and we review its use in determining the inflaton quantum state in the next section. In section 5.3, we compute the ζ power spectrum and the C_ls for a variety of initial conditions for the rolling expectation value of the spectator scalar. Finally, we discuss our results and further research directions in section 5.4.

5.2 The Schrödinger Wave Functional for the ζ – Spectator Scalar System

We have discussed the use of Schrödinger field theory at length in previous work on entangled states [139, 140, 141], so we will settle for a quick summary here. As mentioned in the introduction, we are *not* concerned with observables such as scattering amplitudes, but rather with the form and evolution of the quantum state itself. In the Schrödinger picture this corresponds to the construction of a wavefunctional depending on the relevant field configurations defined on the spatial hypersurface at conformal time η, $\Psi\left[\zeta(\cdot), \Sigma(\cdot); \eta\right]$. This wavefunctional then satisfies the Schrödinger equation

$$i\partial_\eta \Psi\left[\zeta(\cdot), \Sigma(\cdot); \eta\right] = H\left[\Pi_\zeta, \Pi_\Sigma, \zeta, \Sigma; \eta\right] \Psi\left[\zeta(\cdot), \Sigma(\cdot); \eta\right], \tag{5.1}$$

where Π_ζ, Π_Σ are the canonically conjugate momenta to ζ and Σ, respectively. In equation (5.1), we have included the explicit time dependence of the Hamiltonian coming from the expansion of the Universe as encoded in the scale factor $a(\eta)$. Given the wavefunctional, cosmological observables are simply expectation values of the relevant operators, taken in the Schrödinger picture.

5.2.1 Constructing the ζ-Σ Hamiltonian

As mentioned above, the system we will consider is one where the scalar metric perturbations ζ are entangled with a scalar field Σ. Before we proceed with the calculation, though, it is worth taking the time to understand some physics details. We need the spectator field to truly be a spectator. What that means is that we have to ensure that the energy density in Σ must be far smaller than that of the inflaton. This allows us to neglect the effects of the isocurvature perturbations induced by Σ, at least to lowest order. Including such effects will be left to later work.

In order to begin, we need the action for the scalar metric fluctuations ζ coupled to a scalar field Σ whose potential $V(\Sigma)$ drives its dynamics. We take $\langle\Sigma\rangle \equiv \sigma(\eta)$, where the expectation value is taken with the wavefunctional Ψ. Arriving at this action entails using the ADM [147] form of the Einstein action, writing the metric in terms of the lapse and shift functions, $N,\ N_i$ respectively, as well as ζ, and then solving the constraint equations

for the Lagrange multipliers $N,\ N_i$. The fact that Σ has a non-trivial expectation value complicates matters somewhat, and we use the Mathematica package *MathGR* [148] to aid us in our calculations. Also, we take advantage of the spatial flatness of the constant-η hypersurfaces and write the action directly in terms of the momentum space modes $\zeta_{\vec{k}}$ and $\chi_{\vec{k}}$, where we expand the field Σ about its expectation value: $\Sigma(\vec{x},\eta) = \sigma(\eta) + \chi(\vec{x},\eta)$.

We will only keep terms in the action out to quadratic order in the fluctuations $\zeta_{\vec{k}}$ and $\chi_{\vec{k}}$, reasoning that this will suffice in order to set up the Schrödinger equation for a Gaussian state.

There is a term that is independent of the fluctuations but only depends on the background cosmology; we will neglect this term since we can rephase the wavefunctional to absorb its effects. In addition, there exists a term linear in χ that contributes to the tadpole; it's proportional to the zero mode equation of motion, which, at the classical level is given by:

$$\sigma''(\eta) + 2\frac{a'(\eta)}{a(\eta)}\sigma'(\eta) + a^2(\eta)\partial_\sigma V(\sigma) = 0. \tag{5.2}$$

We will assume this equation is satisfied, so we can neglect this term in the action and hence in the Hamiltonian (see [142] for how higher order corrections to the zero mode equation can be implemented in the presence of entanglement).

Doing all of this, we find the action to quadratic order is given by:

$$\begin{aligned} S &= \int d\eta \int \frac{d^3k}{(2\pi)^3}\ \mathcal{L}_k \\ \mathcal{L}_k &= a^2(\eta)\left\{\frac{1}{2}\vec{X}^{T\prime}_{\vec{k}}\ \mathcal{O}\ \vec{X}'_{-\vec{k}} + \vec{X}^{T\prime}_{\vec{k}}\ \mathcal{M}\ \vec{X}_{-\vec{k}} - \frac{1}{2}\vec{X}^{T}_{\vec{k}}\ \Omega_k^2\ \vec{X}_{-\vec{k}}\right\}, \end{aligned} \tag{5.3}$$

where primes denote conformal time derivatives,

$$\vec{X}_{\vec{k}} = \begin{pmatrix} \zeta_{\vec{k}} \\ \chi_{\vec{k}} \end{pmatrix},$$

and the matrices $\mathcal{O}$, $\mathcal{M}$, and Ω_k^2 are given by:

$$\mathcal{O} = \begin{pmatrix} 2M_P^2\,\epsilon & -\frac{\sigma'}{\mathcal{H}} \\ -\frac{\sigma'}{\mathcal{H}} & 1 \end{pmatrix} \tag{5.4a}$$

$$\mathcal{M} = \begin{pmatrix} 0 & \epsilon\sigma' - \frac{a^2(\eta)\partial_\sigma V(\sigma)}{\mathcal{H}} \\ 3\sigma' & 0 \end{pmatrix} \tag{5.4b}$$

$$\Omega^2 = \begin{pmatrix} 2M_P^2\,\epsilon\,k^2 & 3a^2(\eta)\partial_\sigma V(\sigma) - k^2\frac{\sigma'}{\mathcal{H}} \\ 3a^2(\eta)\partial_\sigma V(\sigma) - k^2\frac{\sigma'}{\mathcal{H}} & k^2 + a^2(\eta)\partial_\sigma^2 V(\sigma) + (3-\epsilon)\frac{\sigma'^2}{M_P^2} + \frac{2a^2(\eta)\sigma'\partial_\sigma V(\sigma)}{M_P^2\mathcal{H}} \end{pmatrix}. \tag{5.4c}$$

We have also defined the conformal time Hubble parameter $\mathcal{H}$ via

$$\mathcal{H} \equiv \frac{a'(\eta)}{a(\eta)},$$

as well as the slow-roll parameter ϵ, defined in conformal time by $\mathcal{H}' = (1-\epsilon)\mathcal{H}^2$.

We note the following facts. First, the dimensions of the entries in $\mathcal{O}$ as well as the other matrices are different; this arises due to the fact that in position space, ζ has mass dimension 0 while χ has mass dimension 1, which in turn means that $\zeta_{\vec{k}}$ and $\chi_{\vec{k}}$ have dimensions -3 and -2, respectively. Furthermore, the mixing matrix $\mathcal{M}$, which mixes the positions and velocities, vanishes when σ rests at the minimum (or maximum) of the potential $V(\sigma)$.

More importantly though, we notice that the mixing term involving $\mathcal{M}$ is *not* hermitian. We can see this by noting that for a real field ϕ, $\phi_{\vec{k}}^* = \phi_{-\vec{k}}$, so that, after a $\vec{k} \leftrightarrow -\vec{k}$ change of variable in the k integral, we can write the relevant term in the action as $\vec{X}_{\vec{k}}^{\dagger\prime}\ \mathcal{M}\ \vec{X}_{\vec{k}}$. Taking the hermitian conjugate and noting that $\mathcal{M}$ is a real matrix, we have

$$a^2(\eta)\left(\vec{X}_{\vec{k}}^{\dagger\prime}\ \mathcal{M}\ \vec{X}_{\vec{k}}\right)^\dagger = a^2(\eta)\left(\vec{X}_{\vec{k}}^{\dagger}\ \mathcal{M}^T\ \vec{X}_{\vec{k}}^{\prime}\right). \tag{5.5a}$$

Integrating by parts and discarding the surface term allows us to rewrite this as

$$a^2(\eta)\left(\vec{X}_{\vec{k}}^{\dagger}\ \mathcal{M}^T\ \vec{X}_{\vec{k}}^{\prime}\right) = -a^2(\eta)\left(\vec{X}_{\vec{k}}^{\dagger\prime}\ \mathcal{M}^T\ \vec{X}_{\vec{k}}\right) - \vec{X}_{\vec{k}}^{\dagger}\ \partial_\eta\left(a^2(\eta)\mathcal{M}^T\right)\ \vec{X}_{\vec{k}}. \tag{5.5b}$$

To make the action hermitian, we replace

$$\vec{X}_{\vec{k}}^{T\prime}\ \mathcal{M}\ \vec{X}_{-\vec{k}} \to \frac{1}{2}\left(\vec{X}_{\vec{k}}^{T\prime}\ \mathcal{M}\ \vec{X}_{-\vec{k}} + \left(\vec{X}_{\vec{k}}^{\dagger\prime}\ \mathcal{M}\ \vec{X}_{\vec{k}}\right)^\dagger\right). \tag{5.6}$$

From (5.5b) we see that this is equivalent to the combined operations of (i) replacing $\mathcal{M} \to \mathcal{M}_A$ and (ii) shift $\Omega_k^2 \to \Omega_k^2 + \partial_\eta \left(a^2(\eta)\mathcal{M}_S\right)/a^2(\eta)$, where S, A denote the symmetric and antisymmetric parts of $\mathcal{M}$.

To construct the Hamiltonian, we start with the momenta conjugate to $\zeta_{\vec{k}},\ \chi_{\vec{k}}$:

$$\vec{\Pi}_{\vec{k}} = \frac{\delta \mathcal{L}_k}{\delta \vec{X}'_{-\vec{k}}} = a^2(\eta)\left[\mathcal{O}\vec{X}'_{\vec{k}} + \mathcal{M}_A \vec{X}_{\vec{k}}\right] \Rightarrow \vec{X}'_{\vec{k}} = \frac{1}{a^2(\eta)}\mathcal{O}^{-1}\vec{\Pi}_{\vec{k}} - \mathcal{O}^{-1}\mathcal{M}_A \vec{X}_{\vec{k}}. \tag{5.7}$$

From the definition of the momentum space Hamiltonian density H_k as $H_k = \vec{\Pi}^T_{\vec{k}} \vec{X}'_{-\vec{k}} - \mathcal{L}_k$ we have:

$$\begin{aligned} H_k &= \frac{1}{2a^2(\eta)}\vec{\Pi}^T_{\vec{k}}\ \mathcal{O}^{-1}\ \vec{\Pi}_{-\vec{k}} - \frac{3}{2}\vec{\Pi}^T_{\vec{k}}\ \mathcal{O}^{-1}\mathcal{M}_A\ \vec{X}_{-\vec{k}} + \frac{1}{2}\vec{X}^T_{\vec{k}}\ \mathcal{M}_A^T\mathcal{O}^{-1}\ \vec{\Pi}_{-\vec{k}} \\ &+ \frac{a^2(\eta)}{2}\vec{X}^T_{\vec{k}}\left(\Omega_k^2 + \frac{\partial_\eta\left(a^2(\eta)\mathcal{M}_S\right)}{a^2(\eta)} + \mathcal{M}_A^T\mathcal{O}^{-1}\mathcal{M}_A\right)\vec{X}_{-\vec{k}}. \end{aligned} \tag{5.8}$$

The full Hamiltonian is then a momentum space integral of H_k. We should note that the middle two terms in H_k are quantum mechanically ambiguous due to operator ordering issues. We deal with this by means of the Weyl prescription: $\vec{\Pi}_a \vec{x}_b \to (\vec{\Pi}_a \vec{x}_b + \vec{x}_b \vec{\Pi}_a)/2$, where $a, b = 1, 2$. Doing this and using the fact that $\mathcal{O}$ and hence $\mathcal{O}^{-1}$ is symmetric, we can write

$$\begin{aligned} H_k &= \frac{1}{2a^2(\eta)}\vec{\Pi}^T_{\vec{k}}\ \mathcal{O}^{-1}\ \vec{\Pi}_{-\vec{k}} - \frac{1}{2}\left[\mathcal{O}^{-1}\mathcal{M}_A\right]_{ab}\left(\vec{\Pi}_{\vec{k}a}\vec{X}_{-\vec{k}b} + \vec{X}_{-\vec{k}b}\vec{\Pi}_{\vec{k}a}\right) \\ &+ \frac{a^2(\eta)}{2}\vec{X}^T_{\vec{k}}\ \left(\Omega_k^2 + \frac{\partial_\eta\left(a^2(\eta)\mathcal{M}_S\right)}{a^2(\eta)} + \mathcal{M}_A^T\mathcal{O}^{-1}\mathcal{M}_A\right)\vec{X}_{-\vec{k}}. \end{aligned} \tag{5.9}$$

Quantization of this system now proceeds in the standard way, demanding that $\vec{\Pi}_{\vec{k}},\ \vec{X}_{\vec{q}}$ satisfy the commutation relations:

$$\left[\vec{X}_{\vec{q}a}, \vec{\Pi}_{\vec{k}b}\right] = i\delta_{ab}\left(2\pi\right)^3 \delta^{(3)}\left(\vec{q} + \vec{k}\right). \tag{5.10}$$

In the Schrödinger picture, the commutation relations are enforced by the choice:

$$\vec{\Pi}_{\vec{k}a} = -i\left(2\pi\right)^3 \frac{\delta}{\delta \vec{X}_{-\vec{k}a}}, \quad a, b = 1, 2, \tag{5.11}$$

acting on wavefunctionals that depend on $\vec{X}_{\vec{q}a}$ and time.

Next we turn to the representation of entangled states in the Schrödinger picture and the form of the Schrödinger equation for them.

5.2.2 The Functional Schrödinger Equation for Entangled Wavefunctionals

As discussed in section 5.1, our aim is to construct a class of states that entangle ζ with the field fluctuations χ, yet remain Gaussian. Thus we write the wavefunctional Ψ as:

$$\Psi\left[\left\{\zeta_{\vec{k}}\right\},\left\{\chi_{\vec{k}}\right\};\eta\right] = N(\eta)\exp\left(-\frac{1}{2}\int\frac{d^3k}{(2\pi)^3}\;\vec{X}^T_{\vec{k}}\;\mathcal{K}_k(\eta)\;\vec{X}_{-\vec{k}}\right). \tag{5.12}$$

Here, $\mathcal{K}_k(\eta)$ is a matrix of kernels:

$$\mathcal{K}_k(\eta) = \begin{pmatrix} A_k(\eta) & C_k(\eta) \\ C_k(\eta) & B_k(\eta) \end{pmatrix}, \tag{5.13}$$

with $C_k(\eta)$ encoding the entanglement between the fluctuations.

We now use this wavefunctional in the Schrödinger equation (5.1). The strategy will be to compute both sides separately and then match the powers of $\vec{X}_{\vec{k}}$ that appear. The left hand side is given by:

$$i\partial_\eta\Psi\left[\left\{\zeta_{\vec{k}}\right\},\left\{\chi_{\vec{k}}\right\};\eta\right] = \left(i\frac{N'(\eta)}{N(\eta)} - \frac{i}{2}\langle\vec{X}^T_{\vec{k}}\;\mathcal{K}'_k(\eta)\;\vec{X}_{-\vec{k}}\rangle\right)\Psi\left[\left\{\zeta_{\vec{k}}\right\},\left\{\chi_{\vec{k}}\right\};\eta\right], \tag{5.14}$$

where the angular brackets denote the k-space integral, including the factor of $(2\pi)^{-3}$. On the right hand side we note that the factors of $(2\pi)^3$ between the expression of the momentum as a derivative in (5.11) and in the k-space measure cancel when the momenta act on the exponential. We can also simplify things in advance by noting that:

$$\begin{aligned}\frac{1}{2}\left[\mathcal{O}^{-1}\mathcal{M}_A\right]_{ab}\left(\vec{\Pi}_{\vec{k}a}\vec{X}_{-\vec{k}b} + \vec{X}_{-\vec{k}b}\vec{\Pi}_{\vec{k}a}\right) &= \left[\mathcal{O}^{-1}\mathcal{M}_A\right]_{ab}\vec{X}_{-\vec{k}b}\vec{\Pi}_{\vec{k}a} \\ &- \frac{i(2\pi)^3}{2}\delta^{(3)}\left(\vec{q}=\vec{0}\right)\mathrm{tr}\left(\mathcal{O}^{-1}\mathcal{M}_A\right),\end{aligned} \tag{5.15}$$

and we recognize $(2\pi)^3\delta^{(3)}\left(\vec{q}=\vec{0}\right)$ as the volume factor $\mathcal{V}$ that would appear in box quantization of the system. All terms containing this factor will contribute to the evolution of the normalization factor $N(\eta)$. But since $\mathcal{O}$ is symmetric while $\mathcal{M}_A$ is antisymmetric, the trace vanishes identically.

To compute the right hand side of (5.1), we first compute the action of $\vec{\Pi}_{\vec{k}}$ on the wavefunctional:

$$\vec{\Pi}_{\vec{k}a}\Psi\left[\left\{\zeta_{\vec{k}}\right\},\left\{\chi_{\vec{k}}\right\};\eta\right] = \left(i\mathcal{K}_k(\eta)\vec{X}_{\vec{k}}\right)_a\Psi\left[\left\{\zeta_{\vec{k}}\right\},\left\{\chi_{\vec{k}}\right\};\eta\right]. \tag{5.16}$$

The second application of a momentum operator, as present in the kinetic term of the k-space integrated Hamiltonian, $\langle \vec{\Pi}_{\vec{k}}^T \ \mathcal{O}^{-1} \ \vec{\Pi}_{-\vec{k}} \rangle$, will bring down another factor of $\left(i\mathcal{K}_k(\eta) \vec{X}_{\vec{k}} \right)$, as well as a term proportional to the box volume $\mathcal{V}$:

$$\begin{aligned} &\tfrac{1}{2} \langle \vec{\Pi}_{\vec{k}}^T \ \mathcal{O}^{-1} \ \vec{\Pi}_{-\vec{k}} \rangle \Psi \left[\left\{ \zeta_{\vec{k}} \right\}, \left\{ \chi_{\vec{k}} \right\}; \eta \right] = \\ &\tfrac{1}{2} \left(\mathcal{V} \langle \mathrm{tr} \left[\mathcal{O}^{-1} \mathcal{K}_k \right] \rangle - \langle \vec{X}_{\vec{k}}^T \left(\mathcal{K}_k^T \mathcal{O}^{-1} \mathcal{K}_k \right) \vec{X}_{-\vec{k}} \rangle \right) \Psi \left[\left\{ \zeta_{\vec{k}} \right\}, \left\{ \chi_{\vec{k}} \right\}; \eta \right] \end{aligned} \tag{5.17}$$

The next term to deal with is the operator in (5.15):

$$\langle \left[\mathcal{O}^{-1} \mathcal{M}_A \right]_{ab} \vec{X}_{-\vec{k}b} \vec{\Pi}_{\vec{k}a} \rangle \Psi \left[\left\{ \zeta_{\vec{k}} \right\}, \left\{ \chi_{\vec{k}} \right\}; \eta \right] = i \langle \vec{X}_{\vec{k}}^T \left(\mathcal{K}_k^T \mathcal{O}^{-1} \mathcal{M}_A \right) \vec{X}_{-\vec{k}} \rangle \Psi \left[\left\{ \zeta_{\vec{k}} \right\}, \left\{ \chi_{\vec{k}} \right\}; \eta \right]. \tag{5.18}$$

Combining (5.17), (5.18) with the final term in (5.9) and matching powers of $\vec{X}_{\vec{k}}$ gives the equations for the normalization and the kernel matrix:

$$i \frac{N'(\eta)}{N(\eta)} = \frac{1}{2} \mathcal{V} \langle \mathrm{tr} \left[\mathcal{O}^{-1} \mathcal{K}_k \right] \rangle \tag{5.19a}$$

$$\begin{aligned} i\mathcal{K}_k'(\eta) = &\frac{1}{a^2(\eta)} \left(\mathcal{K}_k^T \mathcal{O}^{-1} \mathcal{K}_k \right) + i \left(\mathcal{K}_k^T \mathcal{O}^{-1} \mathcal{M}_A + \mathcal{M}_A^T \mathcal{O}^{-1} \mathcal{K}_k \right) \\ &- a^2(\eta) \left(\Omega_k^2 + \frac{\partial_\eta \left(a^2(\eta) \mathcal{M}_S \right)}{a^2(\eta)} + \mathcal{M}_A^T \mathcal{O}_k^{-1} \mathcal{M}_A \right), \end{aligned} \tag{5.19b}$$

where we symmetrized the middle term in order to be able to match independent powers of the modes.

We can decompose these equations into those for the individual kernels $A_k(\eta)$, $B_k(\eta)$, $C_k(\eta)$. Let's define:

$$z(\eta) = \sqrt{2 M_{\mathrm{Pl}}^2 \ \epsilon \ a^2(\eta)} \ , \ D = 2 M_{\mathrm{Pl}}^2 \ \epsilon - \left(\frac{\sigma'}{\mathcal{H}} \right)^2. \tag{5.20}$$

D is a measure of how much of a spectator Σ is, as it measures the relative sizes of the field contributions to the kinetic energy density. With these definitions, the equations of

motion for the kernels are given by

$$i\partial_\eta A_k(\eta) = \left[-z(\eta)^2k^2 + \frac{A_k^2}{z(\eta)^2}\right] + \frac{1}{D}\left[\left(\frac{\sigma'}{\mathcal{H}}\right)\frac{A_k}{z(\eta)} + \sqrt{2M_{Pl}^2\epsilon}\,\frac{C_k}{a(\eta)} + \frac{iz(\eta)}{2}\left((3-\epsilon)\sigma' + \frac{a^2(\eta)\partial_\sigma V(\sigma)}{\mathcal{H}}\right)\right]^2, \tag{5.21a}$$

$$\begin{aligned} i\partial_\eta B_k(\eta) = &\left[-a^2(\eta)\left(k^2 + a^2(\eta)\partial_\sigma^2 V(\sigma)\right) + \frac{B_k^2}{a^2(\eta)}\right] \\ &- a^2(\eta)\left[(3-\epsilon)\frac{\sigma'^2}{M_{\rm Pl}^2} + \frac{2a^2(\eta)\ \sigma'\ \partial_\sigma V(\sigma)}{\mathcal{H}\ M_{\rm Pl}^2}\right] \\ &+ \frac{1}{D}\left[\frac{1}{a(\eta)}\left(C_k + \frac{\sigma'}{\mathcal{H}}B_k\right) - \frac{ia(\eta)}{2}\left((3-\epsilon)\sigma' + \frac{a^2(\eta)\partial_\sigma V(\sigma)}{\mathcal{H}}\right)\right]^2, \end{aligned} \tag{5.21b}$$

$$\begin{aligned} i\partial_\eta C_k(\eta) = &\frac{1}{a^2(\eta)D}\left[C_k\left(A_k + 2M_{\rm Pl}^2\epsilon\ B_k\right) + \frac{\sigma'}{\mathcal{H}}\left(C_k^2 + A_kB_k\right)\right] \\ &+ \frac{1}{D}\left[\left(-A_k + 2M_{\rm Pl}^2\epsilon\ B_k\right)\left(\frac{i}{2}\left((3-\epsilon)\sigma' + \frac{a^2(\eta)\partial_\sigma V(\sigma)}{\mathcal{H}}\right)\right)\right] \\ &- \frac{a^2(\eta)}{D}\frac{\sigma'}{\mathcal{H}}\left[\frac{i}{2}\left((3-\epsilon)\sigma' + \frac{a^2(\eta)\partial_\sigma V(\sigma)}{\mathcal{H}}\right)\right]^2 \\ &+ a^2(\eta)\left[\epsilon a^2(\eta)\partial_\sigma V(\sigma) + \frac{\sigma'}{\mathcal{H}}\left(k^2 + \frac{1}{2}a^2(\eta)\partial_\sigma^2 V(\sigma) - \frac{1}{2}\ \epsilon\ \eta_{\rm sl}\mathcal{H}^2\right)\right]. \end{aligned} \tag{5.21c}$$

Here $\eta_{\rm sl}$ denotes the second slow roll parameter $\eta_{\rm sl} \equiv \epsilon'/\mathcal{H}\epsilon$. Note that, for completeness, we have kept the term $\eta_{\rm sl}\epsilon$, as well as terms quadratic in ϵ despite them being higher order in slow-roll. We will only keep the leading terms in slow-roll parameters when we turn to our numerical work. These equations should be solved in conjunction with the zero mode equation (5.2).

5.2.3 Making Contact with the Bunch-Davies Modes

We will use the kernels A_k, B_k, C_k in our further explorations of entanglement below. However, we recognize that this is a somewhat unorthodox way of constructing the power spectrum, as opposed to the standard way using the Bunch-Davies modes. Since we are calculating the same physical quantity, we expect that the kernels and the modes should be related.

We have written equations (5.21a), (5.21b) in a suggestive way. The first parentheses in each equation consists of the terms that would have been present when σ is at the minimum of its potential. The remaining terms involve corrections that act as the sources of entanglement. Let's restrict our attention to the first set of terms and assume that $C = 0,\ \sigma' = \partial_\sigma V(\sigma) = 0$.

In this case equations (5.21a), (5.21b) are decoupled Ricatti equations and there is a well-known prescription to convert the first order non-linear equation into a second order linear one. The most general Ricatti equation takes the form

$$iK'(\eta) = \alpha_2(\eta)K^2(\eta) + \alpha_1(\eta)K(\eta) + \alpha_0(\eta). \tag{5.22}$$

Our goal is to transform this into a linear equation. Thus write

$$iK(\eta) = \frac{1}{\alpha_2(\eta)}\left(\frac{f'(\eta)}{f(\eta)} - \Delta(\eta)\right), \tag{5.23}$$

where Δ is a term that allows us to at least partially control the final form of the second order equation. Inserting (5.23) into (5.22), we arrive at:

$$f''(\eta) + \left(i\alpha_1 - \frac{\alpha_2'}{\alpha_2} - 2\Delta\right) f'(\eta) + \left(-\alpha_0\alpha_2 - i\alpha_1\Delta + \Delta^2 + \frac{\alpha_2'}{\alpha_2}\Delta - \Delta'\right) f(\eta) = 0 \tag{5.24}$$

We see that we have the freedom to choose Δ to eliminate the term linear in $f'(\eta)$: $2\Delta = i\alpha_1 - \alpha_2'/\alpha_2$. Doing this leads to:

$$f''(\eta) + \Omega^2 f(\eta) = 0,\ \Omega^2 = \frac{1}{4}\alpha_1^2 - \alpha_0\alpha_2 - \frac{i}{2}\alpha_1' + \frac{i\alpha_1\alpha_2'}{2\alpha_2} - \frac{3}{4}\left(\frac{\alpha_2'}{\alpha_2}\right)^2 + \frac{\alpha_2''}{2\alpha_2}. \tag{5.25}$$

Applying this procedure to equation (5.21a) yields

$$f''(\eta) + \left(k^2 - \frac{z''(\eta)}{z(\eta)}\right) f(\eta) = 0, \tag{5.26}$$

which is exactly the mode equation that gives rise to the Bunch-Davies modes for ζ [149]. Likewise, applying the Ricatti procedure to (5.21b) gives us:

$$g''(\eta) + \left(k^2 + a^2(\eta)\ \partial_\sigma^2 V(\sigma)\big|_{\sigma=\sigma_{\min}} - \frac{a''(\eta)}{a(\eta)}\right) g(\eta) = 0, \tag{5.27}$$

where $\sigma_{\min}$ is the location of a minimum of $V(\sigma)$. This is again seen to be the mode equation expected for a massive field.

All three of our kernels satisfy Ricatti equations, so we could generate coupled mode equations as above and solve those. This is what was done in [139, 140, 141], though in the situations discussed there, the entanglement kernel equation was not a Ricatti one, but was already linear. However, as shown in [139], the power spectrum is most directly accessible through the real parts of the kernels and as we are computing the power spectrum numerically, we may as well solve for the kernels directly via equation (5.21).

We *will* need to use the relation between kernels and modes when discussing the initial conditions for the kernels. We will choose to match the *modes* to the standard Bunch-Davies ones at the initial time η_0 at which the entangled evolution begins. This allows us to compare the resulting power spectrum directly with the standard non-entangled case. The Ricatti relation then allows us to use the initial conditions for the modes to get at those for the kernels, although we are taking the initial entanglement to vanish, $C(\eta_0) = 0$. For later reference, we write the real and imaginary parts of a generic kernel in terms of the modes:

$$K_R = \frac{iW\left[f, f^*\right]}{2\alpha_2 \left|f\right|^2} - \frac{\Delta_I}{\alpha_2} \tag{5.28a}$$

$$K_I = -\frac{1}{2\alpha_2}\partial_\eta \ln \left|f\right|^2 + \frac{\Delta_R}{\alpha_2}, \tag{5.28b}$$

where $W\left[f, f^*\right]$ is the Wronskian between the mode and its complex conjugate. This is constant in the non-entangled case, but will not remain so once entanglement is included. However, since we are making use of equations (5.28) only to help set initial conditions for the kernels, we can choose the *initial* value of the Wronskian such that $iW\left[f, f^*\right](\eta_0) = 1$. Using the relationship between Δ and the coefficient functions α_1, α_2, we can write

$$K_R(\eta_0) = \frac{1}{2\alpha_2(\eta_0)}\left(\frac{1}{\left|f(\eta_0)\right|^2} - \alpha_{1R}(\eta_0)\right) \tag{5.29a}$$

$$\begin{aligned} K_I(\eta_0) &= -\frac{1}{2\alpha_2(\eta_0)}\left(\partial_\eta \ln \left|f\right|^2\Big|_{\eta=\eta_0} + \alpha_{1I}(\eta_0) + \frac{\alpha_2'}{\alpha_2}\Big|_{\eta=\eta_0}\right) \\ &= -\frac{1}{2\alpha_2(\eta_0)}\left(\partial_\eta \ln\left(\alpha_2 \ \left|f\right|^2\right)\Big|_{\eta=\eta_0} + \alpha_{1I}(\eta_0)\right), \end{aligned} \tag{5.29b}$$

where we have made use of the fact that for the A_k and B_k kernels, α_2 is real and equal to $2M_{\rm Pl}^2\epsilon/z^2(\eta)D$ for A_k and $2M_{\rm Pl}^2\epsilon/a^2(\eta)D$ for B_k. With the Wronskian condition above,

the relevant modes we will use to match to the Bunch-Davies results at the initial time are:

$$f_\zeta(\eta) = \frac{\sqrt{-\pi\eta}}{2} H^{(2)}_{\nu_\zeta}(-k\eta),\ \nu_\zeta^2 = \frac{9}{4} + 3\epsilon + \frac{3}{2}\eta_{\rm sl} \tag{5.30a}$$

$$g_\chi(\eta) = \frac{\sqrt{-\pi\eta}}{2} H^{(2)}_{\nu_\chi}(-k\eta),\ \nu_\chi^2 = \frac{9}{4} + 3\epsilon - \frac{m^2}{(1-\epsilon)^2 H_{\rm dS}^2}, \tag{5.30b}$$

where $H_{\rm dS}$ is the Hubble parameter of the de Sitter spacetime occurring when $\epsilon = 0$, and $H_{\rm dS} \equiv \mathcal{H}_0/a_0$, a_0 being the initial value of the scale factor and $\mathcal{H}_0$ that of the conformal time Hubble parameter. The mass parameter m^2 will be taken to be $|\partial_\sigma^2 V(\sigma)|$ evaluated at the initial value of σ. This is equivalent to replacing the potential at the initial time by an upright mass term, which then switches to the full potential at η_0.

5.3 The Entangled Power Spectrum and CMB Temperature Anisotropies

We now turn to the main part of our project: to use the entangled state described above to compute the ζ power spectrum and the concomitant CMB temperature anisotropies.

We start by using the results in [139, 140, 141] to write the ζ two-point function as:

$$\langle \zeta_{\vec{k}} \zeta_{\vec{k}'} \rangle = (2\pi)^3 \delta^{(3)}\left(\vec{k} + \vec{k}'\right) \left(\frac{B_{kR}}{2\left(A_{kR} B_{kR} - C_{kR}^2\right)} \right) \equiv (2\pi)^3 \delta^{(3)}\left(\vec{k} + \vec{k}'\right) P_\zeta(k). \tag{5.31}$$

The dimensionless form of the power spectrum [149] is given by

$$\Delta_s^2 = \frac{k^3}{2\pi^2} P_\zeta(k). \tag{5.32}$$

To see that this is in fact dimensionless note that, since $\zeta_{\vec{k}},\ \chi_{\vec{k}}$ have mass dimensions -3 and -2, respectively, the kernels have the following mass dimensions: $[A_k] = 3,\ [B_k] = 1,\ [C_k] = 2$. This means that $P_\zeta(k)$ has dimension -3 and thus Δ_s^2 is indeed dimensionless.

We next turn to the actual problem of solving equations (5.21). The first order of business in solving equations (5.21) numerically is to scale all the kernels and the zero mode to make them dimensionless. We also need to rescale the time variable η. The scale factor for a slow-roll spacetime is approximately given by

$$a(\eta) = a_0 \left(-\frac{1}{(1-\epsilon)\mathcal{H}_0 \eta} \right)^{\frac{1}{1-\epsilon}} = a_0 \left(\frac{\eta_0}{\eta} \right)^{\frac{1}{1-\epsilon}}, \tag{5.33}$$

where η_0 is to related to $\mathcal{H}_0$ via $(1-\epsilon)\mathcal{H}_0\eta_0 = -1$. Physically, we can choose to have η_0 vary from being the time at which the largest length scale appearing on the CMB sky leaves the horizon to being a time in which shorter scales or higher wave numbers leave the horizon. The main physical constraint is that of having the energy density due to the difference between the entangled state and the Bunch-Davies state be small enough to allow for a sufficient number of e-folds to occur. Beyond this, we would treat η_0 as part of the set of parameters one would estimate. When considering the sample situations discussed below, we will let η_0 vary so as to exhibit the changes that would occur in the different measured power spectra.

We scale the time and wavenumbers as:

$$\tau = -\frac{\eta}{\eta_0},\ q = \frac{k}{k_0} = \frac{k}{\mathcal{H}_0} = -(1-\epsilon)k\eta_0. \tag{5.34}$$

Note that, since the conformal times are all negative, τ runs from -1 to 0.

The scalings of A_k and B_k are essentially dictated by the parts of equations (5.21a), (5.21b) in the first set of brackets, i.e., those that would have been present even in the absence of entanglement. We define dimensionless kernels $\tilde{A}_q,\ \tilde{B}_q$ as:

$$A_k(\eta) = \frac{z(\eta)^2}{(-\eta_0)}\tilde{A}_q(\tau) \tag{5.35a}$$

$$B_k(\eta) = \frac{a^2(\eta)}{(-\eta_0)}\tilde{B}_q(\tau), \tag{5.35b}$$

where $z(\eta)$ is defined in equation (5.20). Given the dimensions of A_k and B_k, we see that $\tilde{A}_q,\ \tilde{B}_q$ are indeed dimensionless. For C_k we use a combination of $z(\eta)$ and the scale factor,

$$C_k(\eta) = \frac{z(\eta)a(\eta)}{(-\eta_0)}\tilde{C}_q(\tau). \tag{5.35c}$$

In terms of the dimensionless kernels and wavenumbers, the dimensionless power spectrum in (5.32) is given by:

$$\Delta_s^2 = A_s\left(q^3(-\tau)^{2\nu_\zeta - 1}\right)\left(\frac{\tilde{B}_{qR}}{\tilde{A}_{qR}\tilde{B}_{qR} - \tilde{C}_{qR}^2}\right), \tag{5.36}$$

where

$$A_s = \left(\frac{H_{dS}^2}{8\pi^2\epsilon(1-\epsilon)M_{\rm Pl}^2}\right). \tag{5.37}$$

We have also used the definitions of q and τ above as well as that of z in terms of the scale factor, ϵ and $M_{\rm Pl}$, in addition to the relation $(1-\epsilon)\mathcal{H}_0\eta_0 = -1$. We see that the dimensionless time τ makes an explicit appearance here. Since we are *not* assured that the modes become frozen after horizon crossing, we will evaluate Δ_s^2 in the late time limit $\tau \to 0^-$. As discussed in [150], the horizon crossing approximation requires certain conditions to be met and these do not obtain in our situation.

The zero mode should be made dimensionless as well. We choose to use the Planck mass to scale σ with: $\sigma(\eta) = M_{\rm Pl} s(\tau)$. We also construct a dimensionless version of the potential: $V(\sigma) = \Lambda^4 \bar{V}(s)$, where Λ is the natural energy scale associated with $V(\sigma)$. Each derivative of $V(\sigma)$ with respect to σ corresponds to a derivative of $\bar{V}(s)$ with respect to s with a factor of $M_{\rm Pl}$ appropriately inserted.

The final task to accomplish is to now rewrite the kernel equations (5.21) in terms of dimensionless quantities:

$$\begin{aligned} i\partial_\tau \tilde{A}_q(\tau) =& \frac{i(2+\eta_{\rm sl})}{\tau(1-\epsilon)}\tilde{A}_q + \left[-\left(\frac{q}{1-\epsilon}\right)^2 + \tilde{A}_q^2 \right] \\ &+ \frac{1}{\bar{D}}\left[(1-\epsilon)(-\tau\partial_\tau s)\tilde{A}_q + \sqrt{2\epsilon}\,\tilde{C}_q + \frac{i}{2}\left((3-\epsilon)\partial_\tau s + \frac{\mu^2}{1-\epsilon}\left(-\frac{\partial_s \bar{V}(s)}{\tau} \right) \right) \right]^2 , \end{aligned} \tag{5.38a}$$

$$\begin{aligned} i\partial_\tau \tilde{B}_q(\tau) =& \frac{2i}{\tau(1-\epsilon)}\tilde{B}_q + \left[-\left(\left(\frac{q}{1-\epsilon}\right)^2 + \frac{\mu^2\,\partial_s^2 \bar{V}(s)}{\tau^2(1-\epsilon)^2} \right) + \tilde{B}_q^2 \right] \\ &- \left[(3-\epsilon)\,(\partial_\tau s)^2 - \frac{2\mu^2\,\partial_\tau s}{\tau(1-\epsilon)}\partial_s \bar{V}(s) \right] \\ &+ \frac{1}{\bar{D}}\left[(1-\epsilon)(-\tau\partial_\tau s)\tilde{B}_q + \sqrt{2\epsilon}\,\tilde{C}_q - \frac{i}{2}\left((3-\epsilon)\partial_\tau s + \frac{\mu^2}{1-\epsilon}\left(-\frac{\partial_s \bar{V}(s)}{\tau} \right) \right) \right]^2 , \end{aligned} \tag{5.38b}$$

$$
\begin{aligned}
i\partial_\tau \tilde{C}_q(\tau) =& \frac{i(4+\eta_{\rm sl})}{2\tau(1-\epsilon)}\tilde{C}_q + \frac{\sqrt{2\epsilon}}{\bar{D}}\left[\sqrt{2\epsilon}\,\tilde{C}_q\left(\tilde{A}_q+\tilde{B}_q\right) + (1-\epsilon)(-\tau\partial_\tau s)\left(\tilde{C}_q^2+\tilde{A}_q\tilde{B}_q\right)\right] \\
&+ \frac{\sqrt{2\epsilon}}{\bar{D}}\left[\left(-\tilde{A}_q+\tilde{B}_q\right)\left(\frac{i}{2}\left((3-\epsilon)\partial_\tau s + \frac{\mu^2}{1-\epsilon}\left(-\frac{\partial_s\bar{V}(s)}{\tau}\right)\right)\right)\right] \qquad (5.38c) \\
&- \frac{1}{\bar{D}\sqrt{2\epsilon}}(1-\epsilon)(-\tau\partial_\tau s)\left[\frac{i}{2}\left((3-\epsilon)\partial_\tau s + \frac{\mu^2}{1-\epsilon}\left(-\frac{\partial_s\bar{V}(s)}{\tau}\right)\right)\right]^2 \\
&+ \left[\sqrt{\frac{\epsilon}{2}}\frac{\mu^2}{(1-\epsilon)^2\tau^2}\partial_s\bar{V}(s) + \frac{(1-\epsilon)}{\sqrt{2\epsilon}}(-\tau\partial_\tau s)\left(\left(\frac{q}{1-\epsilon}\right)^2 + \frac{\mu^2\,\partial_s^2\bar{V}(s) - \epsilon\,\eta_{\rm sl}}{2\tau^2(1-\epsilon)^2}\right)\right],
\end{aligned}
$$

where $\bar{D} = 2\epsilon - (1-\epsilon)^2(-\tau\partial_\tau s)^2$, and $\mu^2 = \Lambda^4/(M_{\rm Pl}^2 H_{dS}^2)$.

The zero mode equation also needs to be made dimensionless, but this is easily done:

$$
\partial_\tau^2 s - \frac{2}{\tau(1-\epsilon)}\partial_\tau s + \frac{\mu^2}{\tau^2(1-\epsilon)^2}\partial_s\bar{V}(s) = 0. \qquad (5.39)
$$

We turn next to the initial conditions for the kernels. While we have already discussed this above, there are a few points worth focusing on. Our aim is to be able to compare our results with the standard inflationary ones, i.e., for similar parameters $\epsilon, \eta_{\rm sl}$, we want to extract the effect of non-trivial entanglement relative to the no-entanglement case. Thus, we'll choose the entanglement kernel to vanish initially, so that it is generated only by dint of the behavior of the zero mode. Thus $C_k(\eta_0) = 0$, or in terms of the dimensionless quantities above, $\tilde{C}_q(\tau = -1) = 0$. The initial conditions of the zero mode are taken to be free parameters: $s(\tau = -1) = s_0,\ \partial_\tau s|_{\tau=-1} = v_0$.

For the A_k, B_k kernels we follow the discussion leading to equations (5.29). We can either view the entangled inflationary phase as arising during the last $55-60$ e-folds of inflation, so that the initial conditions are set by the prior phase of non-entangled inflation, or inflation only lasts the minimal amount needed in order to solve the horizon and flatness problems and we choose the initial conditions to be as to close to the non-entangled case as possible. Either way, we arrive at equations (5.29) with

$$
\alpha_{1A}(\eta_0) = \frac{i}{D_0}\left(\frac{\sigma'(\eta_0)}{\mathcal{H}_0}\right)\left((3-\epsilon)\sigma'(\eta_0) + \frac{a_0^2 V'(\sigma_0)}{\mathcal{H}_0}\right),\ \alpha_{2A}(\eta_0) = \frac{1}{a_0^2 D_0}, \qquad (5.40)
$$

for the A_k kernel and $\alpha_{1B}(\eta_0) = -\alpha_{1A}(\eta_0),\ \alpha_{2B}(\eta_0) = (2M_{\rm PL}^2\epsilon)\,\alpha_{2A}(\eta_0)$ for the B_k kernel. Here D_0 is the initial value of the quantity D defined in equation (5.20) and we have

made use of the vanishing of the initial entanglement. From this, equations (5.29), and the definitions of the dimensionless kernels equations (5.38), we can write the initial conditions for the real and imaginary parts of the $\tilde{A}_q, \tilde{B}_q$ kernels:

$$\tilde{A}_{qR}(\tau=-1) = \left(\frac{\bar{D}_0}{2\epsilon}\right)\left(\frac{2}{\pi\left|H^{(2)}_{\nu_\zeta}(\frac{q}{1-\epsilon})\right|^2}\right) \tag{5.41a}$$

$$\begin{aligned}\tilde{A}_{qI}(\tau=-1) =& \frac{\bar{D}_0}{4\epsilon(1-\epsilon)}\left(3-\epsilon+q\,\partial_x \ln\left|H^{(2)}_{\nu_\zeta}(x)\right|^2\Big|_{x=\frac{q}{1-\epsilon}}\right) + \frac{\eta_{\rm sl}}{2(1-\epsilon)} + \\ &+ \frac{\eta_{\rm sl}v_0^2}{2} + \frac{v_0}{4\epsilon}\left((1-\epsilon)(3-\epsilon)v_0 + \mu^2\,\partial_s\bar{V}(s)\big|_{s=s_0}\right),\end{aligned} \tag{5.41b}$$

where we recall $\partial_\tau s|_{\tau=-1} = v_0$ and $\bar{D}_0 = 2\epsilon - (1-\epsilon)^2 v_0^2$. An interesting point to note concerns the factors of ϵ in the denominators of both equations (5.38) and equations (5.41). These seem worrisome in the $\epsilon \to 0$ limit; however in this case ζ is a pure gauge degree of freedom so our analysis is moot.

A similar analysis for the $\tilde{B}_q$ kernel yields

$$\tilde{B}_{qR}(\tau=-1) = \left(\frac{\bar{D}_0}{2\epsilon}\right)\left(\frac{2}{\pi\left|H^{(2)}_{\nu_\chi}(\frac{q}{1-\epsilon})\right|^2}\right) \tag{5.42a}$$

$$\begin{aligned}\tilde{B}_{qI}(\tau=-1) =& \frac{\bar{D}_0}{4\epsilon(1-\epsilon)}\left(3-\epsilon+q\,\partial_x \ln\left|H^{(2)}_{\nu_\chi}(x)\right|^2\Big|_{x=\frac{q}{1-\epsilon}}\right) + \frac{(1+\epsilon)v_0^2}{4\epsilon}\eta_{\rm sl} + \\ &+ \frac{3v_0}{4\epsilon}\left((1-\epsilon)(3-\epsilon)v_0 + \mu^2\,\partial_s\bar{V}(s)\big|_{s=s_0}\right).\end{aligned} \tag{5.42b}$$

Before turning to the numerical solution to these equations, we enumerate the various constraints we need to satisfy in order that we may treat the field Σ as a spectator field. First, its energy density should be much less than that of the inflaton:

$$V(\sigma) \ll M_{\rm Pl}^2 H_{\rm dS}^2, \tag{5.43a}$$

and second, the kinetic energy of the inflaton, encoded in the quantity $z(\eta)$ above should be larger than that of the spectator

$$\left(\frac{\sigma'}{\mathcal{H}}\right)^2 \ll 2M_{\rm Pl}^2\epsilon. \tag{5.43b}$$

In terms of the dimensionless quantities introduced earlier, these constraints become:

$$\bar{V}(s) \ll \frac{1}{\mu^2}, \tag{5.44a}$$

$$|-\tau \partial_\tau s| \ll \frac{\sqrt{2\epsilon}}{1-\epsilon}. \tag{5.44b}$$

There is another constraint we have to satisfy. We require that the wavefunctional be normalizable. For each $\vec{k}$ we demand

$$\int \Pi_{\vec{k}}\, \mathcal{D}^2\zeta_{\vec{k}}\, \mathcal{D}^2\chi_{\vec{k}}\ \left|\Psi\left[\left\{\zeta_{\vec{k}}\right\}, \left\{\chi_{\vec{k}}\right\}; \eta\right]\right|^2 < \infty, \tag{5.45}$$

where the wavefunctional is given in equation (5.12). This requirement is equivalent to that of demanding that the two eigenvalues of

$$\mathcal{K}_{kR}(\eta) = \begin{pmatrix} A_{kR}(\eta) & C_{kR}(\eta) \\ C_{kR}(\eta) & B_{kR}(\eta) \end{pmatrix}, \tag{5.46}$$

be positive. This in turn is equivalent to demanding both that $A_{kR}(\eta) + B_{kR}(\eta)$ be positive, as well as that the determinant $A_{kR}(\eta)B_{kR}(\eta) - C_{kR}^2(\eta)$ also be positive. The first constraint holds automatically as can be seen using the Ricatti trick as in equations (5.28). In our case $\alpha_{1R}(\eta) = 0$ for both the A and B kernels and $\alpha_2(\eta)$ is positive as long as equations (5.43) hold, so that both $A_{kR}(\eta)$ and $B_{kR}(\eta)$ are proportional to the modulus squared of a mode, with positive proportionality constants. The determinant constraint has to be checked during the time evolution.

We will consider two different potentials for the spectator: a mass term and an axion-type periodic potential. For each case, we will choose some parameters that help display interesting features of the power spectrum as well as the TT and TE CMB anisotropies. In this work, we will *not* perform an exhaustive parameter search, deferring that to later work.

We turn to the task of obtaining the power spectrum as given in equation (5.36) and from thence obtaining the various CMB anisotropies power spectra. For this last step, we use the CLASS Boltzmann solver [151].

The standard, non-entangled, scalar inflationary power spectrum is typically written

as[1]:

$$\Delta_s^2(k) = A_{s,k}\left(\frac{k}{k_{\rm piv}}\right)^{n(k)}, \tag{5.47}$$

where $k_{\rm piv}$ is the pivot scale and $n(k) = n_s - 1$ if one ignores the running of the spectral index n_s [20].

When our code generates the dimensionless power spectrum, $\Delta_s^2(q)$, (see equation (5.36)), we actually calculate and plot it in units of A_s, so we are in actuality plotting a parameter

$$\tilde{\Delta}_s^2(q) = \left(q^3(-\tau)^{2\nu_\zeta - 1}\right)\left(\frac{\tilde{B}_{qR}}{\tilde{A}_{qR}\tilde{B}_{qR} - \tilde{C}_{qR}^2}\right). \tag{5.48}$$

To compare this with the latest Planck CMB data release [20], we need to find a parameter, f, such that the following is true for the non-entangled case of our equations:

$$f\tilde{\Delta}_{s,\rm NE}^2(q) = \Delta_s^2(k) = A_{s,k}\left(\frac{k_0 q}{k_{\rm piv}}\right)^{n_s - 1}, \tag{5.49}$$

where we used the conversion $k = qk_0$ from equation (5.34) and substituted $n(k)$ for $n_s - 1$ for simplicity. Using Planck values [20] for $A_{s,k}$, n_s, and $k_{\rm piv}$, we can determine f and then employ it to rescale our data.

For both the non-entangled and entangled cases, where $k_0 = 10^{-6}$ Mpc^{-1} is chosen to be the largest observable scale, the parameter f described above allows us to rescale $\tilde{\Delta}_s^2(q)$. Since the entangled power spectra are in essence corrections around a non-entangled baseline, it makes sense to use the non-entangled value to rescale them as well. We then input the resulting $\Delta_s^2(k)$ into CLASS to generate the C_l plots in the subsequent sections. For the cases where we shift the onset of entanglement—which corresponds to shifting k_0 as discussed in section 5.3.3—we obtain a slightly different f in equation (5.49), but otherwise the data processing is exactly the same as the non-shifted case.

5.3.1 Free Massive Scalar

We start by considering the case of a free massive spectator scalar: $V(\sigma) = m^2\sigma^2/2$. In this case, $\Lambda^4 = M_{\rm Pl}^2 m^2$, $\mu^2 = m^2/H_{\rm dS}^2$ and $\bar{V}(s) = s^2/2$.

[1]We have adjusted notation slightly from equation (38a) in [20] here, to make a smoother comparison with our equations.

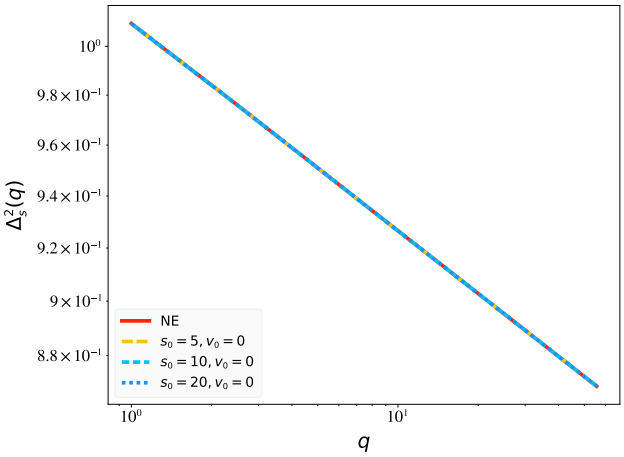

(a) $\mu = 0.01,\ v_0 = 0$

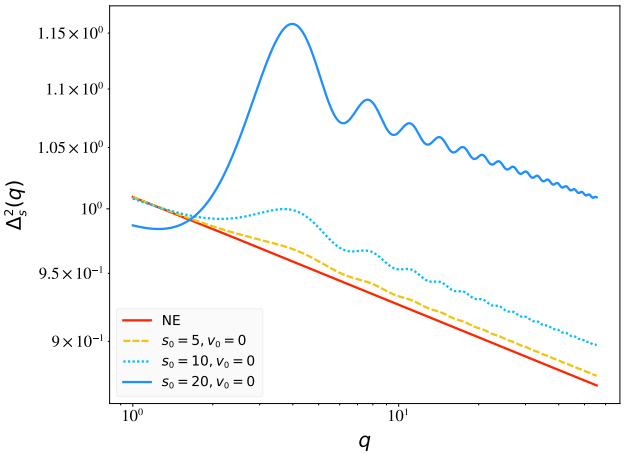

(b) $\mu = 0.1,\ v_0 = 0$

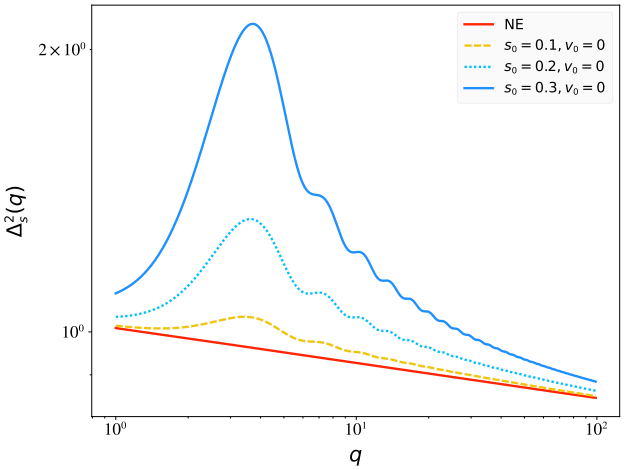

(c) $\mu = 1,\ v_0 = 0$

Figure 5.1: Log-log plots of the power spectrum Δ_s^2 plotted in units of A_s as a function of $q = k/\mathcal{H}_0$, for different values of μ and s_0. In all cases, v_0 is taken to be 0 while $\mu = 0.01, 0.1$, or 1 in (a), (b), and (c), respectively.

In Figure 5.1 we see that, for low enough μ and $v_0 = 0$, the power spectra for the differing values of the initial field do not vary significantly from the non-entangled case $(s_0 = 0, v_0 = 0)$. However, as soon as $\mu \sim 0.1$, features manifest themselves. In particular, damped oscillatory behavior is superposed over the non-entangled power spectrum; there is also an enhancement in the power after $q \sim 2$. For particularly high values of μ the oscillations are not only damped but, after an initial enhancement of power, the entangled power spectrum decays to match the non-entangled one for higher q values (see also Figure 5.5).

What happens as we allow for non-zero v_0? In Figure 5.2, we see that we once again

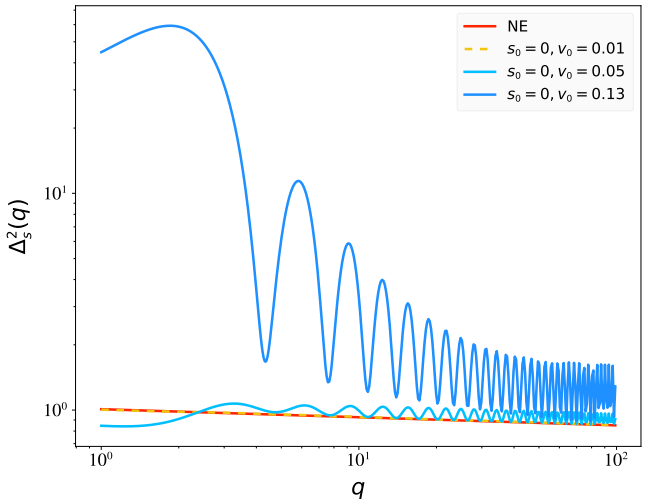

Figure 5.2: Log-log plot of the power spectrum Δ_s^2 plotted in units of A_s as a function of $q = k/\mathcal{H}_0$, for $s_0 = 0$, $\mu = 0.01$, and different choices of v_0.

generate oscillations in the power spectrum. The value $v_0 = 0.13$ is near the boundary delineated in equation (5.44b). For this case, the damped regime of the oscillations lasts for a couple of decades in q. But for the value $v_0 = 0.05$ the damped regime is shorter. In both cases, the oscillations stabilize at large enough q and the troughs of the oscillations eventually sit directly on top of the non-entangled power spectrum, (see also Figure 5.6 for the case $v_0 = 0.05$), though it takes the higher v_0 value longer to exhibit this behavior.

We can use these power spectra as initial conditions for a Boltzmann solver to the various CMB power spectra. In this paper we used CLASS [151] to generate the TT and TE power spectra, given our dimensionless power spectra data and the data processing

described in section 5.3. For the TT and TE graphs generated in CLASS, we look at the unlensed power spectra, with input values for h_0, Ω_b and other required parameters taken from the unlensed values in Table 2 of [20]. We then compare our results with Planck data in the resulting graphs. For this portion of our analysis, we chose a representative subset of the initial parameters that generate the primordial power spectra in Figures 5.1 - 5.2 to investigate the range of possible effects on the CMB power spectra.

Figure 5.3 shows the primordial spectra in k for the standard non-entangled case and the entangled case with $\mu = 0.01$, $s_0 = 10$, and $v_0 = 0$. The corresponding TT and TE angular power spectra are also shown and compared with data from Planck [20]. Predictably, since the primordial power spectra for the entangled and non-entangled case are identical by eye for these parameters, the TT and TE spectra are also indistinguishable. For this set of parameters, one could argue it is hard to tell whether Planck is "seeing" evidence of the BD state or evidence of a state of entanglement with a low mass scalar, since both scenarios appear observationally indistinguishable.

Figure 5.4 provides the same information as the previous figure, except that the entangled case has the following parameters: $\mu = 0.1$, $s_0 = 10$, and $v_0 = 0$. This is the higher-mass version of Figure 5.3 and the differences between the entangled and non-entangled cases are more apparent here. The oscillations in the primordial spectrum for the entangled case quickly damp out and no real oscillations are apparent in the resulting TT spectra. There is an enhancement of power in the peaks of the TT spectrum for the entangled case that puts this set of parameters just outside observational bounds by eye (given the constraints of our analysis). The rest of the curve, however, is well within the error bars of the Planck data. The TE power spectra are barely distinguishable from one another. A full parameter analysis, which we postpone to future work, would be able to determine whether this set of parameter values is truly ruled out by the data or not.

The results in Figure 5.5, which are the same comparisons as the previous two figures for the entangled case $\mu = 1$, $s_0 = 0.3$, and $v_0 = 0$, are curious. Despite the large enhancement of power for low k in the primordial power spectrum in the entangled case, the resulting TT and TE spectra are indistinguishable by eye from the standard non-

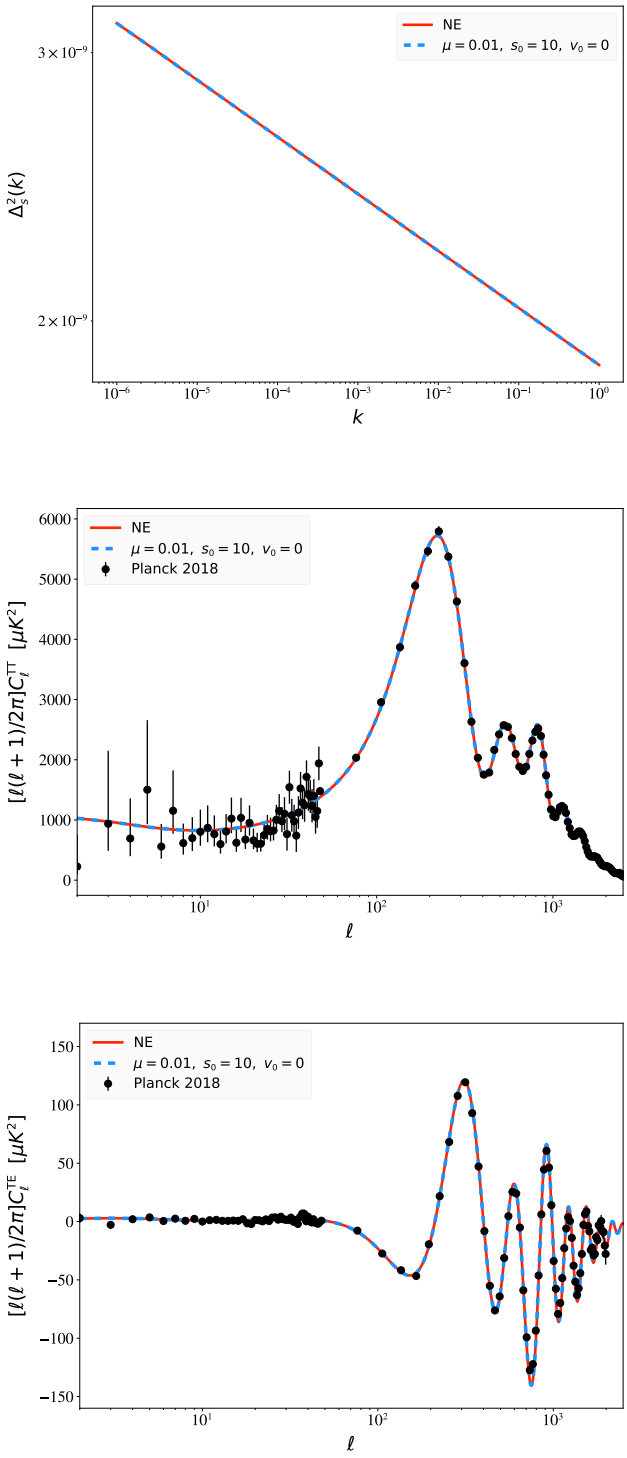

Figure 5.3: The primordial power spectrum (top), the unlensed TT power spectrum (middle), and the unlensed TE power spectrum (bottom) for $\mu = 0.01$, $s_0 = 10$, and $v_0 = 0$. In all cases, the power spectra are compared with the non-entangled versions originating from the use of a Bunch-Davies state in the models. The angular power spectra (middle and bottom) are also compared with the CMB data from Planck.

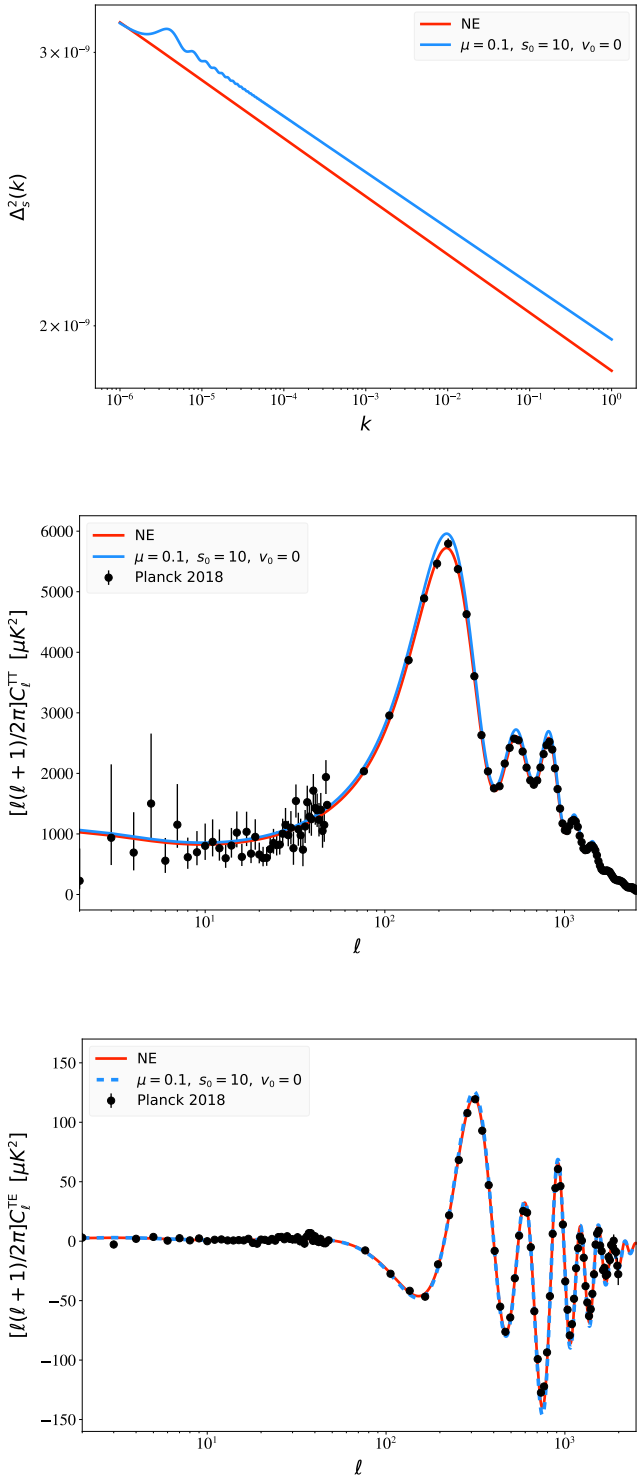

Figure 5.4: The primordial power spectrum (top), the unlensed TT power spectrum (middle), and the unlensed TE power spectrum (bottom) for $\mu = 0.1$, $s_0 = 10$, and $v_0 = 0$. As in Figure 5.3, non-entangled power spectra are also displayed (all subfigures) in addition to the CMB data from Planck (middle and bottom figures only).

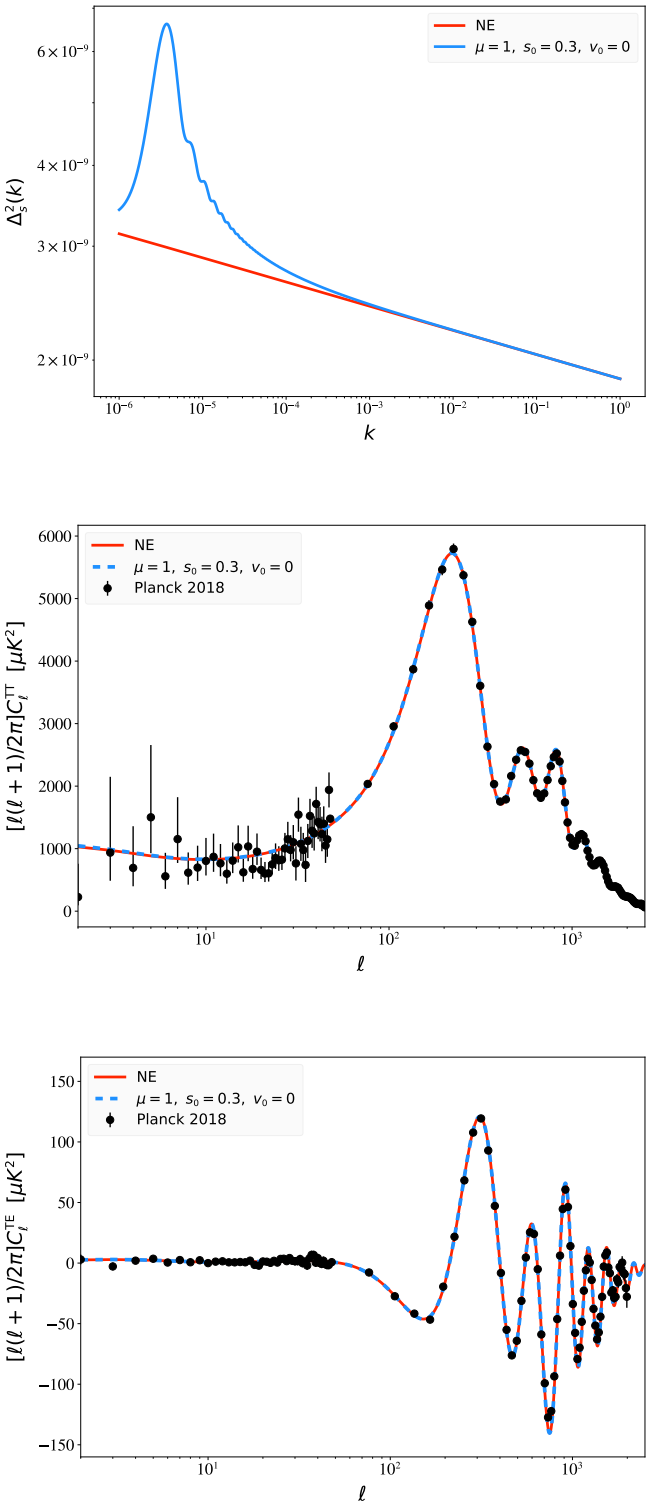

Figure 5.5: The primordial power spectrum (top), the unlensed TT power spectrum (middle), and the unlensed TE power spectrum (bottom) for $\mu = 1$, $s_0 = 0.3$, and $v_0 = 0$. All the subfigures presented are similar to those in Figures 5.3 and 5.4 but for a new set of parameter values μ and s_0.

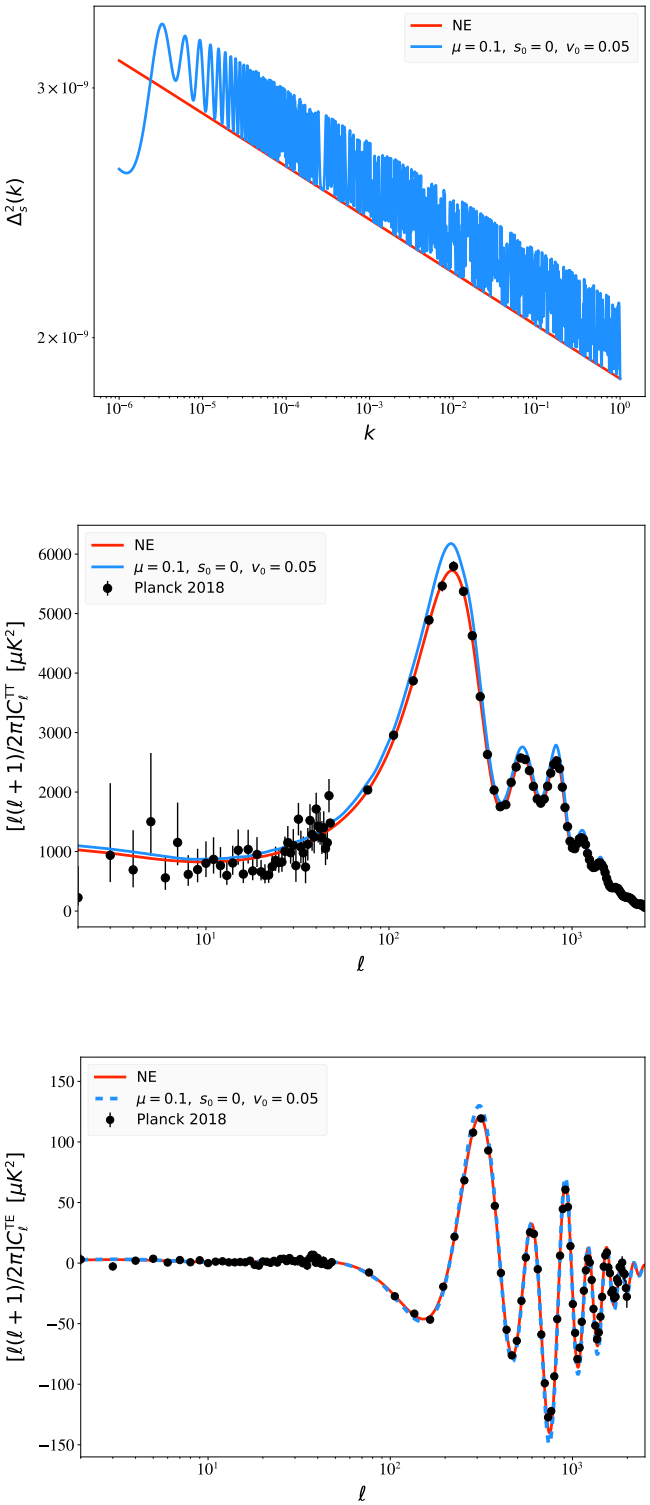

Figure 5.6: The primordial power spectrum (top), the unlensed TT power spectrum (middle), and the unlensed TE power spectrum (bottom) for $\mu = 0.1$, $s_0 = 0$, and $v_0 = 0.05$. All the curves shown are comparable to the ones displayed in Figures 5.3, 5.4, and 5.5 for different choices of parameter values μ, s_0, and v_0.

entangled result. Unlike the outcomes in Figure 5.3, these results are a more dramatic instance of asking whether Planck data can distinguish the BD state from an entangled state. The primordial spectrum here is noticeably different in the entangled case, yet it seems to have no effect on the TT and TE spectra. It was the results of this set of parameters that provoked us to explore changing the onset of entanglement—to see what would happen if we shift features around to effectively higher k values—which we explore in section 5.3.3.

Lastly, Figure 5.6 explores an entangled case with a non-zero initial velocity. For the parameters $\mu = 0.1$, $s_0 = 0$, and $v_0 = 0.05$, the effect is to have high frequency oscillations for the majority of the observable k range in the entangled primordial power spectrum, which translates to a TT spectrum that sits above the non-entangled case. While the distance from the non-entangled TT spectrum is not constant—so one might be able to argue the presence of some oscillations—overall the oscillations from the entangled primordial spectrum appear averaged over. More of the entangled TT spectrum is outside the bounds of Planck compared to Figure 5.4. Furthermore, the TE spectrum overshoots several peaks. This is likely a set of parameters that a full parameter estimation would be able to reject.

5.3.2 Axion Spectator Field

Axions in the early universe are well motivated (see e.g. [152]), so a spectator field with an axion-like potential also merits consideration. We take the potential to be of the form

$$V(\sigma) = \Lambda^4 \left(1 - \cos\left(\frac{\sigma}{f_a}\right)\right), \tag{5.50}$$

where Λ^4 is the energy density associated with the potential and f_a the axion decay constant. Note that this need not be the QCD axion. It follows that the dimensionless potential $\bar{V}(s)$ is then given by:

$$\bar{V}(s) = 1 - \cos\left(s/\tilde{f}_a\right), \tag{5.51}$$

where $\tilde{f}_a = f_a/M_{\rm Pl}$ and the dimensionless mass squared term corresponds to $\mu^2 = \Lambda^4/(M_{\rm Pl}^2 H_{\rm dS}^2)$.

In addition to varying μ, s_0, and v_0, the behavior of the spectator can also change depending on the choice of $\tilde{f}_a$. We illustrate some of these variations in the subsequent figures. Since a full analysis of all possible initial conditions is beyond the scope of this paper, we restrict ourselves to parameters that provide interesting behaviors distinct from the free massive scalar case.

In Figure 5.7, we see different patterns of oscillations for the same initial condition of $s_0 = \tilde{f}_a(\frac{\pi}{2} - 0.01)$ and $v_0 = 0$, depending on the choice of μ and $\tilde{f}_a$. For the choice $\tilde{f}_a = 0.01$ (Figure 5.7a), we see higher values of μ generate more oscillations with a larger amplitude for low q. However, in all cases shown these oscillations damp out and coalesce so that the high q (or k) primordial power spectrum is indistinguishable from the non-entangled case (see also Figure 5.9). In contrast, for the case $\tilde{f}_a = 0.05$ shown in Figure 5.7b (for the same masses and initial condition as Figure 5.7a) we observe a different behavior. After an initial enhancement of power for low q, oscillations damp out and decay in a manner reminiscent of Figure 5.1c. We see larger initial enhancements of power for larger masses.

Since the behaviors in Figure 5.7a are more distinct from the free massive scalar results, we also investigated the effect of adding a small non-zero v_0 to those initial conditions. The result is shown in Figure 5.8. The pattern of large initial oscillations that damp out is still present, although their form is modified compared to Figure 5.7a. However, we notice that the cases shown all exhibit the same behavior at higher q values, after the initial oscillations damp out, regardless of the value of μ. These high q oscillations have an approximately constant amplitude, and their location relative to the non-entangled case is similar to Figure 5.6.

Figure 5.9 investigates the effect of an axion-like potential with $\tilde{f}_a = 0.01$ for the entangled parameters $\mu = 0.07$, $s_0 = \tilde{f}_a(\frac{\pi}{2} - 0.01)$, and $v_0 = 0$ on the CMB power spectra. Similar to what occurred with Figure 5.5, there is no difference in the TT and TE spectra between the non-entangled case and entangled case, despite clear features in the primordial entangled power spectrum for these parameters. This is another case where BD and an entangled state both appear to be equally good fits to the Planck data, though obviously a full parameter estimation would be needed to push the case further.

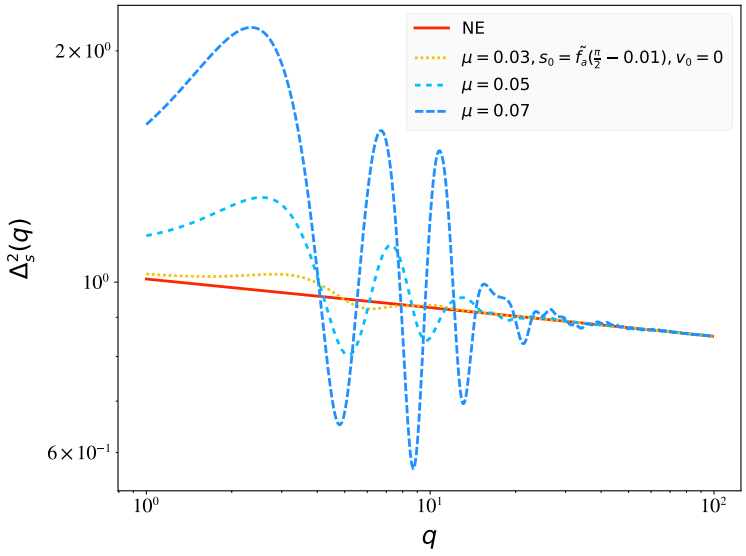

(a) $\tilde{f}_a = 0.01$

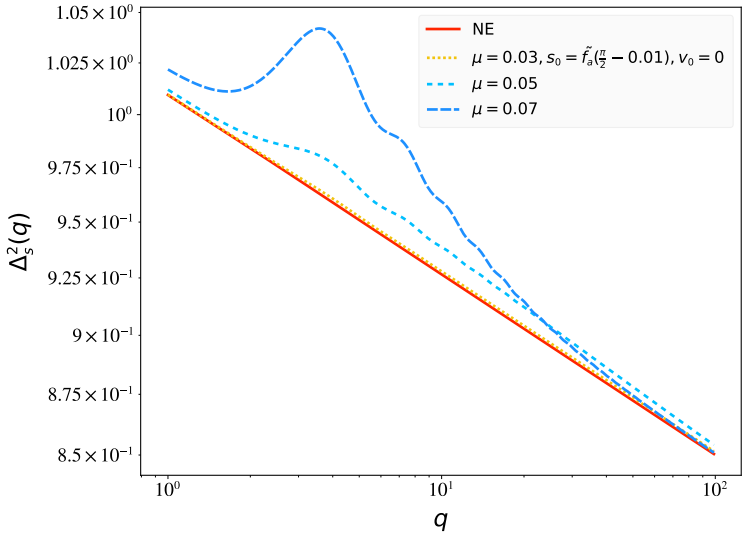

(b) $\tilde{f}_a = 0.05$

Figure 5.7: Log-log plots of the power spectrum Δ_s^2 plotted in units of A_s as a function of $q = k/\mathcal{H}_0$. Here, we compare the impact of adjusting $\tilde{f}_a$ for the axion-like potential on a variety of masses, given the initial condition $s_0 = \tilde{f}_a(\frac{\pi}{2} - 0.01)$ and $v_0 = 0$. We take $\tilde{f}_a = 0.01$ in (a) and $\tilde{f}_a = 0.05$ in (b).

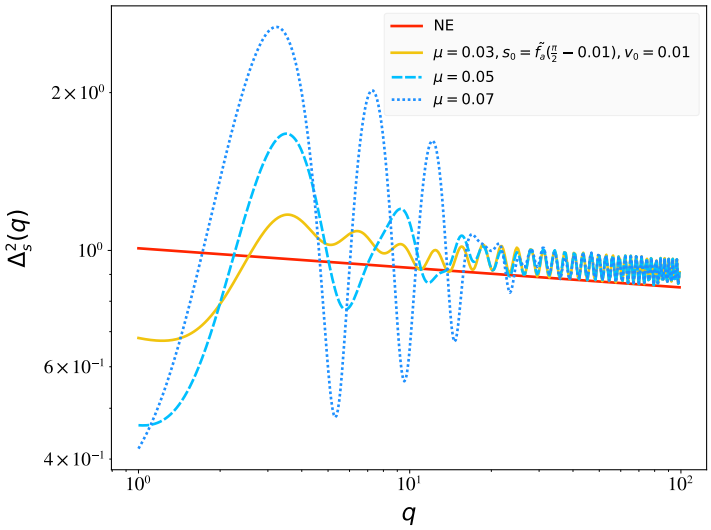

Figure 5.8: Log-log plot of the power spectrum for $s_0 = \tilde{f}_a(\frac{\pi}{2} - 0.01)$, $v_0 = 0.01$, $\tilde{f}_a = 0.01$, and different choices of μ.

As with Figure 5.5, the features in the primordial spectrum occur for low k, so in the next section we investigate what happens to the various power spectra if one changes the onset of entanglement.

5.3.3 Shifting the Onset of Entanglement

As seen above, despite the presence of large changes in the primordial power spectrum for certain parameter choices, surprisingly only small differences were reflected in the CMB anisotropies. One conjecture is that this is due to the fact that we have set the onset of entanglement to coincide with the exiting of the largest length scale appearing on the CMB sky. To check this, we allow for the onset time, set by η_0, to correspond to smaller scales. Thus, we take η_0 to correspond to times well within the last 55 e-folds of inflation, with standard Bunch-Davies inflation being the initial condition.

By the conversions in equation (5.34), shifting the onset of entanglement (shifting η_0), translates to shifting k_0 in our code, where k_0 is the largest observable scale that will show evidence of entanglement. The results of our investigations for various values of k_0, effectively shifting non-standard features to higher k values, are shown in Figures 5.10 - 5.12.

Figure 5.10 explores shifting the onset of entanglement for the free massive scalar po-

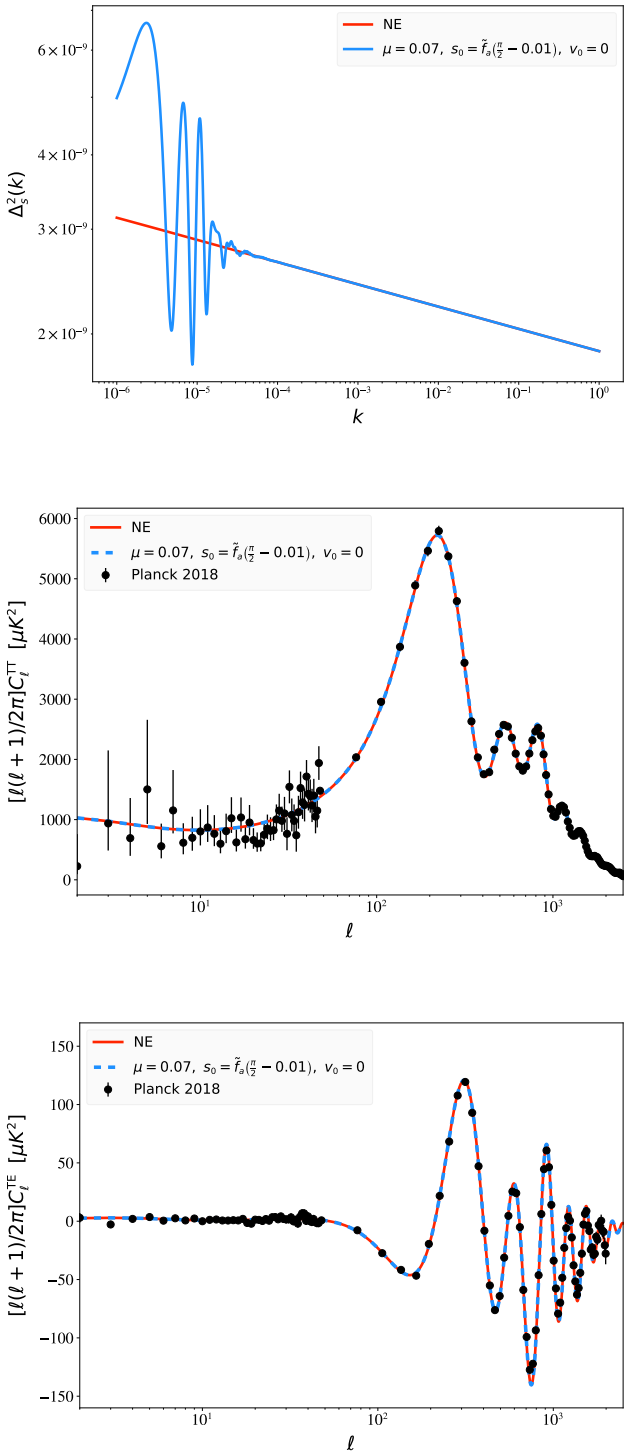

Figure 5.9: The primordial power spectrum (top), the unlensed TT power spectrum (middle), and the unlensed TE power spectrum (bottom) for $\mu = 0.07$, $s_0 = \tilde{f}_a(\frac{\pi}{2} - 0.01)$, and $v_0 = 0$, with $\tilde{f}_a = 0.01$. In all plots, the power spectra are compared with their Bunch-Davies counterparts. Additionally, the angular power spectra (middle and bottom) are compared with the CMB data from the Planck collaboration.

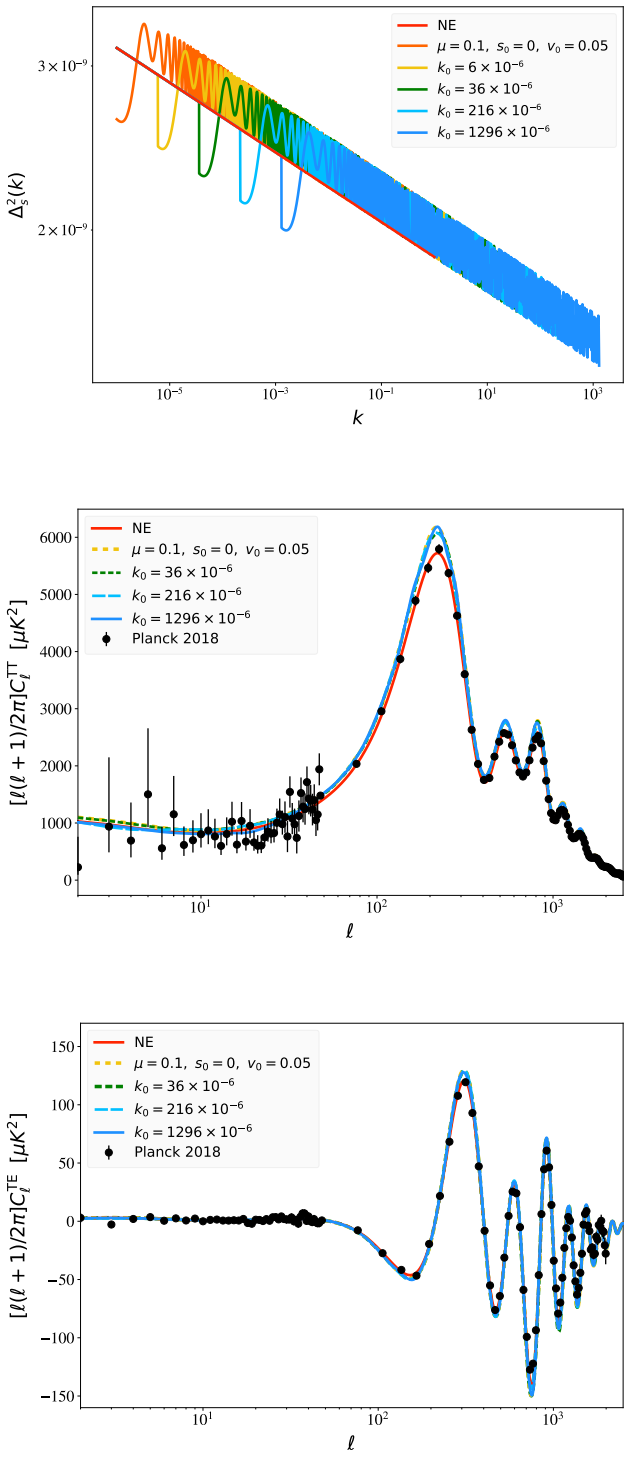

Figure 5.10: The primordial power spectrum (top), the unlensed TT power spectrum (middle), and the unlensed TE power spectrum (bottom) for an entangled state involving a free massive scalar field with $\mu = 0.1$, $s_0 = 0$, and $v_0 = 0.05$, for various values of k_0, compared with the non-entangled case (all subfigures) and CMB data from Planck (middle and bottom subfigures only).

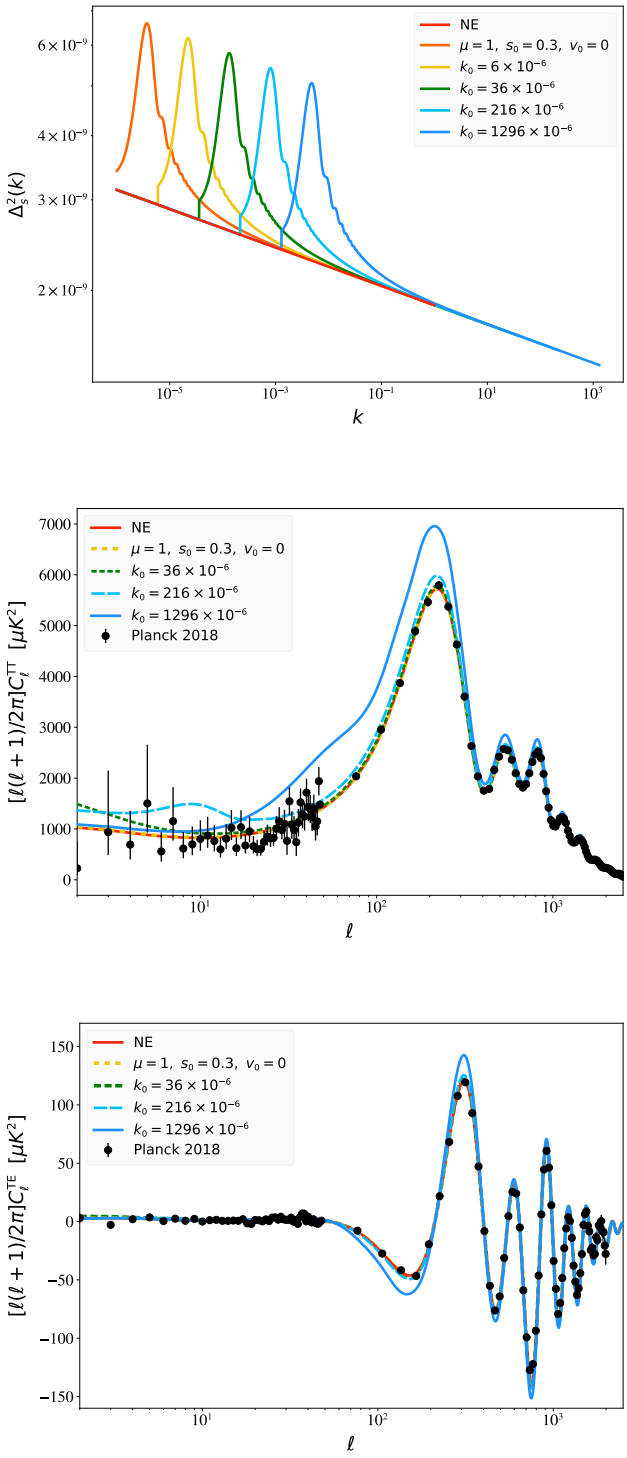

Figure 5.11: The primordial power spectrum (top), the unlensed TT power spectrum (middle), and the unlensed TE power spectrum (bottom) for an entangled state involving a free massive scalar field with $\mu = 1$, $s_0 = 0.3$, and $v_0 = 0$, for various values of k_0. As in Figure 5.10, the non-entangled power spectra are plotted in all subfigures. Furthermore, the Planck CMB data is displayed in the middle and bottom subfigures.

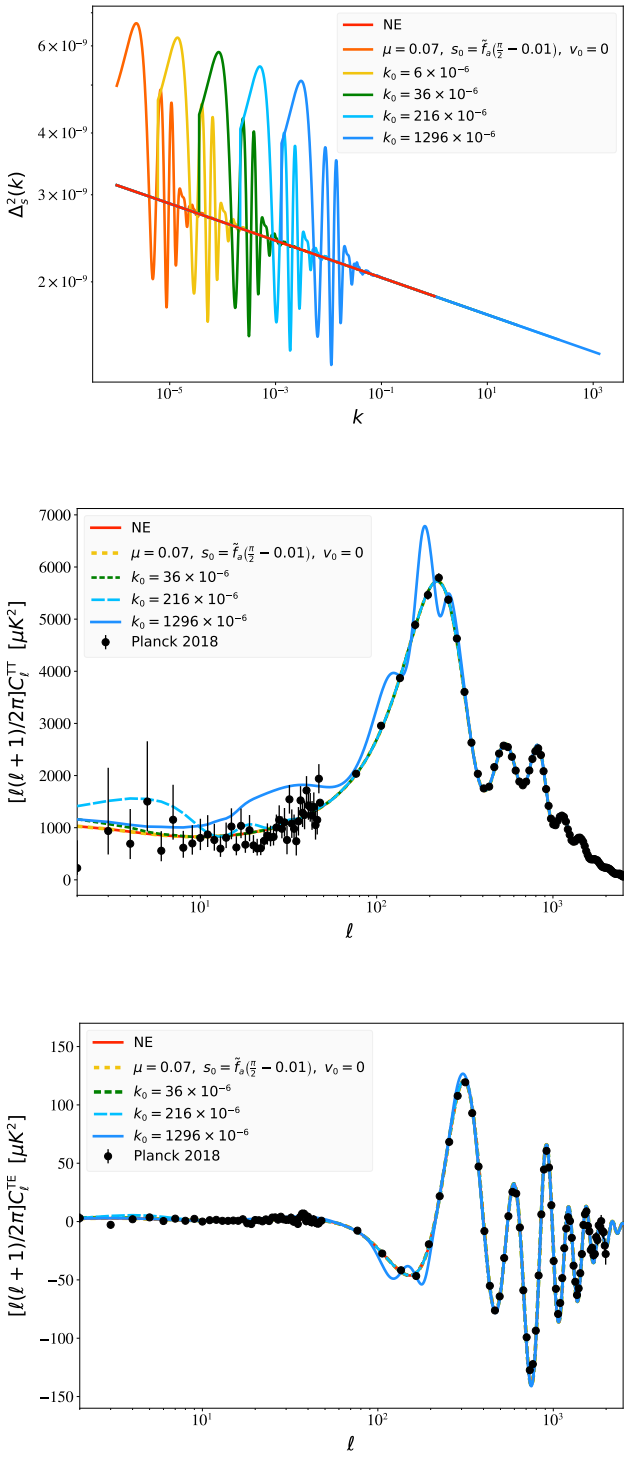

Figure 5.12: The primordial power spectrum (top), the unlensed TT power spectrum (middle), and the unlensed TE power spectrum (bottom) for an entangled state involving an axion with $\mu = 0.07$, $s_0 = \tilde{f}_a(\frac{\pi}{2} - 0.01)$, and $v_0 = 0$, with $f_{decay} = 0.01$, for various values of k_0. In all subfigures, the non-entangled power spectra are presented. Additionally, the Planck CMB data is shown in the middle and bottom subfigures.

tential with parameters $\mu = 0.1$, $s_0 = 0$, and $v_0 = 0.05$. There are some visual differences in the TT spectra in the low-l regime, particularly for the cases where entanglement starts latest or, equivalently, where k_0 is the largest. In those situations, the curves dip below the non-entangled TT spectra. Overall, however, the entangled results are similar to what was obtained with this set of parameters in the previous sections.

Next, Figure 5.11 does the same comparison for the parameters $\mu = 1$, $s_0 = 0.3$, and $v_0 = 0$ in the entangled case. These entangled primordial power spectra contain a dominant isolated feature followed by a behavior that approaches the standard non-entangled case. Consequently, the results of shifting the onset of entanglement are more dramatic. In Figure 5.11, one can see the latest onset of entanglement considered—a value of $k_0 = 1296 \times 10^{-6}$ Mpc^{-1}—gives TT and TE spectra outside the bounds of existing data. However, the rest of the shifts considered are much closer to the non-entangled case and most fit the Planck error bars (by eye) just as well as the standard case. The most notable features that are different from the non-entangled case appear in the low-l region of the TT spectra and appear vaguely oscillatory for some values of k_0.

Finally, Figure 5.12 displays an identical comparison for the axion-like potential, with parameters $s_0 = \tilde{f}_a(\frac{\pi}{2} - 0.01)$, $\mu = 0.07$, $v_0 = 0$, and $\tilde{f}_a = 0.01$ for the entangled case. Like Figure 5.11, the entangled primordial power spectra contain a dominant isolated feature, followed by behavior that matches the non-entangled case. Furthermore, as in Figure 5.11, the latest onset of entanglement considered produces results that appear beyond the bounds of the Planck error bars. However, the rest of the shifts considered in Figure 5.12 show TT spectra that match the standard non-entangled case for $l > 100$, yet have a distinct imprint of damped oscillations (compared to the non-entangled case) for the low-l regime. The amplitude of these low-l oscillations are related to the amplitude of oscillations in the primordial spectrum, so some amount of tuning by adjusting initial parameters is definitely possible. The TE spectra are also a good match for all but the latest onset of entanglement considered.

Overall, Figures 5.10 - 5.12 showcase the effects of changing the onset of entanglement, and they demonstrate how changing this parameter enables one to put features in the CMB

power spectra (particularly in the low-l regime) where, in some cases, there previously were none.

5.4 Conclusions

There are some interesting lessons to take away from our analysis. The first is that entangled Gaussian states might be easier to generate than previously thought. The only ingredient necessary is the existence of a scalar field that is displaced from its minimum and/or has an initial velocity. As we mentioned above, there are enough such fields in most extensions of the standard model with these properties. Furthermore, as opposed to the analysis in [142] where the cubic $\zeta - \Sigma$ action was considered, even the quadratic action considered here can generate a non-trivial entangled state.

So, can the Planck data distinguish the BD state from one of its entangled analogs? It is clear that, even by eye, some parameter values are excluded due to new features generated in the TT and/or TE spectrum. On the other hand, some seemingly reasonable parameter values seem to fit the data well, again at least by eye. Whether these parameter values can survive the scrutiny of a full parameter estimation probe is future work on this project. We can also make use of bi-spectrum information [153] as in [141] to further constrain the parameters of the entangled state.

We note the changes in the C_ls due to entanglement in the state seem to be most significant when the time at which entanglement turns on is well within the last 55 e-folds of inflation. At one level this is not surprising; we note that the trend is to settle back down to the non-entangled case after an initial (sometimes large) deviation from it. If this happens early enough (i.e., when the largest distance scales appearing in the CMB leave the inflationary horizon), then for most of the subsequent evolution, the power spectrum is essentially the standard Bunch-Davies one. Thus we get the largest observational "bang for the buck" when the new features appear later than that.

Our interpretation of what we have done so far is that an entangled state could well be hiding in the Planck data. It remains to be seen what a full attempt at parameter estimation might yield but, at least by eye, there appears to be a range of parameters

$\mu,\ s_0,\ v_0$ that give CMB anistropies consistent with Planck. If this *is* borne out by further analysis, finer probes of the CMB will have to be developed to distinguish entangled states from the Bunch-Davies one.

As a parting thought we reiterate the importance of understanding the quantum state of the inflaton. Clearly it is of great importance in terms of understanding cosmological measurements. More significantly though, we hope that understanding what states can possibly be a consistent inflationary quantum state can be a signpost guiding us to the next layer of physical laws.

5.5 Acknowledgments

RB was supported in part by the U.S. Department of Energy, Office of Science, Office of High Energy Physics QuantISED program under Contract No. KA2401032. SM was supported in part by Prof. Katherine Freese through the College of Natural Sciences Sponsored Research Development funding at The University of Texas at Austin. RB would like to thank Andreas Albrecht for fruitful discussions while RH and BR thank Devon Houtz for title and edit suggestions.

Chapter 6

Entanglement Masquerading in the CMB

The material in this chapter previously appeared in ***Entanglement Masquerading in the CMB*** *by Arsalan Adil, Andreas Albrecht, Rose Baunach, R. Holman, Raquel H. Ribeiro, and Benoit J. Richard [4].*

ABSTRACT: The simplest single-field inflation models capture all the relevant contributions to the patterns in the Cosmic Microwave Background (CMB) observed today. A key assumption in these models is that the quantum inflationary fluctuations that source such patterns are generated by a particular quantum state—the Bunch–Davies (BD) state. While this is a well-motivated choice from a theoretical perspective, the question arises of whether current data can rule out other, also well motivated, choices of states. In particular, as we previously demonstrated in [4], entanglement is naturally and inevitably dynamically generated during inflation given the presence of a "rolling" spectator scalar field—and the resulting entangled state will yield a primordial power spectrum with potentially measurable deviations compared to the canonical BD result. For this work we developed a perturbative framework to allow a systematic exploration of constraints on (or detection of) entangled states with Planck CMB data using Monte Carlo techniques. We have found that most entangled states accessible with our framework are consistent with the data. One would have to expand the framework to allow a greater variety of

entangled states in order to saturate the Planck constraints and more systematically explore any preferences the data may have among the different possibilities.

6.1 Introduction

The currently dominant paradigm for the formation of cosmic structure is the inflationary one [115, 132, 134, 133], where the universe undergoes a period of rapid expansion during which quantum fluctuations are stretched from micro to macro scales. These then freeze out after crossing the inflationary horizon, yielding a computable power spectrum for the anisotropies in the Cosmic Microwave Background radiation (CMB) [135, 136].

Going beyond the paradigmatic aspects of inflation to more concrete and detailed predictions involves model building. The simplest set of assumptions one can make is that inflation is driven by the slowly varying energy density of a single scalar, the *inflaton*, and that its quantum fluctuations drive structure formation.

At this point, we find ourselves facing a veritable smorgasbord of choices for inflationary model building. Inflaton dynamics is driven by its potential and whether or not it has a canonical kinetic term among other choices. However, for the most part, one aspect of inflationary model building seems to be fixed: the choice of quantum state for the quantum fluctuations of the inflaton.

The so-called Bunch–Davies (BD) state [19] is this preferred state. The reasons given for this choice are sound: it is a state that respects the symmetries of de Sitter space, which is an approximation to the inflationary spacetime, it has "good" quantum mechanical behavior (e.g., it satisfies the Hadamard condition [138] i.e. that it has the appropriate short-distance singularity structure), and it is the state that maps into the flat space Poincaré invariant state at short distances.

However, we would argue that these are insufficient reasons to forego considering other possible states. For example, the BD state is only one member of an infinite family of states, the so-called α-vacua [154, 155] that are also de Sitter invariant. It is certainly true that the BD state is the only one of these that satisfies the Hadamard property and this has been used as a reason to discard the other α-vacua. While we would agree that

this might be a mortal flaw if this theory is treated as a UV complete theory of inflation, we are less swayed by this argument viewing it as an effective theory. Given that we only have access to what happened $55 - 60$ e-folds before the end of inflation, we have no idea if the inflaton is even the right degree of freedom to focus on at short distances, for example. Thus, the use of short-distance arguments to rule out choices of the initial quantum states seems to be a somewhat hubristic endeavor to us.

We find it much more palatable to treat the choice of the BD state as *exactly* that: a choice. If inflation starts at a finite time in the past we can choose other possible states for these fluctuations. The only real constraint is that the energy density in these fluctuations does not overwhelm that of the inflaton zero mode that is driving inflation. One way to enforce this is to have short inflation, i.e., have just enough inflation to define the quantum state of the observable universe.

In order to understand how good a choice the BD state is, we need to compare it to other possible choices of states. In particular, the comparison should be a physical one, i.e., one that inquires how well a putative state choice matches observations versus how well the BD state does. Our view is that we should scan among quantum states in the space of states, subject to the constraints that the state is consistent with the onset of inflation. We treat this in the spirit of an effective theory of states [156, 157]. If this set of states is allowed by the theoretical framework, it should be examined.

Actually scanning throughout the full space of states is a daunting task, so we will have to restrict our search to a more amenable subspace to carry out our calculations. Starting in [139] as well as in refs. [140, 141] and culminating in ref. [4], we have investigated the effect of entangling the quantum state of various spectator fields such as scalars, or the tensor metric perturbations with those of the scalar metric perturbations. These states are the most general *Gaussian* states one can consider involving these fields, so one only need consider the quadratic part of the action for the relevant fields in order to compute the power spectrum, a non-trivial simplification!

We can make the case that such entangled states are more generic than not; the Higgs field does in fact exist, and any extension of the standard model comes along with

many scalar fields, of various masses. From this perspective, the unentangled BD state stands out as an anomaly. Our empirical motivation lies in the fact that, with precision cosmology, we might be able to identify hints of entanglement between the inflaton and this spectator field.

It's worth understanding the implications of entanglement (of the type computed in [4] and in this work). Since we match to the Bunch–Davies state at the initial time (see section 6.2.3.2), we are *not* modifying the short distance properties of the theory. Rather we allow for entangled correlations to develop due to the gravitationally induced interactions between the scalar fluctuations and the spectator fields.

In ref. [4], we computed the TT and TE power spectra for the state entangling the scalar metric perturbation, ζ, and a spectator scalar field, Σ, though only for sample values of the various parameters involved. To be able to make definitive statements about whether these states can offer a better explanation of the CMB data than the standard ΛCDM cosmology using the Bunch–Davies state, we need to apply Monte Carlo techniques. The latter allows us to estimate parameters of the model given Planck data.

We consider a free massive scalar field with a rolling zero mode as our spectator field. When all is said and done, the relevant parameters to estimate via Bayesian inference are: (i) the initial position and velocity of the zero mode and (ii) the ratio $m/H_{\rm dS}$, where m is the mass of the scalar field and $H_{\rm dS}$ is the Hubble parameter during inflation. What we find for this model is that while the best fit values of these parameters are small enough to make the state almost indistinguishable from the BD state (at least from the point of view of the CMB power spectrum), there are values of these parameters that lead to an interesting phenomenology—which on the one hand yield likelihoods very close to that for the standard ΛCDM cosmology, but with "bumps" in the primordial power spectrum. This leads to a *masquerading effect*: the state generating the primordial power spectrum could well be an entangled one, but Planck data do not provide strong enough evidence to unmask it.

Certain aspects of our framework were constrained by requiring computational tractability. We have found that these constraints limited the amount of entanglement we could

consider and thus kept us for the most part in the "masquerading" regime. It remains an open question whether a more general treatment allowing greater degrees of entanglement could result in the data being more informative, and possibly even signalling a preference for particular entangled states.

The influence of spectator fields during inflation has, of course, been explored in a variety of other contexts (e.g. [158, 159, 160, 161, 162, 163, 164]). One of the differences between our work and some other approaches is that we only consider gravitational interactions between the two sectors (coupling between the curvature perturbations and the perturbations in the spectator scalar field), rather than imposing a direct coupling term in the potential (i.e. $V(\Phi, \Sigma) \neq V(\Phi) + V(\Sigma)$) or non-canonical kinetic terms linking the two sectors. The gravitational interaction terms arise naturally and become important when the spectator field zero mode is allowed to 'roll', as initially derived in [4] and discussed in section 6.2 of this work. We also do not perform additional phenomenological or data-driven model building in the spectator sector to engineer additional features in the primordial power spectrum—in this paper's analysis, all the features we see simply arise from a free massive scalar spectator with a rolling zero mode evolving in a quasi de Sitter background. Additionally, we also restrict our attention to quasi-single field models such that our formalism requires the spectator to be subdominant during inflation. Lastly, another difference between our work and most other approaches is that, by working in Schrödinger picture quantum field theory, we have explicitly focused our attention on evolution of the quantum state of the perturbations—which is a natural setting to explore entanglement.

In section 6.2, we establish the theoretical foundations of the quantum state used in our calculations. This includes a summary of the work in ref. [4] and extensions to it, notably a perturbative approach to systematically calculate the lowest order corrections to the standard inflationary power spectrum due to entanglement. In section 6.3, we address the foundation for our Monte Carlo analysis. In section 6.4, we present the results of our best-fit parameter estimation and analyze how our models fare against the standard ΛCDM model. We end our discussion in section 6.5 with concluding remarks and ideas

for future work.

6.2 Overview of entangled two-point correlators

In this section, we review the theoretical framework derived in ref. [4] and develop the perturbative approach utilized in our parameter estimation. For more details regarding entangled states please refer to refs. [139, 140, 141], which form the basis for our analysis. The technical results in this section are valid for any choice of spectator scalar field—we restrict our focus to the free massive scalar field beginning in section 6.3.

6.2.1 Constructing the Hamiltonian

Consider the system consisting of the inflaton Φ, driving inflation, together with a spectator scalar field Σ. The conjugate momenta to the fields are then Π_Φ for Φ, and Π_Σ for Σ. We assume that Φ and Σ are directly uncoupled such that their corresponding potential can be linearly separated as

$$V(\Phi, \Sigma) = V(\Phi) + V(\Sigma) \ . \tag{6.1}$$

In this sense, our focus lies in quasi-single field inflation models. The spacetime line element is taken as

$$ds^2 = -dt^2 + a^2(t) \exp(2\zeta(\vec{x}, t)) d\vec{x}^2, \tag{6.2}$$

and we neglect the tensor perturbations in this work.

We next decompose the various fields into background components, defined as their (time dependent) expectation values, and fluctuations around them. The Hamiltonian will be expanded in powers of the fluctuations and associated conjugate momenta. Defining η to be conformal time, ranging from $-\infty$ to 0, and $\phi(\eta) = \langle \Phi(\vec{x}, \eta) \rangle$, we work in the comoving gauge where $\delta\phi = 0$ and ζ alone describes the scalar fluctuations that will imprint themselves in the CMB. This allows the interaction between Φ and Σ to properly be encoded by that of ζ and Σ. We write the field $\Sigma(\vec{x}, \eta)$ as

$$\Sigma(\vec{x}, \eta) = \sigma(\eta) + \chi(\vec{x}, \eta) \tag{6.3}$$

with $\sigma(\eta) = \langle \Sigma(\vec{x}, t) \rangle$. As a result the action and variables derived from it will only involve

functions of the zero mode, $\sigma(\eta)$, and the momentum space counterparts of ζ and χ, $\zeta_{\vec{k}}$ and $\chi_{\vec{k}}$, respectively, within this expansion treatment.

Our one requirement of the zero mode of the inflaton is that its energy density drive a slow-roll phase of inflation. To ensure this, we will have to enforce conditions on the evolution of the spectator zero mode $\sigma(\eta)$ so that *its* energy density does not interfere with inflation. We will see how this is realized below.

To compute the effect of changing the state from BD to a more general entangled state, we make use of the Schrödinger picture field theory. (For discussions of the Schrödinger picture see refs. [145] and [146].) The physics of the system is encoded in a wavefunctional of the form $\Psi\left[\zeta(\cdot), \Sigma(\cdot); \eta\right]$, corresponding to a state in which the scalar metric fluctuations ζ are entangled with Σ. The wavefunctional is a solution to the Schrödinger equation:

$$i\partial_\eta \Psi\left[\zeta(\cdot), \Sigma(\cdot); \eta\right] = \hat{H}\left[\Pi_\zeta, \Pi_\Sigma, \zeta, \Sigma; \eta\right] \Psi\left[\zeta(\cdot), \Sigma(\cdot); \eta\right]. \tag{6.4}$$

Note that eq. (6.4) involves ζ and its canonical conjugate momentum Π_ζ instead of Φ and Π_Φ. This is consistent with our choice of gauge as above. As discussed in the introduction, we want to restrict ourselves to the space of Gaussian entangled states; consistency then dictates that we only keep terms up to quadratic order in the fluctuations and their canonical momenta.

In order to construct the Hamiltonian describing our system, we first create the relevant action using *MathGR* [148], itself relying on the ADM formalism [147]. For notational purposes, and to facilitate intuitive comparisons with standard inflationary literature where appropriate, we perform the following field redefinitions,

$$v_{\vec{k}} = z\ \zeta_{\vec{k}} \quad \text{and} \quad \theta_{\vec{k}} = a\chi_{\vec{k}} \tag{6.5}$$

with $z(\eta) = \sqrt{2M_{\rm Pl}^2\ \epsilon\ a^2(\eta)}$, with ϵ measuring deviations from pure de Sitter space and $M_{\rm Pl}$ being the Planck mass. We can then write the quadratic action as:

$$S = \int d\eta \int \frac{d^3k}{(2\pi)^3}\ \mathcal{L}_k \tag{6.6}$$

where

$$\mathcal{L}_k = \frac{1}{2}\vec{X}^{T\prime}_{\vec{k}}\ \mathcal{O}\ \vec{X}'_{-\vec{k}} + \vec{X}^{T\prime}_{\vec{k}}\ \mathcal{M}_A\ \vec{X}_{-\vec{k}} - \frac{1}{2}\vec{X}^{T}_{\vec{k}}\ \Omega_k^2\ \vec{X}_{-\vec{k}}, \tag{6.7}$$

in which primes denote conformal time derivatives. The field variables are

$$\vec{X}_{\vec{k}} = \begin{pmatrix} v_{\vec{k}} \\ \theta_{\vec{k}} \end{pmatrix}, \tag{6.8}$$

and the matrices $\mathcal{O}$, $\mathcal{M}$, and the symmetric Ω_k^2, to lowest-order in slow-roll, are given by:

$$\mathcal{O} = \begin{pmatrix} 1 & -\tanh\alpha \\ -\tanh\alpha & 1 \end{pmatrix} \tag{6.9a}$$

$$\mathcal{M}_A = \frac{\mathcal{H}}{2}\left[\left(3-\epsilon+\frac{\eta_{\rm sl}}{2}\right)\tanh\alpha + \frac{a^2\ \partial_\sigma V}{\mathcal{H}^2\sqrt{2M_{Pl}^2\epsilon}}\right]\begin{pmatrix} 0 & -1 \\ 1 & 0 \end{pmatrix} \tag{6.9b}$$

$$\Omega_k^2 = \begin{pmatrix} k^2 - \dfrac{z''}{z} & \Omega_{k\ 12}^2 \\ \Omega_{k\ 12}^2 & \Omega_{k\ 22}^2 \end{pmatrix}, \tag{6.9c}$$

with

$$\Omega_{k\ 12}^2 \equiv -\tanh\alpha\left[k^2 + a^2\partial_\sigma^2 V/2 + \mathcal{H}^2\left(1+\frac{5\eta_{\rm sl}}{4}\right)\right] - \mathcal{H}^2\left(1+\epsilon+\frac{\eta_{\rm sl}}{2}\right)\frac{a^2\ \partial_\sigma V}{\mathcal{H}^2\sqrt{2M_{Pl}^2\epsilon}} \tag{6.10a}$$

$$\Omega_{k\ 22}^2 \equiv k^2 + a^2\partial_\sigma^2 V - \frac{a''}{a} - 2\epsilon(\epsilon-3)\mathcal{H}^2\ \tanh^2\alpha + 4\epsilon\mathcal{H}^2\tanh\alpha\left(\frac{a^2\ \partial_\sigma V}{\mathcal{H}^2\sqrt{2M_{Pl}^2\epsilon}}\right). \tag{6.10b}$$

Above, we defined

$$\tanh\alpha \equiv \frac{\sigma'}{\mathcal{H}\sqrt{2M_P^2\epsilon}}\ , \tag{6.11}$$

with the Hubble parameter $\mathcal{H}$ in conformal time being

$$\mathcal{H} \equiv \frac{a'}{a} \tag{6.12}$$

whereby the slow-roll parameter ϵ is given in conformal time by $\mathcal{H}' = (1-\epsilon)\mathcal{H}^2$ and η_{sl} denotes the second slow roll parameter $\eta_{sl} \equiv \epsilon'/\mathcal{H}\epsilon$. The parametrization in terms of hyperbolic functions chosen here stems from the fact that, as discussed above, we are enforcing the subdominance of spectator zero mode dynamics relative to that of the

inflaton field. This implies that $\sigma' \ll \sqrt{2\mathcal{H}^2 M_P^2 \epsilon}$ and, as such, the RHS of eq. (6.11) is bounded from -1 to 1. This will provide a somewhat more intuitive analysis of our results.

From the Lagrangian density in eq. (6.7) and its relationship with the Hamiltonian density via

$$\mathcal{H}_k = \vec{\Pi}_{\vec{k}}^T \vec{X}'_{-\vec{k}} - \mathcal{L}_k, \tag{6.13}$$

one can determine the Hamiltonian density corresponding to our problem, namely,

$$\mathcal{H}_k = \frac{1}{2}\vec{\Pi}_{\vec{k}}^T \, \mathcal{O}^{-1} \, \vec{\Pi}_{-\vec{k}} + \vec{X}_{\vec{k}}^T \, \mathcal{M}_A^T \mathcal{O}^{-1} \, \vec{\Pi}_{-\vec{k}} + \frac{1}{2}\vec{X}_{\vec{k}}^T \left(\Omega_k^2 + \mathcal{M}_A^T \mathcal{O}^{-1} \mathcal{M}_A\right) \vec{X}_{-\vec{k}}, \tag{6.14}$$

in which $\vec{\Pi}_{\pm\vec{k}}$ is the momentum operator conjugate to $\vec{X}_{\pm\vec{k}}$. The Hamiltonian is then given by

$$\hat{H} = \int \frac{d^3k}{(2\pi)^3} \, \mathcal{H}_k \tag{6.15}$$

For more details regarding the derivation of $\mathcal{H}_k$ from $\mathcal{L}_k$, please see [4].[1]

6.2.2 The Schrödinger equation for the entangled wavefunctional

As discussed in the introduction, we are restricting ourselves to Gaussian states that reflect an entanglement between v and θ, defined in eq. (6.5). The most general wave functional that encodes this is given by:

$$\Psi\left[\left\{v_{\vec{k}}\right\}, \left\{\theta_{\vec{k}}\right\}; \eta\right] = \mathcal{N}(\eta) \, \exp\left[-\frac{1}{2}\int \frac{d^3k}{(2\pi)^3} \vec{X}_{\vec{k}} \, \mathcal{K}_k(\eta) \, \vec{X}_{-\vec{k}}\right] \, , \tag{6.16}$$

with $\mathcal{N}(\eta)$ serving to normalize the state and $\mathcal{K}_k(\eta)$ being a matrix of kernels given by:

$$\mathcal{K}_k(\eta) = \begin{pmatrix} A_k(\eta) & C_k(\eta) \\ C_k(\eta) & B_k(\eta) \end{pmatrix} \, . \tag{6.17}$$

Here the off-diagonal entry $C_k(\eta)$ encodes the entanglement between the field fluctuations.

We then solve the functional Schrödinger equation, eq. (6.4), to generate the equation of motion for the kernels, which will specify the time evolution of our entangled state. This yields:

$$i\partial_\eta K_k = K_k^T \mathcal{O}^{-1} K_k - \Omega_k^2 - \mathcal{M}_A^T \mathcal{O}^{-1} \mathcal{M}_A - i\left(\mathcal{M}_A \mathcal{O}^{-1} K_k + K_k^T \mathcal{O}^{-1} \mathcal{M}_A^T\right). \tag{6.18}$$

[1] We note that the Lagrangian density specified in eqs. (6.7) - (6.9c) is equivalent to the fully Hermitian Lagrangian eventually arrived at in ref. [4], up to our field redefinitions and some integration by parts.

Eq. (6.18) can be decomposed into equations for the individual kernels, A_k, B_k, and C_k, given by:

$$\begin{aligned} i\partial_\eta A_k = A_k^2 - \left(k^2 - \frac{z''}{z}\right) \\ + \left\{ \sinh\alpha\ A_k + \cosh\alpha\ C_k + \frac{i}{2}\left[\left(3-\epsilon+\frac{\eta_{\rm sl}}{2}\right)\mathcal{H}\sinh\alpha + \frac{a^2\partial_\sigma V}{\mathcal{H}^2\sqrt{2M_{\rm Pl}^2\epsilon}}\mathcal{H}\cosh\alpha\right]\right\}^2 \end{aligned} \tag{6.19}$$

$$\begin{aligned} i\partial_\eta B_k = B_k^2 - \left(k^2 - \frac{a''}{a} + a^2\partial_\sigma^2 V\right) \\ + \left\{ \sinh\alpha\ B_k + \cosh\alpha\ C_k - \frac{i}{2}\left[\left(3-\epsilon+\frac{\eta_{\rm sl}}{2}\right)\mathcal{H}\sinh\alpha + \frac{a^2\partial_\sigma V}{\mathcal{H}^2\sqrt{2M_{\rm Pl}^2\epsilon}}\mathcal{H}\cosh\alpha\right]\right\}^2 \\ + 2\epsilon\mathcal{H}^2\left[(\epsilon-3)\tanh^2\alpha - 2\tanh\alpha\left(\frac{a^2\partial_\sigma V}{\mathcal{H}^2\sqrt{2M_{\rm Pl}^2\epsilon}}\right)\right] \end{aligned} \tag{6.20}$$

$$\begin{aligned} i\partial_\eta C_k = \cosh^2\alpha\ C_k\Big(A_k + B_k\Big) \\ + \frac{\sinh 2\alpha}{2}\Bigg\{ C_k^2 + A_k B_k \\ + i\frac{\mathcal{H}}{2}\left[\left(3-\epsilon+\frac{\eta_{\rm sl}}{2}\right) + \coth\alpha\frac{a^2\partial_\sigma V}{\mathcal{H}^2\sqrt{2M_{\rm Pl}^2\epsilon}}\right]\Big(B_k - A_k\Big) \\ + \frac{\mathcal{H}^2}{4}\left[\left(3-\epsilon+\frac{\eta_{\rm sl}}{2}\right)\tanh\alpha + \frac{a^2\partial_\sigma V}{\mathcal{H}^2\sqrt{2M_{\rm Pl}^2\epsilon}}\right]^2\Bigg\} \\ + \tanh\alpha\left[k^2 + \frac{1}{2}a^2\partial_\sigma^2 V + \mathcal{H}^2\left(1+\frac{5}{4}\eta_{\rm sl}\right)\right] + \mathcal{H}^2\left(1+\epsilon+\frac{\eta_{\rm sl}}{2}\right)\frac{a^2\partial_\sigma V}{\mathcal{H}^2\sqrt{2M_{\rm Pl}^2\epsilon}}. \end{aligned} \tag{6.21}$$

Lastly, the equation of motion for the zero mode of the spectator field is given by:

$$\sigma''(\eta) + 2\mathcal{H}\sigma'(\eta) + a^2(\eta)\partial_\sigma^2 V(\sigma) = 0 \tag{6.22}$$

The equation for the entanglement kernel C_k shows explicitly that either a non-zero spectator field velocity, encoded by $\tanh\alpha$, or a displacement from the minimum of its

potential, described by non-zero values of $\partial_\sigma V$, can source a non-trivial evolution of this kernel—even if there is no entanglement present at the initial time. To solve these equations requires setting initial conditions for all the kernels and can only be done numerically. This was explored in more detail in ref. [4] to which we refer the reader.

6.2.3 Impact of entanglement in the power spectrum—a perturbative approach

Numerical evaluation of the nonlinear, inhomogeneous, and coupled set of eqs. (6.19 - 6.21) is clearly a formidable task and we make use of a perturbative approach to make the problem numerically tractable. As a side-effect, the perturbative expansion also allows us to better identify parameter degeneracies so that we can justifiably neglect varying the slow-roll parameters ϵ and η_{sl} in our parameter estimation. Here, we focus on the perturbative framework and defer the discussion of identifying parameter degeneracies to section 6.3.1.2.

The results in ref. [4] show that for large enough values of the initial spectator parameters there will be deviations in the angular TT and TE power spectra between the Planck data and the predictions from the entangled state. This means that we could imagine constructing a perturbative expansion in terms of quantities that measure the deviation of the entangled state from the BD one. It should be noted that this simplification leads to a deviation from our original goal. Ideally, we would like to just ask the question of whether a given entangled state can be at least as consistent with the data as the standard ΛCDM cosmology. We have transformed that into the question of how much can our entangled state deviate from the BD one and still be consistent with the data, where consistency can be measured by how close the likelihood for our entangled state is to that of the BD state.

We already know that the CMB angular power spectrum is in good agreement with a primordial spectrum generated by the BD state. Thus, from a perturbative standpoint, it makes sense to consider only deviations from the BD state that are not too extreme. Since these deviations are parametrized by the entanglement kernel C_k, we would like to develop a perturbative expansion around $C_k = 0$. (We take the initial value of C_k to be

zero, so that entanglement is solely dynamically generated, as done in [4].)

What should the control parameters for this expansion be? As stated in the previous subsection, eq. (6.21) shows that the evolution of the spectator zero mode sources the evolution of C_k—either due to the velocity of the spectator field (through $\tanh\alpha$, via eq. (6.11)) or by a non-vanishing slope in the potential for the spectator field. A non-zero value for C_k, signifying entanglement, together with non-zero values for the position and velocity of the zero mode will then evolve the A_k and B_k kernels—corresponding to fluctuations in the inflaton and spectator fields, respectively—away from their BD equivalents.

Guided by these insights, there are two relevant control parameters in eqs. (6.19 - 6.21) that emerge:

$$\lambda_1 \equiv \tanh\alpha \tag{6.23a}$$

$$\lambda_2 \equiv \frac{a^2\partial_\sigma V}{\mathcal{H}^2\sqrt{2M_{\rm Pl}^2\epsilon}}\ . \tag{6.23b}$$

These are already required to be small so that the spectator does not dominate the expansion dynamics relative to the inflaton, so it is natural to expand the deviations of our entangled state from the BD one in powers of $\lambda_1,\ \lambda_2$. (Note that the λ_i evolve in time, so we demand that $|\lambda_i| < 1$ for all times specified by our perturbative equations, for all scales that contribute to the observable CMB sky today.) Specifically, we treat $\lambda_1,\ \lambda_2$ to be of the same formal order, and expand in a generic constant parameter λ which encapsulates this (such that $\lambda_i \lesssim O(\lambda)$).[2]

In this approximation scheme, we expand the kernels in powers of λ as follows[3]:

$$A_k = A_k^{(0)} + \lambda^2 A_k^{(2)} \tag{6.24a}$$

$$B_k = B_k^{(0)} + \lambda^2 B_k^{(2)} \tag{6.24b}$$

$$C_k = \lambda C_k^{(1)} \tag{6.24c}$$

[2]For example, in section 6.3.1.2 we take $\lambda = \lambda_{2,\rm max}$, where $\lambda_{2,\rm max}$ is the maximum value of λ_2 during the course of inflation (as derived in appendix 6.A).

[3]There are no first-order corrections in A_k and B_k because there is nothing in the equations to source them, a point which we will elaborate on subsequently during our discussion of initial conditions.

where for C_k the expansion begins at first order in λ, because $C_k = 0$ is the standard single field limit.

These expansions yield some considerable simplifications in our analysis. First, consider the power spectrum. Following the methods in refs. [139, 140, 141] we can write the two-point function for $v_{\vec{k}} = z\zeta_{\vec{k}}$ as:

$$\langle v_{\vec{k}} v_{\vec{k}'} \rangle = (2\pi)^3 \delta^{(3)}\left(\vec{k}+\vec{k}'\right)\left(\frac{B_{kR}}{2\left(A_{kR}B_{kR}-C_{kR}^2\right)}\right) \equiv (2\pi)^3 \delta^{(3)}\left(\vec{k}+\vec{k}'\right) P_v(k) \ , \quad (6.25)$$

which is related to the standard dimensionless inflationary power spectrum of curvature perturbations [149] via:

$$\Delta_s^2 = \frac{k^3}{2\pi^2} P_\zeta(k) = \frac{k^3}{2\pi^2}\frac{1}{z^2} P_v(k) \ . \quad (6.26)$$

Expanding P_v to lowest order in λ, given eqs. (6.24), we find:

$$P_v = \frac{B_{kR}}{2\left(A_{kR}B_{kR}-C_{kR}^2\right)} = \frac{1}{2A_{kR}^{(0)}}\left[1+\lambda^2\left(\frac{-A_{kR}^{(2)}}{A_{kR}^{(0)}}+\frac{(C_{kR}^{(1)})^2}{A_{kR}^{(0)}B_{kR}^{(0)}}\right)\right] \quad (6.27)$$

where in the absence of entanglement $P_v = P_{v,BD} = \frac{1}{2A_{kR}^{(0)}}$. (The subscript 'R' denotes taking the real part of the kernel.) Since the quantity we wish to compare with the CMB is ultimately $\Delta_s^2 \sim P_v$, this tells us that neither $B_k^{(2)}$ nor higher order terms in C_k are required for our analysis.

It is important to note that unlike the situation with the BD state, we are not guaranteed that ζ will remain constant outside the horizon, so the power spectrum will be evaluated explicitly at late times.

6.2.3.1 Dimensionless kernel equations

To proceed with the numerical analysis, we construct dimensionless versions of our equations. We begin by defining the following for dimensionless conformal time and wavenumbers:

$$\tau = -\frac{\eta}{\eta_0}, \ q = \frac{k}{k_0} = -(1-\epsilon)k\eta_0 \quad (6.28)$$

where η_0 corresponds to the time at which the entangled evolution begins. Note that since the conformal times are all negative, τ runs from -1 to 0. We also define dimensionless kernels according to

$$A_k(\eta) = \frac{A_q(\tau)}{(-\eta_0)}, \quad B_k(\eta) = \frac{B_q(\tau)}{(-\eta_0)}, \quad C_k(\eta) = \frac{C_q(\tau)}{(-\eta_0)} \quad (6.29)$$

since they were all mass dimension 1 originally. Additionally, we define the dimensionless conformal Hubble parameter as

$$\mathcal{H}(\eta) = \frac{\mathcal{H}(\tau)}{(-\eta_0)}, \quad \mathcal{H}(\tau) = \frac{-1}{(1-\epsilon)\tau} \tag{6.30}$$

and rescale the spectator background quantities according to

$$\sigma = sM_{pl}, \quad V(\sigma) = \Lambda^4 V(s), \quad \mu^2 = \frac{\Lambda^4}{H_{ds}^2 M_{pl}^2} \ . \tag{6.31}$$

as was done in ref. [4].

With these definitions, we construct dimensionless versions of eqs. (6.19) – (6.21), and then expand each equation to the lowest order in λ required to compute eq. (6.27). The resulting equations are

$$i\partial_\tau A_q^{(0)} = (A_q^{(0)})^2 - \left[\left(\frac{q}{1-\epsilon}\right)^2 - \frac{\left(\nu_f^2 - \frac{1}{4}\right)}{\tau^2}\right] \tag{6.32a}$$

$$\begin{aligned} i\partial_\tau A_q^{(2)} &= 2A_q^{(0)} A_q^{(2)} \\ &\quad + \left[\tilde{\lambda}_1 A_q^{(0)} + C_q^{(1)} - \frac{i}{2(1-\epsilon)\tau}\left[\left(3 - \epsilon + \frac{\eta_{sl}}{2}\right)\tilde{\lambda}_1 + \tilde{\lambda}_2\right]\right]^2 \end{aligned} \tag{6.32b}$$

$$i\partial_\tau B_q^{(0)} = (B_q^{(0)})^2 - \left[\left(\frac{q}{1-\epsilon}\right)^2 - \frac{\left(\nu_g^2 - \frac{1}{4}\right)}{\tau^2}\right] \tag{6.32c}$$

$$\begin{aligned} i\partial_\tau C_q^{(1)} &= C_q^{(1)}\left(A_q^{(0)} + B_q^{(0)}\right) + \tilde{\lambda}_1 A_q^{(0)} B_q^{(0)} \\ &\quad + \frac{i}{2(1-\epsilon)\tau}\left[\left(3 - \epsilon + \frac{\eta_{sl}}{2}\right)\tilde{\lambda}_1 + \tilde{\lambda}_2\right](A_q^{(0)} - B_q^{(0)}) \\ &\quad + \tilde{\lambda}_1\left[\left(\frac{q}{1-\epsilon}\right)^2 + \frac{\mu^2 \partial_s^2 V(s)}{2(1-\epsilon)^2\tau^2} + \frac{1 + \frac{5}{4}\eta_{sl}}{(1-\epsilon)^2\tau^2}\right] + \tilde{\lambda}_2\left[\frac{1 + \epsilon + \frac{\eta_{sl}}{2}}{(1-\epsilon)^2\tau^2}\right] \end{aligned} \tag{6.32d}$$

where $\tilde{\lambda}_{1,2} = \frac{\lambda_{1,2}}{\lambda}$ is an algebraic simplification, and $\lambda_{1,2}$ are defined in terms of dimensionless quantities as:

$$\lambda_1 = \frac{(1-\epsilon)}{\sqrt{2\epsilon}}(-\tau)\partial_\tau s \tag{6.33a}$$

$$\lambda_2 = \frac{\mu^2}{\sqrt{2\epsilon}}\ \partial_s V(s) \ . \tag{6.33b}$$

The solutions to the zeroth order equations for $A_q^{(0)}$ and $B_q^{(0)}$ are known; these are just the Schrödinger picture version of the Mukhanov–Sasaki mode equations for the inflaton

and spectator. Following [4] we take the Hankel function indices for the BD modes of the inflaton and spectator to be:

$$\nu_f = \frac{3}{2} + \epsilon + \frac{\eta_{sl}}{2} \tag{6.34a}$$

$$\nu_g = \sqrt{\frac{9}{4} + 3\epsilon - \frac{\mu^2 \partial_s^2 \, V(s)|_{s=s_0}}{(1-\epsilon)^2}} \ , \tag{6.34b}$$

with the dimensionless modes themselves and their corresponding zeroth order kernels given by:

$$f_v(\tau) = \frac{\sqrt{-\pi\tau}}{2} H^{(2)}_{\nu_f}\left(\frac{-q\tau}{(1-\epsilon)}\right), \quad A^{(0)}_q(\tau) = -i\frac{f_v'(\tau)}{f_v(\tau)} \tag{6.35a}$$

$$g_\theta(\tau) = \frac{\sqrt{-\pi\tau}}{2} H^{(2)}_{\nu_g}\left(\frac{-q\tau}{(1-\epsilon)}\right), \quad B^{(0)}_q(\tau) = -i\frac{g_\theta'(\tau)}{g_\theta(\tau)} \ . \tag{6.35b}$$

In contrast to the zeroth order equations, eqs. (6.32b) and (6.32d) must be solved numerically, except in very special cases (see appendix 6.B).

Finally, the dimensionless zero mode equation for the spectator is given by:

$$s''(\tau) - \frac{2}{\tau(1-\epsilon)} s'(\tau) + \frac{\mu^2 \partial_s V(s)}{\tau^2 (1-\epsilon)^2} = 0 \ . \tag{6.36}$$

6.2.3.2 Setting up the initial conditions

Guided by the work in [4], we construct our initial conditions for the kernel equations so that the corresponding modes are the standard Bunch–Davies ones at the initial time η_0 (corresponding to $\tau = -1$) at which entanglement begins to be dynamically generated. We do this via a Riccati transform. Given a kernel equation of the form

$$iK'(\tau) = \alpha_2(\tau) K^2(\tau) + \alpha_1(\tau) K(\tau) + \alpha_0(\tau). \tag{6.37}$$

one can transform it into a mode equation of the form

$$f''(\tau) + \Omega^2 f(\tau) = 0, \quad \text{with} \quad \Omega^2 = \frac{1}{4}\alpha_1^2 - \alpha_0\alpha_2 - \frac{i}{2}\alpha_1' + \frac{i\alpha_1\alpha_2'}{2\alpha_2} - \frac{3}{4}\left(\frac{\alpha_2'}{\alpha_2}\right)^2 + \frac{\alpha_2''}{2\alpha_2}. \tag{6.38}$$

by choosing

$$iK(\tau) = \frac{1}{\alpha_2(\tau)}\left(\frac{f'(\tau)}{f(\tau)} - \Delta(\tau)\right), \tag{6.39}$$

with $2\Delta = i\alpha_1 - \alpha_2'/\alpha_2$. We thus use eq. (6.39) to set the initial conditions for the real and imaginary parts of the kernel equations, respectively given by [4]:

$$K_R(\tau_0) = \frac{1}{2\alpha_2(\tau_0)}\left(\frac{1}{|f(\tau_0)|^2} - \alpha_{1R}(\tau_0)\right) \tag{6.40a}$$

$$K_I(\tau_0) = -\frac{1}{2\alpha_2(\tau_0)}\left(\partial_\tau \ln|f|^2\big|_{\tau=\tau_0} + \alpha_{1I}(\tau_0) + \frac{\alpha_2'}{\alpha_2}\bigg|_{\tau=\tau_0}\right) . \tag{6.40b}$$

We need only use eqs. (6.40) to set the initial conditions for $A_q^{(0)}$, $B_q^{(0)}$ and $A_q^{(2)}$—the initial condition for $C_q^{(1)}$ is $C_q^{(1)}(\tau_0 = -1) = 0$. For $A_q^{(0)}$ and $B_q^{(0)}$ the results are straightforward to compute, and we obtain:

$$A_{qR}^{(0)}(\tau_0 = -1) = \frac{2}{\pi\left|H_{\nu_f}^{(2)}(\frac{q}{1-\epsilon})\right|^2} \tag{6.41a}$$

$$A_{qI}^{(0)}(\tau_0 = -1) = \frac{1}{2}\left[1 - 2\nu_f + x\left[\frac{H_{\nu_f-1}^{(1)}(x)}{H_{\nu_f}^{(1)}(x)} + \frac{H_{\nu_f-1}^{(2)}(x)}{H_{\nu_f}^{(2)}(x)}\right]\bigg|_{x=\frac{q}{(1-\epsilon)}}\right] \tag{6.41b}$$

$$B_{qR}^{(0)}(\tau_0 = -1) = \frac{2}{\pi\left|H_{\nu_g}^{(2)}(\frac{q}{1-\epsilon})\right|^2} \tag{6.41c}$$

$$B_{qI}^{(0)}(\tau_0 = -1) = \frac{1}{2}\left[1 - 2\nu_g + x\left[\frac{H_{\nu_g-1}^{(1)}(x)}{H_{\nu_g}^{(1)}(x)} + \frac{H_{\nu_g-1}^{(2)}(x)}{H_{\nu_g}^{(2)}(x)}\right]\bigg|_{x=\frac{q}{(1-\epsilon)}}\right] . \tag{6.41d}$$

For $A_q^{(2)}$ the situation is slightly more obtuse. The easiest thing to do is to start with the dimensionless, but unexpanded, A_q equation, i.e.,

$$\begin{aligned} i\partial_\tau A_q = A_q^2 - \left[\left(\frac{q}{1-\epsilon}\right)^2 - \frac{\left(\nu_f^2 - \frac{1}{4}\right)}{\tau^2}\right] \\ + \frac{1}{1-\lambda_1^2}\left[\lambda_1 A_q + C_q - \frac{i}{2(1-\epsilon)\tau}\left[\left(3 - \epsilon + \frac{\eta_{sl}}{2}\right)\lambda_1 + \lambda_2\right]\right]^2 , \end{aligned} \tag{6.42}$$

identify the α coefficients (of the type in eq. (6.37)), use those along with the λ expansions for A_q and C_q in eqs. (6.40a) and (6.40b), and then collect the second order in λ terms

that remain. Finally, after noting that $C_q(\tau_0 = -1) = 0$, we obtain:

$$A_{qR}^{(2)}(\tau_0 = -1) = -\tilde{\lambda}_{1,0}^2 A_{qR}^{(0)}(\tau_0 = -1) \tag{6.43a}$$

$$\begin{aligned} A_{qI}^{(2)}(\tau_0 = -1) = &-\tilde{\lambda}_{1,0}^2 A_{qI}^{(0)}(\tau_0 = -1) - \frac{1}{2(1-\epsilon)}\left[\left(3 - \epsilon + \frac{\eta_{sl}}{2}\right)\tilde{\lambda}_{1,0}^2 + \tilde{\lambda}_{1,0}\tilde{\lambda}_{2,0}\right] \\ &+ \left[\frac{\eta_{sl}\tilde{\lambda}_{1,0}^2}{2(1-\epsilon)} + \tilde{\lambda}_{1,0}^2 + \frac{2\tilde{\lambda}_{1,0}^2}{(1-\epsilon)} + \frac{\tilde{\lambda}_{1,0}\tilde{\lambda}_{2,0}}{(1-\epsilon)}\right] \end{aligned} \tag{6.43b}$$

where $\tilde{\lambda}_{1,0}$ denotes that $\tilde{\lambda}_1$ should be evaluated at $\tau_0 = -1$, and a term $\mathcal{O}(\eta_{sl}\epsilon)$ has been dropped from $A_{qI}^{(2)}$. From glancing at eqs. (6.43), one can see that $A_q^{(2)}$ will be zero initially, unless there is a non-zero initial velocity in the spectator zero mode (which causes $\tilde{\lambda}_{1,0}$ to be non-zero).

To explain why there are no terms first order in λ in eq. (6.24), consider eq. (6.42). If we add a term $\mathcal{O}(\lambda)$ to A_q and expand (keeping $C_q = \lambda C_q^{(1)}$), the first order result will be

$$i\partial_\tau A_q^{(1)} = 2A_q^{(0)} A_q^{(1)}, \tag{6.44}$$

since the terms in the second line of eq. (6.42) will always be $\mathcal{O}(\lambda^2)$ at lowest order. The solution to this equation is $A_q^{(1)}(\tau) = \frac{D}{f_q^2(\tau)}$ where D is an integration constant and $f_q(\tau)$ is the dimensionless BD mode function given by eq. (6.35), since $A_q^{(0)} = -i\frac{f'}{f}$ by definition.

Then, however, if ones consults the initial conditions for $A_q^{(1)}$, using the same method to obtain them as was described for $A_q^{(2)}$ above, one would find the integration constant D must vanish. This is because the only term that can be $\mathcal{O}(\lambda)$ in the initial conditions is proportional to $C_q^{(1)}$, and we have the condition that $C_q(\tau_0 = -1) = 0$. The exact same procedure holds for the B_q equation. Thus, unless one considers some initial entanglement—which is not part of this analysis—there are no first-order terms in A_q and B_q for the λ expansion because there are no non-zero initial conditions to source them.

This completes our theoretical setup. In the subsequent section we move to discuss what choices make our entangled state framework the most amenable to statistical parameter estimation, since our ultimate goal is to determine whether the CMB data truly prefers the Bunch–Davies state, or if it admits other entangled possibilities.

6.3 Technical perspectives and methodology

The technical work presented in section 6.2 outlines an approach to systematically calculate the lowest order deviations from the standard inflationary power spectrum due to an entangled state. The results so far are valid for any choice of spectator scalar field that one might wish to investigate.

However, since our goal is to perform a proper parameter estimation with our entangled states, we must narrow our focus. The choices we made for this work are summarized in this section, and their results discussed in subsequent ones. We also comment on the physical origin of the oscillations in the entangled primordial power spectrum in section 6.3.1.1.

6.3.1 Model parameters

We restrict our focus to the free massive scalar potential in the rest of this work, by considering

$$V(\sigma) = \frac{1}{2} m_\sigma^2 \sigma^2 \ , \tag{6.45}$$

with dimensionless quantities:

$$V(s) = \frac{1}{2} s^2, \qquad \Lambda^4 = m_\sigma^2 M_{pl}^2, \qquad \mu^2 = \frac{m_\sigma^2}{H_{ds}^2} \ . \tag{6.46}$$

For this potential, the zero mode equation admits analytic solutions, which are discussed in appendix 6.A.

As we initially investigated in ref. [4], even a simple free massive scalar potential admits a variety of different solutions for the primordial power spectrum. If we rewrite terms in eqs. (6.26) and (6.27) to be[4]

$$\Delta_s^2 = \Delta_{s,BD}^2 \left[1 + \lambda^2 \left(\frac{-A_{kR}^{(2)}}{A_{kR}^{(0)}} + \frac{(C_{kR}^{(1)})^2}{A_{kR}^{(0)} B_{kR}^{(0)}} \right) \right] = \Delta_{s,BD}^2 \left[1 + \lambda^2 \left(\frac{-A_{qR}^{(2)}}{A_{qR}^{(0)}} + \frac{(C_{qR}^{(1)})^2}{A_{qR}^{(0)} B_{qR}^{(0)}} \right) \right], \tag{6.47}$$

we see the dimensionless term in the square brackets encapsulates all the lowest-order effects of entanglement on the power spectrum. For simplicity of notation, we denote

[4] $\frac{-A_{kR}^{(2)}}{A_{kR}^{(0)}} = \frac{-A_{qR}^{(2)}}{A_{qR}^{(0)}}$ and similarly for the second term in eq. (6.47), since all k dependent kernels have mass dimension 1.

this term $\Delta^2_{s,\text{norm}} \equiv \Delta^2_s/\Delta^2_{s,BD}$ to emphasize the correction effects relative to the standard BD power spectrum. The kernels themselves directly depend on the values of the slow roll parameters, ϵ and η_{sl}, as well as the mass, initial position, and initial velocity of the spectator field (as described by the equations in section 6.2). We plot $\Delta^2_{s,\text{norm}}$ for several example values of the spectator parameters below, to illustrate the richness of the parameter space.

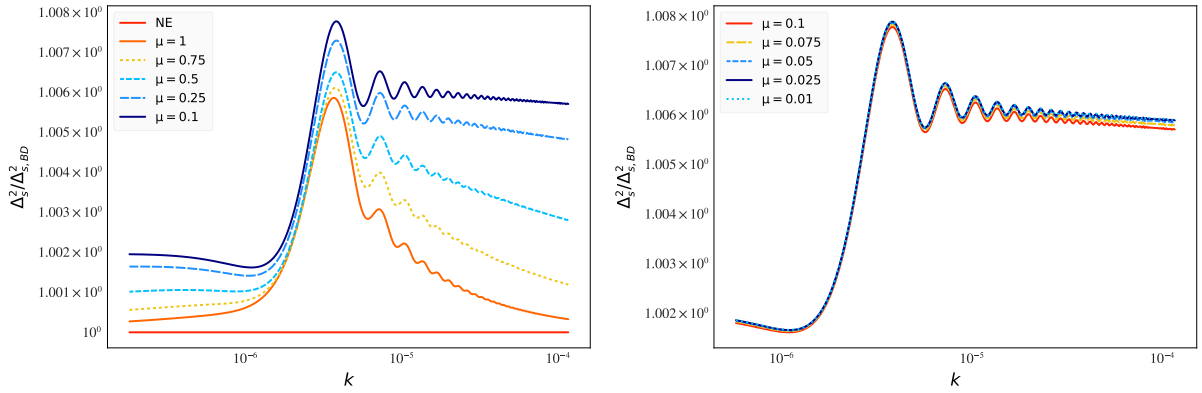

Figure 6.1: Log-log plots of $\Delta^2_{s,\text{norm}}$ for a variety of dimensionless masses, given $s_0 = \frac{0.2\sqrt{2\epsilon}}{\mu^2}$, $\epsilon = 10^{-7}$, and $v_0 = 0$. As discussed in the text, this choice of s_0 sets the expansion parameter λ to be identical for all the curves plotted here. The non entangled (NE) case corresponds to $\Delta^2_{s,\text{norm}} = 1$.

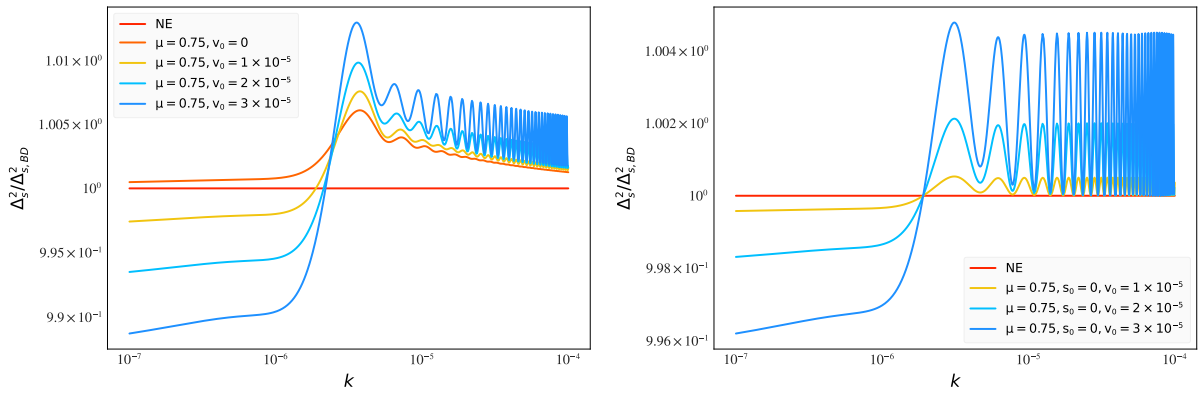

Figure 6.2: Log-log plots of $\Delta^2_{s,\text{norm}}$ for $\mu = 0.75$, showing the effect of adding an initial velocity. In the plot on the left, $s_0 = \frac{0.2\sqrt{2\epsilon}}{\mu^2}$ (with $\epsilon = 10^{-7}$), while $s_0 = 0$ on the right. The non-entangled (NE) case corresponds to $\Delta^2_{s,\text{norm}} = 1$.

Figure 6.1 shows the effect of varying μ in $\Delta^2_{s,\text{norm}}$, given $\epsilon = 10^{-7}$ in addition to the initial conditions $s_0 = \frac{0.2\sqrt{2\epsilon}}{\mu^2}$ and $v_0 = 0$. We take our expansion parameter λ to be $\lambda = \lambda_{2,\text{max}} = \frac{\mu^2 s_0}{\sqrt{2\epsilon}}$ (where $\lambda_{2,\text{max}}$ is defined to be the maximum value of λ_2 during

the course of inflation, given $v_0 = 0$, as discussed in appendix 6.A). For these choices of λ and s_0, one obtains $\lambda = \lambda_{2,\max} = 0.2$ for each curve in figure 6.1—so that they all roughly correspond to the same amount of entanglement, isolating the effect of varying the spectator mass. As the mass of the spectator becomes lighter, differences in $\Delta^2_{s,\text{norm}}$ get less pronounced, as shown in the right plot of figure 6.1. Figure 6.2 shows the effect of adding an initial velocity, for $\mu = 0.75$, in scenarios with and without a nonzero initial position. (In figure 6.2 we take our expansion parameter to be $\lambda = \frac{\mu^2(s_0+v_0)}{\sqrt{2\epsilon}}$.)

6.3.1.1 Origin of oscillations in the primordial power spectrum

In the previous section, we have explored how the mass, initial position, and initial velocity of the spectator field can influence the resulting entangled primordial power spectrum. However, one feature we have not commented on are the oscillations themselves. Oscillations in k in the primordial power spectrum have been a distinctive feature of this and previous work with entangled states [4, 139, 140, 141]. A glance at the equations in section 6.2 shows that there are several parameters that can control the placement, amplitude and persistence of these oscillations—which is also explored graphically in section 6.3.1 and analytically in appendix 6.B. Yet, what physically causes the oscillations in the first place? We believe we can now answer that question.

Consider what happens in standard single-field inflation. Bunch–Davies modes of different wavelengths start their evolution in phase as $\eta \to -\infty$, and continue to evolve in phase throughout their entire oscillatory regime. They reach their late time behavior after horizon crossing, upon which the modes freeze, and the standard primordial power spectrum is computed. There are no oscillations in the standard single-field result because nothing disturbs the in-phase nature of the modes throughout their entire evolution.

Let us now analyze what happens with our entangled states. We take our initial conditions to correspond to the BD modes, so before the onset of entanglement the story is the same as above—all modes begin in phase as $\eta \to -\infty$. However, at $\eta = \eta_0$, (corresponding to $\tau_0 = -1$ in dimensionless conformal time), we say that an event occurs to allow entanglement to begin *for every single k mode at the exact same time*.[5] At this

[5]We do not elaborate on what this special event that starts the entanglement process is. It could be a phase transition and perhaps the actual start of inflation. We chose to let our uncertainty about details

common initial time, every k mode will be at a slightly different phase in its oscillation. This translates to an out-of-phase 'initial condition' for the entangled evolution, which then propagates to late times where we compute the power spectrum. And despite all the complicated details of the modes' evolution due to entanglement between η_0 and the end of inflation, it is this assumption about the onset of entanglement that ultimately sources the k-dependent oscillations in the primordial power spectrum.

We can demonstrate an explicit example of this graphically. In figure 6.3, we plot $\Delta^2_{s,\text{norm}}$ for $\mu = 0.75$ for two different scenarios. The blue curves correspond to the standard set-up used throughout this paper—that the onset of entanglement happens at a fixed time for all modes. The difference between the two is that the darker blue curve also includes an initial velocity. The orange and yellow curves instead set the onset of entanglement such that the argument of the Hankel function piece of the BD mode functions is the same for all k modes[6], effectively making η_0 k-dependent. The BD mode functions are given generically by

$$v_\nu(\eta) = \frac{\sqrt{-\pi\eta}}{2} H^{(2)}_\nu(-k\eta) \quad v_\nu(\tau) = \frac{\sqrt{-\pi\tau}}{2} H^{(2)}_\nu\left(\frac{-q\tau}{(1-\epsilon)}\right) \tag{6.48}$$

and we pick the onset of entanglement such that $x = -k\eta_0 = \frac{-q\tau_0}{(1-\epsilon)} = 1$ in figure 6.3 for this scenario.

The effect of these choices is striking. For the set-up we use in this paper—that entanglement begins at a fixed time but at different phases for each of the mode functions—we see oscillations in $\Delta^2_{s,\text{norm}}$. But, in the case where all the modes begin exactly in phase there are no oscillations in $\Delta^2_{s,\text{norm}}$, despite the fact that $\Delta^2_{s,\text{norm}} \neq 1$ generically, which signifies that there is still some effect of entanglement on the primordial power spectrum. Furthermore, these conclusions hold regardless of whether the spectator has an initial velocity or not.

It's not unusual in early universe phenomenology to assume new physics happens at a given time. However, as we see from the above exploration, that assumption can have real

of the early universe show up phenomenologically in the structure of our formalism through parameters such as η_0.

[6]Note that the background zero mode initial condition remains the same in both scenarios since there is only one zero mode.

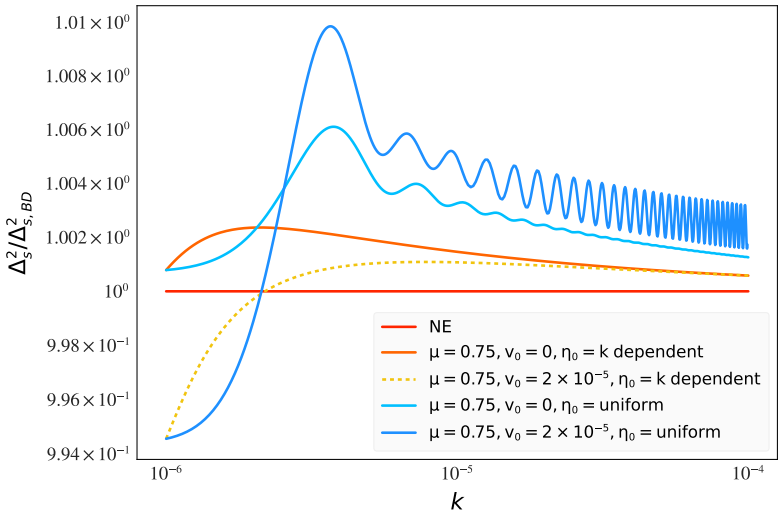

Figure 6.3: Log-log plot of $\Delta^2_{s,\text{norm}}$ for $\mu = 0.75$ and $s_0 = \frac{0.2\sqrt{2\epsilon}}{\mu^2}$ (taking $\epsilon = 10^{-7}$), with and without an initial velocity. We contrast the standard set-up for this paper—that all entanglement begins at the same time for each k mode—with a scenario where all the modes begin in phase, but at a different k-dependent time. As before, the non-entangled case corresponds to $\Delta^2_{s,\text{norm}} = 1$ and the expansion parameter λ is the same as the one used in figure 6.2.

physical consequences. If one had some physical motivation to assume that entanglement begins in a staggered way—corresponding to something like an entanglement horizon—the effects of such a scenario on cosmological observables might be quite different than what has been explored in this work.

6.3.1.2 Restricting the parameter space

As discussed in the literature (e.g. [158]), choosing the best parameterization of an inflationary model to compare with data in a full parameter estimation is something of an art form. One wants to choose effective parameters—which may be the original model parameters found in one's equations or some combination of them—whose effects on the primordial power spectrum are as distinct as possible, to preemptively eliminate as many degeneracies in the parameter estimation results as possible.

For this paper, we limit ourselves to the case where $v_0 = 0$ for the spectator field. This choice was initially motivated by numerical difficulties evaluating highly oscillatory integrals. However, by restricting ourselves to cases where $v_0 = 0$ and choosing $\lambda =$

$\lambda_{2,\max} = \frac{\mu^2 s_0}{\sqrt{2\epsilon}}$ as our expansion parameter[7], we can effectively decouple the effects of mass and initial position on eq. (6.47). This is because when $v_0 = 0$ and $\lambda = \frac{\mu^2 s_0}{\sqrt{2\epsilon}}$, $\tilde{\lambda}_{1,2} = \frac{\lambda_{1,2}}{\lambda}$ will no longer depend on either the initial position or velocity of the spectator field—as one can verify by substituting the analytical solutions in appendix 6.A into eq. (6.33). This eliminates all dependence on s_0 from the equations for $A_q^{(2)}$ and $C_q^{(1)}$, which enables us to reparameterize the scalar power spectrum as the following[8]:

$$\Delta_s^2 = A_s \left(\frac{k}{k_{piv}}\right)^{n_s - 1} \left[1 + \left(\frac{\mu^2 s_0}{\sqrt{2\epsilon}}\right)^2 P_q(\mu, \epsilon, \eta_{sl})\right] \tag{6.49}$$

with the dimensionless quantity $P_q(\mu, \epsilon, \eta_{sl})$ defined as

$$P_q(\mu, \epsilon, \eta_{sl}) = \left[\frac{-A_{qR}^{(2)}}{A_{qR}^{(0)}} + \frac{(C_{qR}^{(1)})^2}{A_{qR}^{(0)} B_{qR}^{(0)}}\right] . \tag{6.50}$$

We next make the choices to fix ϵ and η_{sl} to well motivated fiducial values, so that $P_q(\mu, \epsilon, \eta_{sl}) \equiv P_q(\mu)$ for our parameter estimation. Specifically, we fix:

$$\epsilon = 10^{-7} \tag{6.51}$$

and

$$\eta_{sl} = 1 - 2\epsilon - n_{s,f} \tag{6.52}$$

with $n_{s,f} = 0.9649$, from the best fit values from Planck [165]. These choices both help reduce degeneracy in our model parameter space and make our Monte Carlo analysis feasible in a timely fashion. We first comment on the degeneracy angle.

For $\epsilon < 10^{-6}$, the effect of varying ϵ in Δ_s^2 is degenerate with varying s_0. We have verified this numerically for a variety of values. One can also check this semi-analytically using the results in appendix 6.B. Furthermore, since the tensor-to-scalar ratio—which fully determines ϵ in the slow roll expansion—is currently only an upper bound, it feels uncontroversial to fix ϵ to a fiducial value and use s_0 to explore our parameter space of

[7] $\lambda = \lambda_{2,\max} = \frac{\mu^2 s_0}{\sqrt{2\epsilon}}$ is a well-motivated expansion parameter, because one can show that $\lambda_2 < 1$ guarantees $\lambda_1 < 1$ as well, for $v_0 = 0$, as discussed in appendix 6.A.

[8] Here, we have chosen the typical observational parameterization of the standard single field result, where A_s and n_s are the amplitude and scalar spectral index of the power spectrum, $\Delta_{s,BD}^2 = A_s \left(\frac{k}{k_{piv}}\right)^{n_s - 1}$ and $k_{piv} = 0.05 Mpc^{-1}$ is the pivot scale used by Planck [165].

potential spectator fields. For the case of η_{sl}, it turns out that the effect of varying it (given $\epsilon < 10^{-6}$) in Δ_s^2 can be mimicked by a combination of varying s_0, μ, and A_s for the prior ranges we consider in our analysis. We have also verified this numerically for a variety of values.

After making these choices, we decided to generate an interpolation table for $P_q(\mu)$ in advance of the parameter estimation run. Note that fixing ϵ and η_{sl} to fiducial values means only 2D interpolation is required to generate the table. We find minimal integrity is lost in doing the parameter estimation this way; accuracy between the interpolated and actual numerical solutions is very high, about 10^{-5} percent difference at maximum. Utilizing an interpolation table also considerably speeds up the Monte Carlo analysis, as solving the equations for $A_q^{(2)}$ and $C_q^{(1)}$ is quite numerically intensive for higher wavenumbers. Also, since the entanglement parameters are uncorrelated with the standard ΛCDM ones—e.g., varying ω_b should have no effect on eq. (6.49)—it makes little sense to recompute solutions to the primordial power spectrum for a new step in the cosmological parameter space. With the interpolation table, our parameter estimation code can avoid this, which also speeds up the analysis.

Lastly, we include the effects of varying η_0, the onset of entanglement. As investigated in ref. [4], many modifications to the primordial power spectrum render the CMB observables largely unchanged when η_0 corresponds to the largest observable scale $k = 10^{-6}\text{Mpc}^{-1}$. However, by shifting η_0 closer to the end of inflation, corresponding to smaller observables scales, the effects of entanglement on cosmological observables have the potential to be much more constraining.

Practically, one can see from eq. (6.28) that shifting the initial time η_0 (where entanglement begins) is equivalent to shifting the scale that leaves the horizon at η_0 (the largest observable scale that will show evidence of entanglement). Therefore, the onset of entanglement can be parameterized via this distinctive scale, which we call k_{ent} in our analysis. And since our entangled equations are solved using dimensionless time—i.e., the dimensionless results in eq. (6.50) will be the same no matter what η_0 is—we can post-process our power spectrum to include the effects of shifting the onset of entanglement

with a straightforward k shift. To do this, simply make the conversion

$$k \to k \left(\frac{k_{\rm ent}}{10^{-6}{\rm Mpc}^{-1}} \right) \tag{6.53}$$

in eq. (6.49). We take $k_{\rm ent}/10^{-6} \geq 1$ in our work.

6.3.2 Priors for the Monte Carlo analysis

Given the choices discussed in the previous section, we are left with five parameters to vary in our parameter estimation analysis to probe the space of entangled states: A_s, n_s, μ, s_0 and $k_{\rm ent}$. A_s and n_s are the standard amplitude and scalar spectral index of the primordial power spectrum, $\mu = \frac{m_\sigma}{H_{ds}}$ is the dimensionless mass of our spectator field, and $s_0 = \frac{\sigma_0}{M_{pl}}$ is its dimensionless initial position. Finally, $k_{\rm ent}$ is a parameter that is a proxy for adjusting the onset of entanglement, η_0, as described in the previous section.

We choose our priors for the entangled parameters as listed in table 6.1. The lower

Parameter	Prior	Range
$\log_{10}(\mu)$	uniform	$[-3, 0]$
$\log_{10}(s_0)$	uniform	$[-6, 2]$
$\log_{10}(k_{\rm ent})$	uniform	$[-6, -2]$

Table 6.1: Entanglement parameters priors and ranges.

bound on μ is set so that we probe all of the interesting parameter space in figure 6.1, yet avoid some of the asymptotic degeneracies that set in when μ gets too small (which one can already see evidence of in the right-hand plot of figure 6.1). The upper bound on μ is chosen because for $\mu > 1$ the Hankel function index of the spectator mode quickly becomes imaginary (see eq. (6.34b)), and we have been unable to find reliable numerical routines for Hankel functions of imaginary order which run fast enough to use in our Monte Carlo calculations. Unfortunately, this limitation has prevented us from exploring

cases which are otherwise of interest. The value of $k_{\rm ent}$ is varied within a range that yields interesting phenomenology while being computationally feasible. All three parameters are sampled in log space since they vary over several orders of magnitude.

We additionally apply the following condition on s_0:

$$s_0 \leq \frac{0.5\sqrt{2\epsilon}}{\mu^2}, \tag{6.54}$$

(for $\epsilon = 10^{-7}$), which acts as a joint prior on μ and s_0. This condition ensures our spectator field stays subdominant to the inflaton by requiring $\lambda_{1,2} \leq 0.5$ for the full range of time our perturbative entangled evolution equations are valid. It is specifically derived from ensuring our expansion parameter $\lambda = \lambda_{2,\rm max} \leq 0.5$ for all the values of μ and s_0 we investigate. This also guarantees $\lambda_1 \leq 0.5$, for $v_0 = 0$, as discussed in appendix 6.A.

6.3.2.1 Data and software

For our Monte Carlo analysis we focus on Planck data, since the CMB is the standard probe of primordial effects from inflation. We use the Planck 2018 high- and low-ℓ temperature and polarization likelihoods [20]. For the high-ℓ spectra, we make use of the plik-lite code which differs from the full plik likelihood in the number of nuisance parameters.

Our software choices for our analysis are as follows. We use the Cosmic Linear Anisotropy System Solver (CLASS) [151] as our Einstein-Boltzmann solver, and MontePython [166, 167] to sample the parameter space. To explore the effects of our entangled states we use the MultiNest [168, 169, 170] sampler as implemented in MontePython via PyMultiNest [171]. We use a low evidence threshold of 10^{-5} in MultiNest to reliably perform the likelihood analysis in section 6.4 [172]. Finally, we use GetDist [173] to generate our posterior distribution plots.

6.4 Analysis and insights

In this section, we report our results investigating whether CMB data prefer a primordial power spectrum generated by the BD vacuum or by an entangled state. As detailed in section 6.3, we have restricted our focus to entanglement generated due to a free massive spectator field with no initial velocity in its zero mode. Within the limits of our exploration (the scope of which is significantly bounded by numerical considerations) we have found

that for the most part the effects of entanglement are too small to be constrained by (or favored by) the CMB data. Thus, we say that the entangled states we consider are "masquerading" as BD states.

6.4.1 Bayesian inference results

Figures 6.4 and 6.5 show the resulting posterior distributions in our Monte Carlo study for the usual ΛCDM cosmological parameters and those pertinent to the entangled spectrum respectively. In figure 6.5, one can see the posterior probability favors low values of μ and s_0, corresponding to the region of parameter space that is asymptotically degenerate with the BD state. However, as we explain in this section and appendix 6.C, this preference is largely prior driven.

We first turn to the constraints on the cosmological parameters in figure 6.4. Clearly, there is negligible change in this distribution compared to the standard ΛCDM model, i.e., assuming a BD primordial spectrum. This result is straightforward to understand since,

$$C_\ell \propto \int \frac{dk}{k} \Delta_s^2(k) T_\ell^2(k, \overline{\eta_0}) \tag{6.55}$$

where $T_\ell(k)$ is the transfer function which can be understood as the operator responsible for projecting the three-dimensional Fourier modes onto the two-dimensional spherical last-scattering surface and propagating the CMB photons from recombination ($\overline{\eta_*}$) to us today ($\overline{\eta_0}$). Here, we only focus on the temperature C_ℓ [174]. Notably, all the information of the cosmological parameters ω_b, $\omega_{\rm cdm}$, H_0, and $\tau_{\rm reio}$ is contained in $T_\ell(k, \overline{\eta_0})$. However, one may wonder if the inference of these parameters can be "confused" by inducing changes in the primordial spectrum such that the cosmological parameters shift proportionately to leave the observable quantity, the C_ℓ, unchanged. Though not impossible [175], this seems unlikely since each of the parameters leave distinct fingerprints on the CMB spectrum (see e.g. [176]): ω_b affects the even-odd peak modulation through the baryon loading effect [177]; $\omega_{\rm cdm}$, amongst other features, determines the matter-radiation equality scale which is directly revealed by the radiation driving envelope [9]; and H_0 affects the spacing of the

[9] While we have not rigorously investigated this, one may wonder if it is possible to leave $\theta_{\rm eq}$, the comoving size of the horizon at matter-radiation equality (projected from the last-scattering surface), invariant by boosting power at $k \gtrsim 10^{-2} \approx l_{\rm eq}/\overline{\eta_0}$ accompanied by a commensurate decrease in $\omega_{\rm m}$.

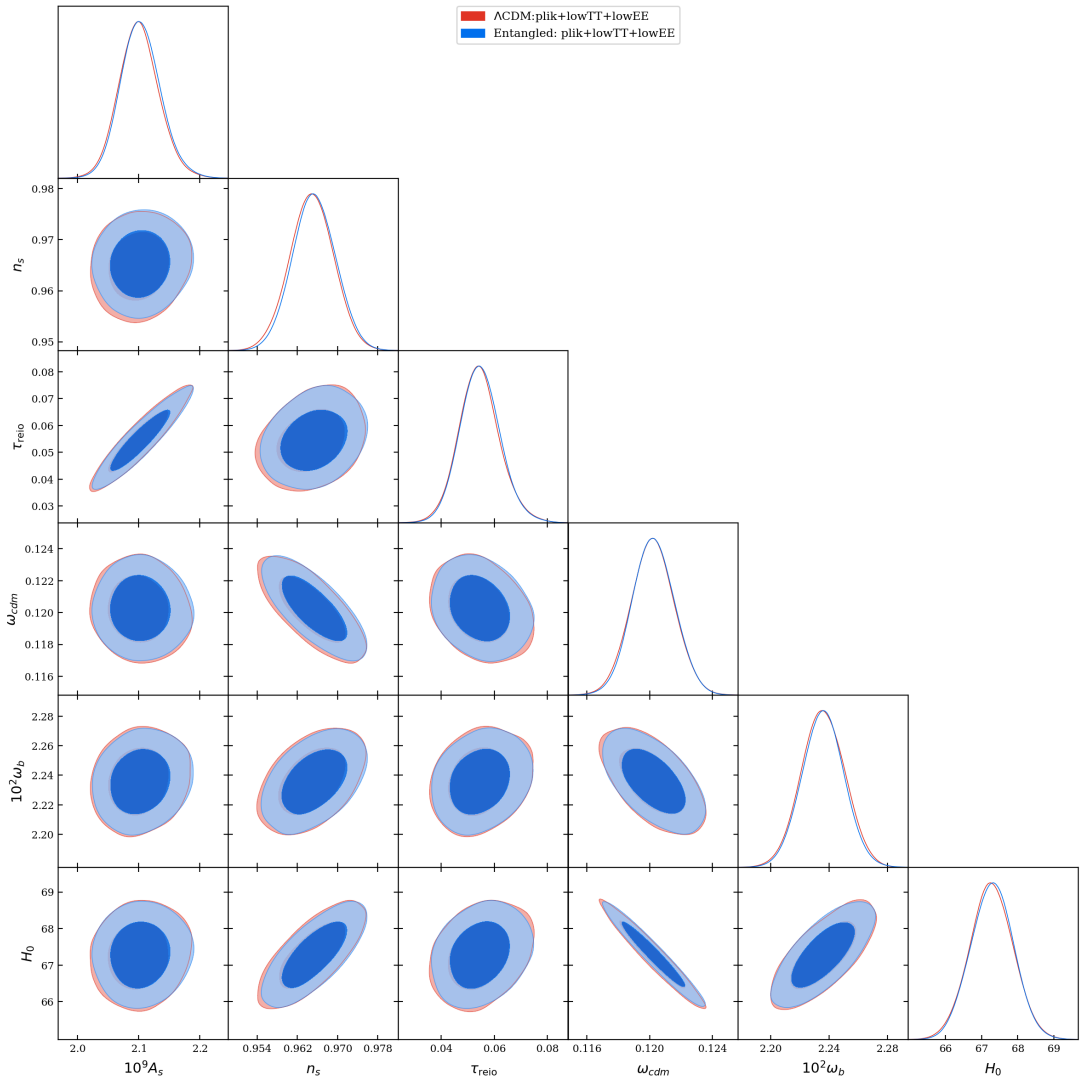

Figure 6.4: Posterior distributions for the cosmological parameters A_s, n_s, τ_{reio}, ω_b, ω_{cdm} and H_0. We compare the standard ΛCDM inflationary scenario, whose primordial power spectrum is generated by the BD vacuum state, versus a primordial power spectrum generated by an entangled state (parameterized by eq. (6.49)).

acoustic peaks via its impact on the angular size of the sound horizon at recombination. Thus, even *a-priori*, judging from some sample power spectra in figure 6.1, it appears unlikely that the features introduced by our perturbative approach to entanglement can mimic any of the imprints induced by variations in the usual cosmological parameters. This reasoning supports the inferences seen in figure 6.4.

Next, we turn to the constraints on the entanglement parameters in figure 6.5. First,

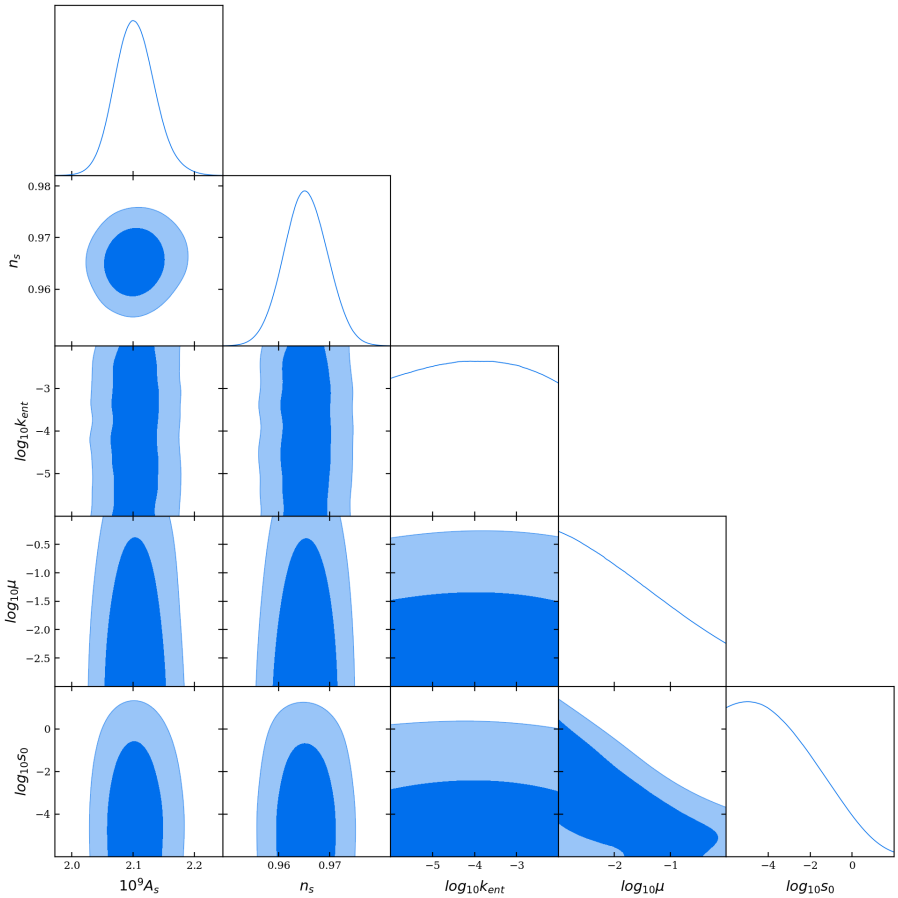

Figure 6.5: Posterior distributions for the entangled power spectrum parameters A_s, n_s, $\log k_{ent}$, $\log \mu$ and $\log s_0$, as defined in eq. (6.49). The corresponding numerical values characterizing the distributions are listed in table 6.3 and χ^2 values are listed in table 6.2.

consider the constraints (or lack thereof) on $k_{\rm ent}$. The uniform distribution on $k_{\rm ent}$ occurs because we vary μ and s_0 over a large range, most notably also sampling small values

While interesting, this is unlikely to change the inference of $\omega_{\rm cdm}$, not only because the parameter is constrained by other effects (prominently the integrated Sachs-Wolfe and the CMB damping tail) [178], but also because, as pointed out in [179], the entire shape of the radiation-driving envelope, and not just $\theta_{\rm eq}$, is sensitive to changes in $\omega_{\rm m}$.

for these parameters which consequently lead to negligibly small deviations from the BD spectrum. Thus, if these distinguishing features are small, it does not matter where on the spectrum they occur as they would all lie in the Planck error budget.

But what about the larger deviations? If the deviations from BD are significant, does the data then prefer where in k these features appear? We address this question by imposing a cut-off and retaining only those sets of parameters that lead to a maximum deviation of at least 2% from the BD spectrum, i.e., $\sup[\Delta^2_{\rm s,norm} > 1.02]$. The resulting power spectra are shown in the right panel of figure 6.6 (note that we additionally impose a cut-off of $\Delta\chi^2 < 2$, relative to the best-fit point, to control for the effect of the variation in the other parameters) and indicate that, while non-negligible deviations of up to $\approx 3\%$ fit the Planck data about as well as the best-fit point, that these deviations preferentially occur in the $k \lesssim 10^{-3}$ regime. In the left-panel of figure 6.6, we contrast the uniform distribution on $k_{\rm ent}$ from figure 6.5 to the distribution generated by seeking only those points that deviate from BD spectrum by at least 1%, which lends evidence to the suspicion garnered from the plot on its right. This skewed distribution, indicating that the highest deviations from BD occur at the large scales, likely reflects the pronounced cosmic variance at $\ell \lesssim 30$. Following the discussion in section 6.3.1.2, this is essentially a constraint on when, during inflation, the most highly entangled states can emerge. The 68% (95%) highest posterior density interval for the reduced $k_{\rm ent}$ distribution in figure 6.6 is $\log_{10}(k_{\rm ent}) < -3.6$ (< -2.5) (given the prior range $\log_{10}(k_{\rm ent}) \in [-6, -2]$).

Finally, we turn towards the constraints on the two parameters controlling the dynamics of the spectator field: the dimensionless mass μ and the initial position of the spectator s_0. The posteriors in figure 6.5 may lead one to erroneously conclude that the data have a preference for lower μ and s_0. However, the profile likelihood for these parameters paints a very different picture than the posterior distribution: both are uniformly distributed in the entire range allowed by our perturbative expansion (see table 6.1). From a strictly "frequentist" perspective, this uniform distribution makes sense: large values of μ can be compensated by small values of s_0 (and vice versa) so that the novel features in the primordial spectrum remain small. In fact, as shown in figure 6.7, even when there is

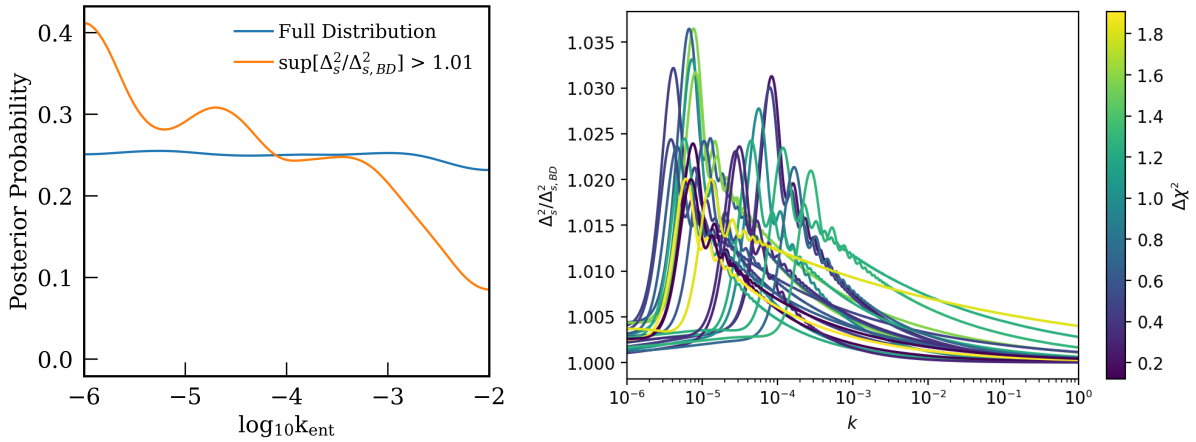

Figure 6.6: To investigate the nature of the spectra with the highest deviations from BD, on the right we show various entanglement primordial power spectra that deviate by at least 2% from BD. Note that the samples are drawn from our Monte Carlo chain so that the χ^2 has dependence on the cosmological parameters. Therefore, we also limit the sample to points with $\Delta\chi^2 < 2$ (relative to the best-fit) so as to minimize the impact of this dependence. The plot on the left shows the distribution in $\log k_{\rm ent}$ if only spectra that deviate by at least 1% from BD are taken into account.

significant deviation from BD, the χ^2 remains approximately the same. This same point is also illustrated in the right panel of figure 6.6. Why then do the posteriors differ from a uniform distribution? The skewness in the posterior is due *entirely* to the prior. It stems from the condition in eq. (6.54) which effectively acts as a joint prior on μ and s_0.

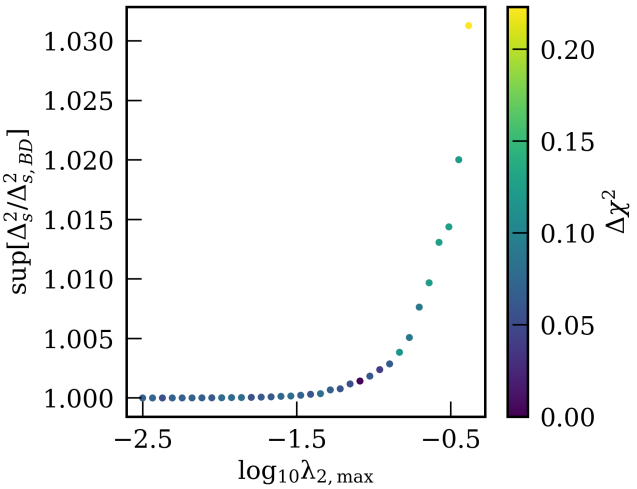

Figure 6.7: Here we depict the maximum deviation from the BD state as a function of $\lambda_{2,max}$. Since the samples are drawn from our Monte Carlo chain, for each bin in $\lambda_{2,max}$ we pick the point with the smallest χ^2 (relative to the best-fit) so as to project out the dependence on the other parameters.

To better understand the effect of this prior, let us *assume* that we are given a likelihood that is uniform in $\log\mu, \log s_0$, and, for completeness, suppose in $\log(k_{\rm ent})$ as well. We then impose the same priors on these parameters as those listed in table 6.1, along with the condition eq. (6.54). The resulting posterior distributions for this toy example are shown in figure 6.8 and match almost exactly what we see in figure 6.5 (note that now we do not make use of any data!). This allows us to conclude that the posterior distribution on $\log\mu$ and $\log s_0$ is entirely prior driven. In fact, the skewed distribution in $\log\mu$ owes itself, at least partially, to a prior-volume effect: because of the condition eq. (6.54), smaller values of μ have more prior volume in s_0 available, while having an equal likelihood, which assigns more posterior weight to the low-μ regime upon marginalizing over s_0.

Certainly the issue of priors affecting parameter inferences is not a new one; the cosmology literature alone has many examples of this effect (e.g. on the inference of inflationary parameters, on the inference of the number of ultra-relativistic species, on dark matter interactions, and recently on the significance of early-dark energy to ameliorate the H_0 cosmological tension [180, 181, 182, 183]). There are several tools available to address such effects. Here we use two methods. First, we do a likelihood profile analysis (see e.g. [184]) and find near uniform distributions on all the entanglement parameters. The results are summarized in table 6.3. This analysis is completely decoupled from priors and strictly tells us that the probability of the Planck data being generated by a BD state is (approximately) the same as the probability of it being generated by an entangled state. Second, we run an MCMC assuming an iso-likelihood, along with our priors on the entanglement parameters, which gives identical results to the posteriors generated using the Planck data (shown in figure 6.8). This reaffirms the profile likelihood analysis indicating that the data are not informative on the model parameters.

Despite the caveats in interpreting the posterior distributions at face value, they nevertheless contain important information of the underlying physics. On a physical level, the posterior of μ being driven to lower values incorporates a penalty for fine-tuning: higher μ values require the initial condition of the spectator field to lie in a smaller phase-space

volume compared to lower values of μ. Very importantly, our priors on both μ and s_0 are guided in part by fundamental physics constraints such that the spectator field remain subdominant to the inflaton energy. These *physical* constraints lead to the joint prior on $\mu - s_0$ (eq. (6.54)) (see appendix 6.C for the effect of increasing the prior volume in s_0 on the parameter inferences). This is in contrast to the oft-studied parameterized/reconstruction approach to the primordial power spectrum (e.g. [185, 186, 165]) where the significance of a particular parameterization, and therefore that of the parameters on which the prior is enforced, is arbitrary and, consequently, the interpretation of prior-dominated posteriors is equally arbitrary [187].

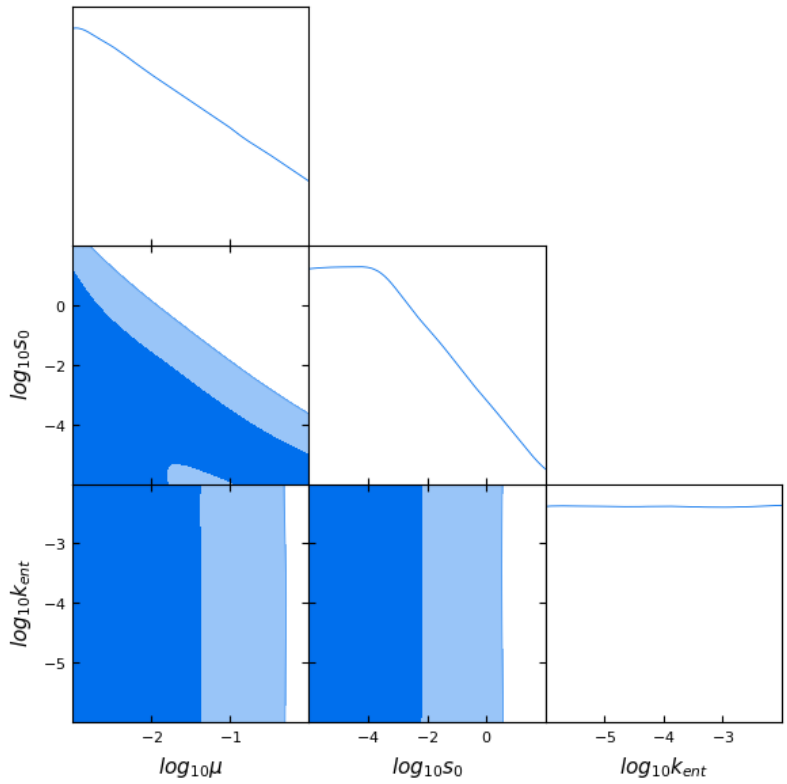

Figure 6.8: Posterior distributions on the entanglement parameters generated in the absence of data by assuming uniform likelihood on the entanglement parameters but imposing the same priors as those used for the posteriors in figure 6.5.

We close this section by returning to the power spectra that show the largest deviations from BD within our perturbative approach. To explicitly demonstrate that even the highly deviating features of figure 6.6 can masquerade in the CMB we plot the corresponding temperature C_ℓ spectrum in figure 6.9. Clearly, the largest spread, by far, occurs in

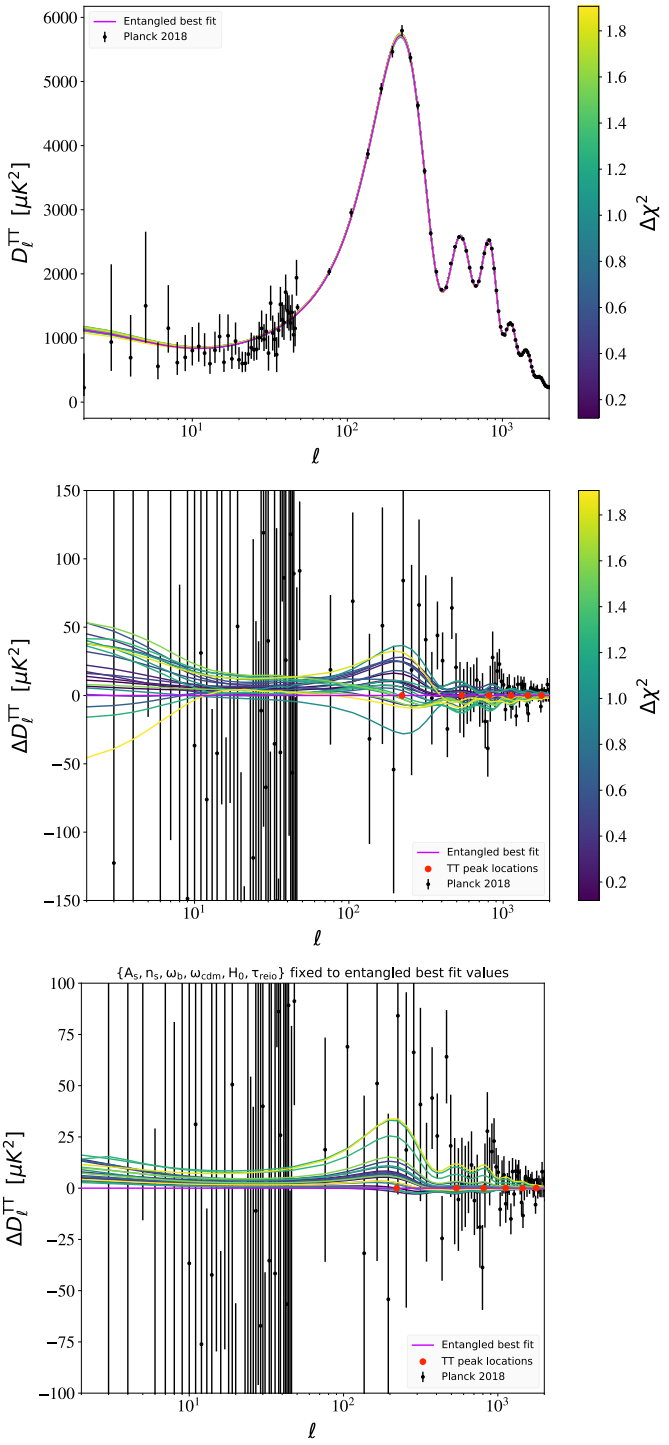

Figure 6.9: TT power spectrum (top) and residuals (middle) with respect to the entangled best fit value. The quantity $D_\ell^{TT} = \frac{\ell(\ell+1)}{2\pi} C_\ell^{TT}$. We plot D_ℓ^{TT} for the entangled best fit parameters, along with those parameters for which $\sup[\Delta^2_{s,\text{norm}}] > 1.02$ and $\Delta\chi^2 < 2$ (whose primordial spectra are shown in Fig 6.6). The locations of the peaks in the TT-spectra are plotted along with the residuals to guide the eye. The bottom plot investigates the effect of just the entangled parameters on the TT-spectra, as discussed in the text. Data is from the Planck 2018 data release.

the low-ℓ regime which is precisely where the data has the largest sampling ("cosmic") variance. Additionally, all the characteristic oscillatory features of the entangled power spectra have been washed out. This is largely due to the smearing effect of the window function, since the transfer function in eq. (6.55) is given by

$$T_\ell(k,\overline{\eta_0}) = \int_{\overline{\eta}_{\rm initial}}^{\overline{\eta_0}} d\overline{\eta} S(k,\overline{\eta}) j_\ell[k(\overline{\eta_0}-\overline{\eta})] \tag{6.56}$$

where $S(k,\overline{\eta})$ contains all the cosmological hydrodynamics while the spherical Bessel function $j_\ell[k(\overline{\eta_0}-\overline{\eta})]$ acts as a window function encoding the geometric effect of projecting onto the CMB surface [177]. Since $j_\ell[..]$ has a non-zero width, it causes a transfer of power from a feature at a particular k-value to a range of ℓ-values (in contrast to the δ-function approximation where all the power is concentrated to a distinctive $\ell = k(\overline{\eta_0}-\overline{\eta})$). In the same spirit, any oscillatory features in the primordial spectrum with frequency much less than the width of the window function see witness suppression [188]. A more thorough understanding regarding the kind of entanglement features that can survive the geometric effect of the transfer function is deferred to a future study. For this work, it suffices to mention that the apparent oscillations in the residuals shown in figure 6.9 should not be mistaken for the characteristic oscillations that appear in the primordial power spectrum.[10] In fact, at least some of the variation in the residual temperature spectrum (middle panel in figure 6.9) can be attributed to slight variations in the best-fit cosmological parameters, primarily in the $A_s - \tau_{\rm reio}$ plane, corresponding to a particular entangled primordial spectrum.

6.5 Conclusions

We have investigated the effects of entanglement in the inflationary universe on CMB observables. Even if inflation is mostly driven by a single light scalar field, many theories predict the existence of multiple, heavier degrees of freedom. As demonstrated in ref. [4], if there exist other spectator fields, an entangled state is expected to emerge, which

[10]Further isolating the effects of the entangled parameters μ, s_0, and $k_{\rm ent}$ by fixing the rest of the parameters to their best fit values, as shown in the bottom part of figure 6.9, supports this conclusion. Note that there is no color bar in the bottom plot of figure 6.9 since the χ^2 was derived while varying all the cosmological parameters.

	ΛCDM	Entangled
Plik	584.8	584.5
lowTT	23.51	23.38
lowEE	395.9	396.3
Total	1004.2	1004.2

Table 6.2: χ^2 comparison for ΛCDM versus our entangled best fit parameters.

could in principle induce some observable imprints in the CMB. Also, as discussed in the introduction, from the point of view of constructing the most general Gaussian state respecting all the symmetries of the system, we need to include the entanglement kernel.

Here we have focused on the simple yet non-trivial situation in which the spectator field starts away from its minimum, but with zero initial velocity. To enable tractable calculations we worked within a perturbative framework. As demonstrated in figure 6.1, deviations from the purely Bunch–Davies predictions for the primordial power spectrum are expected in the form of a modulated oscillatory signal. By performing a Monte Carlo parameter estimation analysis, we further probed the effects of such oscillations on the CMB observables and found that within our framework our predictions are largely compatible with the Planck data.

One immediate consequence is that low levels of entanglement can actively masquerade in the CMB, in such a way that we may be unable to distinguish it from purely single-field inflation models from power spectrum observables alone. In particular, we have found that the kinds of features introduced in the primordial power spectrum within our framework are unable to confuse the inference of the usual six standard cosmology parameters. However, remarkably, even when the cosmological parameters are held ap-

Parameter	Posterior	Likelihood	Best Fit
$10^9 \mathrm{A}_s$	$2.103^{+0.030}_{-0.034}\ (^{+0.070}_{-0.062})$	$---$	2.106
n_s	$0.9653 \pm 0.0043(\pm 0.0084)$	$---$	0.9653
$\log_{10}(\mu)$	$< -1.40(< -0.32)$	U[-3,0]	-0.3002
$\log_{10}(s_0)$	$< -2.51(< 0.10)$	U[-6,2]	-5.482
$\log_{10}(k_{\mathrm{ent}})$	U[-6,-2]	U[-6,-2]	-2.097
$\log_{10}(\lambda_{2,\mathrm{max}})$	$> -4.33(> -6.83)$	U[-8.6,-0.7]	-2.733

Table 6.3: Summary statistics characterizing the distributions of various parameters discussed in section 6.4. For the near-Gaussian posteriors of A_s and n_s, we quote the mean $\pm$ 68%(95%) central credible intervals. For the $\log \mu$, $\log s_0$, and $\log \lambda_{2,\mathrm{max}}$ ($\log \lambda_{2,\mathrm{max}}$ being a derived parameter) posteriors, we quote the 68% (95%) highest posterior density interval. Here, $U[..]$ denotes an approximately uniform distribution.

proximately fixed, our model allows for significant changes to the primordial spectrum, with negligible changes to the Planck χ^2 budget. In other words, current constraints are unable to rule out entanglement, even for the simplest dynamics that we have considered in this paper.

Based on these results, one natural direction to follow up would be to look for other probes to disentangle this effect, which could include the bispectrum of perturbations or the matter power spectrum. Another interesting direction would be to examine the effects of going beyond just a free massive scalar as a spectator, but perhaps looking at an axionic-type potential, as well as entanglement with other spin fields. This latter approach might yield an interesting line of sight into some of the large scale anomalies in CMB data. It

could also be interesting to extend this work by developing a complimentary technical set-up in Heisenberg picture, which would allow one to explore concepts of entanglement in that formalism. Such an investigation might reveal underlying entanglement in other work investigating the imprints of spectator fields during inflation, even though the authors had not previously considered their results from that conceptual lens. Moreover, increased numerical efficiency and/or processing power could allow us to expand the limits of our framework in directions that would allow the data to be more informative. To reiterate our main point, CMB data alone are consistent with the BD initial state, but *cannot* rule out entangled states, even ones with significant amounts of entanglement as measured by the primordial power spectrum.

6.6 Acknowledgements

We thank Lloyd Knox and Marius Millea for useful discussions. This work was supported in part by the U.S. Department of Energy, Office of Science, Office of High Energy Physics QuantISED program under Contract No. KA2401032. Some of our computations were performed on the UC Davis Peloton computer cluster on a node purchased with funds from DOE Office of Science award DE-SC0009999.

Supplementary Results

Here we collect additional results that the main text makes reference to. We also summarize some additional technical extensions to our work that, while not used for the parameter estimation analysis, offer a complement to the reader interested in the details of our entangled states formalism.

6.A Free massive scalar zero mode analytic solution

The equation that describes the classical evolution of the zero mode of a massive spectator field in an expanding spacetime—in terms of the dimensionless parameters described in section 6.2.3.1—is given by:

$$s''(\tau) - \frac{2}{\tau(1-\epsilon)} s'(\tau) + \frac{\mu^2 \partial_s V(s)}{\tau^2 (1-\epsilon)^2} = 0 \ . \tag{6.57}$$

For the free massive scalar potential, given by $V(s) = \frac{1}{2}s^2$ in dimensionless quantities, this has an analytic solution. Given initial conditions $s(\tau_0 = -1) = s_0$, $\partial_\tau s(\tau_0 = -1) = v_0$, the solutions are:

$$s(\tau) = s_+(-\tau)^{p_+} + s_-(-\tau)^{p_-} \tag{6.58a}$$

$$s'(\tau) = -s_+ p_+(-\tau)^{p_+-1} - s_- p_-(-\tau)^{p_--1} \tag{6.58b}$$

with

$$p_\pm = \frac{(3-\epsilon) \pm \sqrt{(3-\epsilon)^2 - 4\mu^2}}{2(1-\epsilon)} \tag{6.59}$$

and

$$s_+ = \frac{p_- s_0 + v_0}{p_- - p_+} \tag{6.60a}$$

$$s_- = \frac{-p_+ s_0 - v_0}{p_- - p_+} \ . \tag{6.60b}$$

Having this analytic solution gives some computation speedup in calculating the entangled power spectrum. It also enables the analytic treatment discussed in appendix 6.B—which is only possible if eq. (6.57) can be solved analytically.

Additionally, one can use eq. (6.58) to exactly specify the λ parameters for a free massive scalar field:

$$\lambda_1 = \frac{(1-\epsilon)}{\sqrt{2\epsilon}}(-\tau)\partial_\tau s = \frac{(1-\epsilon)}{\sqrt{2\epsilon}}\left[-s_+ p_+(-\tau)^{p_+} - s_- p_-(-\tau)^{p_-}\right] \tag{6.61a}$$

$$\lambda_2 = \frac{\mu^2}{\sqrt{2\epsilon}}\,\partial_s V(s) = \frac{\mu^2}{\sqrt{2\epsilon}}\left[s_+(-\tau)^{p_+} + s_-(-\tau)^{p_-}\right] \ . \tag{6.61b}$$

For cases when $v_0 = 0$—which we explore in this paper's Monte Carlo analysis—one can derive the maximum value of the λ parameters during the course of inflation:

$$\lambda_{1,max} = \left| \frac{(1-\epsilon)}{\sqrt{2\epsilon}} s_0 \frac{p_+ p_-}{p_- - p_+}\left[-\left(\frac{p_+}{p_-}\right)^{\frac{p_+}{p_- - p_+}} + \left(\frac{p_+}{p_-}\right)^{\frac{p_-}{p_- - p_+}} \right] \right| \tag{6.62a}$$

$$\lambda_{2,max} = \frac{\mu^2 s_0}{\sqrt{2\epsilon}} \tag{6.62b}$$

by finding the time at which $\frac{\partial \lambda_{1,2}}{\partial \tau} = 0$ and then evaluating eq. (6.61). Furthermore, one can verify that $\lambda_{2,max} < 1$ will always be the more restrictive condition for a given μ, given $v_0 = 0$.

6.B Entanglement kernel analytic solutions and super-Hubble scale spectator masses

In this appendix we discuss two things—the possibility of analytic solutions for the λ expanded power spectrum for a free massive scalar spectator field, and what these analytic solutions might tell us about spectator masses with $\mu = \frac{m_\sigma}{H_{ds}} > 1$.

First, note that for a free massive scalar spectator with $V(s) = \frac{1}{2}s^2$, both eqs. (6.36) and (6.32d) admit analytic solutions. Solutions for the spectator zero mode are discussed in appendix 6.A, here we discuss the exact solutions to $C_q^{(1)}(\tau)$, which are only possible if eq. (6.36) can be solved analytically.

The easiest thing to do is to solve eq. (6.32d) via an integrating factor solution. If one rewrites that equation as:

$$\begin{aligned}\partial_\tau C_q^{(1)} + iC_q^{(1)}\left(A_q^{(0)} + B_q^{(0)}\right) = -i\tilde{\lambda}_1 A_q^{(0)} B_q^{(0)} + \frac{(A_q^{(0)} - B_q^{(0)})}{2(1-\epsilon)\tau}\left[\left(3 - \epsilon + \frac{\eta_{sl}}{2}\right)\tilde{\lambda}_1 + \tilde{\lambda}_2\right] \\ - i\tilde{\lambda}_1\left[\left(\frac{q}{1-\epsilon}\right)^2 + \frac{\mu^2\partial_s^2 V(s)}{2(1-\epsilon)^2\tau^2} + \frac{1 + \frac{5}{4}\eta_{sl}}{(1-\epsilon)^2\tau^2}\right] \\ - i\tilde{\lambda}_2\left[\frac{1 + \epsilon + \frac{\eta_{sl}}{2}}{(1-\epsilon)^2\tau^2}\right]\end{aligned} \tag{6.63}$$

one can see it of the form

$$\partial_\tau C_q^{(1)} + P(\tau)C_q^{(1)} = Q(\tau) \tag{6.64}$$

which has a solution given by:

$$C_q^{(1)}(\tau) = e^{-\int P(\tau)d\tau}\left(\int Q(\tau)e^{\int P(\tau)d\tau}d\tau\right) + Ce^{-\int P(\tau)d\tau} \tag{6.65}$$

and C without subscript is a constant of integration.

If one expresses the dimensionless zeroth order kernels as:

$$A_q^{(0)}(\tau) = -i\frac{f_v'(\tau)}{f_v(\tau)} = i\left[\frac{(1-2\nu_f)}{2(-\tau)} + \frac{q}{(1-\epsilon)}\frac{H^{(2)}_{\nu_f - 1}\left(\frac{-q\tau}{(1-\epsilon)}\right)}{H^{(2)}_{\nu_f}\left(\frac{-q\tau}{(1-\epsilon)}\right)}\right] \tag{6.66a}$$

$$B_q^{(0)}(\tau) = -i\frac{g_\theta'(\tau)}{g_\theta(\tau)} = i\left[\frac{(1-2\nu_g)}{2(-\tau)} + \frac{q}{(1-\epsilon)}\frac{H^{(2)}_{\nu_g - 1}\left(\frac{-q\tau}{(1-\epsilon)}\right)}{H^{(2)}_{\nu_g}\left(\frac{-q\tau}{(1-\epsilon)}\right)}\right] \tag{6.66b}$$

with ν_f and ν_g given in eqs. (6.34a) and (6.34b), deriving the integrating factor proceeds straightforwardly. The result is:

$$e^{\int P(\tau)d\tau} = (-\tau)\left(\frac{q}{1-\epsilon}\right)^{\nu_f+\nu_g}\left[H^{(2)}_{\nu_f}\left(\frac{-q\tau}{(1-\epsilon)}\right)H^{(2)}_{\nu_g}\left(\frac{-q\tau}{(1-\epsilon)}\right)\right] . \tag{6.67}$$

After some fairly intensive algebra, one finds the full solution is given by:

$$C^{(1)}_q(\tau) = \left(\frac{q}{1-\epsilon}\right)^{-\nu_f-\nu_g}\frac{[T(\tau)-T(\tau_0=-1)]}{(-\tau)\left[H^{(2)}_{\nu_f}\left(\frac{-q\tau}{(1-\epsilon)}\right)H^{(2)}_{\nu_g}\left(\frac{-q\tau}{(1-\epsilon)}\right)\right]} \tag{6.68}$$

where the constant of integration was determined by the initial condition $C^{(1)}_q(\tau_0=-1)=0$ and $T(\tau)$ is given by:

$$\begin{aligned}
T(\tau) = \frac{i}{\lambda\sqrt{2\epsilon}}\left(\frac{q}{1-\epsilon}\right)^{\nu_f+\nu_g}\Bigg[&\mathcal{I}_{(p_+-1,\nu_f,\nu_g)}s_+\left(\frac{1-\epsilon}{q}\right)^{p_+}\Bigg(\frac{(1-\epsilon)(1-2\nu_f)(1-2\nu_g)}{4}p_+ \\
&-\frac{\nu_g-\nu_f}{2(1-\epsilon)}\left[\left(3-\epsilon+\frac{\eta}{2}\right)(1-\epsilon)p_+-\mu^2\right]-\frac{(1-\epsilon)\left(1+\frac{5\eta_{sl}}{4}+\frac{\mu^2}{2}\right)p_+-\left(1+\epsilon+\frac{\eta}{2}\right)\mu^2}{(1-\epsilon)^2}\Bigg) \\
&+\mathcal{I}_{(p_--1,\nu_f,\nu_g)}s_-\left(\frac{1-\epsilon}{q}\right)^{p_-}\Bigg(\frac{(1-\epsilon)(1-2\nu_f)(1-2\nu_g)}{4}p_- \\
&-\frac{\nu_g-\nu_f}{2(1-\epsilon)}\left[\left(3-\epsilon+\frac{\eta}{2}\right)(1-\epsilon)p_--\mu^2\right]-\frac{(1-\epsilon)\left(1+\frac{5\eta_{sl}}{4}+\frac{\mu^2}{2}\right)p_--\left(1+\epsilon+\frac{\eta}{2}\right)\mu^2}{(1-\epsilon)^2}\Bigg) \\
&-\frac{(1-\epsilon)^{p_++1}}{q^{P_+}}(s_+p_+)\mathcal{I}_{(p_++1,\nu_f,\nu_g)}-\frac{(1-\epsilon)^{p_-+1}}{q^{P_-}}(s_-p_-)\mathcal{I}_{(p_-+1,\nu_f,\nu_g)} \\
&+\mathcal{I}_{(p_+,\nu_f,\nu_g-1)}s_+\left(\frac{1-\epsilon}{q}\right)^{p_+}\left(\frac{(1-\epsilon)(1-2\nu_f)}{2}p_++\frac{\left[\left(3-\epsilon+\frac{\eta_{sl}}{2}\right)(1-\epsilon)p_+-\mu^2\right]}{2(1-\epsilon)}\right) \\
&+\mathcal{I}_{(p_-,\nu_f,\nu_g-1)}s_-\left(\frac{1-\epsilon}{q}\right)^{p_-}\left(\frac{(1-\epsilon)(1-2\nu_f)}{2}p_-+\frac{\left[\left(3-\epsilon+\frac{\eta_{sl}}{2}\right)(1-\epsilon)p_--\mu^2\right]}{2(1-\epsilon)}\right) \\
&+\mathcal{I}_{(p_+,\nu_g,\nu_f-1)}s_+\left(\frac{1-\epsilon}{q}\right)^{p_+}\left(\frac{(1-\epsilon)(1-2\nu_g)}{2}p_+-\frac{\left[\left(3-\epsilon+\frac{\eta_{sl}}{2}\right)(1-\epsilon)p_+-\mu^2\right]}{2(1-\epsilon)}\right) \\
&+\mathcal{I}_{(p_-,\nu_g,\nu_f-1)}s_-\left(\frac{1-\epsilon}{q}\right)^{p_-}\left(\frac{(1-\epsilon)(1-2\nu_g)}{2}p_--\frac{\left[\left(3-\epsilon+\frac{\eta_{sl}}{2}\right)(1-\epsilon)p_--\mu^2\right]}{2(1-\epsilon)}\right) \\
&+(1-\epsilon)s_+p_+\left(\frac{1-\epsilon}{q}\right)^{p_+}\mathcal{I}_{(p_++1,\nu_f-1,\nu_g-1)}+(1-\epsilon)s_-p_-\left(\frac{1-\epsilon}{q}\right)^{p_-}\mathcal{I}_{(p_-+1,\nu_f-1,\nu_g-1)}\Bigg] .
\end{aligned} \tag{6.69}$$

The parameters $s_\pm$ and $p_\pm$ are defined in appendix 6.A, λ is our expansion parameter (as discussed in section 6.2), and $\mathcal{I}_{(a,b,c)}$ is defined as:

$$\mathcal{I}_{(a,b,c)} = \left[\int x^a H_b^{(2)}(x) H_c^{(2)}(x) dx\right]\Bigg|_{x=\frac{-q\tau}{(1-\epsilon)}} \tag{6.70}$$

which can be exactly evaluated—using Mathematica or other methods of your choice—to be a combination of power laws, generalized hypergeometric functions and gamma functions. The exact evaluated form of $\mathcal{I}_{(a,b,c)}$ is not particularly illuminating, but what is interesting is that eq. (6.70) together with eqs. (6.68) and (6.69) hint that much of the oscillatory nature of our entanglement kernel $C_q^{(1)}$—both in time and as it contributes to $\Delta_s^2(k)$—is sourced by integrals that mix the two Hankel functions from the inflaton and spectator fields.

One might hope to gain further intuition and derive an analytic expression for the power spectrum in eq. (6.47) by also solving the $A_q^{(2)}$ equation in the same way, however this is only partially possible. The contribution to $A_q^{(2)}$ from the C kernel independent terms in eq. (6.32b) can also be solved analytically, using similar methods to what was described above for $C_q^{(1)}$. However, the contribution from the C kernel dependent terms in that equation cannot be solved for analytically—as far as the authors know at this time of writing—due several integrals over multiple generalized hypergeometric functions that show up due to eq. (6.70).

But even though a full analytic treatment of $\Delta_s^2(k)$ is not currently possible, it turns out that the C kernel analytic solution derived here can give a baseline estimate of what the overall behavior of the power spectrum will be. Consider the equation for $\Delta^2_{s,\text{norm}}$, i.e.

$$\Delta^2_{s,\text{norm}} = \left[1 + \lambda^2\left(\frac{-A_{kR}^{(2)}}{A_{kR}^{(0)}} + \frac{(C_{kR}^{(1)})^2}{A_{kR}^{(0)}B_{kR}^{(0)}}\right)\right] = \left[1 + \lambda^2\left(\frac{-A_{qR}^{(2)}}{A_{qR}^{(0)}} + \frac{(C_{qR}^{(1)})^2}{A_{qR}^{(0)}B_{qR}^{(0)}}\right)\right] \tag{6.71}$$

which is just a rewritten form of eq. (6.47). Figure 6.10 plots the full numerical solution to $\Delta^2_{s,\text{norm}}$, along with its 'component parts' —the contribution from just $C_q^{(1)}$ alone (which can be solved numerically or analytically), the contribution from the C kernel independent part of $A_q^{(2)}$ (which can also be solved by either method), and the C dependent part of $A_q^{(2)}$ (which can only be evaluated numerically). Even though the full solution to $\Delta^2_{s,\text{norm}}$

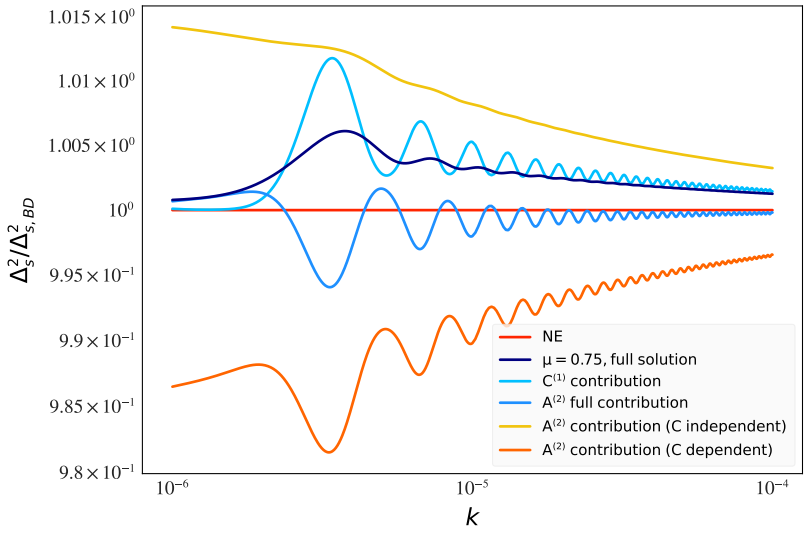

Figure 6.10: Log-log plot of $\Delta^2_{s,\text{norm}}$ for $\mu = 0.75$, $s_0 = \frac{0.2\sqrt{2\epsilon}}{\mu^2}$ (with $\epsilon = 10^{-7}$) and $v_0 = 0$. We plot the full solution for $\Delta^2_{s,\text{norm}}$ along with its 'component parts,' as discussed in the text. The non entangled case corresponds to $\Delta^2_{s,\text{norm}} = 1$, and we take our expansion parameter to be $\lambda = \lambda_{2,\text{max}}$, where $\lambda_{2,\text{max}}$ is defined in eq. (6.62).

is different than that given by the $C^{(1)}$ contribution—$\left[1 + \lambda^2 \left(\frac{(C^{(1)}_{qR})^2}{A^{(0)}_{qR} B^{(0)}_{qR}}\right)\right]$—the latter still hints at many of the features the full solution contains, namely oscillations in k and a decaying exponential envelope for this choice of μ, s_0 and v_0.

One can then use the C kernel analytic solutions to estimate the effects of entanglement on the power spectrum for spectators with $\mu = \frac{m_\sigma}{H_{ds}} > 1$. These solutions are potentially interesting, but not easily amenable to numerical evaluation due to the fact that the Hankel function index for the spectator mode, ν_g, quickly becomes imaginary for $\mu > 1$. Hankel functions of imaginary order can be evaluated in Mathematica, but we have not found a way to evaluate these functions sufficiently rapidly to use in our Monte Carlo calculations.

So, as a preview of possible extensions to our current work, in figure 6.11 we plot the C kernel analytic contribution to the power spectrum, $\left[1 + \lambda^2 \left(\frac{(C^{(1)}_{qR})^2}{A^{(0)}_{qR} B^{(0)}_{qR}}\right)\right]$, for $\mu = 2$, 4 and 6. This plot shows an example of how different the entanglement structure may be for super Hubble scale masses.

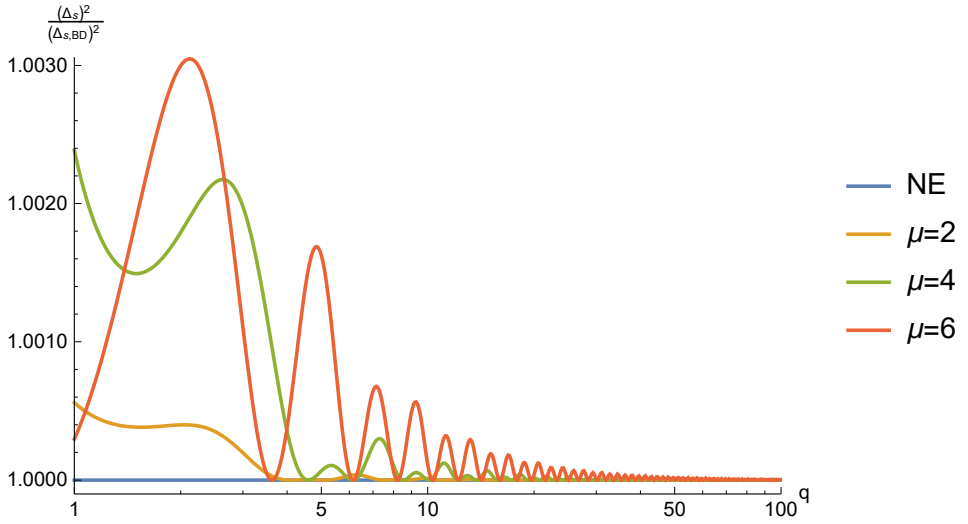

Figure 6.11: Log-log plot of the C kernel contribution to $\Delta^2_{s,\text{norm}}$, $\left[1+\lambda^2\left(\frac{(C^{(1)}_{qR})^2}{A^{(0)}_{qR}B^{(0)}_{qR}}\right)\right]$, for μ = 2,4,6. We take $s_0 = \frac{0.2\sqrt{2\epsilon}}{4^2}$ (with $\epsilon = 10^{-7}$) and $v_0 = 0$ for all three curves, to enable easier comparison. $q = k \times 10^6$ on the horizontal axis, and the non entangled case corresponds to $\Delta^2_{s,\text{norm}} = 1$. (We take our expansion parameter to be $\lambda = \lambda_{2,\text{max}}$, where $\lambda_{2,\text{max}}$ is defined in eq. (6.62).)

6.C Prior volume weighting

In this section we further elucidate the evidence for prior effects, in particular the effect of prior volume weighting, that was alluded to in section 6.4. Recall that the posteriors are prior driven due to the effects of imposing two conditions: that $\mu < 1$ and that the spectator be subdominant to the inflaton energy so that, for a given μ, $s0 < 0.5\sqrt{2\epsilon}/\mu^2$— which is effectively a joint prior on μ and s_0. Meanwhile, there are also the independent uniform priors (the region from which the Monte Carlo will draw samples): $\log\mu \in [-3, 0]$ and $\log s_0 \in [-6, 2]$ where the lower bounds stem from our motivation to exclude regions of very small mass that are practically degenerate with the BD state (i.e. deviate negligibly). However, this choice of limiting the lower bound in s_0 (μ) results in less prior weight to the larger values of μ (s_0). To illustrate this point, suppose that we instead sample $\log s_0 \in [-20, 2]$ so that the higher μ values now have more prior volume available than before. The resulting posterior distribution (again, assuming a uniform likelihood on all the parameters) shows an increased probability density towards larger values of μ; in fact, the posterior is now much closer to a uniform distribution.

Note that often a stricter prior is chosen precisely to mitigate the effect of prior volume effects (see e.g. section III in [189]). In such cases, expanding the prior range will further exacerbate the issue. However, in our case, not only is the data uninformative on the parameters across the range of variation, the joint prior complicates matters by assigning less prior volume to the higher μ regime so that extending the lower bound in the independent $\log s_0$ prior can provide some compensation to alleviate the effect of the joint prior. Of course, because of the symmetry between s_0 and μ^2 in the joint prior, one can achieve the same effect on the marginalized $\log s_0$ posterior by extending the lower bound of the independent $\log \mu$ prior.

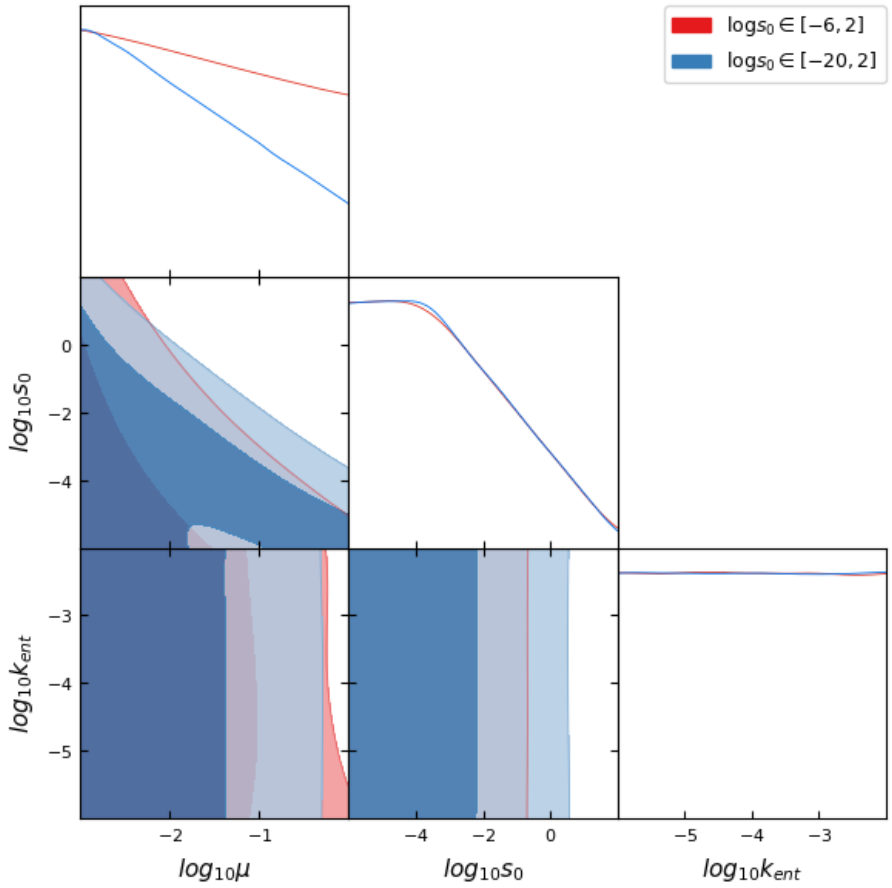

Figure 6.12: The effect of decreasing the lower bound of $\log s_0$ can be clearly seen in the marginalized $\log \mu$ posterior.

Chapter 7

Entangled States as a Probe of Early Universe History: a Higgs Case Study

The material in this chapter previously appeared in ***Entangled States as a Probe of Early Universe History: a Higgs Case Study*** *by Rose Baunach [6].*

ABSTRACT: I investigate whether the technical framework for dynamically generated entangled states developed in [5, 4] can be used to answer other questions about early universe history. Using a Higgs-like potential as the spectator field, I explore whether distinguishing features of phase transitions and/or the inflationary energy scale can be imprinted on cosmological observables due to entanglement during inflation. As a consequence of this analysis, I also present results that illustrate the variety of features a Higgs-like potential can imprint on the primordial power spectrum due to entanglement, as well as how easy it might be to distinguish such spectra from other similar scalar field results at the level of CMB residuals.

7.1 Introduction

We currently believe the anisotropies in the Cosmic Microwave Background radiation (CMB) are due to a period of inflationary expansion [115, 132, 134, 133, 135, 136] that stretches quantum fluctuations in the early universe from micro to macro scales and sources the formation of cosmic structure. While the simplest single-field inflation model predictions are in strong agreement with our current data, they rely on the key assump-

tion that quantum fluctuations during inflation are generated by a particular state—the Bunch-Davies (BD) state [19]. Even though this choice is well-motivated theoretically, it remains an interesting question whether current data can rule out other well-motivated choices of states. As previously demonstrated in [4, 5], entanglement is naturally and inevitably dynamically generated during inflation given the presence of a "rolling" spectator scalar field—and the resulting entangled state will yield a primordial power spectrum with potentially measurable deviations compared to the canonical BD result.

In [5], a Monte Carlo analysis was performed to investigate just how strongly Planck data prefers the standard BD vacuum state, versus an entangled one. The results of that work demonstrated that most entangled states generated by the technical formalism in [5, 4] are consistent with Planck data[1]—which begs the question, what else might you be able to infer from signatures of entangled states in the CMB? For this work, I was motivated to explore whether an entangled state might imprint distinguishing features of the inflationary energy scale and/or cosmological phase transitions on CMB observables—and if such signatures could be used to observationally distinguish between alternate early universe scenarios various research programs might propose.

The inflationary energy scale is of high theoretical interest but is poorly observationally constrained. In theoretical cosmology we are often conditioned to assume inflation occurs at very high energies (e.g. for GUT motivations, etc), but this has not been observationally proven. The upper limit for the inflationary energy scale, parameterized by the value of the Hubble parameter during inflation (in quasi de Sitter space), H_{ds}, is constrained by the tensor-to-scalar ratio, r. The current bound of $r < 0.032$ [190] for single field inflationary models gives an approximate upper limit of $H_{ds} < O(10^{13}\ \text{GeV})$. However, the only universal lower bound on the inflationary energy scale is the requirement that big bang nucleosynthesis (BBN) successfully occur at $O(1\ \text{MeV})$. (There are additional constraints due to reheating and baryogenesis scenarios, but these are model dependent.) So there

[1]Note that as discussed in [5], the analysis in that paper was limited technically from fully saturating the Planck constraints, and one would have to expand the framework utilized in [5] to allow a greater variety of entangled states in order to more systematically determine which states are preferred by the data. However, while the results in [5] cannot claim that the data strongly prefers an entangled state over BD, the analysis did reveal significant entanglement was consistent with Planck data for some model parameters.

are actually a large set of energies at which inflation might occur that are currently within experimental bounds.

Another piece of the early universe narrative that is similarly interesting but poorly constrained is the timing of the electroweak phase transition. Current state of the art lattice calculations place the temperature of this phase transition for the SM Higgs at about 159.5 GeV [191]. This places the EW phase transition before BBN, which occurs at temperatures $O(1\text{ MeV})$ [16], but beyond that things are less clearly defined. One interesting question to consider is whether the EW phase transition might occur during or even before inflation. Given the experimental uncertainty in the inflationary energy scale, this is within the scope of possibility. If one could determine whether the EW phase transition took place before, during, or after inflation, that would have important implications for theories of reheating, baryogenesis, leptogeneis, and other early universe processes. For example, if the Higgs develops a vacuum expectation value before the onset of reheating, that would imply the gauge bosons are no longer massless (due to the Higgs mechanism) during that era, which could alter the channels the inflaton degrees of freedom decay into during reheating, as well as the efficiency of such decays (e.g. [192]). Similarly, knowing the timing of the EW phase transition relative to inflation would automatically place a stronger bound on the inflationary energy scale (which, as discussed above, is currently a poorly constrained quantity experimentally). Lastly, the SM Higgs is not the only field postulated to undergo a phase transition in the early universe. For example, there are various models of the dark sector that contain a 'dark Higgs,' and narrowing down the era of its phase transition would also have strong implications for model building in the dark sector (and would also potentially place constraints on the inflationary energy scale).

This project is a first step towards answering such questions. I have utilized a simple model of a Higgs-like scalar spectator potential to investigate whether signatures of phase transitions (such as the EW transition) and/or the inflationary energy scale might imprint themselves on cosmological observables due to entanglement. Since this is the first instance the technical formalism in [4, 5] has been employed to answer such questions, my

aim was to map out general trends and possibilities in a 'case study' analysis, without attempting to exhaustively prove every possible nuance.

I organize this paper as follows. In section 7.2, I review the technical framework for entangled states as derived in [4, 5]. The reader who is already familiar with [4, 5], and in particular [5], should feel free to skip this section. Then, in section 7.3 I begin by reviewing standard lore for symmetry breaking and restoration in the early universe. I then lay out the definitions and assumptions made for this work in section 7.3.2. Section 7.3.3 presents a summary of my explorations investigating the variety of signatures a Higgs-like spectator can imprint on the primordial power spectrum due to entanglement. In addition to pointing out the variety of solutions, this section also identifies which signals have the potential to be observationally constrained, based on the thresholds phenomenologically identified in previous work [5].

Section 7.4 presents my results investigating whether entanglement with a Higgs-like spectator is distinguishable from entanglement with other scalar spectators at the level of Planck data, given a similar level of entanglement for all spectators. Then in section 7.5 I explore whether the observational imprints of entanglement are fine grained enough to distinguish if the Higgs-like potential is symmetry broken or symmetry restored (with a view of corroborating phase transition narratives). I also explore the uniqueness of the signals identified for a given inflationary energy scale—or whether degeneracies impede utilizing entanglement as an independent probe of that parameter. In section 7.6 I conclude and provide some discussion on what lessons the case study analysis in this work provides for future research. There are also a few technical results from the formalism reviewed in section 7.2 regulated to appendix 7.A, which the reader is directed to as appropriate.

7.2 Review of entangled states formalism

In this section I review the technical formalism developed in [5, 4] for entangled states—describing entanglement between the inflaton perturbations and those of a spectator scalar field. For further details of this formalism beyond what is reviewed here, please see [5, 4].

7.2.1 Entangled two-point function

Here I review the steps necessary to obtain the entangled two-point function—and thus the scalar inflationary power spectrum—in Schrödinger picture QFT.

As discussed in [4, 5], one begins with the action for two scalar fields

$$S = \frac{1}{2}\int d^4x\sqrt{-g}\big(\mathcal{R} - (\partial\Phi)^2 - (\partial\Sigma)^2 - 2V(\Phi) - 2V(\Sigma)\big) \tag{7.1}$$

given $V(\Phi,\Sigma) = V(\Phi) + V(\Sigma)$, with

$$\begin{aligned}\Phi(t,\vec{x}) &= \phi(t) + \delta\phi(t,\vec{x})\\ \Sigma(t,\vec{x}) &= \sigma(t) + \chi(t,\vec{x})\end{aligned} \tag{7.2}$$

describing the background and perturbations of the inflaton field (Φ) and spectator scalar field (Σ). Next, employ the ADM formalism [147] by re-writing the metric as:

$$ds^2 = -N^2dt^2 + h_{ij}(dx^i + N^idt)(dx^j + N^jdt) \tag{7.3}$$

with

$$h_{ij} = a^2e^{2\zeta}\delta_{ij} \tag{7.4}$$

where a is the scale factor, ζ is the co-moving curvature perturbation, and δ_{ij} is the usual Kronecker delta. Making the gauge choice of $\delta\phi = 0$, one effectively re-expresses the scalar degrees of freedom given by the inflaton perturbations, $\delta\phi$, in terms of the scalar metric perturbations, ζ. After solving the ADM constraint equations in the usual way, much integration by parts, and transforming to conformal time, one eventually obtains the following action to second order in perturbations:

$$S = \int d\eta \int \frac{d^3k}{(2\pi)^3}\,\mathcal{L}_k \tag{7.5}$$

where

$$\mathcal{L}_k = \frac{1}{2}\vec{X}^{T\prime}_{\vec{k}}\,\mathcal{O}\,\vec{X}'_{-\vec{k}} + \vec{X}^{T\prime}_{\vec{k}}\,\mathcal{M}_A\,\vec{X}_{-\vec{k}} - \frac{1}{2}\vec{X}^{T}_{\vec{k}}\,\Omega_k^2\,\vec{X}_{-\vec{k}}, \tag{7.6}$$

in which primes denote conformal time derivatives. The field variables are

$$\vec{X}_{\vec{k}} = \begin{pmatrix} v_{\vec{k}} \\ \theta_{\vec{k}} \end{pmatrix}, \tag{7.7}$$

with the following further redefinitions

$$v_{\vec{k}} = z\ \zeta_{\vec{k}} \quad \text{and} \quad \theta_{\vec{k}} = a\chi_{\vec{k}} \tag{7.8}$$

given $z(\eta) = \sqrt{2M_p^2\ \epsilon\ a^2(\eta)}$, ϵ measuring deviations from pure de Sitter space, and M_p being the reduced Planck mass.

The matrices in eq. (7.6), $\mathcal{O}$, $\mathcal{M}$, and the symmetric Ω_k^2, to lowest-order in slow-roll, are given by:

$$\mathcal{O} = \begin{pmatrix} 1 & -\tanh\alpha \\ -\tanh\alpha & 1 \end{pmatrix} \tag{7.9a}$$

$$\mathcal{M}_A = \frac{\mathcal{H}}{2}\left[\left(3-\epsilon+\frac{\eta_{\rm sl}}{2}\right)\tanh\alpha + \frac{a^2\ \partial_\sigma V}{\mathcal{H}^2\sqrt{2M_p^2\epsilon}}\right]\begin{pmatrix} 0 & -1 \\ 1 & 0 \end{pmatrix} \tag{7.9b}$$

$$\Omega_k^2 = \begin{pmatrix} k^2 - \dfrac{z''}{z} & \Omega_{k\ 12}^2 \\ \Omega_{k\ 12}^2 & \Omega_{k\ 22}^2 \end{pmatrix}, \tag{7.9c}$$

with

$$\Omega_{k\ 12}^2 \equiv -\tanh\alpha\left[k^2 + a^2\partial_\sigma^2 V/2 + \mathcal{H}^2\left(1+\frac{5\eta_{\rm sl}}{4}\right)\right] - \mathcal{H}^2\left(1+\epsilon+\frac{\eta_{\rm sl}}{2}\right)\frac{a^2\ \partial_\sigma V}{\mathcal{H}^2\sqrt{2M_p^2\epsilon}} \tag{7.10a}$$

$$\Omega_{k\ 22}^2 \equiv k^2 + a^2\partial_\sigma^2 V - \frac{a''}{a} - 2\epsilon(\epsilon-3)\mathcal{H}^2\ \tanh^2\alpha + 4\epsilon\mathcal{H}^2\tanh\alpha\left(\frac{a^2\ \partial_\sigma V}{\mathcal{H}^2\sqrt{2M_p^2\epsilon}}\right). \tag{7.10b}$$

As done in [5], $\tanh\alpha$ is defined as

$$\tanh\alpha \equiv \frac{\sigma'}{\mathcal{H}\sqrt{2M_P^2\epsilon}}\ , \tag{7.11}$$

with the Hubble parameter $\mathcal{H}$ in conformal time being

$$\mathcal{H} \equiv \frac{a'}{a} \tag{7.12}$$

whereby the slow-roll parameter ϵ is given in conformal time by $\mathcal{H}' = (1-\epsilon)\mathcal{H}^2$ and η_{sl} denotes the second slow roll parameter $\eta_{sl} \equiv \epsilon'/\mathcal{H}\epsilon$.

The corresponding Hamiltonian density can then be calculated via

$$\mathcal{H}_k = \vec{\Pi}^T_{\vec{k}} \vec{X}'_{-\vec{k}} - \mathcal{L}_k, \tag{7.13}$$

and one obtains

$$\mathcal{H}_k = \frac{1}{2}\vec{\Pi}^T_{\vec{k}}\ \mathcal{O}^{-1}\ \vec{\Pi}_{-\vec{k}} + \vec{X}^T_{\vec{k}}\ \mathcal{M}^T_A \mathcal{O}^{-1}\ \vec{\Pi}_{-\vec{k}} + \frac{1}{2}\vec{X}^T_{\vec{k}}\left(\Omega^2_k + \mathcal{M}^T_A \mathcal{O}^{-1}\mathcal{M}_A\right)\vec{X}_{-\vec{k}}, \tag{7.14}$$

in which $\vec{\Pi}_{\pm\vec{k}}$ is the momentum operator conjugate to $\vec{X}_{\pm\vec{k}}$.

The next step is to solve the functional Schrödinger equation for each k-mode[2], via:

$$i\frac{\partial \Psi_k}{\partial \eta} = \mathcal{H}_k \Psi_k \tag{7.15}$$

taking the wavefunctional describing the perturbations in the inflaton and spectator fields to be:

$$\Psi_{\vec{k}}\left[v_{\vec{k}}, \theta_{\vec{k}}; \eta\right] = \mathcal{N}_k(\eta)\ \exp\Bigg[-\frac{1}{2}\Big(A_k(\eta) v_{\vec{k}} v_{-\vec{k}} + B_k(\eta)\theta_{\vec{k}}\theta_{-\vec{k}} + C_k(\eta)\big(v_{\vec{k}}\theta_{-\vec{k}} + \theta_{\vec{k}} v_{-\vec{k}}\big)\Big)\Bigg]\ , \tag{7.16}$$

with $\mathcal{N}_k(\eta)$ normalizing $\Psi_{\vec{k}}$. Solving the Schrödinger equation then generates coupled differential equations for the time evolution kernels $A_k(\eta)$, $B_k(\eta)$, and $C_k(\eta)$, where C_k encodes the entanglement between the field fluctuations[3]. Together with the zero mode equation for the spectator field:

$$\sigma''(\eta) + 2\mathcal{H}\sigma'(\eta) + a^2(\eta)\partial^2_\sigma V(\sigma) = 0\ , \tag{7.17}$$

the solutions of these differential equations specify the time evolution of the two-field vacuum state given by eq. (7.16). (The differential equations for A_k, B_k, and C_k are listed in appendix 7.A, since they were previously derived in [5] and the main analysis in this paper uses a perturbative version of these equations, as discussed in section 7.2.2.) One can then calculate the two-point function for $v_{\vec{k}} = z\ \zeta_{\vec{k}}$, given by [5, 139]:

$$\begin{aligned}\langle v_{\vec{k}} v_{\vec{k}'}\rangle &= (2\pi)^3\delta^{(3)}\left(\vec{k}+\vec{k}'\right)\left(\frac{B_{kR}}{2\left(A_{kR}B_{kR} - C^2_{kR}\right)}\right) \\ &\equiv (2\pi)^3\delta^{(3)}\left(\vec{k}+\vec{k}'\right) P_v(k)\ ,\end{aligned} \tag{7.18}$$

[2]Since the Hamiltonian density has no interactions mixing different k modes, this is fine to do.

[3]If $C_k = 0$ at some time, that means there is no entanglement at that time and the two sectors are decoupled—i.e. $\Psi_{\vec{k}}$ is reduced to a product state.

where 'R' denotes the real part of the kernel. This is related to the standard dimensionless inflationary power spectrum of curvature perturbations via:

$$\Delta_s^2 = \frac{k^3}{2\pi^2} P_\zeta(k) = \frac{k^3}{2\pi^2} \frac{1}{z^2} P_v(k) \ . \tag{7.19}$$

For more details on the steps contained in this section, please see [5, 4, 139] where these quantities are derived and explored in more detail.

7.2.2 Perturbative approach

As in [5], I will ultimately make use of a perturbative approach in this paper to systematically explore the lowest order corrections to the inflationary power spectrum due to entanglement. Expanding the kernels as follows[4]:

$$A_k = A_k^{(0)} + \lambda^2 A_k^{(2)} + ... \tag{7.20a}$$

$$B_k = B_k^{(0)} + \lambda^2 B_k^{(2)} + ... \tag{7.20b}$$

$$C_k = \lambda C_k^{(1)} + ... \tag{7.20c}$$

where the zeroth order terms are the standard Bunch-Davies vacuum (no entanglement) solutions, one can then express the scalar power spectrum to lowest order in λ as:

$$\Delta_s^2 = \Delta_{s,BD}^2 \left[1 + \lambda^2 \left(\frac{-A_{kR}^{(2)}}{A_{kR}^{(0)}} + \frac{(C_{kR}^{(1)})^2}{A_{kR}^{(0)} B_{kR}^{(0)}} \right) \right] \tag{7.21}$$

where

$$\Delta_{s,BD}^2 = \frac{k^3}{2\pi^2} \frac{1}{z^2} \frac{1}{2A_{kR}^{(0)}} \ . \tag{7.22}$$

But what is λ? As discussed in [5], there are two relevant quantities that show up in the Lagrangian:

$$\lambda_1 \equiv \tanh \alpha \equiv \frac{\sigma'}{\mathcal{H}\sqrt{2M_P^2 \epsilon}} \tag{7.23a}$$

$$\lambda_2 \equiv \frac{a^2 \partial_\sigma V}{\mathcal{H}^2 \sqrt{2M_{\rm Pl}^2 \epsilon}} \ . \tag{7.23b}$$

[4]The expansion for C_k begins at first order in λ, because $C_k = 0$ is the standard single field limit. Also, there are no first order terms in A_k and B_k because there is nothing in the equations to source them if C_k is zero initially (which I take to be the case in this paper, as discussed subsequently), as demonstrated in [5].

The λ_i are already required to be small to ensure the spectator field is subdominant to the inflaton during the course of inflation (i.e. one stays within the quasi-single field limit). As done in [5], I take the expansion parameter to be

$$\lambda = \max\{\lambda_i(\eta) : i = 1, 2\} \quad \eta_0 \leq \eta \leq \eta_{end} \tag{7.24}$$

where η_0 is the time at which entangled evolution 'begins' and η_{end} is theoretically the end of inflation (but computationally some explicit late time where all observationally relevant modes are far past the horizon[5]). As shown in [5], this choice of λ ensures increasing λ is directly correlated to increasing the fractional change in Δ_s^2 (due to entanglement) relative to the BD case.

Given these choices, one can expand the full kernel equations (see appendix 7.A) using the expansion specified by eq. (7.20) to obtain the equations needed to compute the power spectrum in eq. (7.21). One obtains:

$$i\partial_\tau A_q^{(0)} = (A_q^{(0)})^2 - \left[\left(\frac{q}{1-\epsilon}\right)^2 - \frac{\left(\nu_f^2 - \frac{1}{4}\right)}{\tau^2}\right] \tag{7.25a}$$

$$i\partial_\tau A_q^{(2)} = 2A_q^{(0)}A_q^{(2)} + \left[\tilde{\lambda}_1 A_q^{(0)} + C_q^{(1)} - \frac{i}{2(1-\epsilon)\tau}\left[\left(3 - \epsilon + \frac{\eta_{sl}}{2}\right)\tilde{\lambda}_1 + \tilde{\lambda}_2\right]\right]^2 \tag{7.25b}$$

$$i\partial_\tau B_q^{(0)} = (B_q^{(0)})^2 - \left[\left(\frac{q}{1-\epsilon}\right)^2 - \frac{\left(\nu_g^2 - \frac{1}{4}\right)}{\tau^2}\right] \tag{7.25c}$$

$$\begin{aligned} i\partial_\tau C_q^{(1)} = {} & C_q^{(1)}\left(A_q^{(0)} + B_q^{(0)}\right) + \tilde{\lambda}_1 A_q^{(0)} B_q^{(0)} \\ & + \frac{i}{2(1-\epsilon)\tau}\left[\left(3 - \epsilon + \frac{\eta_{sl}}{2}\right)\tilde{\lambda}_1 + \tilde{\lambda}_2\right](A_q^{(0)} - B_q^{(0)}) \\ & + \tilde{\lambda}_1\left[\left(\frac{q}{1-\epsilon}\right)^2 + \frac{\mu^2\partial_s^2 V(s)}{2(1-\epsilon)^2\tau^2} + \frac{1 + \frac{5}{4}\eta_{sl}}{(1-\epsilon)^2\tau^2}\right] + \tilde{\lambda}_2\left[\frac{1 + \epsilon + \frac{\eta_{sl}}{2}}{(1-\epsilon)^2\tau^2}\right] \end{aligned} \tag{7.25d}$$

where $\tilde{\lambda}_{1,2} = \frac{\lambda_{1,2}}{\lambda}$ is an algebraic simplification, and the following re-definitions are made to solve the kernel equations in terms of dimensionless quantities (for ease of numerical

[5] As discussed in [5], there is no guarantee that $\zeta_{\vec{k}} = \frac{v_{\vec{k}}}{z}$ remains constant outside the horizon, compared to the standard BD result, so the entangled power spectrum given by eq. (7.21) must be evaluated explicitly at late times.

computations):

$$\tau = -\frac{\eta}{\eta_0},\ q = \frac{k}{k_0} = -(1-\epsilon)k\eta_0 \tag{7.26a}$$

$$\sigma = sM_p,\quad V(\sigma) = \Lambda^4 V(s),\quad \mu^2 = \frac{\Lambda^4}{H_{ds}^2 M_p^2} \tag{7.26b}$$

$$\lambda_1 = \frac{(1-\epsilon)}{\sqrt{2\epsilon}}(-\tau)\partial_\tau s \tag{7.26c}$$

$$\lambda_2 = \frac{\mu^2}{\sqrt{2\epsilon}}\,\partial_s V(s) \tag{7.26d}$$

$$A_k(\eta) = \frac{A_q(\tau)}{(-\eta_0)},\quad B_k(\eta) = \frac{B_q(\tau)}{(-\eta_0)},\quad C_k(\eta) = \frac{C_q(\tau)}{(-\eta_0)} \tag{7.26e}$$

$$\mathcal{H}(\eta) = \frac{\mathcal{H}(\tau)}{(-\eta_0)},\quad \mathcal{H}(\tau) = \frac{-1}{(1-\epsilon)\tau}\ . \tag{7.26f}$$

Note that dimensionless conformal time, τ, runs from -1 to 0, and that the form of eq. (7.21) will be the same in terms of dimensionless variables, since the factors of η_0 will cancel in the ratios of kernels according to the definitions in eq. (7.26). Also, since the zeroth order equations for $A^{(0)}$ and $B^{(0)}$ are just the Schrödinger picture version of the Mukhanov-Sasaki equation, the quantities ν_f and ν_g are defined in the usual way (here in terms of dimensionless variables):

$$\nu_f = \frac{3}{2} + \epsilon + \frac{\eta_{sl}}{2} \tag{7.27a}$$

$$\nu_g(s) = \sqrt{\frac{9}{4} + 3\epsilon - \frac{\mu^2\partial_s^2 V(s)}{(1-\epsilon)^2}}\ , \tag{7.27b}$$

where I highlight to the reader that

$$\mu^2\partial_s^2 V(s) = \frac{\partial_\sigma^2 V(\sigma)}{H_{ds}^2} = \frac{M_{eff}^2(\sigma)}{H_{ds}^2}\ . \tag{7.28}$$

Note that if the spectator is a free massive scalar with a quadratic potential, M_{eff}^2 will be independent of σ and therefore ν_g will be a constant. It is one of the features of this work, discussed in section 7.3, that I allow ν_g to vary—due to the variation of M_{eff}^2—for a Higgs-like potential.

Also, the dimensionless form of the equation describing the evolution of the zero mode, eq. (7.17), becomes:

$$s''(\tau) - \frac{2}{\tau(1-\epsilon)}s'(\tau) + \frac{\mu^2\partial_s V(s)}{\tau^2(1-\epsilon)^2} = 0\ . \tag{7.29}$$

Finally, as previously derived in [5], the initial conditions for eq. (7.25) are:

$$A_{qR}^{(0)}(\tau_0 = -1) = \frac{2}{\pi \left| H_{\nu_f}^{(2)}(\frac{q}{1-\epsilon}) \right|^2} \tag{7.30a}$$

$$A_{qI}^{(0)}(\tau_0 = -1) = \frac{1}{2}\left[1 - 2\nu_f + x \left[\frac{H_{\nu_f-1}^{(1)}(x)}{H_{\nu_f}^{(1)}(x)} + \frac{H_{\nu_f-1}^{(2)}(x)}{H_{\nu_f}^{(2)}(x)}\right]\Bigg|_{x=\frac{q}{(1-\epsilon)}}\right] \tag{7.30b}$$

$$B_{qR}^{(0)}(\tau_0 = -1) = \frac{2}{\pi \left| H_{\nu_g}^{(2)}(\frac{q}{1-\epsilon}) \right|^2} \tag{7.30c}$$

$$B_{qI}^{(0)}(\tau_0 = -1) = \frac{1}{2}\left[1 - 2\nu_g + x \left[\frac{H_{\nu_g-1}^{(1)}(x)}{H_{\nu_g}^{(1)}(x)} + \frac{H_{\nu_g-1}^{(2)}(x)}{H_{\nu_g}^{(2)}(x)}\right]\Bigg|_{x=\frac{q}{(1-\epsilon)}}\right] \tag{7.30d}$$

$$A_{qR}^{(2)}(\tau_0 = -1) = -\tilde{\lambda}_{1,0}^2 A_{qR}^{(0)}(\tau_0 = -1) \tag{7.30e}$$

$$\begin{aligned} A_{qI}^{(2)}(\tau_0 = -1) = &-\tilde{\lambda}_{1,0}^2 A_{qI}^{(0)}(\tau_0 = -1) - \frac{1}{2(1-\epsilon)}\left[\left(3 - \epsilon + \frac{\eta_{sl}}{2}\right)\tilde{\lambda}_{1,0}^2 + \tilde{\lambda}_{1,0}\tilde{\lambda}_{2,0}\right] \\ &+ \left[\frac{\eta_{sl}\tilde{\lambda}_{1,0}^2}{2(1-\epsilon)} + \tilde{\lambda}_{1,0}^2 + \frac{2\tilde{\lambda}_{1,0}^2}{(1-\epsilon)} + \frac{\tilde{\lambda}_{1,0}\tilde{\lambda}_{2,0}}{(1-\epsilon)}\right] \end{aligned} \tag{7.30f}$$

where $\tilde{\lambda}_{1,0}$ denotes that $\tilde{\lambda}_1$ should be evaluated at $\tau_0 = -1$, and a term $\mathcal{O}(\eta_{sl}\epsilon)$ has been dropped from $A_{qI}^{(2)}$.

In this section, I have made the choice—as was also done in [5, 4]—to assume there is no entanglement at some initial time η_0 (corresponding to $\tau = -1$) and to instead study the dynamical generation of entanglement over the course of inflation and its impact on cosmological observables. If I had instead chosen $C_k(\eta_0) \neq 0$, as was done in some earlier work [139, 140, 13], I would have had to consider linear terms in λ in the expansions for A_k and B_k in eq. (7.20) (as discussed in [5]), which would lead to different results for the primordial power spectrum.

To compare my results with Planck data, I use the following form of the perturbative primordial power spectrum in eq. (7.21):

$$\Delta_s^2 = A_s\Big(\frac{k}{k_{\text{piv}}}\Big)^{n_s-1}\left[1 + \lambda^2\left(\frac{-A_{qR}^{(2)}}{A_{qR}^{(0)}} + \frac{(C_{qR}^{(1)})^2}{A_{qR}^{(0)}B_{qR}^{(0)}}\right)\right] \tag{7.31}$$

where I have replaced the theoretical value for $\Delta_{s,BD}^2$ with the usual observational parameterization in terms of A_s and n_s (with $k_{\text{piv}} = 0.05$ Mpc^{-1} [20]), and the entanglement

quantities in the square bracket have been expressed in terms of dimensionless parameters. (However, as noted earlier in this section, the expression in the square brackets in terms of dimensionless variables is equivalent to the one in eq. (7.21), since all dimensionful kernels have mass dimension 1.) Also note that I take the relationship between ϵ, η_{sl}, and n_s to be $\eta_{sl} = 1 - 2\epsilon - n_s$.

Lastly, as in previous work [4, 5], I will often make use of a phenomenological parameter called $k_{\rm ent}$ when comparing the results of entangled power spectra with data. $k_{\rm ent}$ is defined as follows. One can see from eq. (7.26) that shifting the initial time η_0 (where entanglement begins) is equivalent to shifting the scale that leaves the horizon at η_0 (the largest observable scale that will show evidence of entanglement). Therefore, one can chose to parameterize the onset of entanglement via this distinctive scale, called $k_{\rm ent}$ in this analysis. And since the entangled equations are solved using dimensionless time—i.e., the dimensionless quantity in square brackets in eq. (7.31) will be the same no matter what η_0 is—one can post-process power spectra to include the effects of shifting the onset of entanglement with a straightforward k shift. To do this, simply make the conversion

$$k \to k \left(\frac{k_{\rm ent}}{10^{-6}{\rm Mpc}^{-1}} \right) \tag{7.32}$$

in eq. (7.31). I take $k_{\rm ent}/10^{-6} \geq 1$ in this work.

This completes a review of the technical framework. The next section discusses my motivations for the current work and how the technical framework developed in this section will be used to explore them.

7.3 Higgs-like spectator

In this work, I make use of a Higgs-like potential to consider whether signatures of phase transitions and/or the inflationary energy scale might imprint themselves on cosmological observables. In this section I begin by discussing symmetry breaking and restoration in the early universe and the questions related to those concepts that motivated this work. I then outline what choices and approximations were made for this case study analysis. I also present results showcasing the rich phenomenology of entangled primordial power spectra accessible to a Higgs-like spectator.

7.3.1 Symmetry breaking and symmetry restoration

Consider a real scalar field described by

$$\mathcal{L} = \frac{1}{2}\partial_\mu\phi\partial^\mu\phi - V(\phi)$$
$$V(\phi) = -\frac{1}{2}m^2\phi^2 + \frac{1}{4}\lambda\phi^4 \ . \tag{7.33}$$

Formally, this potential has two degenerate stable minima, characterized by a reflection symmetry $\phi \leftrightarrow -\phi$ in the Lagrangian density. To construct a viable quantum theory, one expands the Lagrangian density about one of these stable minima, rather than $\phi = 0$, which is unstable. This requires a choice of vacuum state, and making this choice 'breaks' the reflection symmetry. (Obviously this is a simplified example of symmetry breaking compared to the Higgs mechanism in the Standard Model.)

However, continuing with this simple example for a moment, let us add another piece to the story. In standard lore [17, 16] one comes across the phenomenon of 'high-temperature symmetry restoration.' This arises from considering the fact that at nonzero temperature the ϕ field may no longer exist in isolation. For example, the radiation and matter densities in the early universe are non-negligible at various stages. To model such a background one can imagine the ϕ field in contact with a heat bath. The implications of this scenario can be rigorously dealt with in the language of thermal field theory (e.g. [193]), with a net effect of introducing a temperature dependent mass term in the potential, such that one might have

$$V(\phi, T) = -\frac{1}{2}m^2\phi^2 + \frac{1}{4}\lambda\phi^4 + a\lambda T^2\phi^2 \tag{7.34}$$

in the case of our simplified model (where a is some dimensionless $O(1)$ constant). At a high enough temperature, the temperature dependent term will dominate and $\phi = 0$ will be the single stable minima of the potential—i.e. the symmetry has been 'restored'. However, as the temperature decreases the original mass term will begin to dominate and the degenerate minima will begin to appear, signalling symmetry breaking once again. The simple potential in eq. (7.34) is plotted in figure 7.1 for a few values of T to illustrate this graphically. T_c is the temperature at which $M^2_{eff}(\phi, T) = \partial^2_\phi V(\phi, T)$ evaluated at $\phi = 0$ changes sign, such that $M^2_{eff}(0, T_c) = 0$ and $V(\phi, T_c) = \frac{1}{4}\lambda\phi^4$ (given the potential

in eq. (7.34)).

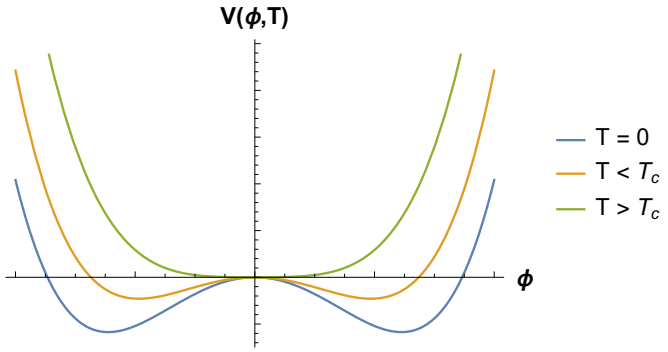

Figure 7.1: The potential $V(\phi, T)$ in eq. (7.34) is plotted for a few values of T above and below T_c—the temperature at which $\partial_\phi^2 V(\phi, T)|_{\phi=0}$ changes sign—in order to graphically illustrate the difference between symmetry broken and symmetry restored behavior for this potential. The x and y axis units are arbitrary.

For the SM Higgs, standard lore [17, 16] does assume a similar behavior to our simplified model—that there exits some temperature in the early universe above which symmetry is 'restored', and the origin of the SM Higgs potential becomes a stable minimum, with a T_c value of about 159.5 GeV [191]. (Alternative scenarios, such as symmetry non-restoration—e.g. [194, 195]—do of course exist.) The process by which the SM Higgs potential transitions from one type of behavior to another is an important component of the electroweak phase transition.

As discussed in the introduction, the timing of the EW phase transition and its proximity to inflation is interesting but poorly determined. The large experimental uncertainty in determining the inflationary energy scale implies that the EW phase transition might have occurred during or even before inflation. Such a scenario would have important implications for early universe processes such as baryogenesis and reheating. And these implications are not unique to the SM Higgs, but would also be relevant for Higgs-like model building in the dark sector. Thus, determining whether signatures of phase transitions (such as the EW transition) and/or the inflationary energy scale might imprint themselves on cosmological observables due to entanglement is a worthwhile goal. I utilize a Higgs-like scalar spectator potential to investigate these questions, with specific choices detailed in the next section.

7.3.2 Definitions and assumptions

In the previous section, I stated my goal was to determine whether signatures of phase transitions (such as the EW phase transition), and/or the inflationary energy scale might imprint themselves on cosmological observables due to entanglement. If such signatures were visible, then one could use them to place further constraints on early universe history using CMB data.

To utilize the entangled states formalism described in section 7.2 to investigate this goal, the spectator zero mode must be allowed to 'roll'. [6] Entanglement will be sourced dynamically if the spectator zero mode has either a non-zero position or velocity [5, 4]. To match this requirement onto a scenario that might resemble the EW phase transition (or a dark Higgs analog), I only consider second order and/or crossover-type phase transitions where the zero mode dynamically rolls to its new symmetry broken vacuum expectation value (rather than a first order transition where the symmetry breaking process is expected to proceed via tunneling [17, 16]). This does not greatly restrict the generality of my investigations, since current bounds forbid a first order phase transition for the SM Higgs due to its mass (i.e. it is too heavy to have a viable first order EW phase transition in the minimal SM [16]).

Before presenting results for entanglement with a Higgs-like spectator in the following section, I first define two quantities that play a key role in my investigations—the spectator potential and the energy scale of inflation.

7.3.2.1 Higgs-like potential

I utilize a Higgs-like spectator potential of the following form

$$V(\sigma, T) = -\frac{1}{2}m_h^2\sigma^2 + \frac{\lambda_h}{4}\sigma^4 + \frac{\lambda_h}{8}T^2\sigma^2 \tag{7.35}$$

where $m_h = M_h/\sqrt{2}$, $M_h = 125$ GeV, $\lambda_h = m_h^2/v^2$, and $v = 246$ GeV, in analogy with the SM Higgs. This is a very simple version of what is often called a 'mean field approximation' in the literature (e.g. [194]), where only leading order thermal corrections—obtained by

[6] Or the two sectors must start with nonzero initial entanglement, as was considered in earlier work [139, 140, 13].

expanding the thermal one-loop effective potential in powers of M_{eff}^2/T^2 [193, 16, 17]—have been considered. [7]

Since this project was designed to be a first pass at answering the motivating questions discussed in section 7.1, I feel justified utilizing such a simple potential. If this 'case study' yields interesting results, one could then go back and substitution the full temperature corrected and renormalized Higgs potential for more fine grained predictions.

The dimensionless version of eq. (7.35) is given by:

$$V(s,T) = -\frac{1}{2}\Big(\frac{m_h}{M_p}\Big)^2 s^2 + \frac{\lambda_h}{4}s^4 + \frac{\lambda_h}{8}\Big(\frac{T}{M_p}\Big)^2 s^2 \tag{7.36}$$

and the quantity $\mu^2\partial_s^2 V(s,T)$ is given by:

$$\mu^2\partial_s^2 V(s,T) = \frac{M_p^2}{H_{ds}^2}\left[-\Big(\frac{m_h}{M_p}\Big)^2 + 3\lambda_h s^2 + \frac{\lambda_h}{4}\Big(\frac{T}{M_p}\Big)^2\right] . \tag{7.37}$$

The fact that eq. (7.37) is s dependent even if T is fixed will be partially responsible for driving some of the new entanglement features exhibited in the plots in subsequent sections—especially compared to the free massive scalar potential studied in [4, 5]—since this will cause the Hankel index for the spectator perturbations, ν_g, to vary as the zero mode rolls through the potential.

Lastly, since this work is focused on exploring observational effects of entanglement during inflation, I take

$$T = T_{GH} = \frac{H_{ds}}{2\pi} \tag{7.38}$$

for the rest of this paper.

7.3.2.2 Inflationary energy scale

The other new ingredient in my analysis compared to previous work is considering the inflationary energy scale explicitly in my equations. Observationally, the scalar primordial power spectrum is parameterized as

$$\Delta_s^2 = A_s\left(\frac{k}{k_{piv}}\right)^{n_s-1} . \tag{7.39}$$

[7] Furthermore, I have ignored any constant (not σ dependent) thermal contributions, because the entanglement equations only depend on $\partial_\sigma V(\sigma)$ and $\partial_\sigma^2 V(\sigma)$.

At the pivot scale $\Delta_s^2 = A_s$, and if one equates this with the standard scale invariant theoretical result

$$\Delta_s^2 = \frac{H_{ds}^2}{8\pi^2 M_p^2 \epsilon} \tag{7.40}$$

one can estimate a value of ϵ to input into the kernel evolution equations

$$\epsilon(H_{ds}) = \frac{H_{ds}^2}{8\pi^2 M_p^2 A_s} \tag{7.41}$$

given observational input for A_s and a value of the inflationary energy scale, H_{ds}, that one would like to investigate (or equivalently T_{GH}, since they are just related by a factor of 2π). These assumptions give the approximate equivalence relation:

$$\epsilon \propto H_{ds}^2 \propto T_{GH}^2 \tag{7.42}$$

modulo important numerical conversion factors. The fact that these three quantities are linked in my simplified model will have some consequences for what questions I can and cannot answer with my subsequent analysis.

7.3.3 Primordial power spectrum phase space

Before investigating possible signatures of phase transitions and/or the inflationary energy scale, I first explored what types of primordial power spectrum features the Higgs-like spectator potential could produce, since this was a novel use of the formalism. This also helped me narrow down which spectator initial conditions yield potentially observationally constrainable signals. A representative sample of my results is shown in figures 7.2 and 7.3.

Figure 7.2 plots the fractional change to the scalar primordial power spectrum due to entanglement, $\frac{\Delta_s^2}{\Delta_{s,BD}^2}$, with Δ_s^2 defined in eq. (7.21) and the standard Bunch-Davies result given by eq. (7.22). For all the results shown in figure 7.2 I took $T = T_{GH} = 100$ GeV—corresponding to an inflationary energy scale of $H_{ds} \approx 628$ GeV—which is below T_c and therefore in the symmetry broken phase for the simple Higgs-like potential defined in eqs. (7.35) - (7.36). As in previous work [5], I set the initial velocity of the spectator zero mode to be zero, so that the variety of oscillatory features in the primordial power spectrum show in figure 7.2 are driven by the initial position of the spectator zero mode and its effective mass. However, in contrast to previous work, the effective mass is no longer constant since the second derivative of the Higgs-like potential depends on the

position of the zero mode. Figure 7.3 shows the evolution of the zero mode location and of the parameter ν_g^2—whose variation is due to variation in the spectator's effective mass, see eqs. (7.27b), (7.28), and (7.37)—during the course of inflation, given the initial conditions specified in figure 7.2.

There are two relevant points to make about the results in figure 7.2. First, there is a interesting transition in the types of oscillatory behaviors that one observes. For smaller initial displacements from the origin, corrections due to entanglement are purely positive (i.e. $\frac{\Delta_s^2}{\Delta_{s,BD}^2} > 1$). However, this changes for larger displacements, and one begins to observe oscillations both above and below the zero point for such initial conditions. The transition point between these two behaviors seems to occur shortly after the initial value of the parameter ν_g equals zero (which corresponds to an initial displacement of $s_0 \approx 1520/M_p$ for the zero mode, given the parameters used for the numerical results in figure 7.2). [8] One can see evidence of this by comparing figures 7.2d and 7.2e, for example.

The second relevant point deals with issues of observability and scale. It's clear from figure 7.2 that a Higgs-like spectator potential can impart a variety of interesting oscillatory features on the primordial power spectrum due to entanglement. For example, some intriguing secondary structure in the oscillations of figure 7.2g and 7.2h occurs when the zero mode has enough energy to explore both sides of the potential (as shown in figure 7.3a). However, if one looks at the y-axis of figure 7.2, most of these features will never be observable. As demonstrated in previous work [4, 5], corrections to the primordial power spectrum of $O(10^{-13})$ or even $O(10^{-4})$ are tiny and completely unobservable with current CMB data. So while the parameter space *is* rich for this type of potential, only larger initial displacements have a hope of being observationally constrained, such as the near percent level corrections in figure 7.2h.

[8] For larger initial displacements, the effective mass term in eq. (7.27b) is greater than the slow roll terms, which causes the parameter ν_g^2 to become negative and ν_g itself to become imaginary. This causes numerical problems for calculating initial conditions for the kernel equations (since Hankel indices of imaginary order are not currently available in Python to the author's knowledge). To mitigate this issue, I generated initial conditions for Hankel indices of imaginary order in Mathematica, and then input these initial conditions into my Python code for the rest of the numerical analysis. This workaround allowed me to study spectators with effective masses greater than H_{ds}, in contrast to the Monte Carlo analysis previously performed in [5]. However, such a workaround was only feasible since this is a 'case study' analysis, as the resource intensiveness of this solution would not be conducive to Monte Carlo work.

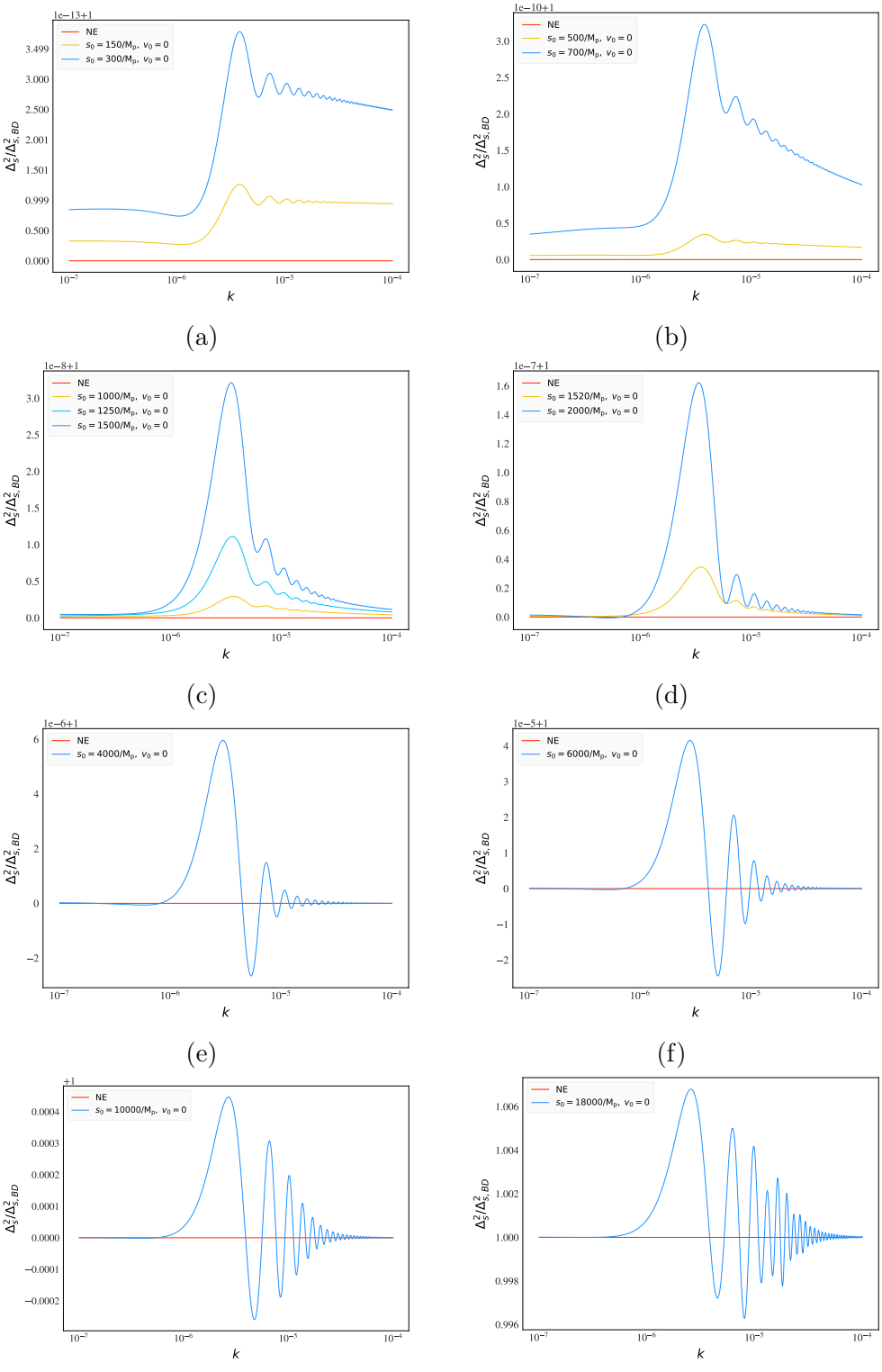

Figure 7.2: A variety of results for fractional corrections to the scalar primordial power spectrum due to entanglement, $\frac{\Delta_s^2}{\Delta_{s,BD}^2}$, given the Higgs-like spectator potential in eq. (7.36). For all plots the spectator had a variety of initial positions and no initial velocity, with $T = T_{GH} = 100$ GeV (corresponding to an inflationary energy scale of $H_{ds} \approx 628$ GeV and $\epsilon = O(10^{-25})$). The non entangled (NE) case corresponds to $\frac{\Delta_s^2}{\Delta_{s,BD}^2} = 1$. $k_{\text{ent}} = 10^{-6}$ for all plots (see eq. 7.32).

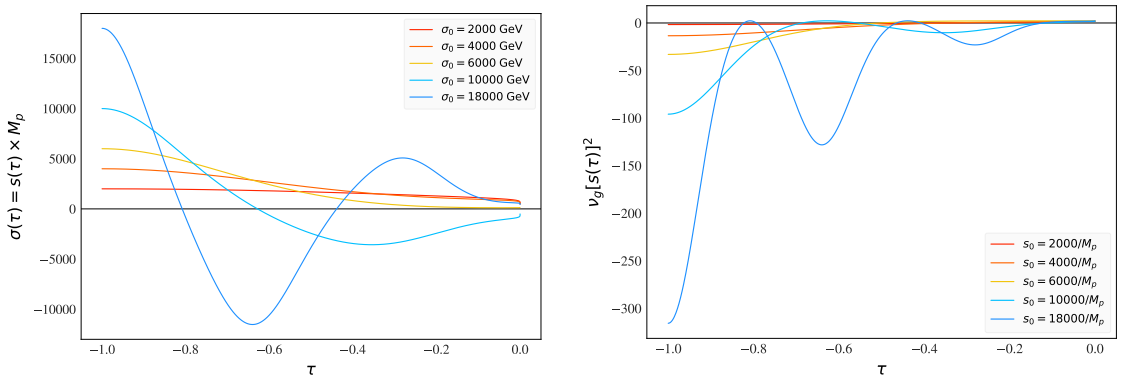

(a) $\sigma(\tau) = s(\tau) \times M_p$ (b) $\nu_g^2\big(s(\tau)\big)$

Figure 7.3: Location of the zero mode, $\sigma = sM_p$, on the Higgs-like spectator potential of eq. (7.36) and evolution of the quantity ν_g^2—where ν_g is given by eqs. (7.27b) and (7.37)—during inflation, corresponding to the primordial cases shown in figure 7.2. As in figure 7.2, $T = T_{GH} = 100$ GeV, $H_{ds} \approx 628$ GeV, and $\epsilon = O(10^{-25})$). Dimensionless conformal time τ is defined in eq. (7.26).

7.3.3.1 Narrative for an observationally relevant result

Despite the case study format of this work, it's worth taking a moment to imagine what theoretical scenario an observationally relevant result like figure 7.2h might correspond to. Let us start with the potential and initial conditions. The results in figure 7.2h utilize a Higgs-like potential in the symmetry broken phase ($T = T_{GH} = 100$ GeV $< T_c$ for my simplified model). They also require the zero mode of the field to begin its entangled evolution far away from the minimum (at an initial position of $\sigma = 18000$ GeV). The zero mode is then allowed to roll during the course of inflation, and it has enough energy to explore both sides of the Higgs-like potential (as shown in figure 7.3a). It then dynamically settles into one of the minima of the potential by the end of inflation as its kinetic energy decreases (a simple form of "vacuum selection").

For such a result to occur, there needs to be some event that precedes the entangled evolution and causes the spectator field to be high up on the potential at η_0. This could be achieved by means of a bubble collison [196], a period of quantum fluctuations that would drive the location of the zero mode up the potential [197, 198], or some hitherto undiscovered mechanism. (For example, the inflaton zero mode is typically assumed to begin inflation away from its potential minimum, and one could argue we do not yet have

a satisfactory mechanism why this should be so.) Such an event or mechanism is not out of the question, but would require a deeper understanding of what precedes inflation in this scenario to fully motivate it.

A related question is 'what is the timing of the (electroweak) phase transition?' for the result in figure 7.2h. If one is interested in the time at which the Higgs-like potential develops a second minimum, then the (electroweak) phase transition precedes inflation in our narrative. However, if one is curious when vacuum selection has occurred, then this would happen at the end of inflation in the narrative corresponding to figure 7.2h. In either case, one would know that the phase transition occurred by the end of inflation, and not afterward, if a result such as figure 7.2h was found to be consistent with observational data.

Lastly, the results in figure 7.2h assume low-scale ($H_{ds} \approx 628$ GeV) inflation as a theoretical input. While this may not be necessarily favored in the literature (i.e. GUT-type motivations), it is also not observationally ruled out (see the discussion in section 7.1). It's also worth pointing out that I only assume the observationally (CMB) relevant part of inflation occurs at a low scale to obtain figure 7.2h. The era of entangled evolution that my equations probe might be proceeded by an era of higher scale inflation, or there may be some other pre-inflationary phase.

However, if a signal such as figure 7.2h has the potential to be observationally constrained, the question then becomes, how unique is it? At the lowest level, since we are fairly ignorant about the intricacies of the very early universe, can Planck data distinguish between the signal in figure 7.2h and other well-motivated scalar spectators with similar levels of entanglement? If it can, then can the data make more fine grained distinctions, such as determining whether a Higgs-like potential is symmetry broken or symmetry restored, at the level of CMB anisotropies? And finally, are such signals unique to a particular inflationary energy scale, or do degeneracies exist? I explore these questions in the next two sections.

7.4 CMB-level potential differentiation

In this section I investigate whether, given an inflationary energy scale, Planck data can distinguish between entanglement with a Higgs-like potential compared to other spectator scalar potentials with similar levels of entanglement. This is a first step towards discerning whether entanglement can be used as a probe of phase transitions—since if differentiation between different scalar potentials proves impossible at the level of CMB anisotropies, it then seems unlikely the data would be able to distinguish between different behaviors of the same potential. I first define the other test cases to compare with the signal of figure 7.2h, and then present some initial results from C_ℓ^{TT} residuals.

7.4.1 Contrasting spectator scalars

In the wild west of the early universe, there are, of course, a myriad of spectator scalars one could consider with a variety of theoretical motivations and UV completions. The list I considered for this case study analysis therefore is definitely not exhaustive, and simply represents some straightforward examples that nevertheless had the potential to confuse the data.

The first contrasting possibility I considered was a free massive scalar with the same mass as the Higgs-like potential at $T = 0$, i.e.

$$V_{125\,GeV} = \frac{1}{2} M_h^2 \sigma^2, \qquad M_h = 125 \text{ GeV} . \tag{7.43}$$

The second possibility was also a free massive scalar, but it was engineered so that its mass was the same as the initial effective mass for the signal in figure 7.2h, i.e.

$$V_{11\,TeV} = \frac{1}{2} M^2 \sigma^2, \qquad M = 11 \text{ TeV } s.t.\ \nu_{g,11\,TeV} = \nu_{g,i,Higgs}. \tag{7.44}$$

This made it so the parameter ν_g was the same for both cases initially. However, after the initial time the Higgs-like spectator's ν_g was allowed to evolve as the zero mode rolled, while ν_g for the 11 TeV free massive scalar remained constant throughout the entangled evolution (since the second derivative of the potential for a free massive scalar is constant).

Finally, the third contrasting case I considered was a 'strongly' symmetry non restored (SSNR) Higgs-like potential. This potential could be used as a proxy for symmetry non-restoration in the early universe, or it could be a simple model of a 'dark Higgs'-type

scalar that is heavier than its standard model counterpart. For this analysis I designed the SSNR potential as follows:

$$V_{SSNR} = -\frac{1}{2}(25m_h)^2\sigma^2 + \frac{\lambda_h}{4}\sigma^4 + \frac{\lambda_h}{8}T^2\sigma^2 \tag{7.45}$$

with $m_h = M_h/\sqrt{2}$, $M_h = 125$ GeV, $\lambda_h = m_h^2/v^2$, and $v = 246$ GeV, as done in eq. (7.35). In essence I increased the mass by a factor of 25, but kept the self coupling the same compared to the Higgs-like potential in eq. (7.35), which deepens the potential wells and therefore raises the temperature at which the SSNR potential becomes 'symmetry restored.'

Figure 7.4 plots these three potentials together with the Higgs-like potential signal from figure 7.2h. For the potentials with explicit temperature dependence, $T = T_{GH} = 100$ GeV as in figure 7.2, and all equations used the same value for ϵ (and therefore H_{ds}), as determined by eq. (7.41). The initial positions for each case are listed in the caption of figure 7.4, and all four cases plotted in figure 7.4 had no initial velocity. These initial conditions were chosen so that each case corresponded to a roughly comparable amount of entanglement, parameterized by λ (see the discussion surrounding eq. 7.24), as well as the degree to which $|\frac{\Delta_s^2}{\Delta_{s,BD}^2}| > 1$. For the cases shown in figure 7.4, $\lambda = \lambda_1(\tau)|_{\tau=-1}$, where λ_1 is defined in eq. 7.26 in terms of dimensionless variables.

At the level of the power spectrum, the free massive scalar potential of eq. (7.43)—plotted in purple in figure 7.4—is the most visually different by eye. However, all the results plotted in figure 7.4 have visual 'tells' that distinguish them. The other free massive scalar potential, given by eq. (7.44), has similar behavior to the Higgs-like potential at smaller k values, but has a prominant secondary oscillatory feature at slightly higher k that the other potentials do not share. Even the SNR vs SSNR Higgs-like potentials are distinguishable at this level—mostly with amplitude, but if one stares closely at the range just to the right of $k = 10^{-5}Mpc^{-1}$ in figure 7.4, there is also some evidence of the two potentials exchanging which one has the greater amplitude for a given oscillation. In the next section I will present results investigating whether a form of these visual distinctions persist at the level of CMB anisotropies.

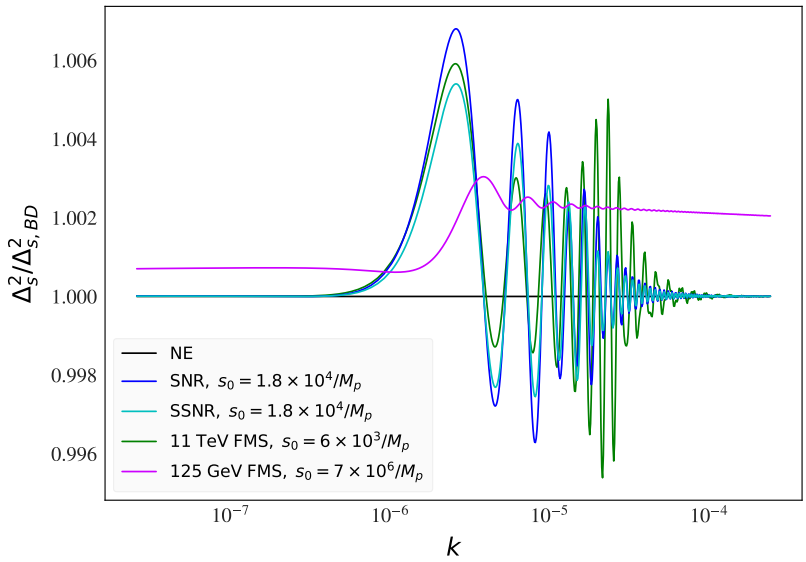

Figure 7.4: Fractional corrections to the scalar primordial power spectrum due to entanglement, $\frac{\Delta_s^2}{\Delta_{s,BD}^2}$, for the SNR Higgs-like spectator potential (eq. 7.36, blue), the SSNR Higgs-like potential (eq. 7.45, cyan), the 11 TeV free massive scalar (eq. 7.44, green), and the 125 GeV free massive scalar (eq. 7.43, purple), for a similar level of entanglement (as discussed in the text). The non entangled (NE) case corresponds to $\frac{\Delta_s^2}{\Delta_{s,BD}^2} = 1$. $k_{\rm ent} = 10^{-6}$ (see eq. 7.32).

7.4.2 CMB residuals

To compare the primordial power spectra results in the previous section with CMB data, I use the form of the scalar power spectrum defined in eq. (7.31) with A_s and n_s taken from best fit Planck values [20]. I also include the effects of varying $k_{\rm ent}$. Varying $k_{\rm ent}$ corresponds to shifting the scale that leaves the inflationary horizon at the onset of entanglement, and therefore the time at which entangled evolution begins (as discussed in section 7.2). As investigated previously [4], many modifications to the primordial power spectrum render CMB observables largely unchanged when the onset of entanglement corresponds to the largest observable scale, $k = 10^{-6}{\rm Mpc}^{-1}$. By shifting $k_{\rm ent}$ to smaller scales, the data becomes much more constraining. Figure 7.5 shows the SNR Higgs-like spectra from figure 7.4 for a few different values of $k_{\rm ent}$.

Figure 7.6 shows the corresponding C_ℓ^{TT} residuals for the SNR Higgs-like potential—computed using CLASS [151]—both with and without error-bars from Planck data [20]. The residuals are with respect to the standard Bunch-Davies non-entangled solution (plot-

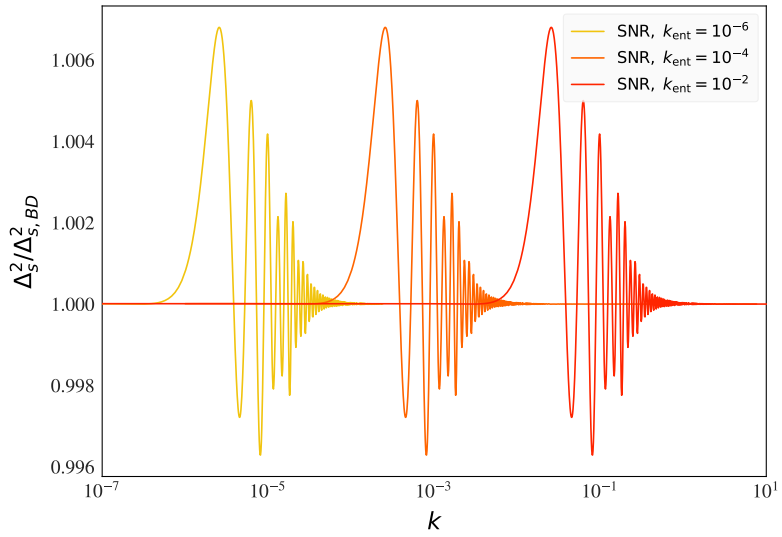

Figure 7.5: Fractional corrections to the scalar primordial power spectrum due to entanglement, $\frac{\Delta_s^2}{\Delta_{s,BD}^2}$, for the SNR Higgs-like spectator potential, given three different values of $k_{\rm ent}$. $k_{\rm ent} = 10^{-6}$ corresponds to the SNR spectra plotted in figure 7.4 and figure 7.2h.

ted as NE in the figure). I found spectra with $k_{\rm ent}$ in the range $10^{-4} \leq k_{\rm ent} \leq 10^{-2}$ were most highly constrained by the data, so I have displayed a selection of solutions within that range in the figure.

The amplitude of the C_ℓ residuals in figure 7.6 are small but not insignificant. In particular, the region near the first three peaks of the TT-spectra has the most potential for constraining power, especially if future experiments are able to shrink some of the errorbars in that region. The signals are also clearly oscillatory—if one compares the results in figure 7.6 to the TT peak locations (plotted in red), the residuals shown clearly have unique oscillatory patterns (rather than simply shifting the amplitude of the TT peaks, for example). Furthermore, note the fact that the largest oscillatory features in the corresponding primordial power spectrum of figure 7.2h occur within 1-2 orders of magnitude (k decades) directly following $k_{\rm ent}$. From figure 7.6, it appears that values of $k_{\rm ent}$ close to k_{piv}—specifically $0.05\ k_{piv} \leq k_{\rm ent} \leq k_{piv}$—are the most observationally relevant signals from the perspective of the TT spectra. For all of those signals, their values of $k_{\rm ent}$ would place the largest oscillatory features in the corresponding primordial spectrum to dominate the scales around k_{piv}.

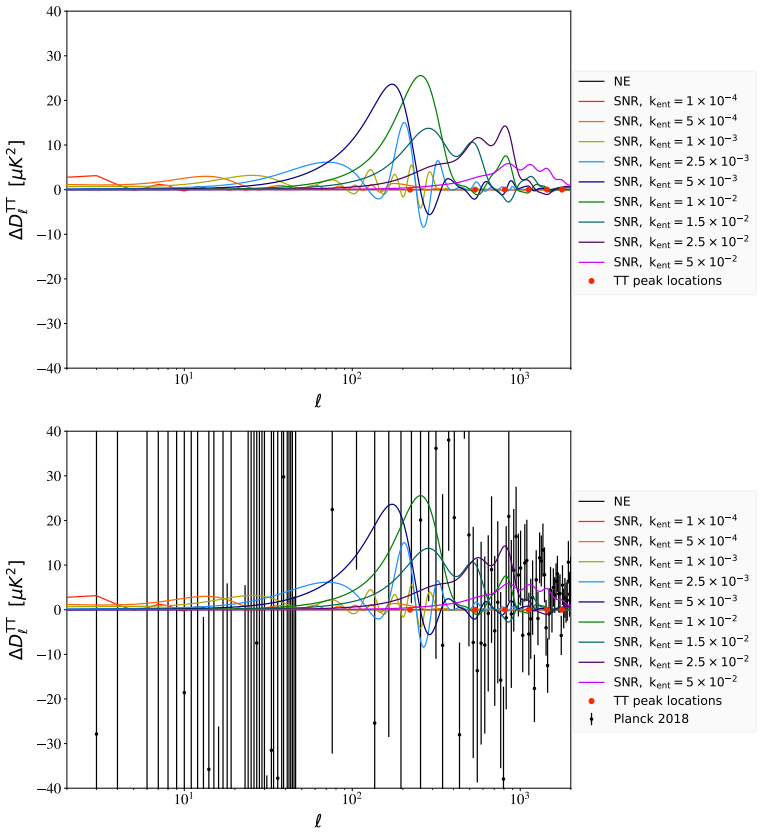

Figure 7.6: TT power spectrum residuals given the primordial power spectrum corrections in figure 7.2h for the SNR Higgs-like potential. $D_\ell^{TT} = \frac{\ell(\ell+1)}{2\pi} C_\ell^{TT}$. Residuals are calculated with respect to the non-entangled (NE) Bunch-Davies result. k_{ent} is varied as labeled in the caption. Locations of the TT peaks are also plotted to guide the eye. Data from the Planck 2018 data release.

One can repeat the same experiments for the other cases plotted in figure 7.4. Figure 7.7 shows the C_ℓ^{TT} residuals for the 125 GeV free massive scalar (figure 7.7a), the 11 TeV free massive scalar (figure 7.7b) and the SSNR Higgs-like spectator (figure 7.7c), given the potentials defined in section 7.4.1.

The results in figure 7.7a are similar to what was seen in previous work [5], in that lower mass (i.e. $M_{eff} \leq H_{ds}$) free massive scalar potentials typically cannot impart many oscillatory features due to entanglement at the level of CMB anisotropies. If one compares the residuals in figure 7.7a to the locations of the TT peaks, one can see the main net effect of entanglement is to increase the amplitude of the TT peaks. Contrast this to the results in figures 7.7b and 7.7c, where there are clearly oscillatory features of the type in

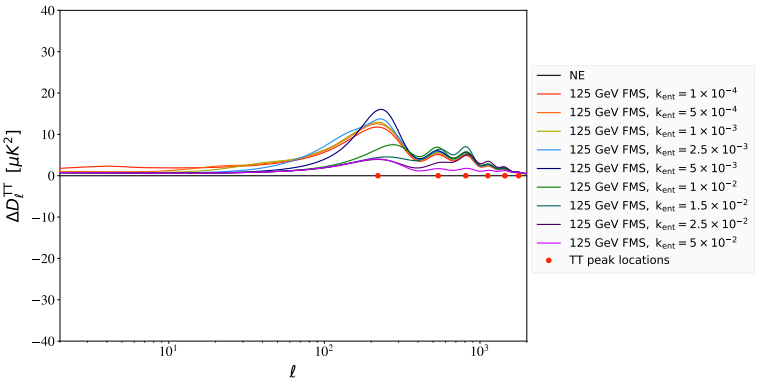

(a) 125 GeV free massive scalar (eq. 7.43)

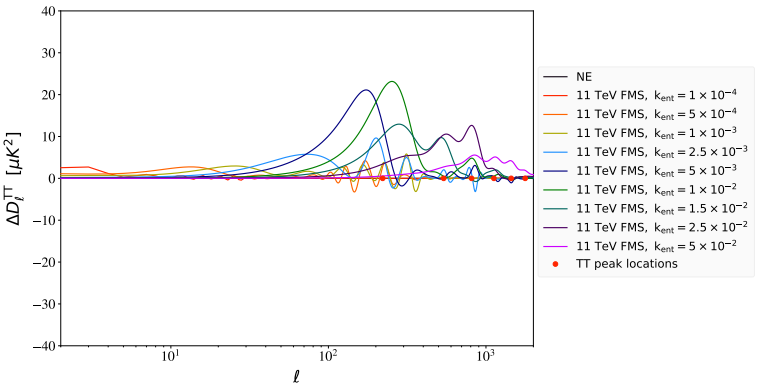

(b) 11 TeV free massive scalar (eq. 7.44)

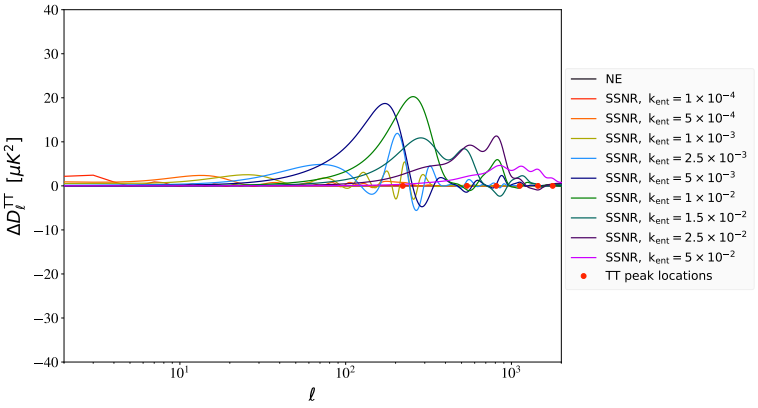

(c) SSNR Higgs-like potential (eq. 7.45)

Figure 7.7: TT power spectrum residuals given the primordial power spectrum corrections in figure 7.4 for the spectator potentials defined in eqs. (7.43), (7.44), and (7.45). $D_\ell^{TT} = \frac{\ell(\ell+1)}{2\pi} C_\ell^{TT}$. Residuals are calculated with respect to the non-entangled (NE) Bunch-Davies result. k_{ent} is varied as labeled in the caption. Locations of the TT peaks are also plotted to guide the eye.

figure 7.6. [9]

[9]The spectator potential that generates the results in figure 7.7b is also a free massive scalar, however its mass is larger than the Hubble scale, H_{ds}, which generates further oscillatory features (as shown in

Having shown that the primordial spectra in figure 7.4 yield CMB residuals that are not completely insignificant, I conclude this section with some direct comparisons. As a representative example, figure 7.8 contrasts the C_ℓ^{TT} residuals for the four potentials in question, for two different values of k_{ent}. If one compares these results to the primordial comparison of figure 7.4, one can see many of the visual 'tells' discussed with the primordial results still exist at the level of CMB anisotropies.

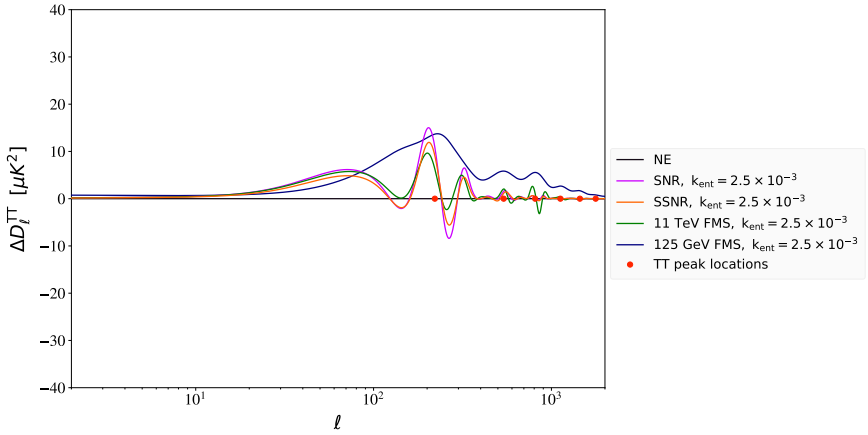

(a) $k_{\text{ent}} = 2.5 \times 10^{-3}$ comparison

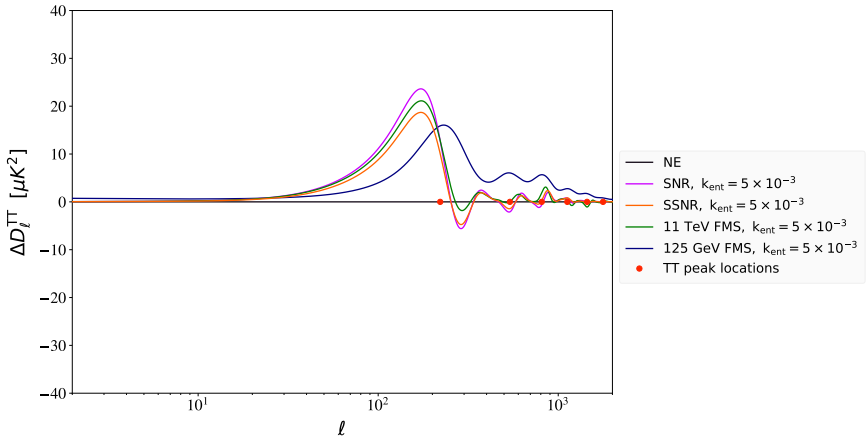

(b) $k_{\text{ent}} = 5 \times 10^{-3}$ comparison

Figure 7.8: Comparison of TT power spectrum residuals, given the primordial power spectrum corrections in figure 7.4. $D_\ell^{TT} = \frac{\ell(\ell+1)}{2\pi} C_\ell^{TT}$. Residuals are calculated with respect to the non-entangled (NE) Bunch-Davies result. k_{ent} is fixed for each subfigure. Locations of the TT peaks are also plotted to guide the eye.

figure 7.4). As discussed in section 7.3.3, this is a mass region the analysis in [5] did not investigate due to technical limitations, but that I was able to investigate for this work given a (non-ideal) workaround in my code.

For example, in both figure 7.8a and figure 7.8b, the 125 GeV free massive scalar has a visually distinct impact compared to the other alternatives, just as its primordial signature in figure 7.4 is also distinct. Differences between the other three potentials are more suble, but still exist by eye. The oscillations in C_ℓ^{TT} residuals for the 11 TeV free massive scalar are phase shifted compared to the Higgs-like and SSNR Higgs-like potentials for several ℓ values in both plots. There is also evidence of a secondary oscillatory feature at higher ℓ (clearest in figure 7.8a) that the other three potentials do not have, most likely due to the secondary feature that also exists in the corresponding primordial power spectrum (see figure 7.4).[10] Even the Higgs-like and SSNR Higgs-like potentials show clear visual differentiation in the amplitudes of their residuals.

Since this work is an exploratory case study, my goal is not to prove every minutia of my guiding questions, but instead explore what might be possible. In this section I have shown it *is* possible to distinguish entanglement with a Higgs-like spectator versus other spectator scalar potentials, at the level of CMB residuals. In fact, I have done one step better, as two of the contrasting spectators had features that were highly similar to the Higgs-like potential at a primordial level. And since this coarse grained distinction appears feasible, I turn to more fine grained questions in the next section—namely whether one can determine if the Higgs-like potential is symmetry broken or symmetry restored, and to what degree such signatures are unique to a given inflationary energy scale.

7.5 Sensitivity to phase transitions and the inflationary energy scale

Given the simple model for a Higgs-like spectator laid out in section 7.3, questions about phase transitions and the inflationary energy scale are inherently linked. The inflationary energy scale, H_{ds}, is linked to the first slow roll parameter, ϵ, and T_{GH}—which plays the role of 'temperature' in this work—in my model, as discussed in section 7.3.2.2. Thus, if one were able to detect a signal in the data consistent with entanglement with a SNR

[10] For example, using the approximation $\ell \approx (14000 \text{ Mpc})k$ and taking the k_{ent} shift in figure 7.8a into account, the secondary oscillatory feature at $\ell = 8{\times}10^2{-}1{\times}10^3$ corresponds to $k = 2.3{-}2.9{\times}10^{-5}\text{Mpc}^{-1}$, which is the approximate location of the secondary feature in figure 7.4 for the 11 TeV free massive scalar.

Higgs-like spectator, then one would also implicitly know the inflationary energy scale. Similarly, if a signal consistent with a Higgs-like spectator at a given inflationary energy scale was detected, then one would know by definition if the potential was symmetry restored or not. In this section I make a first pass investigating how unique such signals are, or if degeneracies exist to impede such an analysis.

Consider again the signal in figure 7.2h. The underlying spectator potential is the symmetry non-restored Higgs-like potential of eq. (7.36). Figure 7.9 shows what happens when $T = T_{GH}$ (and therefore therefore ϵ and H_{ds}) are varied, keeping the rest of the spectator initial conditions fixed.

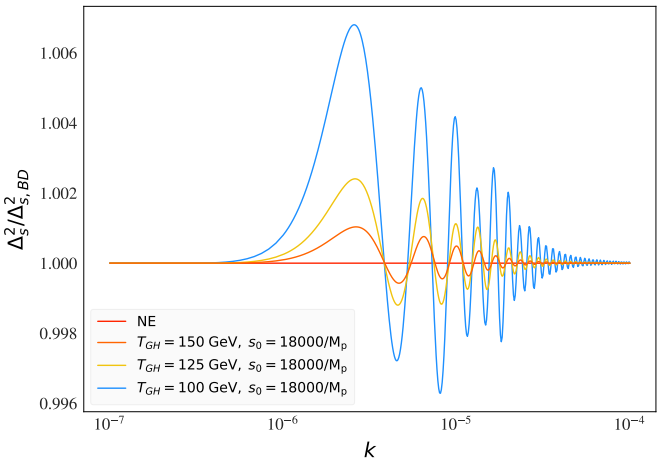

Figure 7.9: Fractional corrections to the scalar primordial power spectrum due to entanglement, $\frac{\Delta_s^2}{\Delta_{s,BD}^2}$, for the Higgs-like spectator potential. Initial conditions for the zero mode are held fixed—with $s_0 = 18000/M_p$ and $v_0 = 0$—but $T = T_{GH}$ (and therefore ϵ and H_{ds}) is varied. The non entangled (NE) case corresponds to $\frac{\Delta_s^2}{\Delta_{s,BD}^2} = 1$. $k_{\text{ent}} = 10^{-6}$ (see eq. 7.32).

Clearly, increasing T causes a decrease in amplitude, as well as subtle shifts in the character of the oscillations. The values of T shown in figure 7.9 are all within $T < T_c$ for my simplified model, and so all correspond to SNR potentials, but I found the trend continues even when $T > T_c$ in my numerical experiments (in that $\frac{\Delta_s^2}{\Delta_{s,BD}^2}$ continues to decrease as T is increased, if the spectator zero mode initial conditions are fixed). From this evidence one might be tempted to say, yes, a signal is unique to a particular inflationary energy scale—which would also enable one to answer questions about phase transitions by definition, as discussed above. However, this is unfortunately not the case.

Figure 7.10 demonstrates a degeneracy that exists within the technical framework. The trend identified previously is still true, i.e. that increasing T (and therefore ϵ and H_{ds}) causes $\frac{\Delta_s^2}{\Delta_{s,BD}^2}$ to decrease. However, it is possible to vary the initial position of the zero mode to compensate for that effect, as shown in figure 7.10a for a few values of T above and below T_c. More precisely, the near exact degeneracy in figure 7.10a was obtained by selecting a value of the initial position of the zero mode such that $\nu_{g,i}$, (eq. 7.27b at the initial time, τ_0), was the same for both potentials despite the change in T (ϵ, H_{ds}). (This then caused the initial conditions in eq. (7.30) to be the same for both cases, since I set the initial velocity of the spectator to be zero.) This degeneracy also persists for very high temperatures, and therefore high scale inflation, as shown in figure 7.10b. And if such a degeneracy already exists at the primordial power spectrum level, it is highly unlikely CMB data will be able to differentiate anything.

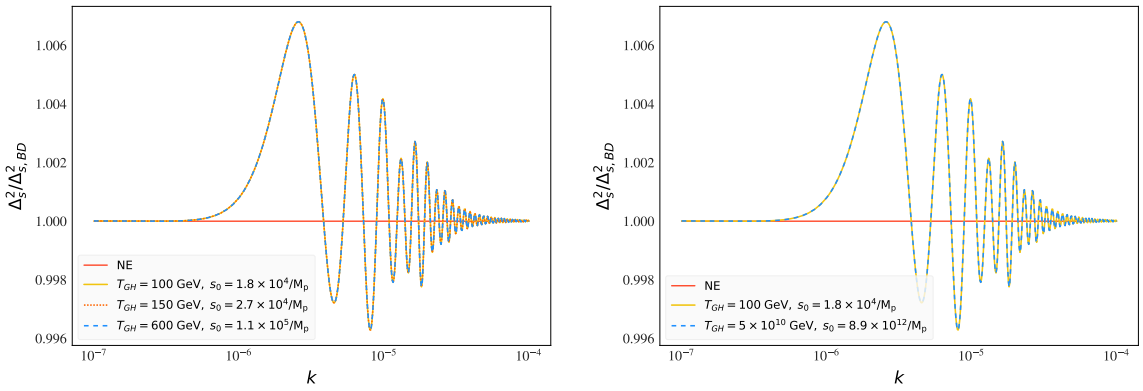

(a) (b)

Figure 7.10: Fractional corrections to the scalar primordial power spectrum due to entanglement, $\frac{\Delta_s^2}{\Delta_{s,BD}^2}$, for the Higgs-like spectator potential. Both the initial position of the zero mode and $T = T_{GH}$ (and therefore ϵ and H_{ds}) are varied. $v_0 = 0$ for all cases, as in figure 7.9. The non entangled (NE) case corresponds to $\frac{\Delta_s^2}{\Delta_{s,BD}^2} = 1$. $k_{\text{ent}} = 10^{-6}$ for both plots (see eq. 7.32).

So given the evidence in figures 7.9 and 7.10, one might conclude it is difficult to determine the energy scale of inflation using entanglement for a Higgs-like potential unless one also knows the initial conditions of the spectator zero mode. If the initial conditions of the zero mode as well as the energy scale of inflation are free parameters in a Monte Carlo analysis, such an analysis would be set up for failure due to the degeneracy demonstrated

in figure 7.10. However, if a model had some theoretical motivation for the values of the initial conditions of the spectator field zero mode—and if such values produced large enough corrections to the primordial power spectrum due to entanglement to be observationally viable, as discussed in section 7.3.3—then one might be able to say something about the energy scale of inflation using CMB data.

7.5.1 Further analysis

There are some additional caveats to the discussion above. First, in figures 7.9 and 7.10 I have restricted my attention to primordial power spectra that have large enough corrections due to entanglement to be potentially observable in CMB data. Figure 7.11 shows what happens if I attempt to set up the degeneracy in figure 7.10—i.e. pick the initial position of the zero mode such that $\nu_{g,i}$ is the same for both potentials despite the change in T (ϵ, H_{ds})—for a case where the initial position of the zero mode is nearer the origin. In contrast to figure 7.10, there is a clear difference between the two power spectra.

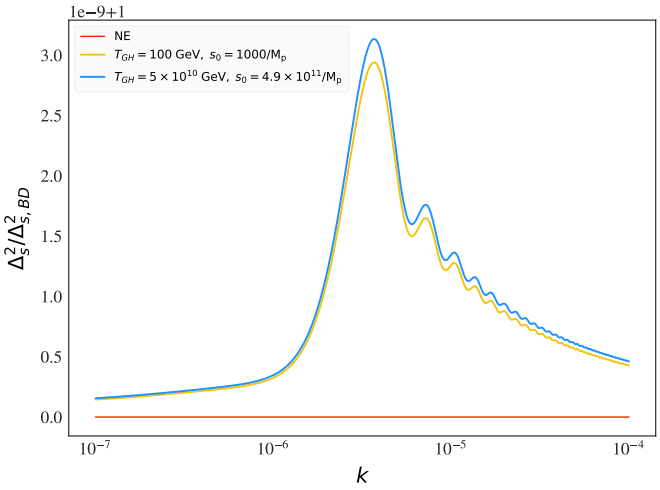

Figure 7.11: Fractional corrections to the scalar primordial power spectrum due to entanglement, $\frac{\Delta_s^2}{\Delta_{s,BD}^2}$, for the Higgs-like spectator potential. Both the initial position of the zero mode and $T = T_{GH}$ (and therefore ϵ and H_{ds}) are varied (see discussion in the text), but with a smaller initial position of the zero mode compared to figure 7.10. The non entangled (NE) case corresponds to $\frac{\Delta_s^2}{\Delta_{s,BD}^2} = 1$. $k_{\text{ent}} = 10^{-6}$ (see eq. 7.32).

As another piece of evidence, consider the SSNR Higgs-like potential from section 7.4.1. The only different between this potential and the standard Higgs-like potential I have

been considering so far in this section is the fact that its mass is 25 times heavier and the location of its minima is 25 times further from the origin (these parameters were chosen so that the quartic and temperature dependant parts of each potential would stay the same). Figure 7.12 shows the result of performing the equivalent experiment to figure 7.10b for this potential. Despite setting up the $\nu_{g,i}$ 'degeneracy conditions' described previously,

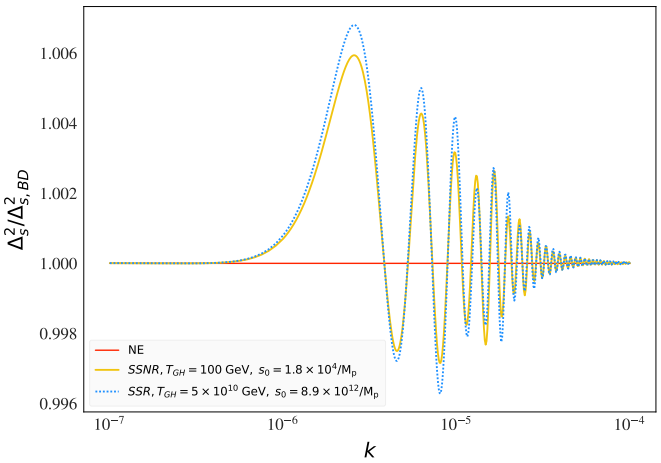

Figure 7.12: Fractional corrections to the scalar primordial power spectrum due to entanglement, $\frac{\Delta_s^2}{\Delta_{s,BD}^2}$, for the SSNR/SSR Higgs-like spectator potential. Both the initial position of the zero mode and $T = T_{GH}$ (and therefore ϵ and H_{ds}) are varied. The non entangled (NE) case corresponds to $\frac{\Delta_s^2}{\Delta_{s,BD}^2} = 1$. $k_{\text{ent}} = 10^{-6}$ (see eq. 7.32).

and choosing an initial value of the spectator zero mode position that corresponds to an observationally viable amount of entanglement, the two potentials are visually different. Unlike with the more standard Higgs-like potential, one appears to be able to distinguish differences in the inflationary energy scale at the primordial level, even though the initial position of the zero mode was artificially varied to make this distinction as difficult as possible.

In both figure 7.10b and 7.12, the comparisons are set up to have identical initial conditions for the entangled evolution equations (kernel equations) between the low and high inflationary energy scale results. Both results correspond to near percent level corrections due to entanglement to the primordial power spectrum. However, the results in figure 7.10b show evidence of a degeneracy, but those in figure 7.12 do not. This suggests that some difference in the entangled evolution during inflation due to the difference be-

tween the two potentials must be sourcing the difference in these results.

To support this claim, figure 7.13 investigates the behavior of the zero mode during inflation for the two cases shown in figure 7.10b and figure 7.12. After applying a vertical scaling for the low-scale inflation results, one can see that the zero mode behaves remarkably similarly for both energy scales for the Higgs-like potential. However this is not the case for the SSNR potential. The high scale, or SSR, results are similar to those in figure 7.13a,[11] however the low-scale results are quite different (i.e. showing evidence of vacuum selection before inflation even finishes). And since the evolution of the zero mode feeds directly into all the equations governing entangled evolution (see section 7.2), any differences or similarities will have an effect on the primordial power spectrum.

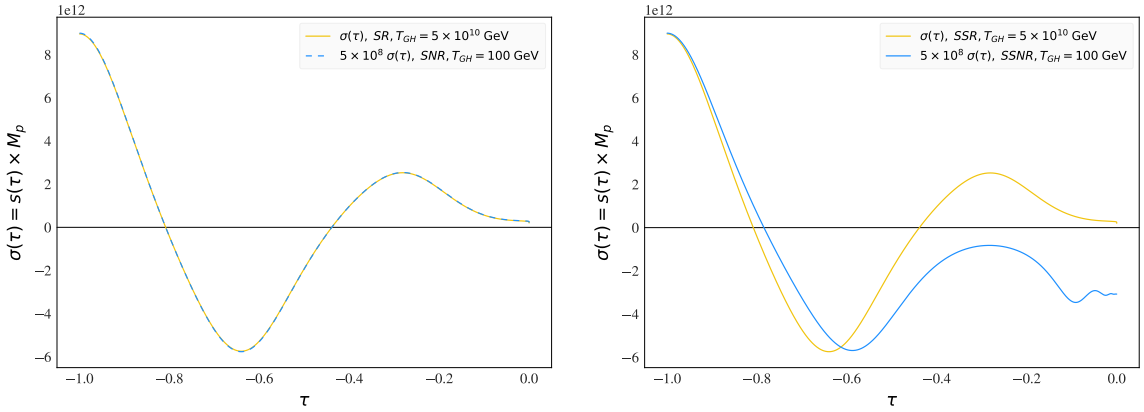

(a) $\sigma = sM_p$, Higgs-like potential

(b) $\sigma = sM_p$, SSNR/SSR Higgs-like potential

Figure 7.13: Location of the zero mode, $\sigma = sM_p$, on the Higgs-like spectator potential of eq. (7.36) and the SSNR/SSR Higgs-like potential of eq. (7.45) during inflation. I qualitatively compare low and high scale inflation by scaling the zero mode location for the low scale results ($T_{GH} = 100\ GeV$ and $s_0 = 1.8 \times 10^4/M_p$) by 5×10^8, to more easily compare with the high scale results ($T_{GH} = 5 \times 10^{10}\ GeV$ and $s_0 = 8.9 \times 10^{12}/M_p$). (Dimensionless conformal time τ is defined in eq. (7.26).)

7.5.1.1 ϕ^4 diagnostics

The analysis in the previous section suggests the following interpretation of the $\sigma - H_{ds}$ degeneracies. Both initial conditions and evolution during inflation play a role in determining entangled corrections to the primordial power spectrum. A degeneracy in

[11] This suggests it may not be quite so easy to distinguish the Higgs-like potential from the SSR Higgs-like potential for high scale inflation, in contrast to the low scale results shown in section 7.4.2.

the initial conditions for the entangled equations (the kernel equations in section 7.2) exists between ϵ and σ (s_0 in dimensionless units), such that the initial position of the zero mode can be adjusted to exactly compensate for a change in ϵ (H_{ds}, T_{GH}). As shown in figure 7.10, this means that a prospective primordial power spectrum result for a Higgs-like potential could correspond to a variety of energy-scale and initial position pairs in parameter space, if the initial position of the zero mode is a free parameter. However, even if such a degeneracy in initial conditions is assumed (a 'worst case scenario'), the degeneracy can still be broken if the evolution of the zero mode position—and therefore the evolution of the entangled wavefunction parameters—is significantly different for the different energy scales (as investigated in figure 7.13 and the surrounding text).

Additional insight into how evolution during inflation can break these degeneracies can be obtained by comparing how similar a given result is to the equivalent ϕ^4 potential (i.e. $V = \frac{\lambda_h}{4}\phi^4$). Figure 7.14 demonstrates that the degeneracies (or lack thereof) show in figures 7.10b, 7.11, and 7.12 between high and low inflationary energy scale results can be mimicked by a comparison with the equivalent ϕ^4 potential at low scale. And figure 7.15 does the same comparison for the evolution of the zero mode for the results in figure 7.14b and 7.14c.

Examining the results of figures 7.14 and 7.15, it appears that there is a threshold above which the quadratic terms in the Higgs-like potential—which control the symmetry breaking features through the presence or absence of multiple minima—become subdominant, such that the zero mode evolution is phenomenologically equivalent to ϕ^4. (This similarity in zero mode evolution then feeds into the primordial spectra result, as discussed above.) For the SSNR Higgs-like potential the degeneracy threshold is higher since the field is more massive. This allows one to choose larger initial positions for a given energy scale and still see noticeable differences with ϕ^4 (see figure 7.14c), or between energy scales comparing SSR vs SSNR behavior (see figure 7.12). For the standard Higgs-like potential this threshold[12] is lower, which is why the results in figures 7.11 and 7.14a are visually

[12]Further work would be needed to identify exactly where this degeneracy line is in the space of possible initial conditions for a given Higgs-like potential. The result would depend in part on resolution at the C_ℓ level between different cases. It would also depend on whether the initial position was being treated as a totally free or partially free parameter in the analysis.

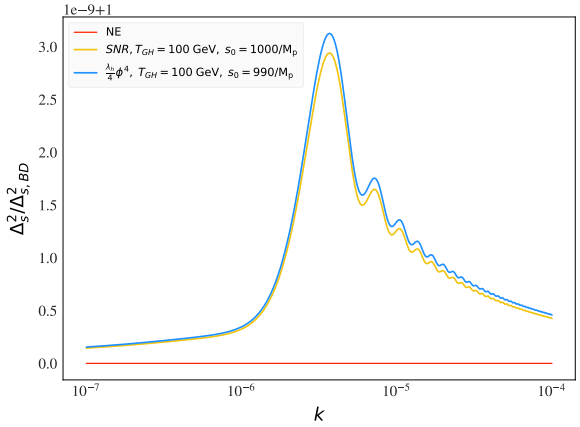

(a) SNR Higgs-like potential vs $\frac{\lambda_h}{4}\phi^4$, compare with figure 7.11

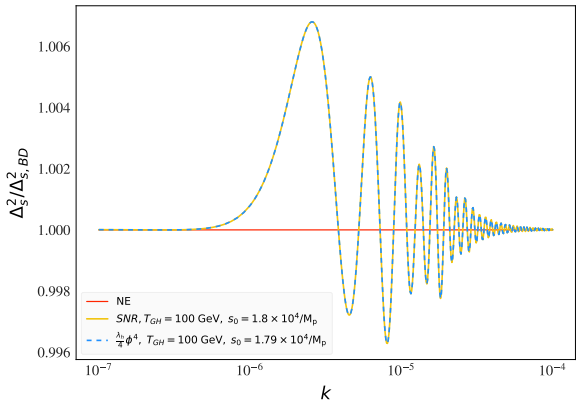

(b) SNR Higgs-like potential vs $\frac{\lambda_h}{4}\phi^4$, compare with figure 7.10b

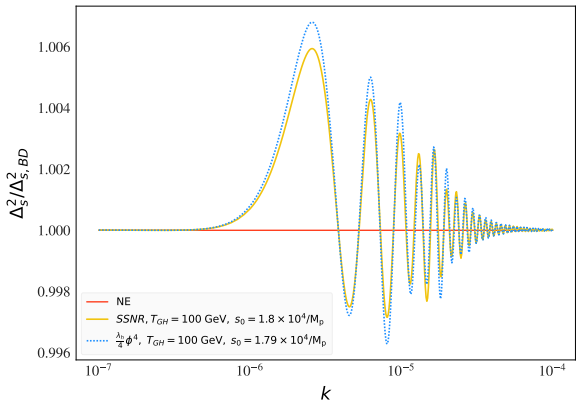

(c) SSNR Higgs-like potential vs $\frac{\lambda_h}{4}\phi^4$, compare with figure 7.12

Figure 7.14: Fractional corrections to the scalar primordial power spectrum due to entanglement, $\frac{\Delta_s^2}{\Delta_{s,BD}^2}$, for the Higgs-like and SSNR Higgs-like spectator potentials and for the equivalent ϕ^4 potential $V = \frac{\lambda_h}{4}\phi^4$. The initial position of the zero mode is varied (such that s_0 causes $\nu_{g,i}$ to be the same for each set of comparisons, as discussed in the text), but $T = T_{GH}$ (and therefore ϵ and H_{ds}) is held fixed. The non entangled (NE) case corresponds to $\frac{\Delta_s^2}{\Delta_{s,BD}^2} = 1$. $k_{\text{ent}} = 10^{-6}$ for all plots (see eq. 7.32).

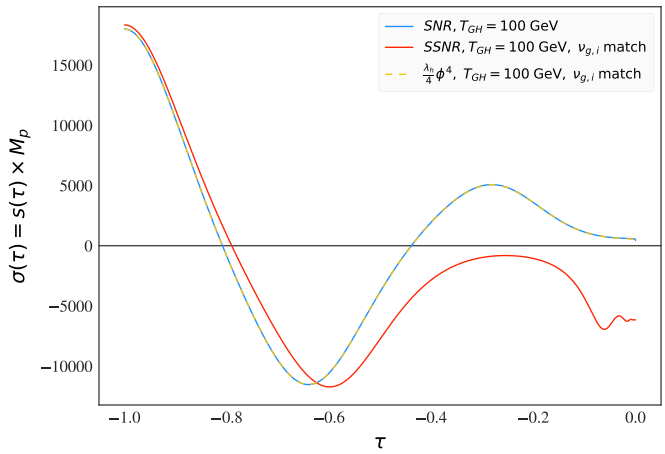

Figure 7.15: Location of the zero mode, $\sigma = sM_p$, on the Higgs-like spectator potential of eq. (7.36), the SSNR Higgs-like potential of eq. (7.45), and $V = \frac{\lambda_h}{4}\phi^4$ during inflation. For all three potentials $T_{GH} = 100\ GeV$, but the initial position of the zero mode has been varied slightly so that $\nu_{g,i}$ is the same for all three cases (to investigate the degeneracy discussed in the text).

distinct, but the results in figures 7.10 and 7.14b are not.

Interpreting further still, the results in figures 7.10 - 7.15 appear to indicate that high-scale inflation results may be degenerate with ϕ^4 for some spectator initial conditions with these types of potentials. Further study would be needed to confirm this, but this is not a total red flag for my motivating questions. For example, take the SSNR Higgs-like potential results. If one had a theoretical reason to put a prior on the initial conditions of that spectator at a level corresponding to potentially observable entanglement, then the results in figures 7.12 and 7.14c—supported by the work in section 7.4.2—demonstrate one could potentially answer whether symmetry breaking has occurred during inflation for that spectator potential. If the data preferred a high-scale result (which may be degenerate with ϕ^4), one could still potentially say with some certainty that symmetry breaking did not occur during inflation, because the low-scale results are visually distinct from both the high-scale and/or ϕ^4 options. In contrast, it appears the SM Higgs may be too light to be able to answer questions about symmetry breaking from the perspective of CMB data with entanglement, since it generates visually indistinct primordial spectra for different energy scales for observationally viable initial conditions.

7.6 Discussion and conclusions

In this paper I have made a case study analysis to investigate whether the technical framework for dynamically generated entangled states developed in [4, 5] can be used to answer questions about early universe phase transitions and/or help determine the inflationary energy scale using CMB data. To investigate this, I used a simple model of a Higgs-like potential as my spectator field. In section 7.3.3 I demonstrated the rich phenomenology of corrections to the primordial power spectrum this type of spectator potential can induce, and noted that only some of these results would produce large enough corrections to be observationally viable. Restricting my focus to observationally viable results, in section 7.4 I then demonstrated how distinct entangled results from a Higgs-like spectator might be compared to other similar scalar spectator potentials, at the level of C_ℓ^{TT} residuals. After demonstrating that such coarse grained distinctions would be possible, I then turned to the related questions of phase transitions and the inflationary energy scale in section 7.5. My analysis in section 7.5 demonstrates that there are some initial values of the spectator zero mode that inhibit distinguishing spectra at different inflationary energy scales—due to a combined degeneracy in initial conditions and dynamical evolution of entangled parameters—and some values that do not. In particular, it appears the SM Higgs (at least in the form of the simple Higgs-like potential I considered here) may be too light to break degeneracies between different energy scales for observationally viable results, whereas a heavier Higgs-like potential—perhaps a 'dark Higgs'—may be able to give some insight into such questions with current data.

The case study format of this work means that not every question was answered in full generality. Still, I hope these results will be a useful signpost for future researchers interested in questions of our Universe's early beginnings. For example, given a narrative of symmetry breaking in the early universe with particular model parameters, this work will give one a rough idea of whether corrections due to entanglement and their potential impact on CMB observables should be considered or not. Also, as discussed in [5], it remains an open question how such corrections due to entanglement might impact the bi-spectrum. Such a calculation might reveal further opportunities to differentiate narratives

of the early universe using entanglement.

7.7 Acknowledgments

I thank A. Adil, A. Albrecht, N. Bolis, R. Holman, L. Knox, R. Ribeiro, and B. Richard for useful discussions. This work was supported in part by the U.S. Department of Energy, Office of Science, Office of High Energy Physics QuantISED program under Contract No. KA2401032. I was also supported by a UC Davis Graduate Research Award.

7.A Supplementary equations

I re-print the kernel equations (as derived in [5]) obtained from solving the functional Schrödinger equation:

$$i\frac{\partial \Psi_k}{\partial \eta} = \mathcal{H}_k \Psi_k \tag{7.46}$$

given a wavefunctional of the form:

$$\Psi_{\vec{k}}\left[v_{\vec{k}}, \theta_{\vec{k}}; \eta\right] = \mathcal{N}_k(\eta)\, \exp\Bigg[-\frac{1}{2}\Big(A_k(\eta) v_{\vec{k}} v_{-\vec{k}} + B_k(\eta)\theta_{\vec{k}}\theta_{-\vec{k}} + C_k(\eta)\big(v_{\vec{k}}\theta_{-\vec{k}} + \theta_{\vec{k}} v_{-\vec{k}}\big)\Big)\Bigg] , \tag{7.47}$$

and Hamiltonian defined in eq. (7.14). One obtains:

$$\begin{aligned} i\partial_\eta A_k = {} & A_k^2 - \left(k^2 - \frac{z''}{z}\right) \\ & + \left\{ \sinh\alpha\ A_k + \cosh\alpha\ C_k + \frac{i}{2}\left[\left(3 - \epsilon + \frac{\eta_{\rm sl}}{2}\right)\mathcal{H}\sinh\alpha + \frac{a^2\partial_\sigma V}{\mathcal{H}^2\sqrt{2M_{\rm Pl}^2\epsilon}}\mathcal{H}\cosh\alpha \right] \right\}^2 \end{aligned} \tag{7.48}$$

$$\begin{aligned} i\partial_\eta B_k = {} & B_k^2 - \left(k^2 - \frac{a''}{a} + a^2\partial_\sigma^2 V\right) \\ & + \left\{ \sinh\alpha\ B_k + \cosh\alpha\ C_k - \frac{i}{2}\left[\left(3 - \epsilon + \frac{\eta_{\rm sl}}{2}\right)\mathcal{H}\sinh\alpha + \frac{a^2\partial_\sigma V}{\mathcal{H}^2\sqrt{2M_{\rm Pl}^2\epsilon}}\mathcal{H}\cosh\alpha \right] \right\}^2 \\ & + 2\epsilon\mathcal{H}^2\left[(\epsilon - 3)\tanh^2\alpha - 2\tanh\alpha\left(\frac{a^2\partial_\sigma V}{\mathcal{H}^2\sqrt{2M_{\rm Pl}^2\epsilon}}\right)\right] \end{aligned} \tag{7.49}$$

$$
\begin{aligned}
i\partial_\eta C_k = {} & \cosh^2\alpha\; C_k\Big(A_k + B_k\Big) \\
& + \frac{\sinh 2\alpha}{2}\Bigg\{ C_k^2 + A_k B_k \\
& \qquad + i\frac{\mathcal{H}}{2}\left[\left(3-\epsilon+\frac{\eta_{\rm sl}}{2}\right) + \coth\alpha\frac{a^2\partial_\sigma V}{\mathcal{H}^2\sqrt{2M_{\rm Pl}^2\epsilon}}\right]\Big(B_k - A_k\Big) \\
& \qquad + \frac{\mathcal{H}^2}{4}\left[\left(3-\epsilon+\frac{\eta_{\rm sl}}{2}\right)\tanh\alpha + \frac{a^2\partial_\sigma V}{\mathcal{H}^2\sqrt{2M_{\rm Pl}^2\epsilon}}\right]^2\Bigg\} \\
& + \tanh\alpha\left[k^2 + \frac{1}{2}a^2\partial_\sigma^2 V + \mathcal{H}^2\left(1+\frac{5}{4}\eta_{\rm sl}\right)\right] + \mathcal{H}^2\left(1+\epsilon+\frac{\eta_{\rm sl}}{2}\right)\frac{a^2\partial_\sigma V}{\mathcal{H}^2\sqrt{2M_{\rm Pl}^2\epsilon}}.
\end{aligned}
\tag{7.50}
$$

where α is defined through eq. (7.11).

Concluding Remarks

Chapter 8

Reflections and Extensions

8.1 Summary of results

In this dissertation I have presented original research that represents concrete technical progress towards illuminating the quantum nature of the world around us. The results demonstrated here have broad impact for both early universe cosmology and quantum information science, as well as their intersections.

In Chapter 2 I introduced the adapted Caldeira-Leggett (ACL) model, a toy model which allowed my collaborators and me to investigate novel quantum entanglement phenomena. After demonstrating that the model reproduces many of the standard results for decoherence and einselection in Chapter 2, in Chapter 3 I presented a derivation and investigation of a unique early time behavior that occurs in the early stages of einselection—the copycat process. Additionally, in Chapter 4 I presented work exploring decoherence and einselection in equilibrium, to see if the emergence of classicality requires an arrow of time, and what that might imply about the initial conditions for our Universe.

Next, in Part Two of this dissertation I presented work from a series of papers investigating dynamically generated entanglement during inflation and its potential observational impact. In Chapter 5 I demonstrated how entanglement is naturally and inevitably generated during inflation given the presence of an additional spectator field with a "rolling" zero mode. I also presented preliminary results showcasing the impact of this entanglement on CMB observables. Then in Chapter 6 I presented results from

a full parameter estimation using Monte Carlo techniques to more precisely determine the amount of entanglement allowed by current data, and what such limits imply for the inflationary vacuum state. Finally, in Chapter 7 I discussed results from a case study investigating whether the observable signatures of entanglement during inflation could be used as a tool to determine the inflationary energy scale and/or the timing of early universe phase transitions.

8.2 Beyond this dissertation

In addition to the extensions suggested in the conclusion sections of Chapters 2 - 7, there are a few additional future directions one could pursue to build off of the work in this dissertation. For work with the ACL model, one might investigate parallels with other models outside the Markovian limit, or explore if the copycat process could be used as a resource for quantum error correction. For work with entangled states during inflation, there are actually several concrete directions one could pursue. I describe some of these ideas in the next subsection.

8.2.1 Further directions for entanglement in the early universe

8.2.1.1 Bispectrum measurements

After thoroughly investigating the observational effects of entanglement on the primordial power spectrum (two point correlator) in the work presented in Chapters 5 - 7 of this dissertation, the next logical step is to look at the bispectrum (three point correlator). The bispectrum is a measure of non-Gaussianity and is highly constrained by data [153], which makes it an excellent tool to distinguish between inflationary models. The simplest standard inflationary scenario predicts Gaussian correlations with a vanishing three point correlator—a result in good agreement with current data—so it would be interesting to investigate whether entanglement can source any deviations from that scenario while still remaining consistent with the data. To investigate this would entail extending the formalism developed in [4, 5] to cubic order in perturbations and then computing the bispectrum to compare with data. It is highly likely that entanglement will source interesting structure in the bispectrum due to the richness of the equations investigated in [4, 5]. Such

work would also extend what was done in [199], which looked at the bispectrum for a more simplified model of entanglement. A calculation of this sort would also lend itself to comparisons with other work, for example bispectrum calculations done in the 'cosmological collider' program (e.g. [200, 201, 202, 203]). Many of the spectator masses that program looks at sit near the inflationary Hubble scale, which is also an interesting parameter range for our entangled states.

8.2.1.2 Heisenberg formalism

The technical framework I helped develop in [4, 5] for entangled states performs calculations in Schrödinger picture quantum field theory. This formalism is ideal for examining evolution of the inflationary state and provides natural field theoretic generalizations of entanglement concepts in standard quantum mechanics. However, most cosmological literature looks at inflationary evolution in the Heisenberg picture. Deriving and developing a complementary formalism for our entangled states in terms of operators and mode function equations of motion—and developing a dictionary to convert between the two pictures—would enable easier comparisons with our work and would help to explore the implications of entanglement in the language of operators. Use of this Heisenberg formalism might also reveal underlying entanglement in other models with oscillatory power spectrum features, e.g. primordial clocks [158]. Such work would also extend and generalize what was done in [204], instead using the Lagrangian in [4, 5] as a starting point.

8.2.1.3 Reheating, gravitational waves

Reheating—the era in our early universe's history where the inflaton decays into standard model particles—is a rich playground for beyond the standard model (BSM) physics. It could be interesting to examine whether entanglement during inflation [4, 5], and the presence of additional spectator field(s) that implies, has interesting effects on reheating. For example, it was shown in [192] that the presence of the Higgs can delay reheating and lower the reheating temperature, which can then affect baryogenesis models. It would be interesting to discover if the presence of spectator scalars during inflation—which are only coupled to the inflaton via gravitational entanglement—can have similar effects. Tools to constrain these effects would include calculating modifications to the transfer functions

used to calculate CMB observables (which could then be constrained with data), and lower bounds on the reheating temperature from nucleosynthesis.

Another interesting direction would be to investigate if our entanglement framework can generate a sizable stochastic gravitational wave background, and to compute whether such a background might be detectable in next generation gravitational wave experiments. This background could be generated, for example, if our spectator field triggers a first order phase transition during reheating, along the lines of what was done in [205] for the primordial clocks model.

References

[1] Andreas Albrecht, Rose Baunach, and Andrew Arrasmith. Adapted caldeira-leggett model. *Phys. Rev. Res.*, 5:023187, Jun 2023.

[2] Rose Baunach, Andreas Albrecht, and Andrew Arrasmith. Copycat process in the early stages of einselection. *Phys. Rev. Res.*, 5:023188, Jun 2023.

[3] Andreas Albrecht, Rose Baunach, and Andrew Arrasmith. Einselection, equilibrium, and cosmology. *Phys. Rev. D*, 106(12):123507, 2022.

[4] Rose Baunach, Nadia Bolis, R. Holman, Stacie Moltner, and Benoit J. Richard. Does Planck actually "see" the Bunch-Davies state? *JCAP*, 07:050, 2021.

[5] Arsalan Adil, Andreas Albrecht, Rose Baunach, R. Holman, Raquel H. Ribeiro, and Benoit J. Richard. Entanglement masquerading in the CMB. *JCAP*, 06:024, 2023.

[6] Rose Baunach. Entangled states as a probe of early universe history: a Higgs case study. 2023, arXiv:2307.00709.

[7] Michael A. Nielsen and Isaac L. Chuang. *Quantum Computation and Quantum Information: 10th Anniversary Edition*. Cambridge University Press, 2011.

[8] H. P. Breuer and F. Petruccione. *The Theory of Open Quantum Systems*. Oxford University Press, 2002.

[9] John Preskill. Quantum information: Chapter 3. Lecture notes for ph219/cs219, California Institute of Technology, 2018.

[10] W. H. Zurek. Environment-induced superselection rules. *Phys. Rev. D*, 26:1862–1880, Oct 1982.

[11] Wojciech Hubert Zurek. Decoherence, einselection, and the quantum origins of the classical. *Rev. Mod. Phys.*, 75:715–775, 2003.

[12] A. O. Caldeira and A. J. Leggett. Path integral approach to quantum brownian motion. *Physica*, 121A:587–616, 1983.

[13] Andreas Albrecht, Nadia Bolis, and R. Holman. Cosmic Inflation: The Most Powerful Microscope in the Universe. 6 2018, arXiv:1806.00392.

[14] Daniel Baumann. Tasi lectures on inflation, 2009.

[15] Scott Dodelson. *Modern Cosmology*. Academic Press, 2003.

[16] V. Mukhanov. *Physical Foundations of Cosmology*. Cambridge University Press, Oxford, 2005.

[17] Edward W. Kolb and Michael S. Turner. *The Early Universe*, volume 69. 1990.

[18] Steven Weinberg. Adiabatic modes in cosmology. *Physical Review D*, 67(12), Jun 2003.

[19] T. S. Bunch and P. C. W. Davies. Quantum Field Theory in de Sitter Space: Renormalization by Point Splitting. *Proc. Roy. Soc. Lond. A*, 360:117–134, 1978.

[20] N. Aghanim, Y. Akrami, M. Ashdown, J. Aumont, C. Baccigalupi, M. Ballardini, A. J. Banday, R. B. Barreiro, N. Bartolo, and et al. Planck 2018 results. *Astronomy & Astrophysics*, 641:A6, Sep 2020.

[21] Y. Akrami et al. Planck 2018 results. X. Constraints on inflation. *Astron. Astrophys.*, 641:A10, 2020.

[22] A. O. Caldeira and A. J. Leggett. Influence of dissipation on quantum tunneling in macroscopic systems. *Phys. Rev. Lett.*, 46:211, 1981.

[23] A. O. Caldeira and A. J. Leggett. Quantum tunneling in a dissipative system. *Annals Phys.*, 149:374–456, 1983.

[24] W. H. Zurek. *Reduction of the Wavepacket: How Long Does it Take?*, pages 145–149. Springer US, Boston, MA, 1986.

[25] Wojciech H. Zurek, Salman Habib, and Juan Pablo Paz. Coherent states via decoherence. *Phys. Rev. Lett.*, 70:1187–1190, 1993.

[26] M.A. Schlosshauer. *Decoherence and the Quantum-To-Classical Transition.* The Frontiers Collection. Springer, 2007.

[27] Wojciech Hubert Zurek. Quantum Theory of the Classical: Einselection, Envariance, Quantum Darwinism and Extantons. *Entropy*, 24(11):1520, 2022.

[28] Philipp Strasberg. Classicality with(out) decoherence: Concepts, relation to Markovianity, and a random matrix theory approach. 1 2023.

[29] Andreas Albrecht. Tuning, Ergodicity, Equilibrium and Cosmology. *Phys. Rev.*, D91(10):103510, 2015.

[30] Andreas Albrecht. Equilibration and "Thermalization" in the Adapted Caldeira–Leggett Model. *Entropy*, 24(3):316, 2022.

[31] Inés de Vega and Daniel Alonso. Dynamics of non-markovian open quantum systems. *Rev. Mod. Phys.*, 89:015001, Jan 2017.

[32] Andreas Albrecht. Investigating decoherence in a simple system. *Phys. Rev.*, D46:5504–5520, 1992.

[33] Andreas Albrecht. Some remarks on quantum coherence. *J. Mod. Opt.*, 41:2467, 1994.

[34] E. Joos and H.D Zeh. The emergence of classical properties through interaction with the environment. *Z. Physik B - Condensed Matter*, 59:223–243, 1985.

[35] B. L. Hu, Juan Pablo Paz, and Yuhong Zhang. Quantum brownian motion in a general environment: Exact master equation with nonlocal dissipation and colored noise. *Phys. Rev. D*, 45:2843–2861, Apr 1992.

[36] W. G. Unruh. Maintaining coherence in quantum computers. *Phys. Rev.*, A51:992, 1995.

[37] J. R. Anglin, J. P. Paz, and W. H. Zurek. Deconstructing decoherence. *Physical Review A*, 55(6):4041–4053, Jun 1997.

[38] F. M. Cucchietti, J. P. Paz, and W. H. Zurek. Decoherence from spin environments. *Phys. Rev. A*, 72:052113, Nov 2005.

[39] W. H. Zurek, F. M. Cucchietti, and J. P. Paz. Gaussian decoherence and gaussian echo from spin environments, 2006.

[40] Patricia R. Levstein, Gonzalo Usaj, and Horacio M. Pastawski. Attenuation of polarization echoes in nuclear magnetic resonance: A study of the emergence of dynamical irreversibility in many-body quantum systems. *The Journal of Chemical Physics*, 108(7):2718–2724, 1998.

[41] A. Goussev, R. A. Jalabert, H. M. Pastawski, and D. Ariel Wisniacki. Loschmidt echo. *Scholarpedia*, 7(8):11687, 2012. revision #127578.

[42] Juan Pablo Paz and Wojciech Hubert Zurek. Quantum limit of decoherence: Environment induced superselection of energy eigenstates. *Phys. Rev. Lett.*, 82:5181–5185, 1999.

[43] Wojciech H. Zurek. Preferred States, Predictability, Classicality and the Environment-Induced Decoherence. *Progress of Theoretical Physics*, 89(2):281–312, 02 1993.

[44] J. J. Halliwell, J. Pérez-Mercader, and W. H. Zurek. *Physical Origins of Time Asymmetry*. 1996.

[45] Michael R. Gallis. Emergence of classicality via decoherence described by lindblad operators. *Phys. Rev. A*, 53:655–660, Feb 1996.

[46] Max Tegmark and Harold S. Shapiro. Decoherence produces coherent states: An explicit proof for harmonic chains. *Phys. Rev. E*, 50:2538–2547, Oct 1994.

[47] D. A. R. Dalvit, J. Dziarmaga, and W. H. Zurek. Predictability sieve, pointer states, and the classicality of quantum trajectories. *Physical Review A*, 72(6), Dec 2005.

[48] Wojciech Hubert Zurek. Decoherence, einselection, and the quantum origins of the classical. *Rev. Mod. Phys.*, 75:715–775, May 2003.

[49] Maximilian Schlosshauer. *Decoherence and the Quantum-To-Classical Transition*. Springer, 2007.

[50] Wojciech H. Zurek, Salman Habib, and Juan Pablo Paz. Coherent states via decoherence. *Phys. Rev. Lett.*, 70:1187–1190, Mar 1993.

[51] O. Kübler and H.D. Zeh. Dynamics of Quantum Correlations. *Annals of Physics*, 76:405–418, 1973.

[52] G. Massimo Palma, Kalle-Antti Suominen, and Artur K. Ekert. Quantum computers and dissipation. *Proc. Roy. Soc. Lond.*, A452:567–584, 1996.

[53] V. V. Dobrovitski, H. A. De Raedt, M. I. Katsnelson, and B. N. Harmon. Quantum oscillations without quantum coherence. *Phys. Rev. Lett.*, 90:210401, May 2003.

[54] Daniel Braun, Fritz Haake, and Walter T. Strunz. Universality of decoherence. *Phys. Rev. Lett.*, 86:2913–2917, Apr 2001.

[55] E. Joos. Continuous measurement: Watchdog effect versus golden rule. *Phys. Rev. D*, 29:1626–1633, Apr 1984.

[56] Asher Peres. Zeno Paradox in Quantum Theory. *Am. J. Phys.*, 48:931–932, 1980.

[57] J. R. Anglin, J. P. Paz, and W. H. Zurek. Deconstructing decoherence. *Physical Review A*, 55(6):4041–4053, Jun 1997.

[58] Asher Peres. Nonexponential decay law. *Annals of Physics*, 129(1):33–46, 1980.

[59] Charles-Alban Deledalle, Loic Denis, Sonia Tabti, and Florence Tupin. Closed-form expressions of the eigen decomposition of 2 x 2 and 3 x 3 hermitian matrices, 2017.

[60] Joachim Kopp. Efficient numerical diagonalization of hermitian 3 x 3 matrices. *Int. J. Mod. Phys.*, C19:523–548, 2008.

[61] R. Penrose. Singularities and time-asymmetry. In *General Relativity, an Einstein Centenary Survey*. Cambridge, 1979.

[62] James B. Hartle. Quantum Buzzwords. 12 2020.

[63] Robert B. Griffiths. Consistent histories and the interpretation of quantum mechanics. *J. Statist. Phys.*, 36:219–272, 1984.

[64] Murray Gell-Mann and James B. Hartle. Quantum Mechanics in the Light of Quantum Cosmology. 1989.

[65] Andreas Albrecht. Following a 'collapsing' wave function. *Phys. Rev. D*, 48:3768–3778, 1993.

[66] Juan Pablo Paz and Wojciech Hubert Zurek. Environment induced decoherence, classicality and consistency of quantum histories. *Phys. Rev. D*, 48:2728–2738, 1993.

[67] Murray Gell-Mann and James B. Hartle. Classical equations for quantum systems. *Phys. Rev. D*, 47:3345–3382, Apr 1993.

[68] Fay Dowker and Adrian Kent. Properties of consistent histories. *Phys. Rev. Lett.*, 75:3038–3041, 1995.

[69] R. Omnès. *Understanding Quantum Mechanics*. Princeton University Press, 1999.

[70] James B. Hartle. Quantum physics and human language. *J. Phys. A*, 40:3101–3121, 2007.

[71] James B. Hartle. The Quasiclassical realms of this quantum universe. *Found. Phys.*, 41:982–1006, 2011.

[72] J.J. Halliwell. Incompatible multiple consistent sets of histories and measures of quantumness. *Phys. Rev. A*, 96(1):012123, 2017.

[73] J. Halliwell. Some recent developments in the decoherent histories approach to quantum theory. *Lect. Notes Phys.*, 633:63–83, 2003.

[74] James B. Hartle. Arrows of Time and Initial and Final Conditions in the Quantum Mechanics of Closed Systems Like the Universe. 2 2020.

[75] P. C. Hohenberg. Colloquium: An introduction to consistent quantum theory. *Rev. Mod. Phys.*, 82:2835–2844, Oct 2010.

[76] Simon Milz, Dario Egloff, Philip Taranto, Thomas Theurer, Martin B. Plenio, Andrea Smirne, and Susana F. Huelga. When is a non-markovian quantum process classical? *Phys. Rev. X*, 10:041049, Dec 2020.

[77] Simon Milz, Fattah Sakuldee, Felix A. Pollock, and Kavan Modi. Kolmogorov extension theorem for (quantum) causal modelling and general probabilistic theories. *Quantum*, 4:255, Apr 2020.

[78] Philipp Strasberg and María García Díaz. Classical quantum stochastic processes. *Physical Review A*, 100(2), Aug 2019.

[79] Fay Dowker and Adrian Kent. On the consistent histories approach to quantum mechanics. *J. Statist. Phys.*, 82:1575–1646, 1996.

[80] Andreas Albrecht. Decoherence and einselection in equilibrium in an adapted Caldeira-Leggett model. Quantum Entanglement in Cosmology, IPMU, 2019.

[81] W. H. Zurek. Quantum Darwinism and Envariance. *arXiv e-prints*, pages quant–ph/0308163, August 2003.

[82] Robin Blume-Kohout and Wojciech H. Zurek. Quantum Darwinism in quantum Brownian motion: the vacuum as a witness. *Phys. Rev. Lett.*, 101:240405, 2008.

[83] C. Jess Riedel, Wojciech H. Zurek, and Michael Zwolak. Objective past of a quantum universe: Redundant records of consistent histories. *Phys. Rev. A*, 93:032126, Mar 2016.

[84] Andrew Arrasmith, Lukasz Cincio, Andrew T. Sornborger, Wojciech H. Zurek, and Patrick J. Coles. Variational consistent histories as a hybrid algorithm for quantum foundations. *Nature Commun.*, 10(1):3438, 2019.

[85] Andreas Albrecht, Robert H. Brandenberger, and R. Matzner. Numerical Analysis of Inflation. *Phys. Rev. D*, 32:1280, 1985.

[86] Andreas Albrecht, Robert H. Brandenberger, and Richard Matzner. Inflation With Generalized Initial Conditions. *Phys. Rev. D*, 35:429, 1987.

[87] Andrei Linde. Inflationary cosmology. *Lecture Notes in Physics*, page 1–54.

[88] William E. East, Matthew Kleban, Andrei Linde, and Leonardo Senatore. Beginning inflation in an inhomogeneous universe. *JCAP*, 09:010, 2016.

[89] Katy Clough, Eugene A. Lim, Brandon S. DiNunno, Willy Fischler, Raphael Flauger, and Sonia Paban. Robustness of Inflation to Inhomogeneous Initial Conditions. *JCAP*, 09:025, 2017.

[90] Katy Clough, Raphael Flauger, and Eugene A. Lim. Robustness of Inflation to Large Tensor Perturbations. *JCAP*, 05:065, 2018.

[91] William G. Cook, Iryna A. Glushchenko, Anna Ijjas, Frans Pretorius, and Paul J. Steinhardt. Supersmoothing through Slow Contraction. *Phys. Lett. B*, 808:135690, 2020.

[92] A. S. Eddington. in *The book of the cosmos: imagining the universe from Heraclitus to Hawking* (Perseus 2000).

[93] R. P. Feynman. *The character of physical law.* MIT, 1956.

[94] R. Penrose. Singularities and time-asymmetry. In *General Relativity, an Einstein Centenary Survey.* Cambridge, 1979.

[95] Dalia S. Goldwirth and Tsvi Piran. Initial conditions for inflation. *Phys. Rept.*, 214:223–291, 1992.

[96] G. W. Gibbons and Neil Turok. The Measure Problem in Cosmology. *Phys. Rev. D*, 77:063516, 2008.

[97] Robert Brandenberger. Initial conditions for inflation — A short review. *Int. J. Mod. Phys. D*, 26(01):1740002, 2016.

[98] Ludwig Boltzmann. On certain questions of the theory of gases. *Nature*, 51(1322):413–415, feb 1895.

[99] Andreas Albrecht. Cosmic inflation and the arrow of time. In John D. Barrow, P. C. W. Davies, and C. L. Harper, editors, *Science and Ultimate Reality*, pages 363–401. Cambridge, 2004.

[100] Stephen W. Hawking. Cosmology from the top down. In *The Davis Meeting on Cosmic Inflation*, pages 91–98, 5 2003.

[101] Andreas Albrecht and Lorenzo Sorbo. Can the universe afford inflation? *Phys. Rev. D*, 70:063528, 2004.

[102] Sean M. Carroll and Jennifer Chen. Spontaneous inflation and the origin of the arrow of time. 10 2004.

[103] Sean M. Carroll and Jennifer Chen. Does inflation provide natural initial conditions for the universe? *Gen. Rel. Grav.*, 37:1671–1674, 2005.

[104] Raphael Bousso, Roni Harnik, Graham D. Kribs, and Gilad Perez. Predicting the Cosmological Constant from the Causal Entropic Principle. *Phys. Rev. D*, 76:043513, 2007.

[105] Alan Guth. Infinite phase space and the two-headed arrow of time. Andrew Chamblin Lecture 2020, University of Cambridge.

[106] Charles Bennett, editor. *Simons Program: Quantum Information in Cosmology*, 2018. Niels Bohr Institute, https://indico.nbi.ku.dk/event/1051/.

[107] J. B. Hartle and S. W. Hawking. Wave function of the universe. *Phys. Rev. D*, 28:2960–2975, Dec 1983.

[108] Alexander Vilenkin. Creation of Universes from Nothing. *Phys. Lett. B*, 117:25–28, 1982.

[109] Job Feldbrugge, Jean-Luc Lehners, and Neil Turok. Lorentzian Quantum Cosmology. *Phys. Rev. D*, 95(10):103508, 2017.

[110] Suddhasattwa Brahma, Robert Brandenberger, and Dong-Han Yeom. Swampland, Trans-Planckian Censorship and Fine-Tuning Problem for Inflation: Tunnelling Wavefunction to the Rescue. *JCAP*, 10:037, 2020.

[111] Caroline Jonas, Jean-Luc Lehners, and Jerome Quintin. Cosmological consequences of a principle of finite amplitudes. 2 2021.

[112] Andreas Albrecht and Alberto Iglesias. The Clock ambiguity and the emergence of physical laws. *Phys. Rev. D*, 77:063506, 2008.

[113] Tom Banks, W. Fischler, and Leonard Susskind. Quantum Cosmology in (2+1)-dimensions and (3+1)-dimensions. *Nucl. Phys. B*, 262:159–186, 1985.

[114] W. Fischler, Bharat Ratra, and Leonard Susskind. Quantum Mechanics of Inflation. *Nucl. Phys. B*, 259:730, 1985. [Erratum: Nucl.Phys.B 268, 747 (1986)].

[115] Alan H. Guth. The Inflationary Universe: A Possible Solution to the Horizon and Flatness Problems. *Phys. Rev. D*, 23:347–356, 1981.

[116] G. W. Gibbons and S. W. Hawking. Cosmological Event Horizons, Thermodynamics, and Particle Creation. *Phys. Rev. D*, 15:2738–2751, 1977.

[117] Don N. Page. The Born Rule Dies. *JCAP*, 07:008, 2009.

[118] Mark Srednicki and James Hartle. The Xerographic Distribution: Scientific Reasoning in a Large Universe. *J. Phys. Conf. Ser.*, 462(1):012050, 2013.

[119] Andreas Albrecht and Daniel Phillips. Origin of probabilities and their application to the multiverse. *Phys. Rev. D*, 90(12):123514, 2014.

[120] C. Jess Riedel. Lock-picking and the anthropic principle. Talk presented at the workshop "A mathematical home for our out of equilibrium universe", QMAP, 2020.

[121] Kimberly K. Boddy, Sean M. Carroll, and Jason Pollack. Why Boltzmann Brains Don't Fluctuate Into Existence From the De Sitter Vacuum. In *Philosophy of Cosmology UK/US Conference*, pages 228–240, 5 2015.

[122] Seth Lloyd. Decoherent histories approach to the cosmological measure problem. 8 2016.

[123] James Hartle and Thomas Hertog. The Observer Strikes Back. In *Philosophy of Cosmology UK/US Conference*, 3 2015.

[124] Andreas Albrecht. de Sitter equilibrium as a fundamental framework for cosmology. *J. Phys. Conf. Ser.*, 174:012006, 2009.

[125] Andreas Albrecht. Cosmic curvature from de Sitter equilibrium cosmology. *Phys. Rev. Lett.*, 107:151102, 2011.

[126] Lisa Dyson, Matthew Kleban, and Leonard Susskind. Disturbing implications of a cosmological constant. *JHEP*, 10:011, 2002.

[127] Sean M. Carroll. Why Boltzmann Brains Are Bad. 2 2017.

[128] Latham Boyle, Kieran Finn, and Neil Turok. CPT-Symmetric Universe. *Phys. Rev. Lett.*, 121(25):251301, 2018.

[129] J. M. Deutsch. Quantum statistical mechanics in a closed system. *Phys. Rev. A*, 43:2046–2049, Feb 1991.

[130] Mark Srednicki. Chaos and quantum thermalization. *Physical Review E*, 50(2):888–901, Aug 1994.

[131] Alexei A. Starobinsky. A New Type of Isotropic Cosmological Models Without Singularity. *Phys. Lett. B*, 91:99–102, 1980.

[132] D. Kazanas. Dynamics of the Universe and Spontaneous Symmetry Breaking. *Astrophys. J. Lett.*, 241:L59–L63, 1980.

[133] Andreas Albrecht and Paul J. Steinhardt. Cosmology for Grand Unified Theories with Radiatively Induced Symmetry Breaking. *Phys. Rev. Lett.*, 48:1220–1223, 1982.

[134] Andrei D. Linde. A New Inflationary Universe Scenario: A Possible Solution of the Horizon, Flatness, Homogeneity, Isotropy and Primordial Monopole Problems. *Phys. Lett. B*, 108:389–393, 1982.

[135] Alan H. Guth and S. Y. Pi. Fluctuations in the New Inflationary Universe. *Phys. Rev. Lett.*, 49:1110–1113, 1982.

[136] James M. Bardeen, Paul J. Steinhardt, and Michael S. Turner. Spontaneous Creation of Almost Scale - Free Density Perturbations in an Inflationary Universe. *Phys. Rev. D*, 28:679, 1983.

[137] S. W. Hawking. The Development of Irregularities in a Single Bubble Inflationary Universe. *Phys. Lett. B*, 115:295, 1982.

[138] N. D. Birrell and P. C. W. Davies. *Quantum Fields in curved space*. Cambridge University Press, 1982.

[139] Andreas Albrecht, Nadia Bolis, and R. Holman. Cosmological Consequences of Initial State Entanglement. *JHEP*, 11:093, 2014.

[140] Nadia Bolis, Andreas Albrecht, and Rich Holman. Modifications to Cosmological Power Spectra from Scalar-Tensor Entanglement and their Observational Consequences. *JCAP*, 12:011, 2016. [Erratum: JCAP 08, E01 (2017)].

[141] Nadia Bolis, Andreas Albrecht, and R. Holman. Non-Gaussianity from Entanglement During Inflation. *JCAP*, 07:021, 2019.

[142] R. Holman and Benoit J. Richard. Generating Entangled Inflationary Quantum States. arXiv:1902.00521 [hep-th] 2019.

[143] Steven Weinberg. Quantum contributions to cosmological correlations. *Phys. Rev. D*, 72:043514, 2005.

[144] Adrián del Rio, Ruth Durrer, and Subodh P. Patil. Tensor Bounds on the Hidden Universe. *JHEP*, 12:094, 2018.

[145] D. Boyanovsky, H. J. de Vega, and R. Holman. Nonequilibrium evolution of scalar fields in FRW cosmologies I. *Phys. Rev. D*, 49:2769–2785, 1994.

[146] Katherine Freese, Christopher T. Hill, and Mark Theodore Mueller. Covariant Functional Schrodinger Formalism and Application to the Hawking Effect. *Nucl. Phys. B*, 255:693–716, 1985.

[147] Richard L. Arnowitt, Stanley Deser, and Charles W. Misner. The Dynamics of general relativity. *Gen. Rel. Grav.*, 40:1997–2027, 2008.

[148] Yi Wang. MathGR: a tensor and GR computation package to keep it simple. ArXiv:1306.1295 [cs.MS], 2013.

[149] Daniel Baumann. *The Physics of Inflation.* Lecture notes available at `https://www.icts.res.in/sites/default/files/baumann_icts_dec2011.pdf`, 2011.

[150] William H. Kinney. Horizon crossing and inflation with large eta. *Phys. Rev. D*, 72:023515, 2005.

[151] Diego Blas, Julien Lesgourgues, and Thomas Tram. The Cosmic Linear Anisotropy Solving System (CLASS). Part II: Approximation schemes. *Journal of Cosmology and Astroparticle Physics*, 2011(07):034–034, Jul 2011.

[152] David J. E. Marsh. Axion Cosmology. *Phys. Rept.*, 643:1–79, 2016.

[153] Y. Akrami et al. Planck 2018 results. IX. Constraints on primordial non-Gaussianity. *Astron. Astrophys.*, 641:A9, 2020.

[154] Bruce Allen. Vacuum States in de Sitter Space. *Phys. Rev. D*, 32:3136, 1985.

[155] E. Mottola. Particle Creation in de Sitter Space. *Phys. Rev. D*, 31:754, 1985.

[156] Hael Collins and R. Holman. An Effective theory of initial conditions in inflation. 7 2005, arXiv:hep-th/0507081.

[157] Hael Collins and R. Holman. The Renormalization of the energy-momentum tensor for an effective initial state. *Phys. Rev. D*, 74:045009, 2006.

[158] Matteo Braglia, Xingang Chen, and Dhiraj Kumar Hazra. Comparing multi-field primordial feature models with the planck data. *Journal of Cosmology and Astroparticle Physics*, 2021(06):005, jun 2021.

[159] Matteo Braglia, Dhiraj Kumar Hazra, L. Sriramkumar, and Fabio Finelli. Generating primordial features at large scales in two field models of inflation. *JCAP*, 08:025, 2020.

[160] Ana Achucarro, Jinn-Ouk Gong, Sjoerd Hardeman, Gonzalo A. Palma, and Subodh P. Patil. Features of heavy physics in the CMB power spectrum. *JCAP*, 01:030, 2011.

[161] Sebastian Cespedes, Vicente Atal, and Gonzalo A. Palma. On the importance of heavy fields during inflation. *JCAP*, 05:008, 2012.

[162] Valentin Assassi, Daniel Baumann, Daniel Green, and Liam McAllister. Planck-Suppressed Operators. *JCAP*, 01:033, 2014.

[163] Thomas Colas, Julien Grain, and Vincent Vennin. Four-mode squeezed states: two-field quantum systems and the symplectic group $\mathrm{Sp}(4,\mathbb{R})$. *Eur. Phys. J. C*, 82(1):6, 2022.

[164] Rathul Nath Raveendran, Krishnamohan Parattu, and L. Sriramkumar. Enhanced power on small scales and evolution of quantum state of perturbations in single and two field inflationary models. *Gen. Rel. Grav.*, 54(8):91, 2022.

[165] Yashar Akrami, Frederico Arroja, M Ashdown, J Aumont, Carlo Baccigalupi, M Ballardini, Anthony J Banday, RB Barreiro, N Bartolo, S Basak, et al. Planck 2018 results-x. constraints on inflation. *Astronomy & Astrophysics*, 641:A10, 2020.

[166] Thejs Brinckmann and Julien Lesgourgues. MontePython 3: boosted MCMC sampler and other features. *Phys. Dark Univ.*, 24:100260, 2019.

[167] Benjamin Audren, Julien Lesgourgues, Karim Benabed, and Simon Prunet. Conservative constraints on early cosmology: an illustration of the monte python cosmological parameter inference code. *Journal of Cosmology and Astroparticle Physics*, 2013(02):001–001, feb 2013.

[168] F. Feroz and M. P. Hobson. Multimodal nested sampling: an efficient and robust alternative to Markov Chain Monte Carlo methods for astronomical data analyses. *Monthly Notices of the Royal Astronomical Society*, 384(2):449–463, 01 2008.

[169] F. Feroz, M. P. Hobson, and M. Bridges. MultiNest: an efficient and robust Bayesian inference tool for cosmology and particle physics. *Monthly Notices of the Royal Astronomical Society*, 398(4):1601–1614, 09 2009.

[170] Farhan Feroz, Michael P. Hobson, Ewan Cameron, and Anthony N. Pettitt. Importance nested sampling and the MultiNest algorithm. *The Open Journal of Astrophysics*, 2(1), nov 2019.

[171] Buchner, J., Georgakakis, A., Nandra, K., Hsu, L., Rangel, C., Brightman, M., Merloni, A., Salvato, M., Donley, J., and Kocevski, D. X-ray spectral modelling of the agn obscuring region in the cdfs: Bayesian model selection and catalogue. *A&A*, 564:A125, 2014.

[172] Farhan Feroz, Kyle Cranmer, Mike Hobson, Roberto Ruiz de Austri, and Roberto Trotta. Challenges of profile likelihood evaluation in multi-dimensional susy scans. *Journal of High Energy Physics*, 2011(6):1–23, 2011.

[173] Antony Lewis. GetDist: a Python package for analysing Monte Carlo samples. 10 2019, arXiv: 1910.13970.

[174] Wayne Hu and Martin White. The damping tail of cosmic microwave background anisotropies. *The Astrophysical Journal*, 479(2):568, 1997.

[175] Dhiraj Kumar Hazra, Akhil Antony, and Arman Shafieloo. One spectrum to cure them all: signature from early Universe solves major anomalies and tensions in cosmology. *JCAP*, 08(08):063, 2022.

[176] Zhen Pan, Lloyd Knox, Brigid Mulroe, and Ali Narimani. Cosmic microwave background acoustic peak locations. *Monthly Notices of the Royal Astronomical Society*, 459(3):2513–2524, 2016.

[177] Wayne Hu and Scott Dodelson. Cosmic microwave background anisotropies. *Annual Review of Astronomy and Astrophysics*, 40(1):171–216, 2002.

[178] Nabila Aghanim, Yashar Akrami, Mark Ashdown, J Aumont, C Baccigalupi, M Ballardini, AJ Banday, R Belén Barreiro, Nicola Bartolo, S Basak, et al. Planck intermediate results-li. features in the cosmic microwave background temperature power spectrum and shifts in cosmological parameters. *Astronomy & Astrophysics*, 607:A95, 2017.

[179] Arsalan Adil, Andreas Albrecht, and Lloyd Knox. Quintessential Cosmological Tensions. 7 2022, arXiv:2207.10235.

[180] Guillermo Ballesteros, JA Casas, JR Espinosa, R Ruiz de Austri, and R Trotta. Flat tree-level inflationary potentials in the light of cosmic microwave background and large scale structure data. *Journal of Cosmology and Astroparticle Physics*, 2008(03):018, 2008.

[181] Alma X. Gonzalez-Morales, Robert Poltis, Blake D. Sherwin, and Licia Verde. Are priors responsible for cosmology favoring additional neutrino species? 6 2011, arXiv:1106.5052.

[182] Alan F Heavens and Elena Sellentin. Objective bayesian analysis of neutrino masses and hierarchy. *Journal of Cosmology and Astroparticle Physics*, 2018(04):047, 2018.

[183] James A. D. Diacoumis and Yvonne Y. Y. Wong. On the prior dependence of cosmological constraints on some dark matter interactions. *JCAP*, 05:025, 2019.

[184] Laura Herold and Elisa G. M. Ferreira. Resolving the Hubble tension with Early Dark Energy. 10 2022, arXiv:2210.16296.

[185] Sarah L Bridle, AM Lewis, J Weller, and G Efstathiou. Reconstructing the primordial power spectrum. *Monthly Notices of the Royal Astronomical Society*, 342(4):L72–L78, 2003.

[186] Pia Mukherjee and Yun Wang. Primordial power spectrum reconstruction. *Journal of Cosmology and astroparticle Physics*, 2005(12):007, 2005.

[187] Roberto Trotta. Bayes in the sky: Bayesian inference and model selection in cosmology. *Contemporary Physics*, 49(2):71–104, 2008.

[188] Jens Chluba, Jan Hamann, and Subodh P Patil. Features and new physical scales in primordial observables: theory and observation. *International Journal of Modern Physics D*, 24(10):1530023, 2015.

[189] Tristan L Smith, Vivian Poulin, José Luis Bernal, Kimberly K Boddy, Marc Kamionkowski, and Riccardo Murgia. Early dark energy is not excluded by current large-scale structure data. *Physical Review D*, 103(12):123542, 2021.

[190] M. Tristram et al. Improved limits on the tensor-to-scalar ratio using BICEP and Planck data. *Phys. Rev. D*, 105(8):083524, 2022.

[191] Michela D'Onofrio and Kari Rummukainen. Standard model cross-over on the lattice. *Phys. Rev. D*, 93:025003, Jan 2016.

[192] Katherine Freese, Evangelos I. Sfakianakis, Patrick Stengel, and Luca Visinelli. The Higgs Boson can delay Reheating after Inflation. *JCAP*, 05:067, 2018.

[193] Mariano Quiros. Finite temperature field theory and phase transitions. In *ICTP Summer School in High-Energy Physics and Cosmology*, pages 187–259, 1 1999.

[194] Marcela Carena, Claudius Krause, Zhen Liu, and Yikun Wang. New approach to electroweak symmetry nonrestoration. *Phys. Rev. D*, 104(5):055016, 2021.

[195] Patrick Meade and Harikrishnan Ramani. Unrestored Electroweak Symmetry. *Phys. Rev. Lett.*, 122(4):041802, 2019.

[196] Anthony Aguirre and Matthew C. Johnson. A Status report on the observability of cosmic bubble collisions. *Rept. Prog. Phys.*, 74:074901, 2011.

[197] Andrei D. Linde. Inflationary Cosmology. *Lect. Notes Phys.*, 738:1–54, 2008.

[198] Alan H. Guth. Eternal inflation and its implications. *J. Phys. A*, 40:6811–6826, 2007.

[199] Nadia Bolis, Andreas Albrecht, and R. Holman. Non-gaussianity from entanglement during inflation. *Journal of Cosmology and Astroparticle Physics*, 2019(07):021–021, jul 2019.

[200] Nima Arkani-Hamed and Juan Maldacena. Cosmological Collider Physics. 2015, arXiv:1503.08043.

[201] Hayden Lee, Daniel Baumann, and Guilherme L. Pimentel. Non-gaussianity as a particle detector. *Journal of High Energy Physics*, 2016(12), dec 2016.

[202] Soubhik Kumar and Raman Sundrum. Heavy-lifting of gauge theories by cosmic inflation. *Journal of High Energy Physics*, 2018(5), may 2018.

[203] Xingang Chen, Reza Ebadi, and Soubhik Kumar. Classical cosmological collider physics and primordial features. *Journal of Cosmology and Astroparticle Physics*, 2022(08):083, aug 2022.

[204] Nadia Bolis, Tomohiro Fujita, Shuntaro Mizuno, and Shinji Mukohyama. Quantum entanglement in multi-field inflation. *Journal of Cosmology and Astroparticle Physics*, 2018(09):004–004, sep 2018.

[205] Arushi Bodas and Raman Sundrum. Primordial clocks within stochastic gravitational wave anisotropies. *Journal of Cosmology and Astroparticle Physics*, 2022(10):012, oct 2022.